

AN INVESTIGATION INTO WALL  
BOUNDARY CONDITIONS AND  
THREE-DIMENSIONAL TURBULENT  
FLOWS USING SMOOTHED  
PARTICLE HYDRODYNAMICS

A THESIS SUBMITTED TO THE UNIVERSITY OF MANCHESTER  
FOR THE DEGREE OF DOCTOR OF PHILOSOPHY  
IN THE FACULTY OF ENGINEERING AND PHYSICAL SCIENCES

2014

By  
Arno Mayrhofer  
School of Mechanical, Aerospace and Civil Engineering

# Contents

<b>Contents</b>	<b>2</b>
<b>List of Tables</b>	<b>7</b>
<b>List of Figures</b>	<b>8</b>
<b>List of Symbols and Operators</b>	<b>11</b>
<b>Abbreviations</b>	<b>14</b>
<b>Abstract</b>	<b>15</b>
<b>Declaration</b>	<b>16</b>
<b>Copyright</b>	<b>17</b>
<b>Acknowledgements</b>	<b>18</b>
<b>1 Introduction</b>	<b>20</b>
1.1 The governing equations . . . . .	21
1.1.1 Numerical treatment . . . . .	22
1.2 Meshless methods . . . . .	22
1.2.1 Construction of basis functions . . . . .	23
1.2.1.1 Smoothed Particle Hydrodynamics . . . . .	23
1.2.1.2 Radial basis functions . . . . .	24
1.2.1.3 Moving least squares . . . . .	24
1.2.1.4 Reproducing kernel particle method . . . . .	25
1.2.1.5 Natural neighbour-based interpolants . . . . .	26
1.2.1.6 Maximum entropy approximants . . . . .	26
1.2.2 The weighted residual procedure . . . . .	27
1.2.3 Disadvantages of meshless methods . . . . .	27
1.2.3.1 Computational effort . . . . .	28

1.2.3.2	Numerical integration . . . . .	28
1.2.3.3	Boundary conditions . . . . .	28
1.3	Smoothed Particle Hydrodynamics . . . . .	29
1.3.1	Applications of SPH . . . . .	32
1.3.1.1	SPH in astrophysics . . . . .	32
1.3.1.2	SPH in solid mechanics . . . . .	32
1.3.1.3	SPH in fluid mechanics . . . . .	32
1.3.1.4	SPH in other areas . . . . .	34
1.3.2	State-of-the-art SPH techniques . . . . .	34
1.3.2.1	Riemann solvers . . . . .	36
1.3.2.2	Arbitrary Lagrange Euler SPH . . . . .	36
1.3.2.3	Incompressible SPH . . . . .	37
1.3.2.4	Chequerboard-free SPH . . . . .	37
1.3.2.5	Dual particle dynamics . . . . .	38
1.3.2.6	Variable resolution . . . . .	38
1.4	Turbulence . . . . .	38
1.4.1	Turbulence experiments . . . . .	40
1.4.2	Direct Numerical Simulation . . . . .	42
1.4.3	Reynolds averaged Navier-Stokes . . . . .	42
1.4.4	Large Eddy Simulation . . . . .	43
1.5	Turbulence simulation with SPH . . . . .	44
1.6	Summary . . . . .	45
<b>2</b>	<b>SPH in fluid dynamics</b> . . . . .	<b>46</b>
2.1	Navier-Stokes equations . . . . .	46
2.1.1	Governing equations . . . . .	46
2.1.2	Boundary conditions . . . . .	48
2.1.3	Calculus of variations . . . . .	49
2.2	Unbounded weakly compressible SPH . . . . .	51
2.2.1	Approximating a value . . . . .	51
2.2.2	Choice of kernel function . . . . .	53
2.2.3	Approximation of first-order derivatives . . . . .	54
2.2.4	Approximation of second-order derivatives . . . . .	57
2.3	Wall-bounded SPH . . . . .	59
2.3.1	Standard wall boundary conditions in SPH . . . . .	60
2.3.2	Unified semi-analytical wall boundary conditions . . . . .	61
2.3.2.1	Compensating the kernel void by $\gamma$ . . . . .	62
2.3.2.2	Governing equation for $\gamma$ . . . . .	64
2.3.2.3	Derivation of gradient and divergence . . . . .	65

2.3.2.4	Second order operators . . . . .	68
2.3.2.5	Prescribing boundary conditions . . . . .	69
2.3.3	Application to the Navier Stokes equations . . . . .	69
2.4	Time-integration . . . . .	71
2.4.1	Time-step restrictions . . . . .	73
<b>3</b>	<b>Investigation of the boundary conditions in 2-D</b>	<b>75</b>
3.1	On the skew-adjoint property including boundaries . . . . .	76
3.1.1	Theoretical investigation . . . . .	76
3.1.2	A numerical experiment . . . . .	80
3.2	A volume diffusion term for numerical turbulence . . . . .	81
3.2.1	Basic idea . . . . .	82
3.2.2	Semi-analytical wall boundary framework . . . . .	84
3.3	Imposing a volume flux in periodic viscous flows . . . . .	85
3.4	Generalization of wall boundary conditions . . . . .	87
3.4.1	Theory . . . . .	87
3.4.2	The wave equation as an example . . . . .	90
3.5	Still water with a free-surface . . . . .	92
3.5.1	Modification of the volume diffusion term . . . . .	92
3.5.2	Modification of the boundary interpolation . . . . .	94
3.6	Dam-break with wedge . . . . .	95
3.7	Preliminary conclusion . . . . .	98
<b>4</b>	<b>Extension to three dimensions</b>	<b>100</b>
4.1	Calculating the mass in 3-D . . . . .	100
4.2	Analytical computation of $\underline{\nabla}\gamma$ in 3-D . . . . .	104
4.2.1	The domain decomposition algorithm . . . . .	105
4.2.2	Analytical formulae for the basic domains . . . . .	108
4.2.2.1	Circular sector . . . . .	108
4.2.2.2	Circular segment . . . . .	109
4.2.2.3	Full circle . . . . .	110
4.2.3	Optimisation on plane walls . . . . .	110
4.3	Simulations . . . . .	111
4.3.1	Particle approaching a plane wall . . . . .	111
4.3.2	Still water . . . . .	112
4.3.3	Dam-break with obstacle . . . . .	115
4.4	Preliminary conclusion . . . . .	119

<b>5</b>	<b>The turbulent channel flow</b>	<b>121</b>
5.1	Physics of turbulent flow in a channel . . . . .	121
5.1.1	Geometrical properties . . . . .	121
5.1.2	Reynolds averaged Navier-Stokes . . . . .	122
5.1.3	The balance of forces . . . . .	123
5.1.4	Turbulent scales . . . . .	124
5.1.5	Mean velocity profiles . . . . .	125
5.1.5.1	Near wall profile . . . . .	127
5.1.5.2	The log law . . . . .	128
5.1.5.3	Velocity near the center . . . . .	128
5.2	Numerical approaches for simulating turbulent wall-bounded flows . . .	128
5.2.1	Direct numerical simulation . . . . .	129
5.2.1.1	Quasi DNS . . . . .	129
5.2.2	Large eddy simulation . . . . .	130
5.2.2.1	The Smagorinsky and Yoshizawa models . . . . .	131
5.2.2.2	Wall modelling . . . . .	133
5.2.3	Statistics . . . . .	133
5.2.3.1	Eulerian statistics . . . . .	134
5.2.3.2	Lagrangian statistics . . . . .	135
<b>6</b>	<b>SPH Simulation of the turbulent channel flow</b>	<b>137</b>
6.1	Quasi direct numerical simulation . . . . .	138
6.1.1	Setup . . . . .	138
6.1.2	Eulerian statistics . . . . .	141
6.1.3	Lagrangian statistics . . . . .	145
6.1.4	Preliminary conclusion . . . . .	146
6.2	Large eddy simulation . . . . .	148
6.2.1	The simulation . . . . .	148
6.2.2	Taylor-Green vortices . . . . .	152
6.2.3	Concluding remarks . . . . .	154
<b>7</b>	<b>Conclusions</b>	<b>156</b>
7.1	General conclusions . . . . .	156
7.2	Detailed conclusions . . . . .	157
7.2.1	Investigation into wall-boundary conditions for SPH . . . . .	157
7.2.2	Extension to three dimensions . . . . .	157
7.2.3	Simulations of the turbulent channel flow . . . . .	158
7.3	Recommendations for future work . . . . .	158

<b>Bibliography</b>	<b>160</b>
<b>A Derivation of skew-adjointness</b>	<b>178</b>
<b>B <math>C_s</math> for the Wendland kernel</b>	<b>180</b>

Word count 41790

# List of Tables

2.1	Overview of elements . . . . .	63
6.1	Comparison of the two different minimal channel configurations . . . . .	139

# List of Figures

1.1	Simulation of two colliding galaxies . . . . .	30
1.2	Bullet impact with SPH . . . . .	31
1.3	Simulation of lava flow . . . . .	33
1.4	Flooding of a town with shallow water SPH . . . . .	34
1.5	Simulation of pedestrian crowds . . . . .	35
1.6	Different flow regimes of a flow around a cylinder . . . . .	39
1.7	Vorticity iso-surfaces from tomographic image velocimetry . . . . .	41
2.1	Three classic boundary conditions . . . . .	60
2.2	Kernel support of a particle $a$ . . . . .	61
2.3	Vertex particles and boundary elements along a boundary . . . . .	62
2.4	Illustration of distances . . . . .	64
3.1	Non-dimensional energy budget over time $t^+ = tc_0/h$ for ghost particles and present approach. Black dots correspond to time time instants in Figure 3.2. . . . .	80
3.2	Values of $v^+$ at different times (Figure 3.2(a): $t^+ = 0$ , Figure 3.2(b): $t^+ = 9.0$ ) . . . . .	81
3.3	Comparison of the error in the bulk velocity of the Poiseuille flow . . . . .	86
3.4	Illustration of the arbitrary order Robin boundary conditions for SPH . . . . .	88
3.5	Wave equation (3.55) with Robin boundary conditions Eq. (3.56) at four different time-steps. Analytical solution given by Eq. (3.58). For the SPH solution, the matrix size in Eq. (3.54) is given by first ( $m = 1$ ) or second ( $m = 2$ ) order according to Eq. (3.46) . . . . .	90
3.6	Wave equation with Robin boundary conditions: Relative error of the SPH solution over time at the boundary. . . . .	92
3.7	Position of free-surface in infinite open channel at rest. . . . .	93
3.8	Still water in a closed tank (left: without correction (3.62), right: with correction (3.63)). . . . .	94

3.9	Schematic dam-break on a wedge: Comparison of forces on left wedge wall. . . . .	95
3.10	Comparison between VOF and SPH. . . . .	96
3.11	Steady flow on a wedge: Without (Figure 3.11(a)) and with (Figure 3.11(b)) the volume diffusion term (3.64) to avoid particle repulsion. . . . .	97
4.1	Partition of the boundary extended in wall-normal direction. . . . .	100
4.2	Initial view of coplanar faces surrounding a vertex. . . . .	101
4.3	Creating two cubes according to the highlighted face. . . . .	102
4.4	Use of tetrahedron (orange) to delete parts outside of geometry. . . . .	102
4.5	Voronoi tessellation. . . . .	103
4.6	Cutting off at face boundaries. . . . .	103
4.7	Final vertex particle volume. . . . .	104
4.8	Illustration of the general problem . . . . .	105
4.9	The 8 different cases . . . . .	106
4.10	The 3 building blocks . . . . .	107
4.11	Illustration of the domain decomposition algorithm . . . . .	107
4.12	Algorithm for Case 1 in detail . . . . .	108
4.13	The circular sector in detail . . . . .	110
4.14	Discretizations of the plane walls . . . . .	111
4.15	Error of the gradient of $\gamma$ for different walls . . . . .	112
4.16	Geometry of the still water test case . . . . .	112
4.17	Residual velocity . . . . .	113
4.18	$L_2$ norm using the boundary conditions by Monaghan and Kajtar (2009) . . . . .	114
4.19	Pressure of all particles at the end of the simulation . . . . .	115
4.20	Comparison between the approximative and the analytical approach . . . . .	115
4.21	Location of probes according to Kleefsman <i>et al.</i> (2005) . . . . .	116
4.22	Snapshots of the simulation coloured according to velocity magnitude . . . . .	117
4.23	Water levels . . . . .	118
4.24	Pressure gauges . . . . .	118
4.25	Comparison of water levels using different boundary conditions . . . . .	119
4.26	Pressure gauges using different boundary conditions . . . . .	119
5.1	Geometry of the channel flow . . . . .	122
5.2	Comparison of contributions of viscous and Reynolds stress to the total stress. Data by Moser <i>et al.</i> (1999) for a channel flow with $Re_\tau = 395$ . . . . .	126
5.3	Profile of mean-velocity close to the wall including both the linear and the log law. Data by Moser <i>et al.</i> (1999) for a channel flow with $Re_\tau = 395$ . . . . .	127
6.1	Snapshot of the instantaneous velocity of MCF1 . . . . .	140

6.2	Minimal channel: average velocity ( $y^+$ in log scale)	141
6.3	Minimal channel: $\sqrt{v_x'^2}$	142
6.4	Minimal channel: $\sqrt{v_y'^2}$	143
6.5	Minimal channel: $\sqrt{v_x'^2}$ on log scale	143
6.6	Minimal channel: $\sqrt{v_y'^2}$ on log scale	144
6.7	Minimal channel: autocorrelation along the $x$ -axis	144
6.8	Minimal channel: autocorrelation along the $z$ -axis	145
6.9	Minimal channel: probability density function at $y^+ = 30$	146
6.10	Minimal channel: probability density function at $y^+ = 100$	147
6.11	Minimal channel: probability density function at $y^+ = 210$	147
6.12	Average velocity	149
6.13	Velocity fluctuations in streamwise direction: $\sqrt{\langle v_x'^2 \rangle}$	150
6.14	Velocity fluctuations in wall normal and cross-stream direction: $\sqrt{\langle v_{y,z}'^2 \rangle}$	150
6.15	Snapshots of velocity magnitude and components from the LES after $tv_\tau/\delta = 14$	151
6.16	Velocity redistribution due to pressure gradient	152
6.17	Analytical solutions of the Taylor-Green vortex	153
6.18	Relative error in $\Pi_{xx}$ for the Taylor-Green vortex	154

# List of Symbols and Operators

$\alpha_n$	Kernel renormalization factor.
$\underline{B}$	Arbitrary vector field.
$c_0$	Numerical speed of sound.
$C_S$	Smagorinsky constant.
$C_Y$	Yoshizawa constant.
$\delta$	Delta function.
$\Delta_G$	Filter with of the LES filter.
$\Delta r$	Initial particle spacing.
$\delta_\tau$	Friction length scale.
$E$	Energy of the system.
$E_{ext}$	External energy.
$E_{int}$	Internal energy of the system.
$e_{int}$	Internal energy per unit mass.
$E_{kin}$	Kinetic energy of the system.
$\epsilon$	Dissipation.
$\eta$	Kolmogorov scale.
$f$	Arbitrary scalar function.
$\mathcal{F}$	Set of all fluid particles.
$G$	LES filter.
$g$	Gravitational acceleration.
$\gamma$	Interpolation renormalization factor.
$\gamma_{as}$	Integral of kernel on segment.
$\mathbf{Grad}^{b,c}$	Basic continuous gradient.
$\mathbf{Grad}^{\gamma,c,k}$	Symmetrized renormalized continuous gradient with power $k$ .
$\mathbf{Grad}^{\gamma,F}$	Renormalized kernel (using $\gamma$ ) according to Ferrand.

$\mathbf{Grad}^{\gamma,K}$	Renormalized kernel (using $\gamma$ ) according to Kulasegaram.
$\mathbf{Grad}^{\gamma,c,k}$	Symmetrized renormalized discrete gradient with power $k$ .
$\mathbf{Grad}^{s,c,k}$	Symmetrized continuous gradient with power $k$ .
$\mathbf{Grad}^{std,-,k}$	Standard symmetric gradient with power $k$ .
$\mathbf{Grad}^{std,+,k}$	Standard anti-symmetric gradient with power $k$ .
$\widetilde{\mathbf{Grad}}^{std,-,k}$	Standard first-order corrected gradient with power $k$ .
$h$	Smoothing length.
$\underline{\underline{I}}$	Identity matrix.
$k$	Power used in differential operators.
$k_r$	Residual kinetic energy.
$L$	Lagrangian.
$\mathbf{Lap}^F$	Laplacian according to Ferrand.
$L$	Characteristic lengthscale.
$\underline{\underline{L}}$	Kernel gradient renormalization matrix.
$l_S$	Smagorinsky length scale.
$m$	Mass of a particle.
$\mu$	Dynamic viscosity.
$n$	Dimension of the problem.
$\nabla$	Nabla (del) operator.
$\nu$	Kinematic viscosity.
$\nu_r$	Turbulent eddy viscosity.
$\underline{n}$	Normal vector into the domain.
$\Omega$	Domain of computation.
$\omega$	Non-normalized kernel function.
$\Omega_a$	Compact support of kernel around particle $a$ .
$\partial\Omega$	Boundary of the computation domain.
$\mathcal{P}$	Set of all particles.
$p$	Pressure.
$\underline{\underline{\Pi}}$	Velocity pressure-gradient tensor.
$Re$	Reynolds number based on bulk velocity.
$Re_0$	Reynolds number based on centerline velocity.
$Re_\tau$	Reynolds number based on friction velocity.
$\rho$	Density.

$\rho_0$	Reference density.
$\underline{r}$	Position vector.
$\bar{S}$	Filtered rate of strain.
$\mathcal{S}$	Set of all boundary segments.
$t$	Time.
$\tau$	Total shear stress.
$\underline{\tau}$	Stress tensor.
$\underline{\tau}_R$	Residual stress tensor.
$\underline{\tau}_r$	Anisotropic residual-stress tensor.
$\tau_w$	Wall shear stress.
$U$	Characteristic velocity.
$V$	Volume of a particle.
$v_0$	Centerline velocity.
$\langle \underline{v} \rangle$	Time averaged velocity.
$\bar{v}$	Filtered velocity.
$v^+$	Velocity normalized by $v_\tau$ .
$\underline{v}'$	Fluctuating velocity vector.
$\mathcal{V}$	Set of all vertex particles.
$\underline{v}_\tau$	Friction velocity.
$\tilde{v}$	Bulk velocity.
$\tilde{\underline{v}}$	Favre averaged velocity.
$\underline{v}$	Velocity.
$w$	Kernel function.
$y^+$	Distance normalized by $y^+$ .
$\zeta$	Power in Equation of State.

# Abbreviations

CFL	Courant-Friedrichs-Lewy.
DNS	Direct Numerical Simulation.
EOS	Equation of state.
LES	Large Eddy Simulation.
NS	Navier-Stokes.
PDF	Probability Density Functions.
PIV	Particle Image Velocimetry.
RANS	Reynolds averaged Navier Stokes.
SPH	Smoothed Particle Hydrodynamics.

# Abstract

University of Manchester

Arno Mayrhofer

Doctor of Philosophy

**An investigation into wall boundary conditions and three-dimensional turbulent flows using Smoothed Particle Hydrodynamics**

February 24, 2014

This thesis investigates turbulent wall-bounded flows using the Smoothed Particle Hydrodynamics (SPH) method. The first part focuses on the SPH method itself in the context of the Navier-Stokes equations with a special emphasis on wall boundary conditions. After discussing classical wall boundary conditions a detailed introduction to unified semi-analytical wall boundary conditions is given where the key parameter is a renormalization factor that accounts for the truncated kernel support in wall-bounded flows.

In the following chapter it is shown that these boundary conditions fulfill energy conservation only approximately. This leads to numerical noise which, interpreted as form of Brownian motion, is treated using an additional volume diffusion term in the continuity equation where it is shown to be equivalent to an approximate Riemann solver. Two extensions to the boundary conditions are presented dealing with variable driving forces and a generalization to Robin type and arbitrary-order interpolation. Two modifications for free-surface flows are then presented, one for the volume diffusion term and the other for the algorithm that imposes Robin boundary conditions. The variable driving force is validated using a Poiseuille flow and the results indicate an error which is five orders of magnitude smaller than with the previous formulation. Discretising the wave equation with Robin boundary conditions proves that these are correctly imposed and that increasing the order of the interpolation decreases the error. The two modifications for flows under the influence of external forces significantly reduce the error at the free-surface. Finally, a dam break over a wedge demonstrates the capabilities of all the proposed modifications.

With the aim of simulating turbulent flows in channels, the thesis moves on to extending the unified semi-analytical wall-boundary conditions to three dimensions. The thesis first presents the consistent computation of the vertex particle mass. Then, the computation of the kernel renormalization factor is considered, which in 3-D consists of solving an integral over a two dimensional manifold where the smoothing kernel intersects the boundary. Using a domain decomposition algorithm special integration areas are obtained for which this integral can be solved for the 5<sup>th</sup>-order Wendland kernel. This algorithm is successfully applied to several validation cases including a dam break with an obstacle which show a significant improvement compared to other approximative methods and boundary conditions.

The second part of this thesis investigates turbulent flows, in particular turbulent channel flow. This test case is introduced in detail showing both the physical properties as well as established numerical methods such as direct numerical simulation (DNS) and large eddy simulation (LES). In the penultimate chapter several SPH simulations of the turbulent channel flow are shown. The first section deals with a quasi DNS of the minimal-flow unit, a channel flow with a minimal domain size to sustain turbulent flow structures. The Eulerian statistics are compared to literature and show good agreement except for some wall-normal quantities. Furthermore, preliminary Lagrangian statistics are shown and compared to results obtained from a mesh-based DNS. The final simulation shows a LES of a full-sized channel at Reynolds number  $Re_\tau = 1000$ . The Eulerian statistics are compared to literature and the discrepancies found are explained using simulations of the Taylor-Green vortex, indicating that the momentum is not transferred appropriately due to an unresolved velocity-pressure-gradient tensor.

# Declaration

No portion of the work referred to in this report has been submitted in support of an application for another degree or qualification of this or any other university or other institution of learning.

# Copyright

1. The author of this thesis (including any appendices and/or schedules to this thesis) owns certain copyright or related rights in it (the “Copyright”) and s/he has given The University of Manchester certain rights to use such Copyright, including for administrative purposes.
2. Copies of this thesis, either in full or in extracts and whether in hard or electronic copy, may be made **only** in accordance with the Copyright, Designs and Patents Act 1988 (as amended) and regulations issued under it or, where appropriate, in accordance with licensing agreements which the University has from time to time. This page must form part of any such copies made.
3. The ownership of certain Copyright, patents, designs, trade marks and other intellectual property (the “Intellectual Property”) and any reproductions of copyright works in the thesis, (for example graphs and tables the “Reproduction”), which may be described in this thesis, may not be owned by the author and may be owned by third parties. Such Intellectual Property and Reproductions cannot and must not be made available for use without the prior written permission of the owner(s) of the relevant Intellectual Property and/or Reproductions.
4. Further information on the conditions under which disclosure, publication and commercialisation of this report, the Copyright and any Intellectual Property and/or Reproductions described in it may take place is available in the University IP Policy  
(see <http://documents.manchester.ac.uk/display.aspx?DocID=487>),  
in any relevant Thesis restriction declarations deposited in the University Library,  
The University Library’s regulations  
(see <http://www.manchester.ac.uk/library/aboutus/regulations>)  
and in The University’s policy on presentation of Theses.

# Acknowledgements

Even though this thesis has only one author on the front page there were a great many people involved. First and foremost I would like to thank my three supervisors Prof. Dominique Laurence, Dr. Benedict Rogers and Damien Violeau. As Adolf Hurwitz said “A PhD dissertation is a paper of the professor written under aggravating circumstances.” I certainly hope that this is not true for this thesis but without the support and guidance that I obtained from my supervisors this thesis would certainly not have come together. I am deeply grateful for the possibility to work not only for them but also with these three academics. That I even got the chance of doing this thesis is thanks to Martin Ferrand who got hired to work on *Code\_Saturne* and leave SPH. That the last statement is not entirely true is an open secret and indeed he helped me to get into the topic in the beginning and supported me until the very end providing a link to the finite volume world. His rigorous approach was a continuous inspiration which is hopefully reflected in this thesis.

Besides the academic support I received the best possible moral support from my lovely Marie-Theres who was always in my heart albeit the fact that this thesis required us to live in different countries. I also wish to thank my parents for their continued support without which I certainly would not be where I am today.

During my PhD I had the unique opportunity to work both at the University of Manchester and at EDF in Chatou. EDF in particular was funding this PhD and provided computational resources which was highly appreciated. The University of Manchester was my basis for the first and last year and despite their disability of changing the local weather it has been a pleasure to work there and I am grateful for the administrative support I received. During my thesis I was allowed to perform computations on several supercomputers which were administered by EDF, IBM, STFC Darsbury, University of Leeds and the University of Manchester. I wish to thank the administrators at the respective institutions for their help and support. In particular I would like to mention Dr. Charles Moulinec who did not only proofread this thesis but also shared both his knowledge on programming and a few beers.

During my time in Paris I had the pleasure of working together with Dr. Christophe Kassiotis and Agnès Leroy with whom I shared many fruitful conversations. They were

also, together with Martin Ferrand and Francois-Xavier Morel, part of the geek evenings which not only were about SPH but also introduced me to French culture with plenty of good food. I am indebted to Cedric Flageul who provided several initial conditions for my turbulent simulation. I also wish to thank the Laboratoire d'Hydraulique Saint-Venant headed by Dr. Michel Benoit for their warm welcome and their patience with my initially poor knowledge of French. That it is no longer that poor is mostly thanks to Nathalie de Solere who provided excellent lessons. On a more personal side there was Thomas Novak with whom I shared one or two expensive glasses of beer and who is now living in the apartment which was kindly provided to me by Elfie Kaiser-Weber. The largest part of my PhD was spent in Manchester where I had the pleasure to work with both the turbulence group as well as the SPH group. In particular I'd like to mention Dr. Stefano Rolfo, Dr. Juan Uribe, my office mate Umair Ahmed and Maël Morellec. A thanks also to my lunch group in Manchester with whom I also shared several weekends in and around Manchester. Besides working I was also part of the University of Manchester and Marvels volleyball clubs which provided the necessary physical activity to balance the countless hours spent in front of a monitor. In particular I'd like to name Dr. Marije van Hattum who was my coach during the first year and housemate for a couple of days. During my last year I picked up freediving which is so much more than an ordinary sport and I could not have found any better instructor than Steve Millard. It was a pleasure to get to know all the individuals involved and particularly the Apneists UK group and share this common passion. Finally, I wish to acknowledge the help from the community on the Stackexchange websites, in particular Dr. Pedro Gonnet, where I could find many answers to many little issues I encountered. Nearly everything related to this thesis was created using open source software and I am grateful that I can participate and benefit from this amazing global collaboration.

# Chapter 1

## Introduction

Most fluid flows observed in nature are turbulent featuring unsteady and irregular behaviour. This is also true for flows related to engineering problems such as the flow of water in a pipe. These flows feature a wide range of different length and time scales. The interest in turbulent flows dates back over two thousand years and until the end of the last century experiments and observations were the main method of studying these flows. The advent of computers has given rise to the numerical simulation of such flows and now provide an important tool in the analysis of turbulence in both engineering applications as well as theoretical perspectives.

The methods used to solve problems in computational fluid dynamics can generally be divided into two categories. The first is the Eulerian approach which decomposes the fluid domain into a mesh. In general, the mesh remains the same throughout a simulation and does not move. The most prominent of the methods belonging to this category are Finite Volume, Finite Differences and Finite Elements which can be found in software such as Code\_Saturne, OpenFOAM, Fluent, Alya and Incompact3D. These techniques have been successfully applied to engineering problems for several decades. However, simulating highly violent flows with large deformations is difficult with these methods.

The second class of methods are Lagrangian techniques. Some of the methods associated with this category are also based on a mesh. One example would be the Particle-In-Cell method by Harlow (1957). On the other hand there is a wide variety of meshless techniques such as the Element-free Galerkin (Belytschko *et al.*, 1994), Reproducing Kernel Particle Method (Liu *et al.*, 1995) and many others. In recent years, the most popular Lagrangian method to have emerged is Smoothed Particle Hydrodynamics (SPH). Although turbulence has been investigated using Eulerian methods for decades, using meshless methods has received little attention. Hence, this thesis presents an investigation into using SPH for turbulent flows. In the following a brief

introduction to meshless methods is given in Section 1.2. This chapter provides an overview of state-of-the-art SPH methods and its applications.

This is followed by a brief introduction to turbulence. Besides giving an introduction to experimental turbulent research the three main approaches to the simulation of turbulent flows are discussed. Next, a literature review of turbulent simulation with SPH is conducted in Section 1.5.

Finally, this chapter is concluded with a summary and motivation for the remainder of this work.

## 1.1 The governing equations

At the beginning of this chapter the governing equations of fluid flow will be presented. A more detailed view on them will be presented in the beginning of Chapter 2. Throughout this thesis Newtonian fluids will be considered whose behaviour is governed by the Navier-Stokes (NS) equations given by

$$\frac{d\mathbf{v}}{dt} = -\frac{1}{\rho}\nabla p + \nabla \cdot (\nu \nabla \cdot \otimes \mathbf{v}) + \mathbf{f}_{ext}, \quad (1.1)$$

where  $\mathbf{v}$  is the velocity,  $t$  the time,  $\rho$  the density,  $p$  the pressure,  $\nu$  the kinematic viscosity and  $\mathbf{f}_{ext}$  an external force acting on the fluid. Furthermore,  $\nabla$  denotes the del operator. The Navier-Stokes equations are complemented with the continuity equation given by

$$\frac{d\rho}{dt} = -\rho \nabla \cdot \mathbf{v}. \quad (1.2)$$

Finally, to close the system of equations an equation of state (EOS) is used, which determines the pressure as function of density. In the following this equation of state is chosen such that the fluid is weakly compressible, *i.e.* the density can vary by up to 1% of the reference density  $\rho_0$ . More background and the details of these equations are presented in Chapter 2.

Most theoretical analysis on fluid flows is normally performed by assuming the flow to be incompressible, *i.e.*  $\rho = \rho_0$ . This reduces the continuity equation (1.2) to  $\nabla \cdot \mathbf{v} = 0$ . This makes the theoretical analysis easier and no equation of state is required. As a result most numerical solvers of the Navier-Stokes equations also solve the incompressible equations. This separates the weakly compressible used throughout this thesis from the purely incompressible results. However, due to the low density fluctuations the weakly compressible solution of the NS equations can be seen as an approximation to the incompressible solutions and as such comparison with those is justified.

### 1.1.1 Numerical treatment

In order to simulate the Navier-Stokes equations with numerical methods two steps need to be taken. The first one consists in calculating the derivatives on the right hand side of Eqs. (1.1) and (1.2). Secondly, the variables need to be integrated in time. These two problems are generally related from a numerical analysis point of view but in practice are often regarded separately. The issue of time integration will be covered in detail in Section 2.4. In the present section the focus will lie on discretizing space for differentiation.

There are two approaches that can generally be differentiated. The first approach is based on meshing the domain of interest. This consists of subdividing the domain into certain small elements such as triangles or polyhedra. Generally, these meshes do not move over time and one mesh element only interacts with its direct neighbours. In contrast to that there is the so called meshless approach. This will be considered in detail in the following with a particular emphasis on the Smoothed Particle Hydrodynamics method. In contrast to most mesh based methods meshfree methods allow their nodes, *i.e.* the points that carry the physical information, to move with the local flow field.

## 1.2 Meshless methods

The main difference between a mesh-based method, such as the finite element method, and meshless methods is that the domain of interest for the latter is only discretized with nodes as opposed to geometrical shapes, *e.g.* triangles. Probably the most striking difference is that node connectivity does not remain constant but can change easily over time. This is especially useful when large deformations occur as in free-surface flows, fractures or fragmentation. Another difference is that the order of the shape functions is higher than for most mesh-based methods which can be exploited for certain properties. While expensive mesh generation is avoided, meshless methods are computationally more expensive as they have a very large stencil and some methods suffer instabilities. One source of these instabilities is that the integration is not exact. Another source is created by the fact that meshless methods shape functions do not fulfil the Kronecker-Delta property which is problematic when it comes to the imposition of Essential Boundary Conditions.

After the development of a number of meshless methods a pattern for their construction methodologies emerges. This pattern can be used to classify these methods and provide a framework to understand them:

- The first step is to create basis functions for the domain  $\Omega$  where different approaches are available. These approaches mostly depend on the choice of a weighting function with compact support and the positions of the nodes.

- To approximate an unknown function the calculated basis functions which are sometimes called intrinsic basis functions are used. If there is *a priori* knowledge of the solution this can also be added as an extrinsic basis. To do so the approximating function is defined to be a linear combination of the basis functions with unknown coefficients.
- To determine these unknowns it is necessary to impose some conditions on the approximating function. A weighted residual procedure is chosen which depends on specific test functions. Depending on those, a collocation procedure such as Bubnov-Galerkin methods is the result.

After this overview the first and third step are described in greater detail. The second step is neglected because there is no extrinsic basis used in this thesis, so the approximation is a linear combination of the intrinsic basis functions.

This thesis is not about meshless methods in general, the interested reader is referred to Fries and Matthies (2003) where a more detailed overview of most of the meshless methods can be found.

### 1.2.1 Construction of basis functions

This section is mainly about approximation theory and its various methods. Specifically a function

$$f : \Omega \subseteq \mathbb{R}^n \rightarrow \mathbb{R} \quad (1.3)$$

is to be approximated by a family  $(\Phi_i)_{i=1,\dots,n}$  of basis functions. We define the approximation  $\tilde{f}$  of  $f$  as

$$f(x) \approx \tilde{f}(x) = \sum_{i=1}^n a_i \Phi_i(x) \quad \forall x \in \Omega \quad (1.4)$$

where  $a_i \in \mathbb{R}$  are the nodal parameters. Note that  $a_i \neq \tilde{f}(x_i)$ .

The choice of the basis functions is of high importance and influences the error of the approximation. One should note that the error depends on a specific norm which is to be minimised and this is discussed in Section 1.2.2. One of the key ideas when using these basis function for interpolation is that when approximating a derivative the differentiation can be shifted from the unknown function  $f$  to the basis function. This will be detailed in Chapter 2.2.3. In the present section several approaches to basis functions will be presented and discussed.

#### 1.2.1.1 Smoothed Particle Hydrodynamics

Smoothed Particle Hydrodynamics is the oldest type of meshless method originally introduced by Lucy (1977) and Gingold and Monaghan (1977). As such as it is also

rather basic in terms of mathematical properties. All basis functions  $\Phi_i$  are equal to one function  $w$  which is commonly taken to be a radial polynomial or spline. This method will be discussed in much greater detail in Chapter 2 and in the present section only a few general remarks are made. Due to the particular explicit choice of basis function the issue of inverting a global matrix to define coefficients is avoided. This is in contrast with the other methods below, but has the downside of not ensuring consistency, not even of zeroth order.

### 1.2.1.2 Radial basis functions

In 1990 Kansa (1990) was the first to introduce radial basis functions to collocated meshless methods. Collocated here refers to the fact that all physical properties of the system are stored at each node. Compactly supported as well as global radial basis functions are still under active research.

An arbitrary function  $\phi$  can be approximated by

$$\phi(x) = P(x) + \sum_{i=1}^n \lambda_i \Phi_i(\|x - x_i\|) \quad (1.5)$$

where  $P(x)$  is a polynomial of fixed degree,  $\lambda_i \in \mathbb{R}$  and the  $\Phi_i$  are radially symmetric basis functions, *i.e.*  $\Phi_i : \mathbb{R}^+ \rightarrow \mathbb{R}$ . Possible choices of  $\Phi_i$  include the Thin-Plate Spline, the Gaussian or other harmonic Splines. The polynomial is used to allow global polynomial reproducibility which might be desirable in some problems as noted by Sukumar (2009). Radially symmetric basis functions do not satisfy the Kronecker-Delta property  $\Phi_i(x_j) = \delta_{ij}$  which is a significant drawback. However one of their advantages is that the resulting system of linear equations is easily invertible under mild conditions regarding the node positions as shown by Micchelli (1986).

### 1.2.1.3 Moving least squares

A desirable feature when approximating functions is consistency of a specific order  $n$ . This means that the method is able to reproduce polynomials of order less or equal to  $n$  exactly. For moving least squares it is very easy to determine its consistency, since it coincides with the number of elements in the polynomial basis. Generally, a function  $f$  is approximated by a linear combination of the polynomial basis of order  $n$  ( $P(x) = (1, x, \dots, x^n)$ ), where the coefficients depend on the position  $x$ . Hence, the description “moving”. Now the distance from the approximation to the function  $f$  is minimised in a  $l^2$  norm and this results in an equation as seen in (1.4) where

$$\Phi^T(x) = P^T(x)(M(x))^{-1}B(x) \quad (1.6)$$

using the notation of Fries and Matthies (2003). The matrices  $M$  and  $B$  depend on a compactly supported weighting function and the polynomial basis  $P$ . Finally important properties of moving least squares shape functions are:

- They build a partition of unity, whereas their derivatives build a partition of Nullities.
- They are smooth but their derivatives tend to have an increasing non-polynomial behaviour. Indeed all functions contained in the vector  $P$  can be reproduced exactly.
- Similar to radial basis functions they do not possess the Kronecker-Delta property.
- In Eq. (1.6) it can be seen that the matrix  $M$  has to be inverted for every  $x$  which leads to a huge computational effort. Depending on the positions of the nodes the matrix  $M$  might be singular as shown by Nguyen *et al.* (2008).
- It is also possible to add non-polynomials to the vector  $P$ , which is especially useful if *a priori* knowledge about the solution is available according to Sukumar (2009).

#### 1.2.1.4 Reproducing kernel particle method

The reproducing kernel particle method was developed by Liu *et al.* (1995) due to consistency problems with several meshless methods such as SPH. The basic difference to the continuous SPH is a correction function  $C(x, y)$  which enforces consistency. The continuous approximation reads

$$\tilde{f} = \int_{\Omega_y} C(x, y)\omega(x - y)f(y)d\Omega_y, \quad (1.7)$$

where  $\Omega_y = \{x \in \mathbb{R}^n : \omega(x - y) \neq 0\}$ . Choosing again  $P$  as above and letting  $\omega$  be a weight function similar to the one used in SPH methods. Approximating  $f$  via  $f(x) = P^T(x)a$  yields a system of equations for  $a \in \mathbb{R}$ . Solving this and transforming the integral into a sum yields

$$\tilde{f} = P^T(x)(M(x))^{-1} \sum_{i=1}^n P(x_i)\omega(x - x_i)f_i\Delta V_i. \quad (1.8)$$

The full deduction can be seen in the paper by Fries and Matthies (2003).  $\Delta V_i$  is a measure for the node volume and is also present in the matrix  $M$ . It should be noted that if  $\Delta V_i = 1$ , then the reproducing kernel particle method reduces to the moving least squares approach.

The correction function  $C(x, y)$  allows this method to be  $n$ -th order consistent, if  $P$  is  $n$ -th order consistent.

#### 1.2.1.5 Natural neighbour-based interpolants

Unlike the finite element method, natural neighbour-based interpolants are not based on the Delaunay triangulation but rather on the Voronoi diagram. Due to the uniqueness of these diagrams the interpolants are well defined and robust. Unlike all of the methods mentioned above these basis functions actually fulfil the Kronecker-Delta property which makes it easy to impose essential boundary conditions. Furthermore they build a partition of unity and have continuous first derivatives. However, to achieve smoother functions more effort is required than in the moving least squares case. For further details the reader is referred to Sukumar *et al.* (2005) and Sukumar (2009).

#### 1.2.1.6 Maximum entropy approximants

The discussion so far has concentrated upon the differences between meshless methods and the finite element method but with the development of maximum entropy approximants, a continuous link between a meshless method and the finite element method could be established. The underlying idea is simple: there is an unknown function which should be approximated, so basis functions that are least biased are preferred. The Shannon Entropy functional was used as a starting point (Shannon, 1948). This method was transformed by Arroyo and Ortiz (2006) to obtain local maximum entropy basis functions. They also pointed out the link to convex analysis since this method belongs to the group of convex approximation schemes. This method also makes the imposition of essential boundary conditions relatively easy since it possesses a weak Kronecker-Delta property, *i.e.* every basis function associated with a node not belonging to the boundary is zero at the boundary. However, this is only true for convex domains. Another problem (similar to the natural neighbour-based interpolants) is that approximation orders higher than one are difficult to achieve according to Cyron *et al.* (2008).

Problems with Kronecker-Delta properties led to mixing finite element methods with meshless methods where the finite element method was used for the boundaries whereas the meshless method was used for the interior (Krongauz and Belytschko, 1996). However these two methods have to be connected which might cause serious difficulties. Again maximum entropy approximation allows a smooth transition between those two. Another advantage of maximum entropy approximants is their stability with respect to integration in Galerkin methods (see below).

### 1.2.2 The weighted residual procedure

Like the finite element method, the finite volume method or the finite difference method, meshless methods are based on the weighted residual procedure.

Let the differential operator  $\mathcal{L}$  belong to a partial differential equation  $\mathcal{L}f = g$ . Since in general there is no exact solution  $f$  it can be replaced with its approximation  $\tilde{f}$ . This of course leads to an error  $\epsilon$  in the partial differential equation, which can now be rewritten as  $\mathcal{L}\tilde{f} - g = \epsilon$ .

The next step is to impose certain conditions on that error to determine the nodal parameters in Eq. (1.4). Consider the standard scalar product in  $L^2$

$$(f, g) = \int_{\Omega} fg \, d\Omega \quad (1.9)$$

and choose a set of test functions  $\mathcal{T} = \{\Psi_i : i = 1, \dots, n\}$ . Requiring that the error  $\epsilon$  is orthogonal to the set  $\mathcal{T}$  yields

$$0 = (\Psi_i, \epsilon) = \int_{\Omega} \Psi_i (\mathcal{L}\tilde{f} - g) \, d\Omega \quad \forall i = 1, \dots, n. \quad (1.10)$$

The choice of the test functions is again essential. When  $\mathcal{T}$  is chosen to consist of Dirac delta distributions the integral equations in Eq. (1.10) become a discrete equation. In this case the procedure is called a collocation method. Another possible choice is the set of shape functions itself, *i.e.*  $\mathcal{T} = \{\Phi_i\}$  which results in the Bubnov-Galerkin method (Atluri and Zhu, 1998). For any other choice of test functions one usually speaks of Petrov-Galerkin methods. In the last two methods it is sometimes possible to shift differentiation from the shape to the test functions, via the divergence theorem, which might be useful for solving the equations.

As the thesis in the following will only consider the SPH method, it should be noted that this particular method uses  $\Psi \equiv \delta$ , *i.e.* the delta function. As stated before this results in a collocation method which is known to result in numerical instabilities. On the other hand, having an explicit system of linear equations simplifies the numerical tools required to solve the system.

### 1.2.3 Disadvantages of meshless methods

After the beginning of intensive research regarding meshless methods they showed promising results for some specific problems, and especially for problems with variable geometries and discontinuities. However, there are still problems associated with them that need to be resolved in order to make them applicable to a wider range of problems. In the following three major disadvantages are discussed.

### 1.2.3.1 Computational effort

When compared to mesh-based methods, meshless methods usually need more computation power, a fact that is often claimed but no side-by-side comparison could be found in the literature. Consider, for example, the moving least squares approximation in Eq. (1.6); there the inversion of a matrix is required every time the shape function is evaluated. Furthermore, meshless methods are usually used for changing geometries and since the shape functions depend on the nodal position, recalculation is required each time these change. However, compared to the mesh generation in mesh-based methods this happens fully automatically, while the most time consuming operation is the numerical integration in Eq. (1.10).

### 1.2.3.2 Numerical integration

The fact that most shape functions for meshless methods are rational implies that for accurate integration it is necessary to use high order quadrature rules.

One method around the difficulties associated with integration is the use of collocation methods but this results in decreased accuracy and stability. One reason, amongst others, is that the divergence theorem cannot be applied, which results in the need to calculate high order derivatives of the shape functions.

For Galerkin methods the highly non-polynomial form of meshless basis functions makes exact integration very difficult. Various approaches have been applied to tackle this problem, but according to Sukumar (2009) it seems that for true meshless methods only nodal integration seems to be fruitful. Direct nodal integration is very similar to the collocation methods where it has already been shown that problems arise. Thus stabilised nodal integration is of current research interest and shows significantly better results than direct nodal integration or Gaussian quadrature rules, according to Chen *et al.* (2002). Direct nodal integration exhibits oscillations which result from rank deficiency of the stiffness matrix. To avoid this a stabilisation technique is introduced which enforces local conservation properties, see Li and Liu (2004).

There are also integration rules which make use of background meshes, and this results in pseudo-meshless methods. A small overview can be found in the paper by Fries and Matthies (2003).

Another problem with the aforementioned divergence theorem is that it is not exactly fulfilled if the integration is not exact, which again gives rise to inaccuracies.

### 1.2.3.3 Boundary conditions

Since most meshless shape functions do not possess the Kronecker Delta property, it is not possible to impose essential boundary conditions as easily as for the finite element method. There are numerous algorithms to address this problem, amongst the earliest

are Lagrangian multipliers, the penalty approach or Nietzsche's method, which all modify the weak form in Eq. (1.10). Another way to deal with essential boundary conditions is to use shape functions with Kronecker Delta property at the boundaries. One possibility of achieving this is the use of finite element method shape functions in a coupling approach.

However, as noted earlier, maximum entropy approximants have the weak Kronecker Delta property which allows direct imposition of essential boundary condition. The only requirement to be met is the convexity of  $\Omega$ .

After reviewing some of these meshless methods the next section focuses on Smoothed Particle Hydrodynamics. Compared to some of the methods above it does not possess as many mathematical properties. However, being derived from conservation principles of physical quantities it has been successful for a wide range of applications. After reviewing some of the disadvantages of meshless methods, including SPH, the following section will focus on some areas of application where the strengths of SPH are shown.

### 1.3 Smoothed Particle Hydrodynamics

Smoothed Particle Hydrodynamics (SPH) was introduced by Lucy (1977) and Gingold and Monaghan (1977). Both papers use SPH to simulate astrophysical systems. The problems considered in the early days of SPH often feature unbounded domains thereby avoiding the treatment of boundary conditions. Throughout the 1980s SPH gained popularity in the astrophysical community and was applied to many problems in this area. In the 1990s SPH was first used for weakly compressible fluid flow by Monaghan (1992). Since then many authors have modified the SPH method to simulate a very broad range of compressible and incompressible applications including strongly compressible flows by Sigalotti *et al.* (2009) and incompressible flows which were first simulated by Cummins and Rudman (1999). It has also gained considerable interest in the field of solid mechanics starting with the work of Swegle (1992).

As mentioned in the beginning of this chapter, SPH does not need an underlying grid for the discretization of the governing equations. Instead the physical values at a specific node are given as a weighted average of computation nodes called particles that are more or less randomly distributed throughout the domain. These particles move according to the forces calculated from the governing equations of the problem under consideration. The interaction between particles is only determined by a weighting function which depends on its compact support size. The connectivity between particles is not fixed and interacting particles are usually referred to as neighbours.

The comparably large number of neighbours (typically up to 200 in 3-D) causes SPH to be slower than Cartesian mesh-based methods, as shown by Crespo *et al.* (2011)

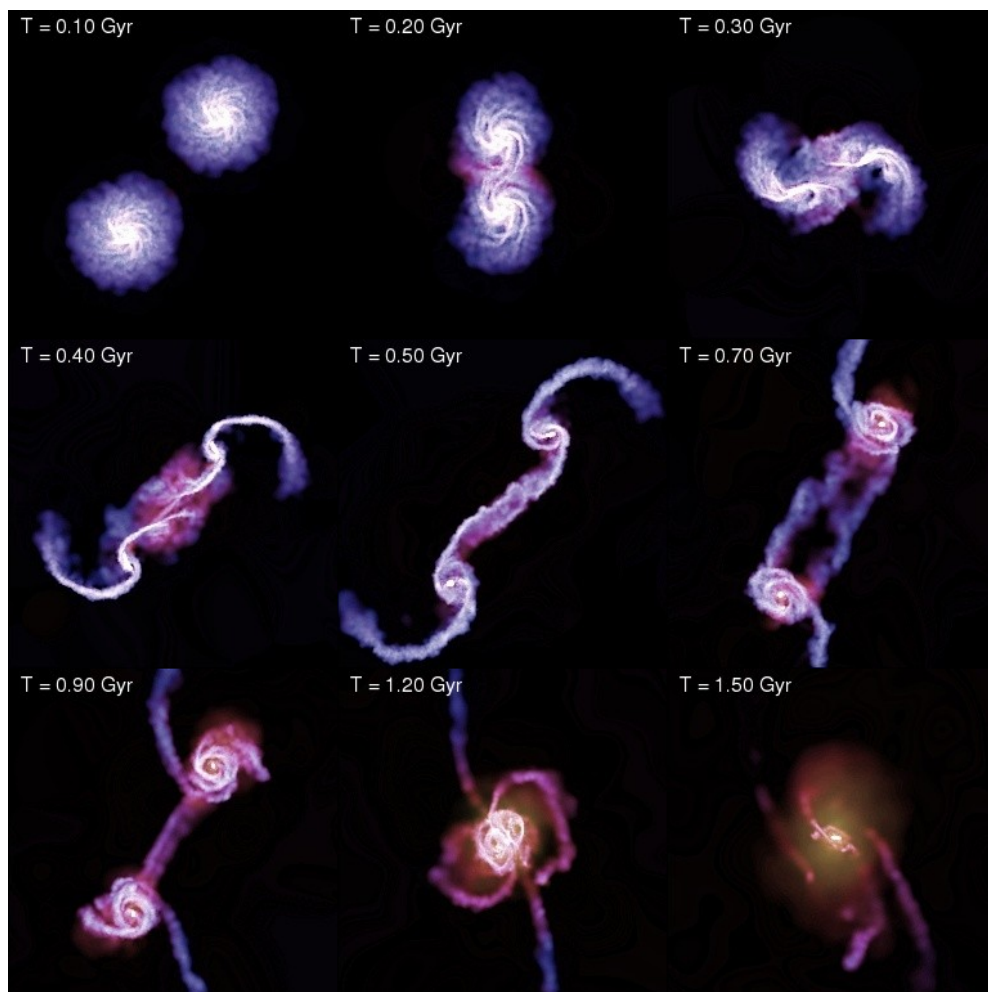


Figure 1.1: Simulation of two colliding galaxies (Springel, 2011).

making it very computationally demanding. On the other hand it is usually straightforward to capture complex, violent free-surface behaviour with SPH, an open problem in mesh-based methods. Another advantage of the meshless formulation is that there is no diffusion of interfaces and a discretization of the convection term is not needed. As SPH did not originate from a mathematical background fundamental theoretical analysis is scarce and, until recently, little emphasis was laid on accuracy issues. However, despite these downsides SPH has proven to be successful in numerical simulations for a wide range of application fields.

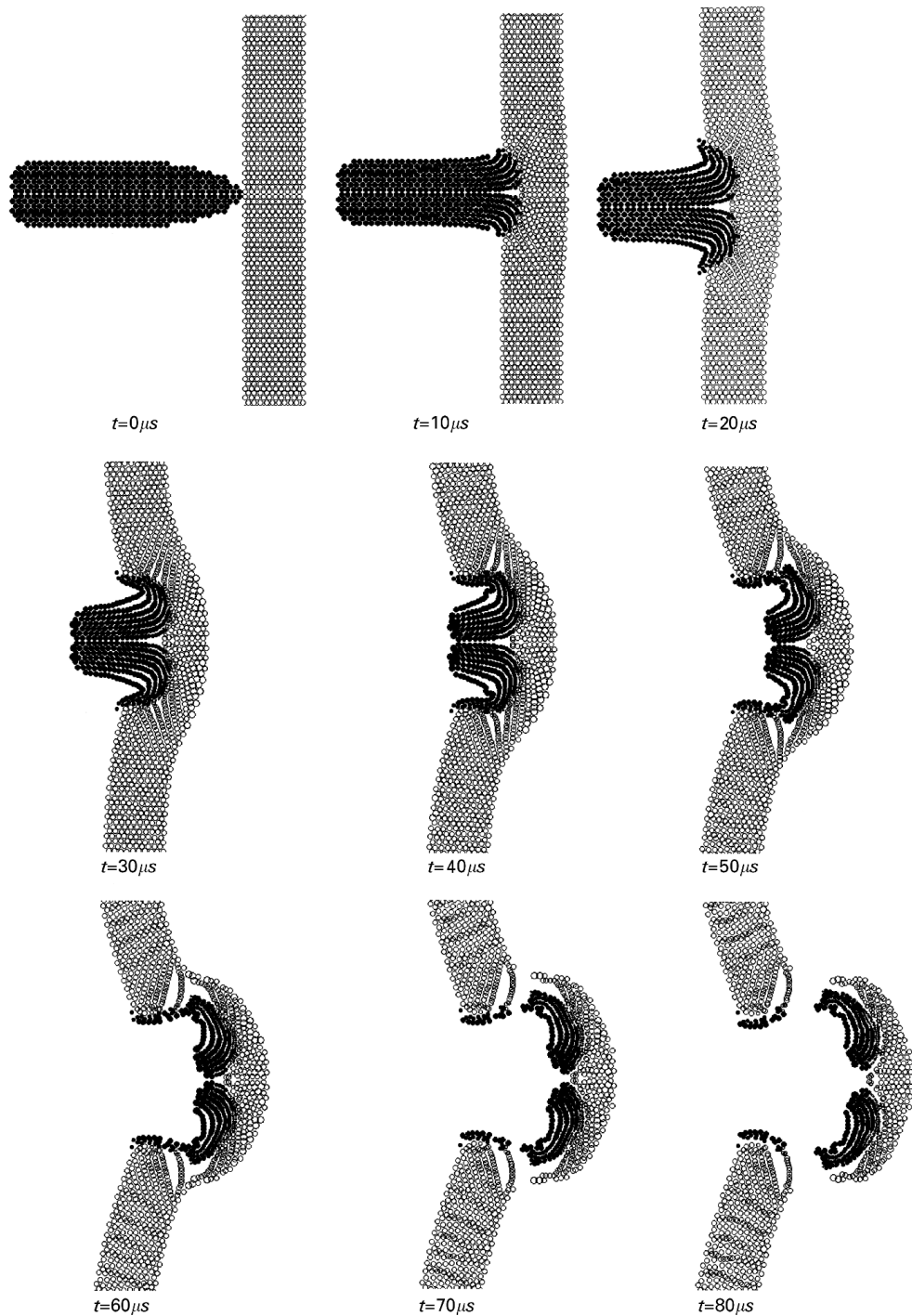


Figure 1.2: Bullet impact with SPH (Parshikov *et al.*, 2000).

### 1.3.1 Applications of SPH

#### 1.3.1.1 SPH in astrophysics

SPH is still widely used in the field in which it was initially introduced. Applications include the collision of celestial bodies, *e.g.* Cameron (1997), or entire galaxies as shown in Figure 1.1 and *e.g.* Struck (1997). Large-scale galaxy formation simulations, *e.g.* Springel and Hernquist (2003), can also be simulated via SPH. Due to the inherent unboundedness of such problems SPH is highly suitable. The simulations in astrophysics often feature large density fluctuations for which SPH formulations with a variable smoothing length are used. An open-source code named GADGET, *e.g.* Springel (2005), is available for such types of problems. The code has been successfully used to conduct large simulations with up to 10 billion particles according to Springel *et al.* (2005).

#### 1.3.1.2 SPH in solid mechanics

Although not as popular as in other fields SPH is also applied in various areas of solid mechanics. One reason for this is that discontinuities and fragmentation can easily be modelled with SPH which makes the method applicable to the simulation of bullet impacts (see Figure 1.2) and crack propagation, *e.g.* Batra and Zhang (2006). Groenenboom and Lobovsky (2009) used SPH to simulate the elasto-plastic necking phenomena in 3-D. It is also possible to model phase changes of a material which occurs in arc welding, *e.g.* Das and Cleary (2010), and die casting, *e.g.* Cleary *et al.* (2000). SPH also allows the simulation of different cutting techniques due to the aforementioned advantages. Examples include laser cutting, *e.g.* Gross (2008) and conventional metal cutting, *e.g.* Villumsen and Fauerholdt (2008).

#### 1.3.1.3 SPH in fluid mechanics

A wide variety of fluid flows exhibit a free surface which can be difficult to treat with mesh-based methods. Due to this deficiency of grid-based solvers, SPH gained significant interest from engineering communities dealing with complex fluid flows. There are a few examples where SPH is used for the simulation of non-Newtonian fluids. Examples include the simulation of lava by Prakash and Cleary (2011) illustrated in Figure 1.3 and the simulation of microscopic flows by Ellero and Tanner (2005). However, most effort has been put into the simulation of Newtonian fluids, especially water where the focus was on the solution of weakly-compressible or incompressible formulations of the Navier-Stokes equations. SPH has been applied to various problems in coastal engineering with one example being the simulation of a caisson breakwater by Rogers *et al.* (2010). Marongiu *et al.* (2007) applied the method to simulating Pelton

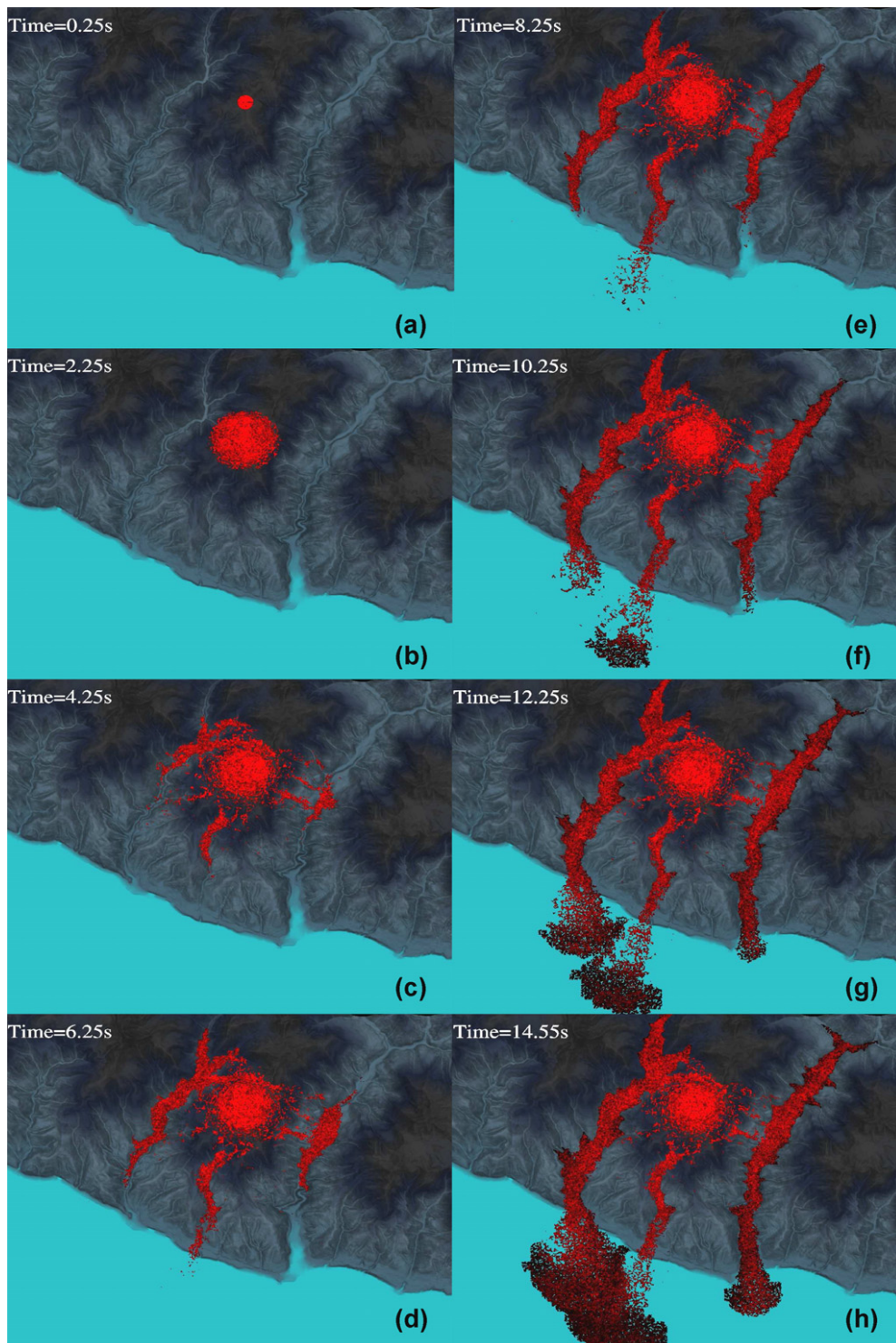


Figure 1.3: Simulation of lava flow (Prakash and Cleary, 2011).

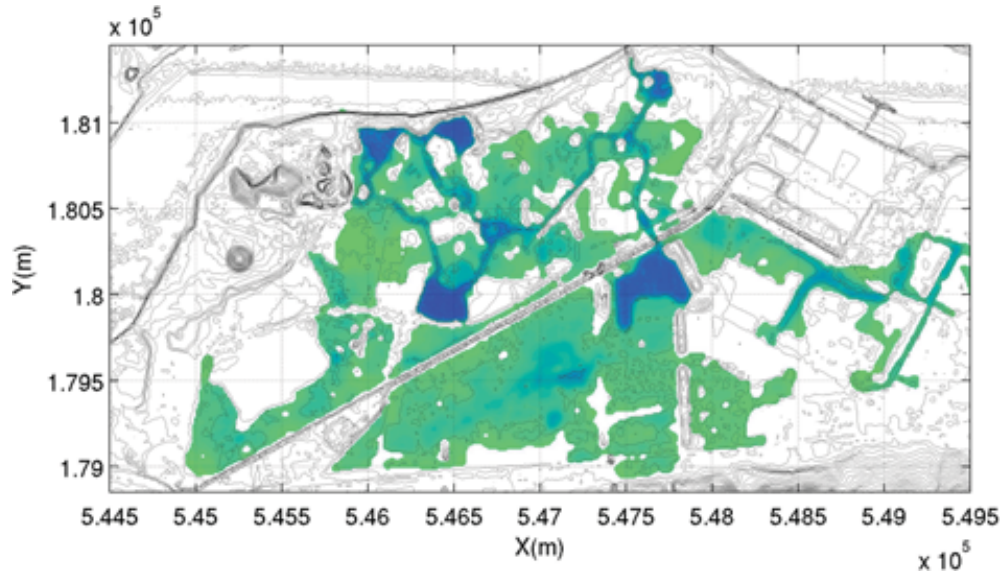


Figure 1.4: Flooding of a town with shallow water SPH (Vacondio *et al.*, 2010).

turbines and this specific code is now used in a industrial environment. Due to the high computational cost it is not straightforward to simulate large areas with comparatively shallow depth with a fully three-dimensional approach. Thus, SPH has been adapted by Vacondio *et al.* (2010) to solve the shallow water equations to simulate flooding scenarios (see Figure 1.4). Another advantage of the method is that it allows the simulation of multi-phase flows. The most prominent examples are the simulation of air and water such as by Colagrossi and Landrini (2003) or the simulation of sediments and water, see Bui *et al.* (2007).

#### 1.3.1.4 SPH in other areas

To conclude the SPH application overview another application shall be mentioned. Vetter *et al.* (2011) used the SPH method to simulate the behaviour of pedestrian crowds with specific application to evacuation scenarios as shown in Figure 1.5. The simulations were conducted with a modified version of the aforementioned astrophysical code GADGET.

### 1.3.2 State-of-the-art SPH techniques

There are several advanced methods that have extended the standard SPH formulation. In this section a brief overview over a few of them are given including references to the respective literature.

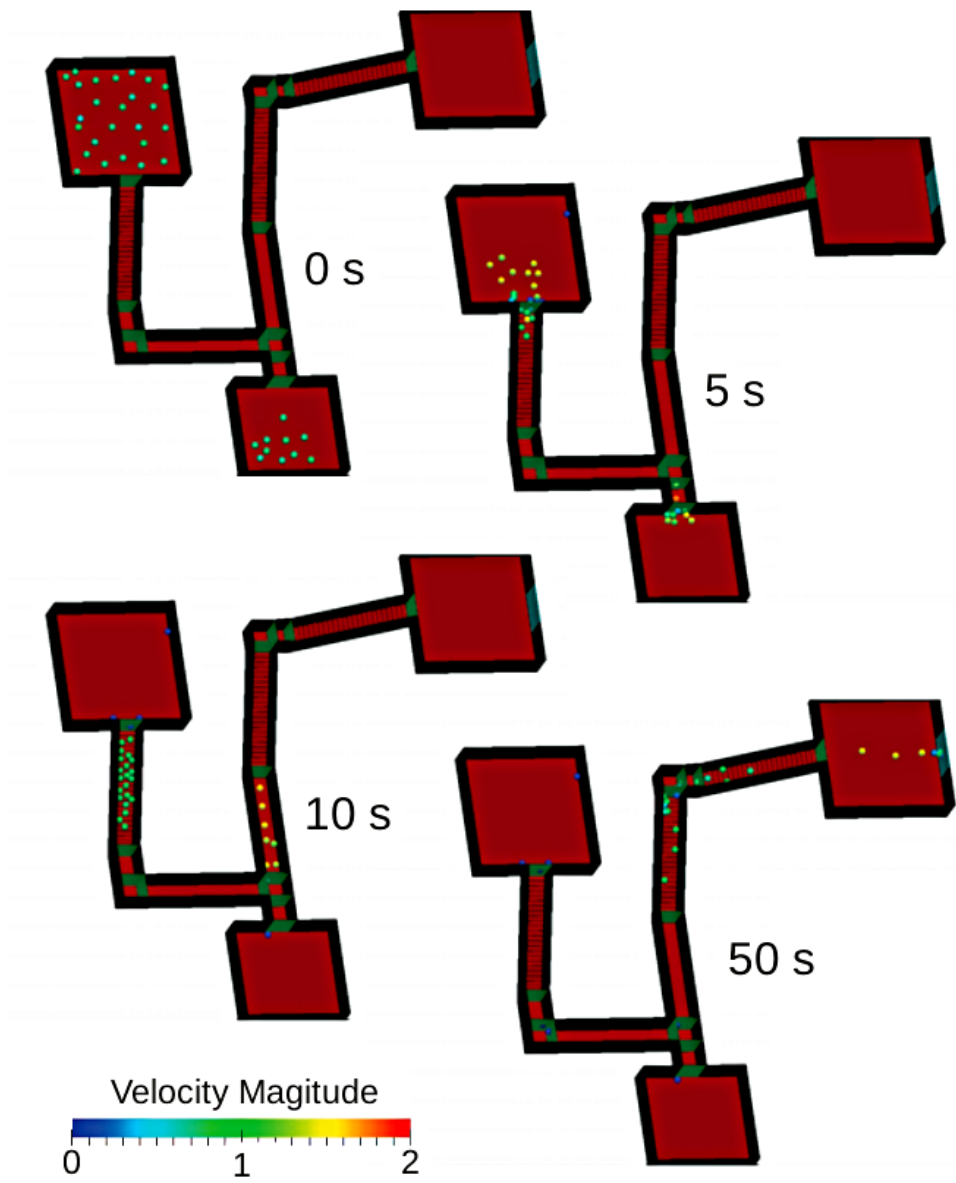


Figure 1.5: Simulation of pedestrian crowds (Vetter *et al.*, 2011).

### 1.3.2.1 Riemann solvers

As shown later one of the biggest disadvantages of the weakly compressible SPH method is the relatively noisy pressure field. Besides the use of numerical diffusion terms such as in  $\delta$ -SPH (Antuono *et al.*, 2010) one of the main methods used to tackle this issue is based on Riemann solvers. They are widely used in mesh-based methods and an in depth description of these methods can be found in the book by (Toro, 1999).

Monaghan (1997) first suggested their use in SPH. In classical SPH the gradient can be viewed as a sum of interaction between two particles where the flux between these two particles is calculated by an arithmetic average. Starting from this viewpoint Vila (1999) proposed to substitute this simple flux calculation by a more sophisticated Riemann solver. That means that a one dimensional Riemann problem is solved between two interacting particles in order to calculate the flux between them. As there exist no closed-form solutions for the Riemann problem for ideal gases it is necessary to utilize approximative solvers. As the theory is identical to mesh-based Riemann solvers, a vast array of them are readily available, Toro (1999). One common choice is the Harten-Lax-van Leer contact solver as used by Rogers *et al.* (2010). Vila (1999) also proposed the use of a MUSCL upwind scheme in order to obtain second order scheme which reduces numerical dissipation significantly as shown by Omidvar (2010).

There are two similar SPH approaches. The first one stems from Parshikov *et al.* (2000) who also used an approximate Riemann solver and showed that the, still popular, artificial viscosity is not required in order to stabilize SPH simulations. Finally, there are several variants of Godunov Particle Hydrodynamics which shares similarities with the approach by Vila (1999). One of the initial papers on this topic is by Inutsuka (1999) who later proposed improvements to satisfy conservations (Inutsuka, 2002). Cha and Whitworth (2003) analyze the stability of their Godunov particle method by means of a von Neumann analysis and show that it is stable regardless of the wavelength which is not true for classical SPH with artificial viscosity.

### 1.3.2.2 Arbitrary Lagrange Euler SPH

This formulation allows the fluid particles to be moved with a velocity that is different from that of the local fluid flow. When this arbitrary velocity is reduced to zero, the Eulerian framework NS equations are recovered. The idea was pioneered by Vila (1999) and allows the linking of SPH to Eulerian mesh-based methods. One significant difference is that the calculation nodes can no longer be seen as particles but as moving control volumes. Marongiu *et al.* (2009) showed that the Arbitrary Lagrange Euler formulation provides increased stability and improved pressure fields when used in combination with pre-conditioned Riemann solvers as discussed in Section 1.3.2.1 above. This approach is not feasible in the context of the present work as the Lagrangian nature

of SPH is of central importance in the extraction of Lagrangian statistics.

### 1.3.2.3 Incompressible SPH

Instead of using an equation of state to calculate the pressure a Poisson equation equation is solved. The physical meaning behind this is that the fluid is no longer considered weakly compressible but incompressible.

There are three main techniques that are used to enforce incompressibility. The oldest is the divergence-free SPH by Cummins and Rudman (1999). This method consists of solving a pressure Poisson equation that enforces that the divergence of the velocity vanishes. This method was also used in an alternative formulation by Lee *et al.* (2008) and it was extended by Xu *et al.* (2009) who added a shifting technique to increase stability. Recently Lind *et al.* (2011) extended this technique to free-surface flows.

The second technique that is used stems from the work of Shao and Lo (2003), who propose an incompressible solver that employs a variable density. Again a Poisson equation is used to calculate the pressure. However, Xu *et al.* (2009) has shown that this formulation exhibits spurious noise just as the weakly compressible SPH does.

Finally the two methods above were combined by Hu and Adams (2007). Although this approach improves the results, it requires two Poisson equations to be solved. As this means solving a global system of equations (twice) the computational cost is significantly larger.

The methods described above were compared side-by-side in the work of Xu *et al.* (2009).

As with Riemann solvers the pressure field obtained by incompressible SPH methods is generally smoother and promising results are obtained. On the other hand, solving the Poisson equation requires solving a global system of linear equations which is time consuming. This is balanced to a certain extent by the fact that higher Courant numbers can be used. The prediction of pressure is much improved in comparison to the use of a state equation as shown by Lee *et al.* (2008).

Several of the above mentioned methods make use of a shifting algorithm which means that they are not truly Lagrangian methods. Additionally, the shifting requires a free-surface detection algorithm, which removes one of the biggest advantages of the SPH method.

### 1.3.2.4 Chequerboard-free SPH

Recently Fatehi and Manzari (2010) showed that by modifying the gradient and divergence operators in such a way that they are slightly different from each other, the numerical oscillations can be significantly reduced. In their paper they use ideas from

mesh-based collocated methods that show the same type of artefacts and with a combination of traditional differential operators of first and second order they construct a scheme which shows good results for low Reynolds number flows. However, numerical experiments show that this method cannot, without modifications, be used for turbulent free-surface flows.

### 1.3.2.5 Dual particle dynamics

The above mentioned issue of noisy pressure fields was also observed in mesh-based methods that use a collocated grid. One possibility to avoid these numerical artefacts is the use of staggered grids. Dyka *et al.* (1997) proposed an SPH method that also stores pressure and velocity values on particles at different locations in space. Although this approach, commonly referred to as Dual Particle Dynamics, provided good results in one-dimensional simulations extension to higher dimensions is still an open problem.

### 1.3.2.6 Variable resolution

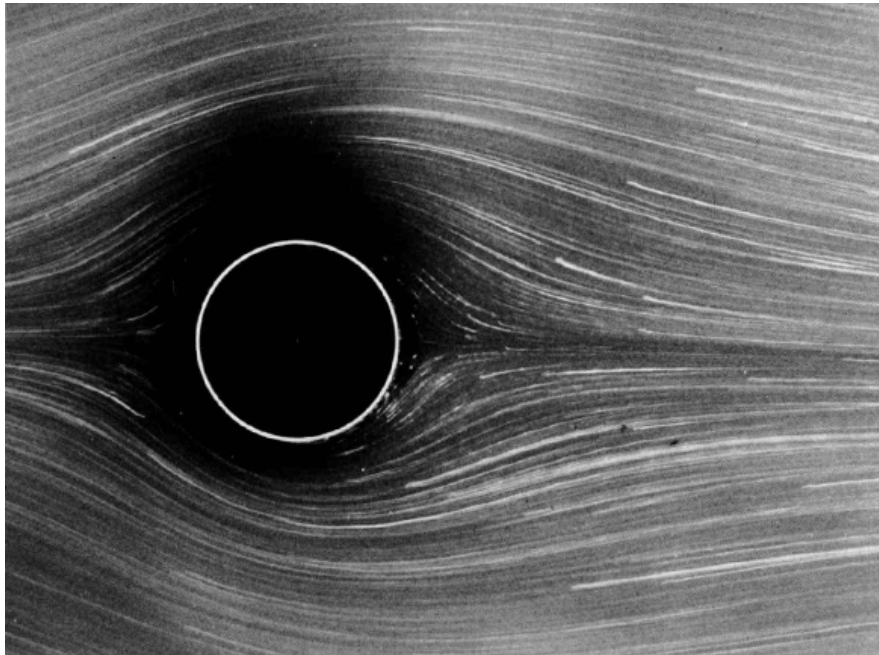
Most SPH formulations consider particles with approximately the same volume throughout the domain. In contrast, most mesh-based methods make use of grids with variable resolution or adaptive mesh refinement, making it possible to obtain higher accuracy where needed while reducing the computational load on areas which do not require high resolution. Monaghan (2005) describes one form of variable resolution that uses a variable smoothing length that is linked to the volume of a particle. Omidvar *et al.* (2012) used nested regions of particles with variable mass. Ulrich *et al.* (2011) demonstrated a variable mass SPH algorithm that features a geometrically fixed region where particle mass varies linearly. More recently Vacondio *et al.* (2012) presented an SPH scheme which allows for dynamic coalescing and splitting of particles in 2-D. The formulation conserves both momentum and total energy while minimizing the error in the density field. The two formulations with variable mass also employ variable smoothing lengths which was also discussed by Vila (1999).

## 1.4 Turbulence

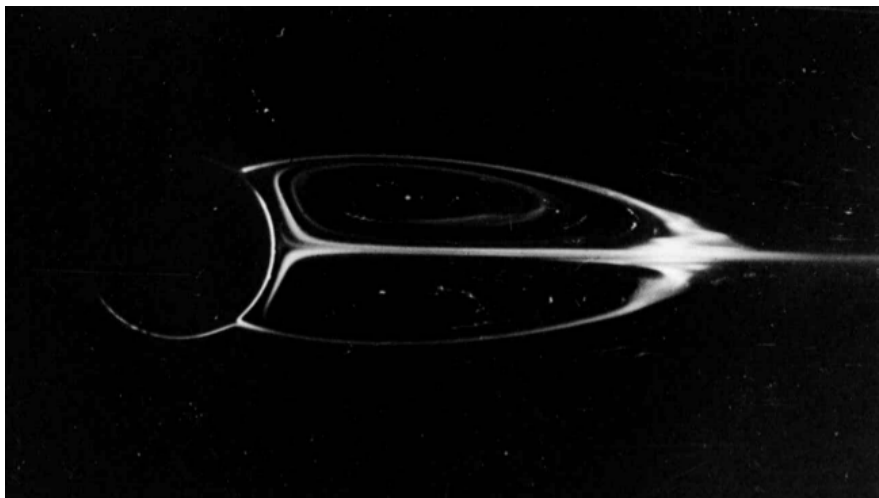
An area of research and application for meshless methods that has received little attention to date is turbulence which is a flow regime where the motion of the fluid flow is generally chaotic. The most significant number related to any flow is the Reynolds number which is defined as

$$Re = \frac{LU}{\nu}, \quad (1.11)$$

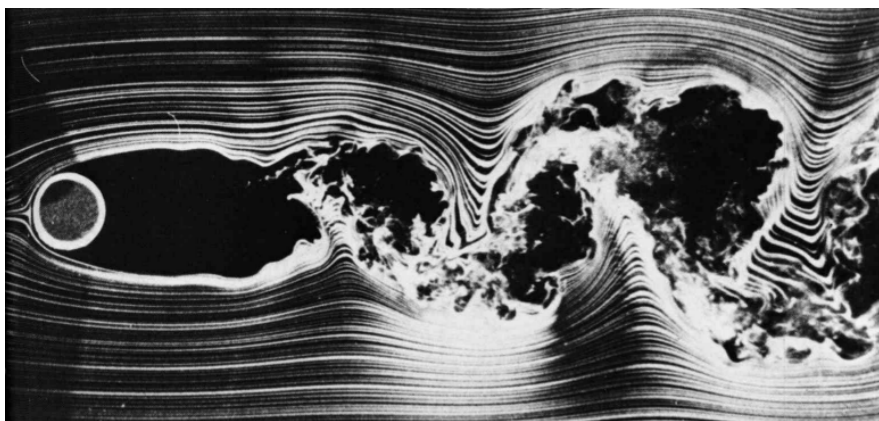
where  $L$  is a characteristic length-scale,  $U$  a characteristic velocity and  $\nu$  the kinematic viscosity of the flow. Flows with a Reynolds number lower than 1000 are generally



(a) Laminar flow



(b) Transient flow



(c) Turbulent flow

Figure 1.6: Different flow regimes of a flow around a cylinder (Van Dyke, 1982).

laminar, *i.e.* the streamlines of the flow are nearly parallel and no lateral mixing occurs. This can be seen in Figure 1.6(a) where the flow past a cylinder is shown, taken from the book by Van Dyke (1982). At higher Reynolds numbers the flow enters the transition region in which flow symmetries are spontaneously broken as observed by Figure 1.6(b). Reynolds numbers of 5000 or higher usually indicate a fully turbulent flow in which the flow symmetries are no longer present instantaneously as the flow is fully chaotic (1.6(c)). Still, several symmetries can be recovered in a statistical sense. Turbulence is a non-linear aspect of the Navier-Stokes equations and although these equations are well known there exists no theoretical model to describe turbulent flow. This is despite the fact that turbulence has been studied for centuries by means of experimental and theoretical research. Herein, several approaches to study turbulent effects are shown. The first section deals with experimental research which is followed by three sections on computational fluid dynamics. These three sections provide an overview of the main turbulence modelling frameworks: Direct Numerical Simulation (DNS), Reynolds averaged Navier-Stokes (RANS) and Large Eddy Simulation (LES). Equations are not presented in the following sections which concern incompressible flow, but equations are presented in Section 5.2 before turbulence simulations are presented. Finally, for a complete review of turbulent flows the interested reader is referred to the book by Pope (2001).

#### 1.4.1 Turbulence experiments

When Lucretius described eddy motion in his book *De rerum natura* more than two thousand years ago he had to resort to observing nature to study turbulence. Similarly Leonardo da Vinci, who observed the vortices behind a pillar of a bridge over the river Arno. Despite the advent of computers, experiments still give important insights into the nature of fluid flow and are widely used to study engineering applications.

Besides purely qualitative observation the 20<sup>th</sup> century saw the introduction of several techniques to quantitatively characterize the flow. Historically, the first method to measure fluctuating quantities was the hot-wire introduced by King (1915). The hot-wire is a heated wire which, due to flow convection, experiences changes in temperature and thus resistance. This change in resistance can be used to reveal a continuous signal of the velocity at the position of the wire. This method has several disadvantages such as being intrusive and in order to obtain two-point correlations two probes are required. Some of the downsides have been alleviated by Laser-Doppler anemometry introduced by Yeh and Cummins (1964).

Particle image velocimetry (PIV) (see *e.g.* Westerweel (1993)) is a method that manages to capture flow quantities of tracer particles contained in a thin slice which is illuminated with a laser. This non-intrusive method saw its advent in the 1980s and

enables the capture of instantaneous flow fields. This method is still widely used as its setup is rather simple.

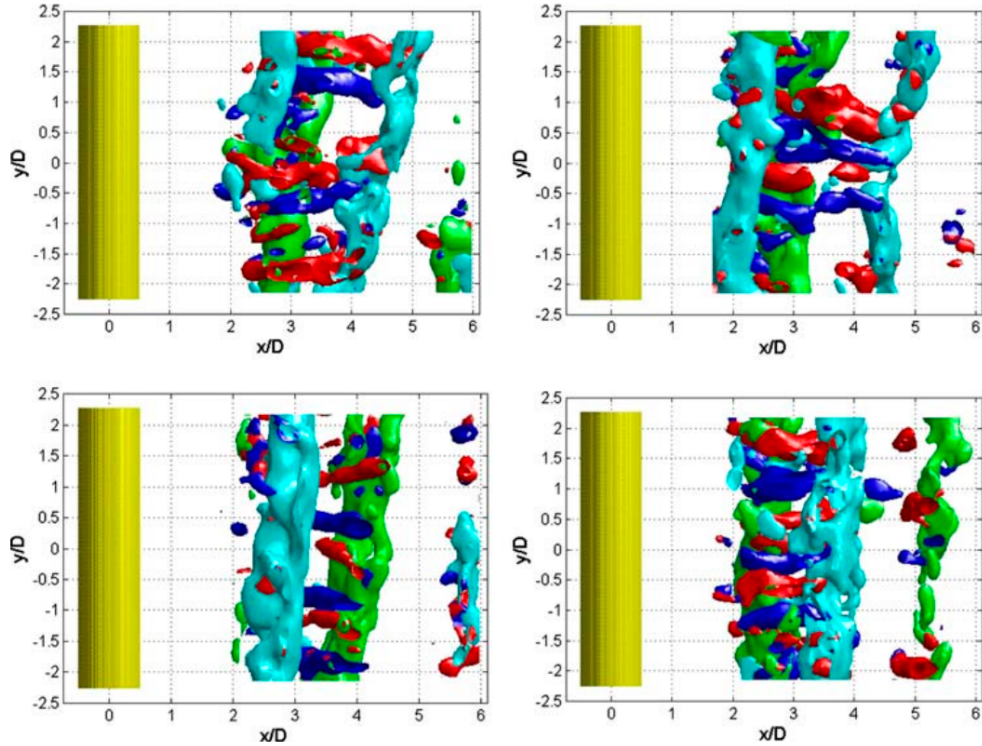


Figure 1.7: Vorticity iso-surfaces from tomographic image velocimetry by Elsinga *et al.* (2006).

At the beginning of the 21<sup>st</sup> century several three-dimensional methods were invented in order to overcome the restrictions of the classical particle image velocimetry. Amongst the earliest is the holographic image velocimetry by Blackshire and Humphreys (1994). More recently three-dimensional tomographic PIV was introduced by Elsinga *et al.* (2006) which is also able to reconstruct the three-dimensional particle distribution and the associated quantities, however, it can also be used on high-Reynolds number flows. An example of a dataset obtained with the latter method can be seen in Figure 1.7.

The measurement methods discussed all provide Eulerian measurements. In contrast, there exist several techniques to study Lagrangian properties of a fluid flow. One of the earliest methods allowed to calculate the Lagrangian velocity correlation based on scalar dispersion (Shlien and Corrsin, 1974). More popular is the use of particle tracking methods which employ (passive) tracer particles which are tracked optically. First measurements of this type were conducted by Snyder and Lumley (1971). This technique has since been refined and with the miniaturization of electronics instrumented particles currently being developed, *e.g.* Gasteuil *et al.* (2007). However, until now these instrumented particles are still too large and thus they cannot be considered

passive. In order to extract meaningful information from a flow the interrogation domain and time-scale must be of the length and time-scale of the largest eddies and in turn the resolution must be smaller than the Kolmogorov length and time. As the ratio between the two grows super-linearly as a function of the Reynolds number this causes Lagrangian measurements to only be feasible for flows with moderate Reynolds numbers. A more detailed overview can be found in the review paper by Toschi and Bodenschatz (2009).

### 1.4.2 Direct Numerical Simulation

Direct Numerical Simulation (DNS) deals with the simulation of turbulent flows by solving the Navier-Stokes equations without any additional modelling. In order to capture all the eddies it is necessary that the simulation resolves the Kolmogorov scales  $\eta$ . As the size of these scales is related to the Reynolds number via  $\eta/L \propto Re^{-3/4}$  it is clear that high Reynolds number flow requires significant computing resources. The first DNS was performed by Kim *et al.* (1987) for a Reynolds number of 5300 with a supercomputer capable of several gigaFLOPs. Morishita *et al.* (2011) presented a DNS of a channel flow with a Reynolds number of approximately 38000 using the Earth Simulator which is capable of 131 teraFLOPs. Finally, the first pipe flow DNS was conducted by Eggels *et al.* (1994) with a Reynolds number of 5300.

The methods which are generally used in direct numerical simulations are high order finite difference methods or spectral methods (Pope, 2001). The first are generally problematic when it comes to the resolution of small scales as they tend to oscillate. Spectral methods are in general very accurate but are restricted to simple geometries, often with periodic boundary conditions.

Extracting Eulerian statistics is mostly straight-forward using the methods mentioned above. In contrast, Lagrangian statistics need to be extracted with means of interpolation (Toschi and Bodenschatz, 2009). This must be done at run-time as otherwise prohibitive data storage would be required. A discussion of different interpolation approaches can be found in the paper by Choi *et al.* (2004) which deals with Lagrangian statistics in a turbulent channel flow.

### 1.4.3 Reynolds averaged Navier-Stokes

As mentioned Direct Numerical Simulation is computationally very expensive, thus the first simulations used models in order to lower the computational load. The first type of modelling approach is based on the averaged Navier-Stokes equations, more widely known as Reynolds averaged Navier-Stokes (RANS) equations (Pope, 2001). If the averaging is applied over an infinite time only statistically stationary flows can be solved with this approach. In contrast, the averaging in unsteady RANS is only over

a certain time allowing the simulation of flows which are not stationary. When the velocity is split into mean and fluctuating parts, the momentum equation for the mean velocity contains an additional term because of the non-linearity, the Reynolds stresses, which depends only on fluctuating quantities. In order to solve the equation it is thus necessary to find a closure for this term. This is achieved via the turbulent viscosity hypothesis, introduced by Boussinesq, which relates the Reynolds stresses to the mean rate of strain via a turbulent viscosity.

The latter can be modelled via several approaches, the simplest being the mixing length model developed by Prandtl (1925) which is an algebraic model. It is also possible to use one additional partial differential equation to calculate the turbulent kinetic energy  $k$  which in turn is used in the  $k - l_m$  model by Kolmogorov (1942). In most industrial applications two equation models like the  $k - \epsilon$  model devised by Jones and Launder (1972) and the  $k - \omega$  model (Wilcox, 1988) are used where, two additional partial differential equations are solved to model the turbulent viscosity. All of these models contain constants which are tuned towards certain basic turbulent flows even though they are flow-dependent.

Finally, it shall be noted that the turbulent viscosity hypothesis is an approximation and is violated even in simple shear flows. To overcome this deficiency several other models have been proposed. Amongst them are Reynolds-stress models, algebraic stress models and non-linear eddy viscosity models. For a more detailed discussion refer again to the book by Pope (2001).

#### 1.4.4 Large Eddy Simulation

Between the two extremes of DNS and RANS lies Large Eddy Simulation (LES) which resolves the large eddies of a flow but models the small ones with subgrid scale schemes. Hence, both a coarser grid and a larger time-step is possible significantly lowering the computational cost compared to DNS. This also implies that higher Reynolds number flows can be simulated and often in engineering applications it is not necessary to know all the flow details. Compared to RANS models, LES allows the study of flows which are not statistically stationary. Similarly to RANS, the velocity is split into two, but with a filtered velocity using a spatial average and the residual fluctuating velocity. This again yields a momentum equation containing a residual stress tensor, similar to the Reynolds stresses in RANS. Thus a closure model is required for this tensor, which is often an eddy-viscosity model. Finally these filtered equations are solved to compute the filtered velocity.

The first LES model was proposed by Smagorinsky (1963) which, analogous to the mixing length model, determines the eddy viscosity via a length-scale, which in turn is given as the filter width times the Smagorinsky constant  $C_s$ . The solution often

depends on the choice of the Smagorinsky constant. However, Germano *et al.* (1991) introduced a model which enables the determination of constant from the flow itself. In order to achieve this two filters need to be applied with varying filter width. The gain in accuracy is overshadowed by a higher computational cost. During the last decades several LES models have been developed and as such there is no standard model. The interested reader is referred to the books by Pope (2001) or Sagaut (2001) for further models and references.

In turbulent flows the smallest eddies have the largest influence close to the wall. As these small eddies are modelled in LES it is often necessary to apply special models close to the wall. One of the earliest such models is due to Schumann (1975). An alternative approach to avoid the issue of modelling the wall is to use hybrid RANS/LES schemes (Spalart *et al.*, 1997) where the wall region is simulated using RANS and the remaining flow via LES. Further information on this topic can be found in the book by Sagaut (2006).

## 1.5 Turbulence simulation with SPH

Although SPH is commonly used to study non-linear flow phenomena, turbulence has been studied systematically only by very few researchers. This is even more true for three-dimensional turbulence which, due to the high computational demand, has become feasible only in recent years. In the following several contributions towards turbulent research via SPH simulations are highlighted.

The models discussed in Section 1.3 were also implemented in SPH. The RANS approach was pursued by Violeau (2004) and the LES approach was first applied by Issa (2004) who used the basic Smagorinsky model. Alternatively to that Monaghan (2002) implemented the  $\alpha$  turbulence model by Holm (1999), which was later revised by himself (Monaghan, 2011) as the implicit smoothing caused exceedingly high computational demand.

There are two PhD thesis on the topic of SPH and turbulence, the first one by Mansour (2007) which also deals with the  $\alpha$  turbulence model looking at two-dimensional turbulence with random forcing. The second one is by Robinson (2009) who was investigating two-dimensional turbulence as well in the context of turbulent mixing.

Dedicated two-dimensional turbulence simulations were also conducted by Rafiee *et al.* (2011) and Valizadeh and Monaghan (2012) who both focus on decaying turbulence in a box. Arena *et al.* (2010) published a paper characterizing the noise inherent in the SPH method and compared it to turbulence models. Similarly, Shi *et al.* (2011) used the numerical diffusivity of SPH to simulate the decay of isotropic turbulence in a three-dimensional periodic box. They also investigated different mechanisms of interpolation of SPH data to a grid. Decay of isotropic turbulence as well as the three

dimensional Taylor-Green vortex was also simulated by Adami *et al.* (2013) using a modified SPH formulation based on an Arbitrary Lagrange Euler formulation. Another three-dimensional simulation was conducted by Dalrymple and Rogers (2006) who simulated turbulent water waves using a LES model.

All the papers presented above use the weakly compressible SPH model. To the best of the author's knowledge Hu and Adams (2012) is the only paper on incompressible turbulence with SPH. Besides the above mentioned papers, there are several which use turbulence models in order to compare them against each other in more applied simulations, such as the simulation of a hydraulic jump by De Padova *et al.* (2010). From this it is evident that turbulence in SPH has not been thoroughly investigated in three dimensions and is therefore a particular aim for this thesis.

## 1.6 Summary

On the preceding pages a literature review was given spanning certain meshless methods as well as the SPH method in detail. This was followed by an overview of methods used in turbulent research and specifically the use of SPH in turbulent flow simulation. In this final section of this chapter, a motivation for the remaining part of this work is given.

Although SPH has been used for the simulation of turbulent flows, research into the properties of SPH in turbulent flows is surprisingly scarce. Additionally to that, nearly all the quantitative investigations were limited to two-dimensional flows which behave significantly different to their three-dimensional counterparts. The three-dimensional simulation of turbulent flows demands high performance codes capable of running on supercomputers in a parallel fashion and due to the high computational cost of SPH this has only recently become feasible. In turbulent flows the most critical area is the wall region, requiring correct imposition of wall boundary conditions. This has long been a difficult issue with SPH methods, especially when it comes to complex geometries. In the following the focus lies thus initially on improving wall boundary conditions for a specific SPH method proposed by Ferrand *et al.* (2012). This method was already applied to turbulent flows, however, it is only available for two-dimensional geometries, requiring an extension to 3-D. After that, this method is validated with laminar flows before attempting to conduct direct numerical simulations and large eddy simulations of turbulent flows.

## Chapter 2

# SPH in fluid dynamics

This chapter starts with a short introduction to the Navier-Stokes equations. Following the introduction in the previous chapter a more detailed overview of SPH is given for both the unbounded and bounded case. Although both sections on SPH are as general as possible the main focus lies on the weakly-compressible SPH variant devised by Ferrand (2010). Finally this chapter is concluded by describing the time-integration techniques used in combination with SPH.

### 2.1 Navier-Stokes equations

The following definitions are used throughout this work. The domain of computation is denoted by  $\Omega \subseteq \mathbb{R}^n$ . Any underlined variable such as  $\underline{v}$  and a twice underlined quantity such as  $\underline{\underline{M}}$  denotes a vector or matrix in  $\mathbb{R}^n$ , respectively.  $\underline{u} \cdot \underline{v}$  denotes the standard scalar product and  $\underline{u} \otimes \underline{v}$  the tensor product in  $\mathbb{R}^n$  between the vectors  $\underline{u}$  and  $\underline{v}$ . A particle  $a$  is a set containing the position  $\underline{r}$ , a volume  $V$  and the physical state variables  $\Phi$ , *i.e.*

$$a := \{\underline{r}_a(t), V_a(t), \Phi_a(t)\}, \quad (2.1)$$

where  $t$  is the time. The set of all particles  $a$  is denoted by  $\mathcal{P}$ . Let  $f$  be any regular scalar or vector field in  $\mathbb{R}^n$  then  $f_a$  denotes the value of  $f$  at  $\underline{r}_a$ . Finally,  $\underline{\nabla}$  is the nabla, or del, operator defined as

$$\underline{\nabla} = \sum_{i=1}^n \underline{e}_i \frac{\partial}{\partial x_i}, \quad (2.2)$$

where  $\underline{e}_i : 1 \leq i \leq n$  is the standard basis in  $\mathbb{R}^n$ .

#### 2.1.1 Governing equations

The Navier-Stokes (NS) equations (for a more detailed introduction see *e.g.* Batchelor (2000)) relate the acceleration  $\underline{a} = d\underline{v}/dt$  of a fluid particle to the internal and external

forces  $\underline{F}$  that a fluid experiences where  $\underline{v}$  is the velocity. The internal forces are based on molecular interactions which are described by the stress tensor  $\underline{\tau}$ . The external force that is of interest in the following is gravity. If the gravity is given by a force per unit mass  $\underline{g}$  then the gravitational potential  $\Psi$  is defined according to

$$\underline{g} =: -\underline{\nabla}\Psi. \quad (2.3)$$

In the following  $\Psi = gy$  where  $g$  is the gravitational constant and  $y$  the vertical coordinate. The NS equations are then given by

$$\rho \frac{d\underline{v}}{dt} = \underline{\nabla}\underline{\tau} - \rho \underline{\nabla}\Psi, \quad (2.4)$$

where  $\rho$  denotes the density of the fluid. For the remaining part of this work only compressible constant-property Newtonian fluids are considered which results in the stress tensor being expressed as

$$\underline{\tau} = -p\underline{I} + \mu \left( \underline{\nabla} \otimes \underline{v} + (\underline{\nabla} \otimes \underline{v})^T \right) - \frac{2\mu}{3} \underline{\nabla} \cdot \underline{v}, \quad (2.5)$$

where  $p$  is the pressure and  $\mu$  the dynamic viscosity. In the following it is assumed that the fluid is weakly compressible, *i.e.* the density  $\rho$  only varies by about 1%. Thus the incompressible Navier-Stokes equations are used as a close approximation, which are given by

$$\frac{d\underline{v}}{dt} = -\frac{1}{\rho} \underline{\nabla}p + \underline{\nabla} \cdot [\nu (\underline{\nabla} \otimes \underline{v})] + \underline{g}, \quad (2.6)$$

with  $\nu = \mu/\rho$  the dynamic viscosity. The Euler equations are the NS equations with  $\nu = 0$ , *i.e.*

$$\frac{d\underline{v}}{dt} = -\frac{1}{\rho} \underline{\nabla}p + \underline{g}. \quad (2.7)$$

They are sometimes also referred to as inviscid Navier-Stokes equations.

Furthermore in the Lagrangian formulation the velocity is given by

$$\underline{v} = \frac{d\underline{r}}{dt}. \quad (2.8)$$

The density of a fluid is given due to the conservation of mass which is summarized in the continuity equation

$$\frac{d\rho}{dt} = -\rho \underline{\nabla} \cdot \underline{v}. \quad (2.9)$$

To close the system of equations represented by the NS and continuity equation the pressure needs to be determined. In general the pressure depends on the internal energy of the system as well as its density. Based on thermodynamic principles of an adiabatic

reversible process the following holds

$$p = \rho^2 \frac{de_{int}}{d\rho}, \quad (2.10)$$

where  $e_{int}$  is the internal energy per unit mass. An approximation to the above is given in the form of the Tait (1888) equation of state which reads

$$p = \frac{\rho_0 c_0^2}{\zeta} \left[ \left( \frac{\rho}{\rho_0} \right)^\zeta - 1 \right], \quad (2.11)$$

where  $\rho_0$  is the reference density,  $c_0$  the speed of sound and  $\zeta$  is a coefficient taken to be equal to 7 in the case of the fluid being water. Note that the particular choice of equation of state ensures that the density variation is at most 1% which is necessary to justify the incompressible approximation of the NS equations. This effect is achieved by choosing the speed of sound appropriately as discussed in the following.

### 2.1.2 Boundary conditions

With the equation of state (EOS) the system of equations is closed and all that remains is to specify boundary conditions. The boundary of the computation domain  $\Omega$  is denoted by  $\partial\Omega$ . Two specific boundary conditions are important in the following. The first one being the boundary conditions on a solid wall ( $\partial\Omega_s$ ) and the second the boundary conditions along the free-surface ( $\partial\Omega_f$ ). For a solid wall the inviscid boundary conditions are approximated as

$$\underline{v} \cdot \underline{n}|_{\partial\Omega_s} = 0, \quad (2.12)$$

$$\frac{\partial p}{\partial \underline{n}}|_{\partial\Omega_s} = 0, \quad (2.13)$$

where  $\underline{n}$  is the inward normal. In case of a viscous fluid the boundary conditions are approximated as

$$\underline{v} \cdot \underline{n}|_{\partial\Omega_s} = 0, \quad (2.14)$$

$$\mu (\underline{\nabla} \otimes \underline{v}) \cdot \underline{n}|_{\partial\Omega_s} = \rho \underline{v}_\tau \|\underline{v}_\tau\|, \quad (2.15)$$

$$\frac{\partial p}{\partial \underline{n}}|_{\partial\Omega_s} = 0, \quad (2.16)$$

where  $\underline{v}_\tau$  is the friction velocity. As can be seen the velocity at a solid boundary is given by a Dirichlet boundary condition, whereas the pressure is determined via a von Neumann condition. In contrast to that, on the free-surface the boundary conditions

are all of Dirichlet type and read

$$\underline{v}|_{\partial\Omega_f} = \underline{v}_\eta, \quad (2.17)$$

$$p|_{\partial\Omega_f} = p_{atm}, \quad (2.18)$$

where  $\underline{v}_\eta$  is the velocity of the interface and  $p_{atm}$  the atmospheric pressure. As the latter is generally taken to be constant it can be set to zero.

### 2.1.3 Calculus of variations

A physical system can be described by means of the Lagrange formalism (see *e.g.* Violeau (2012)). Let  $\underline{r}$  and  $\underline{v}$  be the sets (discrete vector fields) that contain all  $\underline{r}_a$  and  $\underline{v}_a$  respectively. The Lagrangian represents the mechanical state of a system at a specified time. For a system of particles  $\mathcal{P}$  it is defined by

$$L(\underline{r}, \underline{v}) = E_{kin}(\underline{v}) - E_{int}(\underline{r}) - E_{ext}(\underline{r}), \quad (2.19)$$

where  $E_{kin}$ ,  $E_{int}$  and  $E_{ext}$  are the kinetic, internal and external energy respectively. They are given as

$$E_{kin} = \frac{1}{2} \sum_{b \in \mathcal{P}} m_b \underline{v}_b^2, \quad (2.20)$$

$$E_{int} = \sum_{b \in \mathcal{P}} m_b e_{int}(\rho_b), \quad (2.21)$$

$$E_{ext} = \sum_{b \in \mathcal{P}} m_b \underline{r}_b \cdot \underline{g}, \quad (2.22)$$

where  $b$  represents a particle. The motion of a particle  $a \in \mathcal{P}$  is then governed by the Euler-Lagrange equations

$$\frac{d}{dt} \left( \frac{\partial L}{\partial \underline{v}_a} \right) - \frac{\partial L}{\partial \underline{r}_a} = 0. \quad (2.23)$$

The equations are based on the least action principle. Inserting the definition of  $L$  and the energies into the Lagrange equations yields

$$m_a \frac{d\underline{v}_a}{dt} = - \frac{\partial E_{int}}{\partial \underline{r}_a} + m_a \underline{g}. \quad (2.24)$$

Before the derivation is continued an observation needs to be made for which the definition of a scalar product is necessary. Let  $f, g$  be two scalar fields and  $\underline{B}, \underline{C}$  be two vector fields defined on a set  $\Omega \subseteq \mathbb{R}^n$ , then the continuous scalar products are defined

as

$$\langle f, g \rangle^c := \int_{\Omega} f(\underline{r}) g(\underline{r}) d\underline{r}, \quad (2.25)$$

$$\langle \underline{B}, \underline{C} \rangle^c := \int_{\Omega} \underline{B}(\underline{r}) \cdot \underline{C}(\underline{r}) d\underline{r}. \quad (2.26)$$

The discrete analogue is given by approximating the above with a quadrature rule and reads

$$\langle f, g \rangle := \sum_{a \in \mathcal{P}} V_a f_a g_a, \quad (2.27)$$

$$\langle \underline{B}, \underline{C} \rangle := \sum_{a \in \mathcal{P}} V_a \underline{B}_a \cdot \underline{C}_a, \quad (2.28)$$

where  $V_a$  approximates  $d\underline{r}$ .

Recalling the Navier-Stokes equations the following holds

$$\langle p, \underline{\nabla} \cdot \underline{v} \rangle^c = \int_{\Omega} p \underline{\nabla} \cdot \underline{v} d\underline{r} \quad (2.29)$$

$$= \int_{\Omega} \underline{\nabla} \cdot (p \underline{v}) d\underline{r} - \int_{\Omega} \underline{\nabla} p \cdot \underline{v} d\underline{r} \quad (2.30)$$

$$= \int_{\partial\Omega} p \underline{v} \cdot \underline{n} d\underline{r} - \int_{\Omega} \underline{\nabla} p \cdot \underline{v} d\underline{r}. \quad (2.31)$$

Finally, using the boundary conditions discussed in the previous section one can see that either  $p = p_{atm}$  or  $\underline{v} \cdot \underline{n}$  is equal to zero and thus the first term on the right hand side vanishes. This yields

$$\langle p, \underline{\nabla} \cdot \underline{v} \rangle^c = - \langle \underline{\nabla} p, \underline{v} \rangle^c. \quad (2.32)$$

This relation is in the following referred to as skew-adjoint divergence and gradient and should hold similarly in the discrete scalar product. When using skew-adjoint operators the boundary conditions  $p = 0$  and  $\underline{v} \cdot \underline{n} = 0$  are automatically satisfied and thus need not be imposed explicitly.

Returning to Eq. (2.24) and considering the work induced by a small displacement field  $d\underline{r}_s$  under the influence of the force  $F_{int}$  resulting from the internal energy one obtains

$$\left\langle \frac{\rho}{m} F_{int}, d\underline{r} \right\rangle = \sum_{a \in \mathcal{P}} F_{int,a} \cdot d\underline{r}_a \quad (2.33)$$

$$= - \sum_{a \in \mathcal{P}} \frac{\partial E_{int}}{\partial \underline{r}_a} \cdot d\underline{r}_a \quad (2.34)$$

$$\text{using Eq. (2.21)} \quad = - \sum_{a,b \in \mathcal{P}} m_b \frac{\partial e_{int}(\rho_b)}{\partial \underline{r}_a} \cdot d\underline{r}_a \quad (2.35)$$

$$= - \sum_{a,b \in \mathcal{P}} m_b \frac{de_{int}(\rho_b)}{d\rho_b} \frac{\partial \rho_b}{\partial \underline{r}_a} \cdot d\underline{r}_a \quad (2.36)$$

$$\stackrel{(2.10)}{=} - \sum_{a \in \mathcal{P}} m_b \frac{p_b}{\rho_b^2} \partial \rho_b \quad (2.37)$$

$$= - \sum_{a \in \mathcal{P}} V_b p_b \left( \frac{1}{\rho_b} \frac{d\rho_b}{dt} \right) dt \quad (2.38)$$

$$\stackrel{(2.9)}{=} \sum_{a \in \mathcal{P}} V_b p_b \underline{\nabla} \cdot \underline{v}_b dt \quad (2.39)$$

$$= \langle p, \underline{\nabla} \cdot \underline{v} \rangle dt \quad (2.40)$$

$$\stackrel{(2.32)}{=} - \langle \underline{\nabla} p, \underline{v} \rangle dt \quad (2.41)$$

$$\stackrel{(2.8)}{=} - \langle \underline{\nabla} p, d\underline{r} \rangle. \quad (2.42)$$

As this holds for every displacement field it can be concluded that

$$\frac{1}{m_a} \frac{\partial E_{int}}{\partial \underline{r}_a} = \frac{1}{\rho_a} \underline{\nabla} p. \quad (2.43)$$

Inserting this into Eq. (2.24) the Euler equations (2.7) are retrieved

$$\frac{d\underline{v}_a}{dt} = - \frac{1}{\rho_a} \underline{\nabla} p + \underline{g}. \quad (2.44)$$

The calculation presented in this section highlights the importance of the skew-adjoint property of gradient and divergence as it is equivalent to the conservation of the momentum represented by the Lagrange equation.

## 2.2 Unbounded weakly compressible SPH

### 2.2.1 Approximating a value

In the following section the SPH method is introduced on a infinite domain in an  $n$ -dimensional Euclidean space, *i.e.*  $\Omega = \mathbb{R}^n$ . Let  $f$  be a scalar field. Then  $f_a$  can be represented by

$$f_a = f(\underline{r}_a) = \int_{\Omega} f(\underline{r}) \delta(\underline{r} - \underline{r}_a) d\underline{r}, \quad (2.45)$$

where  $\delta$  is the Dirac delta function. The main idea of the continuous SPH approximation then is to approximate the  $\delta$  function by a so-called weighting or kernel function  $w$ . This gives rise to the definition of the SPH continuous smoothing interpolant

$$\langle f \rangle_a^c := \int_{\Omega} f(\underline{r}) w(\underline{r} - \underline{r}_a, h) d\underline{r}, \quad (2.46)$$

where the superscript  $c$  indicates the continuous approximation and the subscript  $a$  the particle at which position  $f$  is approximated. The smoothing length  $h$  is defined such that  $w$  can be written as

$$w(\underline{r} - \underline{r}_a, h) = \frac{\alpha_n}{h^n} \omega\left(\frac{\|\underline{r} - \underline{r}_a\|}{h}\right), \quad (2.47)$$

with a dimensionless function  $\omega$  and such that  $w(\cdot, h) \rightarrow \delta(\cdot)$  for  $h \rightarrow 0$ . So far, there are no additional requirements on the kernel function  $w$ . However, considering the Taylor expansion of a function

$$f(\underline{r}) = f(\underline{r}_a) - \left(\frac{\partial f}{\partial \underline{r}}\right)_a \cdot (\underline{r}_a - \underline{r}) + \mathcal{O}\left(\|\underline{r}_a - \underline{r}\|^2\right), \quad (2.48)$$

and inserting it into Eq. (2.46) yields

$$\langle f \rangle_a^c = f_a \int_{\Omega} w(\underline{r} - \underline{r}_a, h) d\underline{r} - \left(\frac{\partial f}{\partial \underline{r}}\right)_a \cdot \int_{\Omega} (\underline{r}_a - \underline{r}) w(\underline{r} - \underline{r}_a, h) d\underline{r} + \mathcal{O}\left(\|\underline{r}_a - \underline{r}\|^2\right). \quad (2.49)$$

This implies that to obtain a first-order consistent approximation the following needs to hold

$$\int_{\Omega} w(\underline{r} - \underline{r}_a, h) d\underline{r} = 1, \quad (2.50)$$

$$\int_{\Omega} (\underline{r}_a - \underline{r}) w(\underline{r} - \underline{r}_a, h) d\underline{r} = \underline{0}. \quad (2.51)$$

The first equation can be satisfied by choosing the parameter  $\alpha_n > 0$  in Eq. (2.47) appropriately. To satisfy the second equation observe that it is true if

$$\underline{\nabla} w(\underline{r} - \underline{r}_a, h) = -\underline{\nabla} w(-\underline{r} + \underline{r}_a, h). \quad (2.52)$$

It is standard in the SPH literature to fulfil this criterion by letting  $\omega$  in Eq. (2.47) depend only on the distance, *i.e.*

$$w(\underline{r} - \underline{r}_a, h) = \frac{\alpha_n}{h^n} \omega\left(\frac{\|\underline{r} - \underline{r}_a\|}{h}\right). \quad (2.53)$$

As the kernel only depends on the radius its derivative is given by

$$\frac{\partial}{\partial \underline{r}} w(\underline{r} - \underline{r}_a, h) = \frac{\partial}{\partial \underline{r}} \frac{\alpha_n}{h^n} \omega\left(\frac{\|\underline{r} - \underline{r}_a\|}{h}\right) \quad (2.54)$$

$$= \frac{\alpha_n}{h^n} \frac{\partial \omega(q)}{\partial q} \frac{\partial q}{\partial \underline{r}} \quad (2.55)$$

$$= \frac{\alpha_n}{h^n} \frac{\partial \omega(q)}{\partial q} \frac{1}{h} \frac{\underline{r} - \underline{r}_a}{\|\underline{r} - \underline{r}_a\|}, \quad (2.56)$$

where  $q = \frac{\|\underline{r} - \underline{r}_a\|}{h}$ . Thus,  $w'(q)$  can be defined as

$$w'(q) = \frac{\alpha_n}{h^{n+1}} \frac{\partial \omega(q)}{\partial q}. \quad (2.57)$$

Thus,

$$\frac{\partial}{\partial \underline{r}} w(\underline{r} - \underline{r}_a, h) = w'(q) \frac{\underline{r} - \underline{r}_a}{\|\underline{r} - \underline{r}_a\|}, \quad (2.58)$$

which shows that the orientation of the kernel gradient only depends on the relative position vector of two particles. Note that due to this fact the kernel gradient is subject to the following antisymmetry property

$$\underline{\nabla} w(\underline{r} - \underline{r}_a, h) = -\underline{\nabla}_a w(\underline{r} - \underline{r}_a, h). \quad (2.59)$$

where  $\underline{\nabla}_a$  denotes the derivative with respect to  $\underline{r}_a$ .

Lastly, due to numerical stability issues (see *e.g.* Violeau (2012)) it is advantageous to demand that the kernel function  $w$  is monotonic and positive, which is equivalent to  $\text{sgn}(q)d\omega/dq < 0 (q \neq 0)$  and  $\omega \geq 0$  respectively, where  $\text{sgn}$  is the sign function. In most cases the support of the kernel is compact in order to reduce computational cost. The support of a kernel function centered around a particle  $a$  is denoted by  $\Omega_a$ . Due to these constraints the continuous approximation can also be seen as a weighted average, thus the name weighting function for  $w$ . Note that these conditions do not imply that

$$f_a = \langle f \rangle_a^c. \quad (2.60)$$

the error being of the order  $h^2$  according to Eq. (2.49).

As the domain needs to be discretised into a finite set of particles, the integral in the continuous approximation needs to be replaced by a sum. A straightforward quadrature rule gives rise to the definition of the SPH approximation of a function  $f$  as

$$\langle f \rangle_a = \sum_{b \in \mathcal{P}} V_b f_b w_{ab}, \quad (2.61)$$

where  $w_{ab} = w(\underline{r}_b - \underline{r}_a, h)$ . Note that the sum does not run over all particles as for most of them  $w_{ab}$  is zero since the support is often compact.

### 2.2.2 Choice of kernel function

There are several possible choices for the dimensionless kernel function  $\omega$ . One of the simplest is the Gaussian kernel for which

$$\omega(q) = e^{-q^2}. \quad (2.62)$$

As this function has infinite support it needs to be truncated in order to avoid having too many neighbours. Other possibilities include B-Splines of various orders (common are third to fifth order splines, see *e.g.* Violeau (2012)). In the following however, the only kernel considered in the following is the Wendland kernel (Wendland (1995)). It is defined as

$$\omega(q) = \begin{cases} \alpha_m (1 - \frac{q}{2})^4 (1 + 2q) & \text{if } 0 \leq q \leq 2, \\ 0 & \text{if } 2 < q, \end{cases} \quad (2.63)$$

with the normalisation constant being given as

$$\alpha_1 = \frac{3}{4}, \quad (2.64)$$

$$\alpha_2 = \frac{7}{4\pi}, \quad (2.65)$$

$$\alpha_3 = \frac{21}{16\pi}, \quad (2.66)$$

depending on the dimension  $m$  of the problem. The choice of the kernel can have significant impact on the SPH method. This has been observed by Robinson (2009) in the context of tensile instability which describes the effect of particles clumping together. It was shown that using the Wendland kernel this deficiency can be overcome. More fundamental however is the influence of the Fourier transform on the stability of the method which has been highlighted by Morris (1996). A von Neumann stability analysis as presented by Violeau (2012) shows that the Fourier transform of a kernel should be strictly positive and decreasing, another property of the Wendland kernel. As noted by Violeau (2012) this analysis depends also on the chosen time integration scheme as discussed later.

### 2.2.3 Approximation of first-order derivatives

Returning to the continuous SPH approximation (Eq. (2.46)) the gradient of a scalar field  $f$  can be written as

$$\langle \nabla f \rangle_a^c = \int_{\Omega} \nabla f(\underline{r}) w(\underline{r} - \underline{r}_a, h) d\underline{r}. \quad (2.67)$$

Integration by parts then yields

$$\langle \nabla f \rangle_a^c = - \int_{\Omega} f(\underline{r}) \nabla w(\underline{r} - \underline{r}_a, h) d\underline{r} + \int_{\Omega} \nabla(f(\underline{r}) w(\underline{r} - \underline{r}_a, h)) d\underline{r}, \quad (2.68)$$

which can be also written as

$$\langle \nabla f \rangle_a^c = \int_{\Omega \cap \Omega_a} f(\underline{r}) \nabla_a w(\underline{r} - \underline{r}_a, h) d\underline{r} + \int_{\Omega \cap \Omega_a} \nabla(f(\underline{r}) w(\underline{r} - \underline{r}_a, h)) d\underline{r}, \quad (2.69)$$

where  $\Omega_a$  is the support of the kernel function  $w$  centred around  $r_a$ , and Eq. (2.59) was used. Applying Stokes' theorem to the above and remembering that  $\Omega_a \subset \Omega = \mathbb{R}^n$  and thus  $\Omega \cap \Omega_a = \Omega_a$ , as well as  $\partial(\Omega \cap \Omega_a) = \partial\Omega_a$ , gives

$$\langle \nabla f \rangle_a^c = \int_{\Omega_a} f(\underline{r}) \nabla_a w(\underline{r} - \underline{r}_a, h) d\underline{r} - \int_{\partial\Omega_a} f(\underline{r}) w(\underline{r} - \underline{r}_a, h) \underline{n} d\underline{r}, \quad (2.70)$$

with  $\underline{n}$  being the inward normal of  $\partial\Omega_a$ . As the kernel has compact support and as  $\Omega = \mathbb{R}^n$  the boundary term in the equation above vanishes. Thus, the final result reads

$$\langle \nabla f \rangle_a^c = \int_{\Omega_a} f(\underline{r}) \nabla_a w(\underline{r} - \underline{r}_a, h) d\underline{r}. \quad (2.71)$$

The above equation has the advantage of shifting the derivative from the unknown  $f$  to the analytically known kernel  $w$ . Discretizing yields

$$\langle \nabla f \rangle_a = \sum_{b \in \mathcal{P}} V_b f_b \nabla_a w_{ab}. \quad (2.72)$$

Considering a system of only two particles that interact via a force originating from  $\frac{1}{\rho} \nabla p$ , the force acting from particle  $b$  on particle  $a$  is given by

$$\underline{F}_{b \rightarrow a} = m_b \frac{1}{\rho_a \rho_b} p_b \nabla_a w_{ab}, \quad (2.73)$$

whereas the force acting from  $a$  on  $b$  is given by

$$\underline{F}_{a \rightarrow b} = m_a \frac{1}{\rho_b \rho_a} p_a \nabla_b w_{ab} = -m_a \frac{1}{\rho_b \rho_a} p_a \nabla_a w_{ab}. \quad (2.74)$$

Newton's third law of equal but opposite forces states that  $\underline{F}_{b \rightarrow a} = -\underline{F}_{a \rightarrow b}$  but as  $p_a \neq p_b$  this law is violated when using the gradient given by Eq. (2.72). Thus, the following approach is more common in the SPH literature.

Let  $k \in \mathbb{N}$  then

$$\nabla f = \nabla \left( \rho^k \frac{f}{\rho^k} \right) = \rho^k \nabla \frac{f}{\rho^k} + \frac{f}{\rho^k} \nabla \rho^k, \quad (2.75)$$

for any function  $\rho$ . Approximating the above gives

$$\langle \nabla f \rangle_a = \langle \rho^k \nabla \frac{f}{\rho^k} \rangle_a + \langle \frac{f}{\rho^k} \nabla \rho^k \rangle_a. \quad (2.76)$$

This is written as

$$\langle \nabla f \rangle_a \approx \rho_a^k \langle \nabla \frac{f}{\rho^k} \rangle_a + \frac{f_a}{\rho_a^k} \langle \nabla \rho^k \rangle_a, \quad (2.77)$$

which in a strictly mathematical sense is only an approximation, if  $k \neq 0$  due to Eq. (2.60). The case  $k = 0$  is exact if the particle distribution is such that

$$\sum_{b \in \mathcal{P}} V_b \nabla_a w_{ab} = 0. \quad (2.78)$$

Assuming that Eq. (2.77) holds the approximation of the gradient finally reads

$$\langle \nabla f \rangle_a \approx \sum_{b \in \mathcal{P}} V_b \underbrace{\frac{\rho_a^{2k} f_b + \rho_b^{2k} f_a}{\rho_b^k \rho_a^k}}_{(*)} \nabla_a w_{ab}. \quad (2.79)$$

The expression  $(*)$  in the summand is symmetric with respect to  $a$  and  $b$  which enforces Newton's third law in combination with the antisymmetric kernel gradient as shown in Eq. (2.59). For future reference the standard additive (*std*,  $+$ ) SPH gradient is defined by

$$\mathbf{Grad}_a^{std,+,k}(f) = \sum_{b \in \mathcal{P}} V_b \frac{\rho_a^{2k} f_b + \rho_b^{2k} f_a}{\rho_b^k \rho_a^k} \nabla_a w_{ab}. \quad (2.80)$$

The above can also be applied to a vector field  $\underline{B}$  which gives rise to the definition of the standard additive SPH divergence as

$$\mathbf{Div}_a^{std,+,k}(\underline{B}) := \sum_{b \in \mathcal{P}} V_b \frac{\rho_a^{2k} \underline{B}_b + \rho_b^{2k} \underline{B}_a}{\rho_b^k \rho_a^k} \cdot \nabla_a w_{ab}. \quad (2.81)$$

Instead of using the product rule as in Eq. (2.76) it is also possible to use the quotient rule

$$\langle \nabla f \rangle_a = \langle \frac{1}{\rho^k} \nabla (f \rho^k) \rangle_a - \langle \frac{f}{\rho^k} \nabla \rho^k \rangle_a, \quad (2.82)$$

which leads to the following set of standard subtractive (*std*,  $-$ ) SPH operators

$$\mathbf{Grad}_a^{std,-,k}(f) := \frac{1}{\rho_a^{2k}} \sum_{b \in \mathcal{P}} V_b \rho_a^k \rho_b^k (f_b - f_a) \nabla_a w_{ab}, \quad (2.83)$$

$$\mathbf{Div}_a^{std,-,k}(\underline{B}) := \frac{1}{\rho_a^{2k}} \sum_{b \in \mathcal{P}} V_b \rho_a^k \rho_b^k (\underline{B}_b - \underline{B}_a) \cdot \nabla_a w_{ab}. \quad (2.84)$$

Note that the subtractive operators are zeroth-order consistent, *i.e.* the operator applied to a constant function yields zero. On the other hand, the gradient does not satisfy Newton's third law.

Oger *et al.* (2007) pointed out that higher order accurate schemes can produce better results although they disobey certain physical laws, such as the conservation of energy. It is possible to construct a first-order accurate set of differential operators, an idea pioneered by Randles and Libersky (1996). The core is a renormalisation procedure

such that a gradient operator satisfies

$$\underline{\nabla} \otimes (\underline{r} - \underline{r}_a) = \underline{I} \quad \forall a \in \mathcal{P}, \quad (2.85)$$

where  $\underline{I}$  is the identity matrix and  $\underline{r}$  a linear function. As a gradient operator generally does not satisfy Eq. (2.85), the kernel gradient is multiplied by a matrix  $\underline{L}$ . To obtain an expression for  $\underline{L}$  the standard additive SPH operator (Eq. (2.80)) is inserted into the renormalisation equation (2.85) which gives in vector notation

$$\sum_{b \in \mathcal{P}} V_b \frac{\rho_a^k}{\rho_b^k} (\underline{r}_b - \underline{r}_a) \left( \underline{L}_a \underline{\nabla}_a w_{ab} \right)^T = \underline{I}, \quad (2.86)$$

where the superscript  $T$  denotes the transpose of a matrix. This can be rewritten as

$$\left[ \sum_{b \in \mathcal{P}} V_b \frac{\rho_a^k}{\rho_b^k} (\underline{r}_b - \underline{r}_a) (\underline{\nabla}_a w_{ab})^T \right] \underline{L}_a^T = \underline{I}. \quad (2.87)$$

Inverting the leftmost matrix and transposing the whole equation subsequently yields

$$\underline{L}_a = \left[ \sum_{b \in \mathcal{P}} V_b \frac{\rho_a^k}{\rho_b^k} (\underline{\nabla}_a w_{ab}) \otimes (\underline{r}_b - \underline{r}_a) \right]^{-1}. \quad (2.88)$$

This implies that the matrix  $\underline{L}$  as calculated via Eq. (2.88) is symmetric thanks to (2.59). Finally a the first-order corrected gradient is given by

$$\widetilde{\mathbf{Grad}}_a^{std,+,k}(f) := \sum_{b \in \mathcal{P}} V_b \frac{\rho_a^{2k} f_b \underline{L}_b + \rho_b^{2k} f_a \underline{L}_a}{\rho_b^k \rho_a^k} \cdot \underline{\nabla}_a w_{ab}. \quad (2.89)$$

The use of both  $\underline{L}_a$  and  $\underline{L}_b$  is justified again by Newton's third law.

Note that this gradient is still not zeroth-order accurate. To obtain a truly first-order accurate gradient the matrix  $\underline{L}$  needs to be applied to the standard subtractive gradient Eq. (2.83) which then reads

$$\widetilde{\mathbf{Grad}}_a^{std,-,k}(f) := \frac{1}{\rho_a^{2k}} \sum_{b \in \mathcal{P}} V_b \rho_a^k \rho_b^k (f_b - f_a) \underline{L}_a \cdot \underline{\nabla}_a w_{ab}. \quad (2.90)$$

The matrix correction can also be applied to the divergence operators in a similar fashion.

## 2.2.4 Approximation of second-order derivatives

It was demonstrated above that there are various ways of approximating a first-order derivative with the SPH method. The same is true for second-order operators. There

are two approaches to second-order operators that are based on the considerations presented in the previous section.

Firstly, it is possible to approximate the derivative of  $\underline{\nabla}f$  via Eq. (2.72) and after applying Stokes' theorem again one would obtain

$$\langle \underline{\nabla} \otimes \underline{\nabla}f \rangle_a = \sum_{b \in \mathcal{P}} V_b f_b \underline{\nabla}_a \otimes \underline{\nabla}_a w_{ab}. \quad (2.91)$$

However, this equation contains second derivatives of the kernel and that makes this formulation sensitive to particle positions as pointed out by Monaghan (2005). The reason for this effect is that the second derivative of the kernel changes its sign.

Alternatively, a second-order derivative can be obtained by twice applying a first-order differential operator. However, this results in a time consuming double sum.

Because these two approaches have significant disadvantages, a different approach is favoured in the SPH community. In the following the discussion is limited to the operator  $\underline{\nabla} \cdot (f \underline{\nabla} \otimes \underline{B})$ . To approximate the term in the brackets consider the Taylor approximation of  $\underline{B}$  given by

$$\underline{B}_b = \underline{B}_a - (\underline{\nabla}_a \otimes \underline{B})^T \cdot \underline{r}_{ab} + \mathcal{O}(r_{ab}^2), \quad (2.92)$$

where  $\Phi_{ab} = \Phi_a - \Phi_b$  (here  $\Phi = \underline{r}$ ), a notation that is used on several occasions below. The equation above yields

$$(\underline{\nabla}_a \otimes \underline{B})^T \cdot \frac{\underline{r}_{ab}}{\|\underline{r}_{ab}\|} \approx \frac{1}{\|\underline{r}_{ab}\|} \underline{B}_{ab}, \quad (2.93)$$

and similarly

$$(\underline{\nabla}_b \otimes \underline{B})^T \cdot \frac{\underline{r}_{ab}}{\|\underline{r}_{ab}\|} \approx \frac{1}{\|\underline{r}_{ab}\|} \underline{B}_{ab}. \quad (2.94)$$

To obtain the desired second-order operator the standard additive divergence is applied to the above. This results in

$$\langle \underline{\nabla} \cdot (f \underline{\nabla} \otimes \underline{B}) \rangle_a = \sum_{b \in \mathcal{P}} V_b \frac{\rho_a^{2k} f_b + \rho_b^{2k} f_a}{\rho_b^k \rho_a^k} \frac{\underline{B}_{ab}}{\|\underline{r}_{ab}\|} \|\underline{\nabla}_a w_{ab}\|. \quad (2.95)$$

The above second-order operator is due to Morris *et al.* (1997) for  $k = 1$ . Monaghan (1992) also derived a second-order operator which is given by

$$\langle \underline{\nabla} \cdot (f \underline{\nabla} \otimes \underline{B}) \rangle_a = 2(n+2) \sum_{b \in \mathcal{P}} V_b \frac{\rho_a^{2k} f_b + \rho_b^{2k} f_a}{\rho_b^k \rho_a^k} \frac{\underline{B}_{ab} \cdot \underline{r}_{ab}}{\|\underline{r}_{ab}\|^2} \underline{\nabla}_a w_{ab}, \quad (2.96)$$

where  $n$  is the dimension. Both of these operators are first-order consistent if Eq. (2.78) holds. These operators can be corrected with a matrix in order to obtain second-order

accuracy as demonstrated by Schwaiger (2008) and Fatehi and Manzari (2011). The latter operator is given as

$$\langle \underline{\nabla} \cdot \underline{\nabla} f \rangle_a = \hat{\underline{L}}_a : \sum_{b \in \mathcal{P}} 2V_b \underline{r}_{ab} \otimes \underline{\nabla}_a w_{ab} \left( \frac{f_{ab}}{\|\underline{r}_{ab}\|^2} - \frac{\underline{r}_{ab}}{\|\underline{r}_{ab}\|^2} \cdot \langle \underline{\nabla} f \rangle_a \right), \quad (2.97)$$

where  $:$  denotes the Frobenius inner product and  $f_{ab} = f_a - f_b$ . The gradient of  $f$  is calculated via a first-order scheme, *i.e.* Eq. (2.90) with  $k = 0$  and  $\hat{\underline{L}}_a$  is given by

$$-\underline{I} = \hat{\underline{L}}_a : \left[ \sum_{b \in \mathcal{P}} 2 \frac{V_b}{\|\underline{r}_{ab}\|^2} \underline{r}_{ab} \otimes \underline{r}_{ab} \otimes \underline{r}_{ab} \otimes \underline{\nabla}_a w_{ab} + \left( \sum_{b \in \mathcal{P}} \frac{V_b}{\|\underline{r}_{ab}\|^2} \underline{r}_{ab} \otimes \underline{r}_{ab} \otimes \underline{\nabla}_a w_{ab} \right) \cdot \underline{L}_a \cdot \left( \sum_{b \in \mathcal{P}} V_b \underline{r}_{ab} \otimes \underline{r}_{ab} \otimes \underline{\nabla}_a w_{ab} \right) \right]. \quad (2.98)$$

The latter equation is a system of linear equations and can be solved by means of a Gaussian elimination algorithm.

One disadvantage of these modified operators is that they are not able to approximate  $\underline{\nabla}(f \underline{\nabla} \cdot \underline{B})$ ; or any arbitrary second derivative (see *e.g.* Espanol and Revenga (2003)). Violeau (2009) proved that the following operator provides a suitable approximation to any second-order derivative

$$\underline{\nabla} \otimes (f \underline{\nabla} \otimes \underline{B})_a = \sum_{b \in \mathcal{P}} V_b \frac{f_b + f_a}{2} \left( (n+2) \frac{\underline{r}_{ab} \otimes \underline{r}_{ab}}{\|\underline{r}_{ab}\|^2} - \underline{I} \right) \otimes \frac{\underline{B}_{ab}}{\|\underline{r}_{ab}\|} \|\underline{\nabla}_a w_{ab}\|. \quad (2.99)$$

All second-order derivatives are needed in turbulent flows when the NS equations (2.6) have to be solved with  $\mu \neq \text{const}$ . Using the general formula presented above it is possible to obtain the expression

$$\begin{aligned} \langle \underline{\nabla} \cdot (f \underline{\nabla} \otimes \underline{B}) + \underline{\nabla} f (\underline{\nabla} \cdot \underline{B}) \rangle_a = \\ \sum_{b \in \mathcal{P}} V_b \frac{f_b + f_a}{2} \left( (n+2) \frac{\underline{B}_{ab} \cdot \underline{r}_{ab}}{\|\underline{r}_{ab}\|^2} \underline{\nabla}_a w_{ab} + \frac{\underline{\nabla}_a w_{ab} \cdot \underline{r}_{ab}}{\|\underline{r}_{ab}\|^2} \underline{B}_{ab} \right). \end{aligned} \quad (2.100)$$

The disadvantage of this scheme is that there is no second-order correction available yet.

### 2.3 Wall-bounded SPH

There are various ways of defining boundary conditions in SPH. In the following section a small overview is given concentrating on the traditional approaches. In Section 2.3.2 a special type of boundary condition is examined in detail.

### 2.3.1 Standard wall boundary conditions in SPH

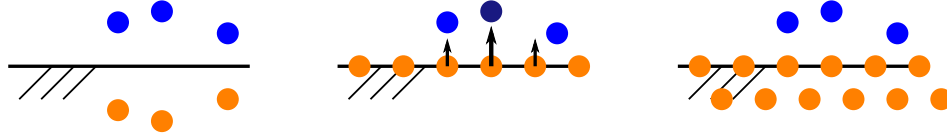


Figure 2.1: Three classic wall boundary conditions.

There are three classic wall boundary conditions in SPH. An illustration for each one is shown in Figure 2.1.

On the left hand side the ghost particle approach introduced by Libersky *et al.* (1993) is displayed. The idea is to mirror each fluid particle (blue) at the boundary (black line) to create a ghost particle (orange). To enforce boundary conditions with a zero derivative normal to the wall of a value  $f$ , the value of  $f$  for a ghost particle is set identical to the value of its corresponding fluid particle. For Dirichlet boundary conditions the value of the fluid particle is linearly extrapolated to obtain the value for the ghost particle. In case of  $f|_{\partial\Omega} = 0$  the value of  $f$  at the ghost particle is  $-f$  at the fluid particle. Although this method provides a solid basis for implementing boundary conditions it is difficult to adapt the formulation to deal with complex boundary shapes. This issue has been addressed in several papers (*e.g.* Borve (2011)) but cannot be considered to be completely solved.

The boundary condition illustrated in the centre of Figure 2.1 corresponds to the repulsive force boundary conditions that were introduced by Monaghan (1994). The idea of these boundary conditions is that each boundary particle exerts a repulsive force on a specific fluid particle. This force is modelled after the Lennard-Jones potential (see *e.g.* Reif (1965)). Additionally, the boundary particles are considered in the standard viscous term in order to impose a viscous force. Although these boundary conditions are relatively simple and have low computational cost it is not possible to enforce Dirichlet or Neumann boundary conditions through them explicitly. Besides that, the repulsive forces also break the property of momentum conservation.

The last boundary condition shown in Figure 2.1 is commonly called dynamic boundary conditions or fictitious particle technique. Dalrymple and Knio (2001) proposed to model solid wall boundaries simply by placing two (or more as demonstrated by Violeau and Issa (2007)) rows of particles along the boundaries. As illustrated above this is usually done in a staggered fashion. The boundary particles have a pressure that is determined by the continuity equation and generally behave like fluid particles with the exception that they do not move. Similar to the repulsive force boundary conditions the dynamic boundary conditions are simple to implement but again it is not possible to explicitly enforce Dirichlet or Neumann boundary conditions.

The list of wall boundary conditions presented above is not exhaustive. There are several other possibilities for implementing solid boundaries in SPH (*e.g.* Vacondio *et al.* (2011), Fatehi and Manzari (2010)). This continues to be an area of active research. Compared to solid wall boundary conditions, open boundaries for inflow and outflow are much more complicated (see *e.g.* Mahmood *et al.* (2011)). The most stable formulation is by Lastiwka *et al.* (2009) which uses Riemann invariants in order to avoid reflection from acoustic pressure waves. A similar technique was applied to free-surface flows by Mahmood (2011). Kassiotis *et al.* (2011) showed that it is also possible to combine inflow and outflow conditions in order to couple SPH with a Finite Difference model.

### 2.3.2 Unified semi-analytical wall boundary conditions

In this section a type of boundary condition is described that originates from the work of Kulasegaram *et al.* (2004) and was refined later by De Leffe *et al.* (2009). The central idea presented in this section was developed by Ferrand (2010) to compensate for the kernel void that exists when a particle is close to a boundary, *i.e.* when the kernel has incomplete support. This is illustrated in Figure 2.2 where the domain  $\Omega$  is shown as well as a particle  $a$  which is close to a boundary and has a kernel with support of radius  $R$ . Note that  $\Omega$  is now bounded, contrary to Section 2.2 where  $\Omega$  was identified with  $\mathbb{R}^n$ . This newly proposed approach is discussed in detail in the following and

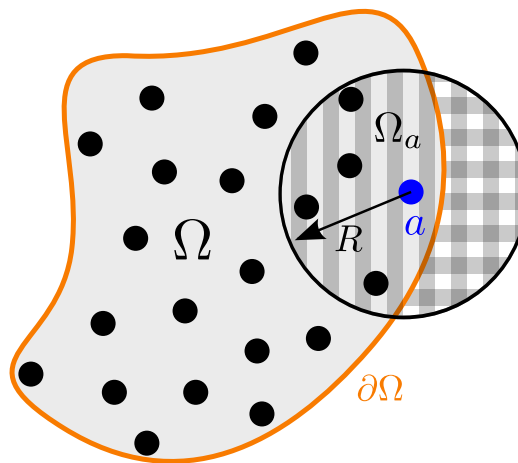


Figure 2.2: Kernel support of a particle  $a$ .

improvements are suggested in Chapter 3.

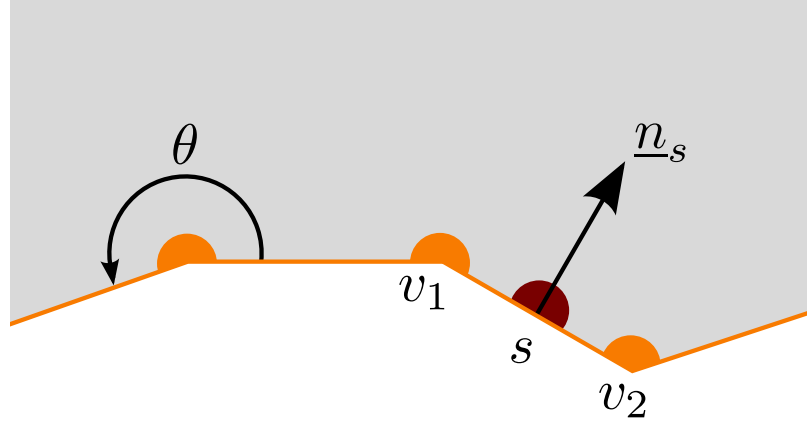


Figure 2.3: Vertex particles and boundary elements along a boundary.

### 2.3.2.1 Compensating the kernel void by $\gamma$

Clearly Eq. (2.50) does not hold if a particle  $a$  is close to a boundary as the kernel support  $\Omega_a$  is not entirely contained in the domain  $\Omega$ . To compensate for the incomplete support, *i.e.* the chequered area in Figure 2.2, a new field  $\gamma$  is introduced which is used for renormalizing. This variable is defined as

$$\gamma_a = \int_{\Omega \cap \Omega_a} w(\underline{r} - \underline{r}_a, h) d\underline{r}. \quad (2.101)$$

From this it is clear that  $\gamma \leq 1$ , with  $\gamma_a = 1$  if  $\Omega_a \subseteq \Omega$ . This gives rise to the definition of a new SPH approximation of a function  $f$  as

$$\langle f \rangle_a^\gamma := \frac{1}{\gamma_a} \sum_{b \in \mathcal{P}} V_b f_b w_{ab}, \quad (2.102)$$

and in the continuous form

$$\langle f \rangle_a^{c,\gamma} := \frac{1}{\gamma_a} \int_{\Omega_a} f(\underline{r}) w(\underline{r} - \underline{r}_a, h) d\underline{r}. \quad (2.103)$$

To calculate  $\gamma$  we obtain from Eq. (2.101) that

$$\underline{\nabla} \gamma_a = \int_{\Omega \cap \Omega_a} \underline{\nabla} w(\underline{r} - \underline{r}_a, h) d\underline{r} = \int_{\partial \Omega \cap \Omega_a} w(\underline{r} - \underline{r}_a, h) \underline{n} d\underline{r}, \quad (2.104)$$

where  $\underline{n}$  is the inward normal at the boundary  $\partial \Omega$ . In this new SPH boundary method a boundary consists of a row of boundary particles or, if the boundary particles are considered as vertices, boundary elements  $\mathcal{S}$  (a boundary element  $s \in \mathcal{S}$  has two vertices  $v_1 \in \mathcal{V}$  and  $v_2 \in \mathcal{V}$  as well as an inward normal  $n_s$ ). In two dimensions, a boundary

Set	Description
$\mathcal{P}$	All particles
$\mathcal{V}$	Particles on boundary
$\mathcal{F}$	Particles inside the fluid domain
$\mathcal{S}$	Boundary-elements

Table 2.1: Overview of elements.

element is a line segment. This is illustrated in Figure 2.3. The different types of elements are summarized in Table 2.1. The following holds

$$\nabla\gamma_a = \sum_{s \in \mathcal{S}} \int_{r_{v_1}}^{r_{v_2}} w(\underline{r} - \underline{r}_a, h) d\underline{r} \underline{n}_s =: \sum_{s \in \mathcal{S}} \nabla\gamma_{as}. \quad (2.105)$$

This equation means that  $\nabla\gamma_a$  for particle  $a$  is computed by summing the contributions from the boundary elements. Note that

$$\nabla\gamma_{as} = \int_{\Omega_a \cap \Omega} w(\underline{r} - \underline{r}_a, h) \underline{n}(\underline{r}) d\underline{r} \approx w_{as} \underline{n}_s S_s, \quad (2.106)$$

where  $S_s$  is the size of the boundary element  $s$ .

As this part of the calculation is quite critical, due to numerical errors accumulating in the time-integration described in the next section, it is necessary to calculate the value of  $\nabla\gamma_{as}$  analytically. The formula for the Wendland kernel (2.63) is given by Ferrand *et al.* (2012) as

$$\begin{aligned} \nabla\gamma_{as} = & \frac{q_2 \cos \alpha_2}{\pi} P(q_2) - \frac{q_1 \cos \alpha_1}{\pi} P(q_1) + \frac{q_0^4}{\pi} \left( \frac{105}{64} + \frac{35}{512} q_0^2 \right) \cdot \quad (2.107) \\ & \left[ \text{sign}(q_2 \cos \alpha_2) \ln \left( \frac{q_2 + |q_2 \cos \alpha_2|}{|q_0|} \right) - \right. \\ & \left. \text{sign}(q_1 \cos \alpha_1) \ln \left( \frac{q_1 + |q_1 \cos \alpha_1|}{|q_0|} \right) \right], \end{aligned}$$

where

$$\begin{aligned} P(q) = & \frac{7}{129} q^5 - \frac{21}{64} q^4 + \frac{35}{32} q^3 - \frac{35}{24} q^2 + \frac{7}{4} + \quad (2.108) \\ & q_0^2 \left( \frac{35}{768} q^3 - \frac{7}{16} q^2 + \frac{105}{64} q - \frac{35}{12} \right) + \\ & q_0^4 \left( \frac{35}{512} q - \frac{7}{8} \right), \end{aligned}$$

and  $q_0$  is the normal distance of particle  $a$  to the boundary element  $s$ ,  $q_i = \|r_{v_i} - r_a\|$  where  $v_i$  are the two vertices connected to segment  $s$  and  $\alpha_i$  is the inclined angle between  $q_0$  and  $q_i$  (measured anti-clockwise). All these distances are illustrated in Figure 2.4.

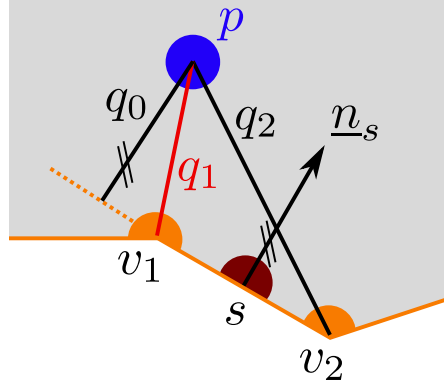


Figure 2.4: Illustration of distances.

As the vertex particles are taken into account in the modified discrete SPH interpolation given by Eq. (2.102) it is necessary to calculate their volume  $V_v$ . The volume depends on the angle with which the two adjacent line segments are inclined. This is denoted by  $\theta$  in Figure 2.3. Then  $V_v = \theta/2\pi V_a$  and as the density close to a wall is assumed to be uniform the mass  $m_v$  of an edge particle is given by  $m_v = \theta/2\pi m_a$ . A boundary element has no mass and its virtual position is assumed to be located at the centroid.

### 2.3.2.2 Governing equation for $\gamma$

After calculating the gradient of  $\gamma$  all that remains is to calculate  $\gamma$  itself. As Ferrand (2010) shows this can be achieved by using a governing equation. Thus, it is necessary to analyse how the value of  $\gamma$  changes for a fluid particle once it is close to a boundary. By definition,

$$\frac{d\gamma}{dt} = \frac{\partial\gamma}{\partial t} + \underline{v} \cdot \underline{\nabla}\gamma. \quad (2.109)$$

The first term on the right hand side requires further investigation.

$$\frac{\partial\gamma_a}{\partial t} = \frac{\partial}{\partial t} \int_{\Omega} w(\underline{r} - \underline{r}_a, h) dV \quad (2.110)$$

$$= \int_{\Omega} \frac{\partial w(\underline{r} - \underline{r}_a, h)}{\partial t} dV, \quad (2.111)$$

assuming  $\Omega$  does not change as  $\delta t \rightarrow 0$ . Note that  $\frac{\partial w(\underline{r} - \underline{r}_a, h)}{\partial t}$  is equal to zero. This immediately leads to

$$\frac{d\gamma}{dt} = \underline{v} \cdot \underline{\nabla}\gamma, \quad (2.112)$$

As the gradient of  $\gamma$  is zero whenever  $\partial\Omega \cap \Omega_a$  is empty for a particle  $a$  it can be concluded that

$$\begin{aligned} \gamma_a &= 1 && \text{if } \partial\Omega \cap \Omega_a = \emptyset \\ \frac{d\gamma_a}{dt} &= \underline{v}_a \cdot \underline{\nabla}\gamma_a && \text{else.} \end{aligned} \quad (2.113)$$

If the wall is moving then the velocity  $\underline{v}_a$  of a particle needs to be determined in the reference frame of the wall. To avoid any confusion we call this velocity  $v_a^{\mathcal{R}}$ . It is given as

$$\underline{v}_a^{\mathcal{R}} = \underline{v}_a - \underline{v}_w - \underline{\Omega}_w \times (\underline{r}_a - \underline{r}_w), \quad (2.114)$$

where  $\underline{r}_w$  is the centre of rotation of a moving wall,  $\underline{\Omega}_w$  the angular velocity vector and  $\underline{v}_w$  the velocity of the centre of rotation. As shown above  $\underline{\nabla}\gamma_a$  can be estimated as a sum from multible segments to yield

$$\begin{aligned} \gamma_a &= 1 && \text{if } \partial\Omega \cap \Omega_a = \emptyset \\ \frac{d\gamma_a}{dt} &= \sum_{s \in \mathcal{S}} \underline{v}_a^{\mathcal{R}_s} \cdot \underline{\nabla}\gamma_{as} && \text{else.} \end{aligned} \quad (2.115)$$

**Initializing  $\gamma$ :** To initialize  $\gamma$  at the beginning of a simulation each particle close to a boundary (*i.e.*  $\underline{\nabla}\gamma_a > 0$ ) is moved to an area where  $\gamma = 1$ . The easiest way to obtain this is to use the following transformation

$$\underline{r}_a = \underline{r}_a^0 + l \frac{\underline{\nabla}\gamma_a^0}{\|\underline{\nabla}\gamma_a^0\|}, \quad (2.116)$$

where  $l = 2R$  with  $R$  being the radius of the kernel. Now the particles are moved back to their original positions  $\underline{r}_a^0$  using Eq. (2.115).

### 2.3.2.3 Derivation of gradient and divergence

In his work Ferrand (2010) describes two different approaches to obtain an SPH gradient incorporating  $\gamma$ . Although the first one by Kulasegaram *et al.* (2004) is not used eventually it provides important insight into the Lagrangian formulation which is of use herein. The second gradient is based on an idea by De Lefte *et al.* (2009) and provides a correct repulsive force for boundary particles.

**The divergence:** Eq. (2.102) yields with  $f = \rho$  and assuming that  $\rho_a = \langle \rho \rangle_a^\gamma$

$$\rho_a = \frac{1}{\gamma_a} \sum_{b \in \mathcal{P}} V_b \rho_b w_{ab}, \quad (2.117)$$

which can be simplified to

$$\rho_a = \frac{1}{\gamma_a} \sum_{b \in \mathcal{P}} m_b w_{ab}. \quad (2.118)$$

Bringing  $\gamma$  to the other side and differentiating with respect to time yields

$$\frac{d\gamma_a \rho_a}{dt} = \frac{d}{dt} \left( \sum_{b \in \mathcal{P}} m_b w_{ab} \right), \quad (2.119)$$

or subsequently

$$\frac{d\rho_a}{dt} = \frac{1}{\gamma_a} \frac{d}{dt} \left( \sum_{b \in \mathcal{P}} m_b w_{ab} \right) - \frac{1}{\gamma_a} \rho_a \frac{d\gamma_a}{dt}. \quad (2.120)$$

Observing that the mass is constant and using Eq. (2.113) (for non-moving walls) this can be furthermore written as

$$\frac{d\rho_a}{dt} = \frac{1}{\gamma_a} \sum_{b \in \mathcal{P}} m_b \frac{dw_{ab}}{dt} - \frac{1}{\gamma_a} \rho_a \underline{v}_a \cdot \underline{\nabla} \gamma_a \quad (2.121)$$

$$= \frac{1}{\gamma_a} \sum_{b \in \mathcal{P}} m_b \frac{dr_{ab}}{dt} \cdot \frac{dw_{ab}}{dr_a} - \frac{1}{\gamma_a} \rho_a \underline{v}_a \cdot \underline{\nabla} \gamma_a. \quad (2.122)$$

Note that for arbitrary moving walls Eq. (2.115) needs to be applied. However, as the derivation by Ferrand (2010) is followed, this is neglected.

Finally

$$\frac{d\rho_a}{dt} = \frac{1}{\gamma_a} \sum_{b \in \mathcal{P}} m_b \underline{v}_{ab} \cdot \underline{\nabla}_a w_{ab} - \frac{1}{\gamma_a} \rho_a \underline{v}_a \cdot \underline{\nabla} \gamma_a, \quad (2.123)$$

where  $\underline{v}_{ab} = \underline{v}_a - \underline{v}_b$ .

The above equation is then a discretised version of the continuity equation (Eq. (2.9)).

Thus we can rewrite the above as

$$\frac{d\rho_a}{dt} = -\rho_a \mathbf{Div}_a^{\gamma, K}(\underline{v}), \quad (2.124)$$

with

$$\mathbf{Div}_a^{\gamma, K}(\underline{v}) := -\frac{1}{\gamma_a \rho_a} \sum_{b \in \mathcal{P}} m_b \underline{v}_{ab} \cdot \underline{\nabla}_a w_{ab} + \frac{1}{\gamma_a} \underline{v}_a \cdot \underline{\nabla} \gamma_a. \quad (2.125)$$

The superscript  $K$  stands for "Kulasegaram".

**Gradient based on variational principle:** To find a formulation for the gradient the divergence  $\mathbf{Div}^{\gamma, K}$  is used and multiplied with a vector field via the scalar product. Considering the skew-adjoint property that is valid for operators that solve the NS

equations the following gradient is obtained

$$\mathbf{Grad}_a^{\gamma,K}(f) := \rho_a \sum_{b \in \mathcal{P}} m_b \left( \frac{f_a}{\gamma_a \rho_a^2} + \frac{f_b}{\gamma_b \rho_b^2} \right) \nabla_a w_{ab} - \frac{1}{\gamma_a} f_a \nabla \gamma_a. \quad (2.126)$$

Ferrand (2010) proves the skew-adjoint property in his appendix. Note that due to this property the momentum equation discretised by the above gradient and the continuity equation as given by Eq. (2.118) fulfil the Calculus of Variations as shown in Section 2.1.3.

**Gradient based on interpolation:** The above gradient is not accurate as a boundary term is missing and thus De Lefe *et al.* (2009) proposed an alternate way of deriving a gradient starting with the continuous SPH approximation Eq. (2.103) and following the route of Section 2.2.3. Approximating a derivative and using the product rule as well as the Stoke's Theorem gives

$$\langle \nabla f \rangle_a^{c,\gamma} = \frac{1}{\gamma_a} \int_{\Omega} f(\underline{r}) \nabla_a w(\underline{r} - \underline{r}_a, h) d\underline{r} - \frac{1}{\gamma_a} \int_{\partial\Omega} f(\underline{r}) w(\underline{r} - \underline{r}_a, h) \underline{n} d\underline{r}. \quad (2.127)$$

As already noted by Monaghan (1988) it is of advantage with respect to the conservation properties to use  $\nabla f = \rho \nabla \frac{f}{\rho} + \frac{f}{\rho} \nabla \rho$  (Eq. (2.75) with  $k = 1$ ) which yields

$$\begin{aligned} \langle \nabla f \rangle_a^{c,\gamma} &= \frac{1}{\gamma_a} \int_{\Omega} \rho_a \rho(\underline{r}) \left( \frac{f(\underline{r})}{\rho(\underline{r})^2} + \frac{f_a}{\rho_a^2} \right) \nabla w(\underline{r} - \underline{r}_a, h) d\underline{r} \\ &\quad - \frac{1}{\gamma_a} \int_{\partial\Omega} \rho_a \rho(\underline{r}) \left( \frac{f(\underline{r})}{\rho(\underline{r})^2} + \frac{f_a}{\rho_a^2} \right) w(\underline{r} - \underline{r}_a, h) \underline{n} d\underline{r}. \end{aligned} \quad (2.128)$$

Discretizing the above equations finally gives

$$\mathbf{Grad}_a^{\gamma,F}(f) = \frac{\rho_a}{\gamma_a} \sum_{b \in \mathcal{P}} m_b \left( \frac{f_a}{\rho_a^2} + \frac{f_b}{\rho_b^2} \right) \nabla w_{ab} - \frac{\rho_a}{\gamma_a} \sum_{s \in \mathcal{S}} \left( \frac{f_a}{\rho_a^2} + \frac{f_s}{\rho_s^2} \right) \rho_s \nabla \gamma_{as}. \quad (2.129)$$

The superscript  $F$  stands for "Ferrand" since he demonstrated the superiority of (2.129) over (2.126). As described by Ferrand (2010) the gradient operators described in this and the previous section are equal inside the fluid. However, close to the boundary there is a fundamental difference which produces wrong results in the case of the Kulasegaram gradient  $\mathbf{Grad}^{\gamma,K}$ . On the other hand the Gradient  $\mathbf{Grad}^{\gamma,F}$  gives the correct results, but it is no longer skew-adjoint to the divergence that results from the continuity equation Eq. (2.118).

### 2.3.2.4 Second order operators

To approximate operators of the form  $\underline{\nabla} \cdot (f \underline{\nabla} \otimes \underline{B})$  a correction along the boundaries is also required. In Section 2.2.4 the second-order derivative was derived from a divergence with positive sign. The divergence presented in the previous section however,  $\mathbf{Div}^{\gamma, K}$  has a negative sign. In a continuous setting the following holds

$$\langle \underline{\nabla}(f \underline{\nabla} \otimes \underline{B}) \rangle_a^{c, \gamma} = \langle f_a \underline{\nabla}_a \otimes \underline{B} \cdot \underline{\nabla}(1) + \underline{\nabla} \cdot (f \underline{\nabla} \otimes \underline{B}) \rangle_a^{c, \gamma} \quad (2.130)$$

$$\begin{aligned} &= \frac{1}{\gamma_a} \int_{\Omega} (f_a \underline{\nabla}_a \otimes \underline{B}(r) + (f \underline{\nabla} \otimes \underline{B})(r)) \cdot \underline{\nabla} w(r - r_a, h) dr \\ &\quad - \frac{1}{\gamma_a} \int_{\partial\Omega} (f_a \underline{\nabla}_a \otimes \underline{B}(r) + (f \underline{\nabla} \otimes \underline{B})(r)) \cdot \underline{n} w(r - r_a, h) dr. \end{aligned} \quad (2.131)$$

The first term in the equation above can be discretised by using the Taylor expansion. The boundary integral can be approximated by

$$- \frac{2}{\gamma_a} \int_{\partial\Omega} (f \underline{\nabla} \otimes \underline{B})(r) \cdot \underline{n} w(r - r_a, h) dr, \quad (2.132)$$

in case of  $f \underline{\nabla} \otimes \underline{B}$  being continuous close to the wall so that

$$(f \underline{\nabla} \otimes \underline{B})_a \approx (f \underline{\nabla} \otimes \underline{B})(r) \quad \forall r \in \partial\Omega : w(r - r_a, h) > 0. \quad (2.133)$$

A full discretization using Morris' second-order term as given by Eq. (2.95) finally yields the "Laplacian" operator as

$$\begin{aligned} \mathbf{Lap}_a^F(f, \underline{B}) &= \langle \underline{\nabla} \cdot (f \underline{\nabla} \otimes \underline{B}) \rangle_a^\gamma \\ &= \frac{\rho_a}{\gamma_a} \sum_{b \in \mathcal{P}} m_b \frac{f_a + f_b}{\rho_a \rho_b} \frac{\underline{B}_{ab}}{\|r_{ab}\|^2} r_{ab} \cdot \underline{\nabla}_a w_{ab} \\ &\quad - \frac{2}{\gamma_a} \sum_{s \in \mathcal{S}} f_s \frac{\partial \underline{B}_s}{\partial \underline{n}_s} \|\underline{\nabla} \gamma_{as}\|, \end{aligned} \quad (2.134)$$

where  $\frac{\partial \underline{B}_s}{\partial \underline{n}_s} = (\underline{\nabla}_s \otimes \underline{B}) \cdot \underline{n}_s$ . When multiplied by  $f$  the second term is the flux of  $\underline{B}$  through the wall. If  $\underline{B}$  is a velocity and  $f$  the dynamic viscosity then the flux represents the wall shear stress.

As mentioned before in the turbulent case with varying  $\mu$  Eq. (2.100) with  $\underline{B} = \underline{v}$  and  $f = \mu$  needs to be used to discretise the viscous term. Following the same procedure as above a similar boundary term can be calculated for Eq. (2.100). However, due to  $\underline{\nabla} \otimes \underline{v} \cdot \underline{n} = 0$  it is exactly the same boundary term as in Eq. (2.135).

### 2.3.2.5 Prescribing boundary conditions

Dirichlet boundary conditions can be implemented simply by setting the desired value to all vertices  $\mathcal{V}$  and boundary-elements  $\mathcal{S}$ .

Neumann boundary conditions are not as straightforward. Assume that the value of a function  $f$  at the boundary is given by

$$\frac{\partial f}{\partial \underline{n}} = 0. \quad (2.135)$$

Again vertices  $\mathcal{V}$  and boundary-elements  $\mathcal{S}$  need to be considered. First the density of the vertex particles can be obtained up to first-order by

$$f_v = \frac{1}{\alpha_v} \sum_{b \in \mathcal{F}} V_b f_b w_{vb}, \quad (2.136)$$

where

$$\alpha_v := \sum_{b \in \mathcal{F}} V_b w_{qb}. \quad (2.137)$$

The values for the boundary elements could be calculated in a similar fashion. However, to increase computational efficiency their density can be defined as the arithmetic mean of its neighbouring vertex particles, *i.e.*

$$f_s = \frac{f_{v_1} + f_{v_2}}{2}. \quad (2.138)$$

In the case of second-order operators the Neumann boundary conditions can be prescribed in (2.135), the quantity of  $f_s \frac{\partial \underline{B}_s}{\partial \underline{n}_s}$  representing the prescribed flux of  $\underline{B}$  through the wall at point  $s$ .

### 2.3.3 Application to the Navier Stokes equations

The following section describes the application of the theoretical considerations presented above to the NS equations. Although only the special case of the unified semi-analytical boundary conditions is presented, the principles are fairly general.

The Euler equations (inviscid NS equations, Eq. (2.7)) are discretised using the gradient defined by Eq. (2.129) which gives

$$\frac{dv_a}{dt} = -\frac{1}{\rho_a} \mathbf{Grad}_a^{\gamma, F}(p) + \underline{g} \quad \forall a \in \mathcal{F}. \quad (2.139)$$

On solid walls  $\underline{v} = 0$  for all vertex particles and boundary elements. No specific treatment is used for the free-surface.

To close the system of equations a continuity equation is necessary. Instead of using the

time-dependent formulation based on the divergence (see Eq. (2.124)) the equivalent time-independent version is often used which was already described in Eq. (2.118). However, in this case it turns out that a free-surface correction is necessary as detailed by Ferrand *et al.* (2012). The issue comes from the fact that  $\gamma$  is equal to unity at the free-surface despite the fact that the kernel support is not fully populated. In order to compensate this the following modified equation was proposed by Ferrand *et al.* (2012)

$$\rho_a = \frac{1}{\beta_a \gamma_a + (1 - \beta_a) \alpha_a} \sum_{b \in \mathcal{P}} m_b w_{ab} \quad \forall a \in \mathcal{F}, \quad (2.140)$$

where  $\alpha_a$  is the Shepard filter given as

$$\alpha_a = \sum_{b \in \mathcal{P}} \frac{m_b}{\rho_b} w_{ab}, \quad (2.141)$$

and  $\beta_a$  is defined to be

$$\beta_a = \exp \left\{ -K \left[ \min \left( \frac{\alpha_a}{\gamma_a}, 1 \right) - 1 \right]^2 \right\}, \quad (2.142)$$

where  $K = 30000$  is an arbitrary high value. The boundary condition for the density  $\rho$  is given by  $\partial \rho / \partial \underline{n} = 0$  and the values can thus be calculated according to Eq. (2.136). The pressure  $p$  can be determined via the Equation of State as given by Eq. (2.11). The boundary condition on the pressure is given by

$$\frac{\partial}{\partial \underline{n}} \left( \frac{p}{\rho} - \underline{g} \cdot \underline{r} + \frac{v^2}{2} \right) = 0. \quad (2.143)$$

This can be discretised using the same principles as for the density. Note that in practice the  $\underline{v}^2$  term can be neglected as the velocity close to the boundary is small compared to the other terms.

Finally,  $\gamma$  is calculated by Eq. (2.115) which closes the set of discretised equations.

To obtain the full viscid NS equations the viscous term needs to be discretized as well. In the laminar case the corrected second-order term based on the operator (2.135) is used. Thus the viscous term then reads

$$\begin{aligned} \left\langle \frac{1}{\rho} \underline{\nabla} \cdot (\mu \underline{\nabla} \otimes \underline{v}) \right\rangle_a &= \frac{1}{\gamma_a} \sum_{b \in \mathcal{P}} m_b \frac{\mu_a + \mu_b}{\rho_a \rho_b} \frac{\underline{v}_{ab}}{\|\underline{r}_{ab}\|^2} \underline{r}_{ab} \cdot \underline{\nabla}_a w_{ab} \\ &\quad - \frac{2}{\gamma_a \rho_a} \sum_{s \in \mathcal{S}} \mu_s \frac{\partial \underline{v}_s}{\partial \underline{n}_s} \|\underline{\nabla} \gamma_{as}\|. \end{aligned} \quad (2.144)$$

The shear stress normal to the wall is given by

$$\mu \frac{\partial v}{\partial n} = \rho \|\underline{v}_\tau\| \underline{v}_\tau, \quad (2.145)$$

where  $\underline{v}_\tau$  is the friction velocity. In the case of laminar flow this is given by

$$\|\underline{v}_\tau\| \underline{v}_\tau = \frac{\nu \underline{v}(y)}{y}, \quad (2.146)$$

where  $y$  is the distance from the wall and  $\nu = \mu/\rho$ . This equation only holds for  $y \ll L$ , where  $L$  is a characteristic length-scale of the flow geometry. Thus the viscous term is given by

$$\begin{aligned} \mathbf{Lap}_a^{\gamma, F}(\mu, \underline{v}) &= \frac{1}{\gamma_a} \sum_{b \in \mathcal{P}} m_b \frac{\mu_a + \mu_b}{\rho_a \rho_b} \frac{\underline{v}_{ab}}{\|\underline{r}_{ab}\|^2} \underline{r}_{ab} \cdot \nabla_a w_{ab} \\ &\quad - \frac{2\nu_a \underline{v}_a}{\gamma_a} \sum_{s \in \mathcal{S}} \frac{\|\nabla \gamma_{as}\|}{\delta r_{as}}, \end{aligned} \quad (2.147)$$

where

$$\delta r_{as} = \max(\underline{r}_{as} \cdot \underline{n}_s; \delta r), \quad (2.148)$$

with  $\delta r$  being a small number greater than zero to avoid division by zero. Ferrand (2010) uses the initial particle spacing as  $\delta r$ . The main term of Eq. (2.147) contains an  $\|\underline{r}_{ab}\|^2$  which can be zero. This is avoided by adding  $10^{-4}h^2$  to the norm. It is not clear how these arbitrarily chosen values affect the outcome of the simulations.

When the above viscous term is included in the time-discretised equations the velocity of the boundary term appears explicitly. This can be used to make this term implicit as pointed out by Ferrand (2010).

Alternatively the second-order term by Violeau (Eq. (2.100)) can be used to discretise the viscous term in the case of turbulent flow. Again the boundary term needs to be added and in the case of turbulence the friction velocity needs to be modified in order to satisfy the log law. The influence of the choice of the discretization of the Laplacian for turbulent flows is discussed later.

Finally, the discrete NS equations can be written as

$$\frac{d\underline{v}_a}{dt} = -\frac{1}{\rho_a} \mathbf{Grad}_a^{\gamma, F}(p) + \mathbf{Lap}_a^{\gamma, F}(\mu, \underline{v}) + \underline{g} \quad (2.149)$$

## 2.4 Time-integration

The last step to a full discretisation of the NS equations is to find a suitable time-integration scheme. In the following a simple physical system is considered that consists

of the following coupled partial differential equations (the particle label  $a$  is dropped here for the sake of simplicity)

$$\frac{d\underline{v}}{dt} = F(\underline{r}), \quad (2.150)$$

$$\frac{d\underline{r}}{dt} = G(\underline{v}), \quad (2.151)$$

where  $F$  is given by (2.149) and  $G = id$ , with  $id$  being the identity function.

The forward Euler scheme is then given by

$$\underline{v}^{n+1} = \underline{v}^n + \delta t^n F(\underline{r}^n), \quad (2.152)$$

$$\underline{r}^{n+1} = \underline{r}^n + \delta t^n G(\underline{v}^n), \quad (2.153)$$

where  $\delta t^n$  is the size of the  $n$ -th time-step and

$$\underline{v}^n := \underline{v}(t = \sum_{i=1}^n \delta t^i). \quad (2.154)$$

This scheme is first-order accurate and explicit. Similarly the following semi-implicit scheme can be used

$$\underline{v}^{n+1} = \underline{v}^n + \delta t^n F(\underline{r}^n), \quad (2.155)$$

$$\underline{r}^{n+1} = \underline{r}^n + \delta t^n G(\underline{v}^{n+1}), \quad (2.156)$$

which makes use of the fact that  $\underline{v}^{n+1}$  is already calculated. For a more detailed discussion on these schemes see Violeau (2012). It can be shown that the semi-implicit scheme is optimal in a way that it can be derived from the discrete-in-time Hamiltonian which corresponds to conservation principles. Schemes that fulfil this property are called symplectic. The semi-implicit scheme presented above is first-order accurate as well. The second-order accurate symplectic scheme is commonly called Leap-Frog. It is given by

$$\underline{v}^{n+1/2} = \underline{v}^{n-1/2} + \delta t F(\underline{r}^n), \quad (2.157)$$

$$\underline{r}^{n+1} = \underline{r}^n + \delta t G(\underline{v}^{n+1/2}), \quad (2.158)$$

Another interesting feature of these schemes is that in the absence of friction forces they are time-reversible and thus conserve the energy.

Besides these, there are several non-symplectic but higher-order schemes Leimkuhler and Reich (2004) that are frequently used in SPH simulations. Amongst them are Runge-Kutta schemes as well as the Beeman algorithm (Capone *et al.* (2007)).

This section is now concluded by giving the time-integration algorithm used by Ferrand (2010) for the NS equations

$$\begin{aligned}
\underline{v}_a^{n+1} &= \underline{v}_a^n - \frac{\delta t}{\rho_a^n} \left( \mathbf{Grad}_a^{\gamma, F}(p^n) + \mathbf{Lap}_a^{\gamma, F}(\mu, \underline{v}) + \rho_a^n \underline{g} \right), \\
\underline{r}_a^{n+1} &= \underline{r}_a^n + \delta t \underline{v}_a^{n+1}, \\
\gamma_a^{n+1} &= \gamma_a^n + \frac{\delta t}{2} \sum_{s \in \mathcal{S}} (\nabla \gamma_{as}^n + \nabla \gamma_{as}^{n+1}) \cdot (\underline{v}_a^{\mathcal{R}_s})^{n+1}, \\
\rho_a^{n+1} &= \frac{1}{\gamma_a^{n+1}} \sum_{b \in \mathcal{P}} m_b w_{ab}^{n+1}.
\end{aligned} \tag{2.159}$$

This clearly originates from the semi-implicit, symplectic, first-order scheme. Note, that the integration of  $\gamma$  is modified such that it is of second order, as the gradient of  $\gamma$  is averaged between two successive time-steps. The full NS equations destroy the time-reversible nature of this system due to the added viscous term.

#### 2.4.1 Time-step restrictions

In order to guarantee numerical stability the time-step  $\delta t$  has to obey certain restrictions (see *e.g.* Violeau (2012)). There are three restrictions that apply to every SPH simulation. The first is the Courant-Friedrichs-Lewy (CFL) condition (Courant *et al.*, 1928) which is given by

$$\delta t_{CFL} = 0.4 \frac{h}{c_0}, \tag{2.160}$$

where  $c_0$  is the speed of sound.

The viscous forces impose that  $\delta t$  is smaller than

$$\delta t_{visc} = \frac{1}{8} \min_{a \in \mathcal{P}} \left( \frac{h^2}{\nu_a} \right). \tag{2.161}$$

The last of the three is the maximum time-step due to acceleration which is given by

$$\delta t_{force} = \frac{1}{4} \min_{a \in \mathcal{P}} \sqrt{\frac{h}{\|F_a\|}}, \tag{2.162}$$

where  $F$  is the acceleration due to pressure and gravity. The coefficients in Eqs. (2.160) to (2.162) are taken from Morris *et al.* (1997). Violeau and Leroy (2014) investigate the time step conditions both analytically in the unbounded case and using numerical experiments in the wall-bounded case. They show that the factor 0.4 in the CFL condition (Eq. (2.160)) can safely be increased to 0.8 which is used in the following. Finally, the introduction of the governing equation for  $\gamma$  calls for an additional condition

given by

$$\delta t_\gamma = C \frac{1}{\max_{a \in \mathcal{P}, s \in \mathcal{S}} (|\nabla^n \gamma_{as} \cdot (\underline{v}_a^{\mathcal{R}_s})^n|)}, \quad (2.163)$$

where the factor of  $C = 0.005$  stems from numerical experience according to Ferrand (2010).

The time-step  $\delta t$  is thus given by

$$\delta t = \min(\delta t_{CFL}, \delta t_{visc}, \delta t_{force}, \delta t_\gamma). \quad (2.164)$$

## Chapter 3

# Investigation of the boundary conditions in two dimensions

Despite its ability to predict flows with good accuracy, SPH with the semi-analytical wall boundary conditions presented in Section 2.3.2 still suffers from numerical drawbacks. This can be observed, for example, when considering the energy budget from an inviscid flow between two infinite plates. As the energy is not constant the skew-adjoint principle is violated thus warranting an investigation of this property with respect to the semi-analytical wall boundary conditions. In addition to a theoretical analysis a numerical simulation shows stability issues associated with this property. This leads to the question of whether it is possible to counter the instabilities by some numerical procedure. If a diffusion term is chosen, as in this work, then its properties and influence on the fluid flow need to be investigated. The question of how to impose a volume flux or specific boundary conditions are also closely linked to modelling wall boundary conditions. In free-surface flows certain difficulties can occur which are not apparent in confined flows. To solve these, it is necessary to revisit certain investigations by separating hydrostatic and dynamic pressure differences.

In the following section the wall boundary conditions are introduced in detail and are then investigated with respect to the skew-adjoint property in Section 3.1. This is done by considering analytical as well as numerical calculations. The instabilities that are observed are then treated by using a volume diffusion term that is derived from turbulent Reynolds-averaged considerations and implemented into the continuity equation. This term is related to an approximate Riemann solver proposed by Ferrari *et al.* (2009) and adapted to the present wall boundary conditions.

The next two sections deal with improvements regarding the imposition of boundary values. In Section 3.3 a new formula for imposing a non-constant driving force based on a volume flux is introduced and compared to a standard formulation. Subsequently,

the method of imposing Neumann wall boundary conditions is generalized to Robin boundary conditions and arbitrary orders of accuracy. A wave equation with Robin boundary conditions is solved numerically in order to demonstrate the capability of the present model.

The last theoretical contribution presented in this chapter deals with minor modifications to the volume diffusion term as well as the wall boundary conditions to take external forces, *e.g.* gravity, into account. These two modifications are validated by two still water simulations.

Finally, the present methodology is applied to a violent free-surface flow, a schematic dam-break over a wedge. Quantitative comparison of wall pressure forces is made with respect to other numerical formulations including a Volume-of-Fluid method and it is shown that the volume diffusion term avoids using any free-surface correction in the continuity equation as required in previous work by Ferrand *et al.* (2012).

### 3.1 On the skew-adjoint property including boundaries

#### 3.1.1 Theoretical investigation

Now, new developments are presented in order to better understand and improve the model by Ferrand *et al.* (2012) presented in Section 2.3.2. The boundary corrected formulation has already been theoretically investigated by Macià *et al.* (2012) with respect to its approximation property in 1-D. The goal of this section is to investigate another aspect of this formulation which is the energy conservation.

In this section the focus is on the property of skew-adjointness of the two arbitrary (discrete or continuous) operators **Grad** and **Div**. These two operators are skew-adjoint if, and only if,

$$\langle \mathbf{Grad}(f), \underline{B} \rangle = - \langle f, \mathbf{Div}(\underline{B}) \rangle, \quad (3.1)$$

where  $\langle \rangle$  are the respective  $L^2$  scalar products and  $f$  and  $\underline{B}$  are arbitrary scalar and vector fields, respectively. Before starting the actual investigation the importance of this property shall be highlighted. Consider a system of particles representing a fluid without external influence nor dissipative forces, then its energy is given by

$$E = E_{kin} + E_{int} = \sum_{a \in \mathcal{P}} m_a \left( \frac{1}{2} \|\underline{v}_a\|^2 + e_{int,a}(\rho_a) \right), \quad (3.2)$$

where  $E_{kin}$  and  $E_{int}$  are the total kinetic and internal energy respectively, while  $e_{int,a}$  is the specific internal energy of particle  $a$ . The time derivative of the kinetic energy is given by

$$\frac{dE_{kin}}{dt} = \sum_{a \in \mathcal{P}} m_a \underline{v}_a \cdot \frac{d\underline{v}_a}{dt} = - \sum_{a \in \mathcal{P}} m_a \underline{v}_a \cdot \frac{1}{\rho_a} \mathbf{Grad}_a(p), \quad (3.3)$$

where the Euler momentum equation was used, *i.e.* Eq. (2.6) without the **Lap** and  $\underline{g}$  terms. The time derivative of the internal energy can in turn be written as

$$\frac{dE_{int}}{dt} = \sum_{a \in \mathcal{P}} m_a \left( \frac{\partial e_{int}}{\partial \rho} \right)_a \frac{d\rho_a}{dt} = \sum_{a \in \mathcal{P}} \frac{m_a p_a}{\rho_a^2} \frac{d\rho_a}{dt}, \quad (3.4)$$

where the last equality follows from thermodynamic principles that relate the internal energy per unit mass to pressure and density via  $p = \rho^2 de_{int}/d\rho$ . Looking at the time derivative of the total energy one thus obtains with the help of the continuity equation (Eq. (2.124)):

$$\frac{dE}{dt} = - \sum_{a \in \mathcal{P}} V_a \underline{v}_a \cdot \mathbf{Grad}_a(p) - \sum_{a \in \mathcal{P}} V_a p_a \mathbf{Div}_a(\underline{v}). \quad (3.5)$$

Written in notation with discrete scalar products this yields

$$\frac{dE}{dt} = - \langle \mathbf{Grad}_a(p), \underline{v}_a \rangle - \langle p_a, \mathbf{Div}_a(\underline{v}) \rangle. \quad (3.6)$$

This shows that the energy is exactly conserved if the two discrete differential operators **Grad** and **Div** are skew-adjoint (Eq. (3.1)), *i.e.* if the right-hand-side of (3.6) is equal to zero. This property is natural, since the same occurs with ordinary differential operators when changing the discrete sums with integrals (see *e.g.* Violeau (2012))

Skew-adjoint operator definition: 
$$\underbrace{\langle \nabla f, \underline{B} \rangle + \langle f, \nabla \cdot \underline{B} \rangle}_{=: SA} = - \int_{\partial\Omega} f(\underline{r}) \underline{B}(\underline{r}) \cdot \underline{n}(\underline{r}) d\underline{r}. \quad (3.7)$$

If  $f = p$  and  $\underline{B} = \underline{v}$ , the pressure and velocity, respectively, which solve the Navier-Stokes equations, then the right-hand side is equal to zero. This is due to  $p = 0$  at a free-surface and  $\underline{v} \cdot \underline{n} = 0$  at a solid wall. It would thus be advantageous if the SPH operators adhere to this property.

The investigation into skew-adjoint operators commences by first considering basic continuous SPH operators without boundary terms, *i.e.* using integrals instead of discrete sums and assuming that no boundaries are present. The operators under investigation are given by

$$\mathbf{Grad}_a^{b,c}(f) = \int_{\Omega} f_b \nabla_a w_{ab} d\underline{r}_b \quad (3.8)$$

$$\mathbf{Div}_a^{b,c}(\underline{B}) = \int_{\Omega} \underline{B}_b \cdot \nabla_a w_{ab} d\underline{r}_b, \quad (3.9)$$

where the superscript  $b$  stands for “basic” in the sense that it is the SPH operator which can be derived directly from the interpolation without the addition of any other terms. The superscript  $c$  stands for “continuous” similar to the SPH interpolation. The

left-hand side of the skew-adjoint operator definition (Eq. (3.7)) is then given by

$$SA = \int_{\Omega} \int_{\Omega} (f_b \underline{\nabla}_a w_{ab} \cdot \underline{B}_a + f_a \underline{B}_b \cdot \underline{\nabla}_a w_{ab}) \underline{dr}_b \underline{dr}_a. \quad (3.10)$$

Due to integral additivity it is possible to swap the dummy labels  $a, b$  in the second term which yields

$$SA = \int_{\Omega} \int_{\Omega} (f_b \underline{B}_a \cdot \underline{\nabla}_a w_{ab} + f_b \underline{B}_a \cdot \underline{\nabla}_b w_{ab}) \underline{dr}_b \underline{dr}_a. \quad (3.11)$$

The kernel isotropy result in the asymmetry of its gradient, *i.e.*  $\underline{\nabla}_a w_{ab} = -\underline{\nabla}_b w_{ab}$ , shows finally that  $SA = 0$ , *i.e.* that  $\mathbf{Grad}^{b,c}$  and  $\mathbf{Div}^{b,c}$  are skew-adjoint. Note that this property also holds true in the discrete case, where the integrals are replaced by sums, from the same properties.

Now the following symmetrized operators shall be defined:

$$\mathbf{Grad}_a^{s,c,k}(f) = \int_{\Omega} \frac{\rho_a^{2k} f_b + \rho_b^{2k} f_a}{\rho_a^k \rho_b^k} \underline{\nabla}_a w_{ab} \underline{dr}_b, \quad (3.12)$$

$$\mathbf{Div}_a^{s,c,k}(\underline{B}) = \frac{1}{\rho_a^{2k}} \int_{\Omega} \rho_a^k \rho_b^k (\underline{B}_b - \underline{B}_a) \cdot \underline{\nabla}_a w_{ab} \underline{dr}_b, \quad (3.13)$$

where the superscript  $s$  stands for “standard” and  $k$  is a power used to discuss a wide range of operators using a sole notation. Its effect is discussed in the following. Note, apart from the lack of boundary terms, the symmetrized gradient (3.12) differs from the discrete form (2.129) by the presence of density terms. Eq. (2.129) can be recovered by setting  $k = 1$ . The above operators in Equations (3.12) and (3.13) are skew-adjoint if the newly added terms have opposing signs. The proof, which is omitted, can be found in the book by Violeau (2012). As in the previous case it holds true in the discrete case also.

When removing the assumption of no boundaries the calculations are no longer as straightforward. Following a procedure similar to Section 2.3.2.3, in the vicinity of a boundary the operators of interest are given in continuous form by

$$\mathbf{Grad}_a^{\gamma,c,k}(f) = \frac{1}{\gamma_a} \int_{\Omega} \frac{\rho_a^{2k} f_b + \rho_b^{2k} f_a}{\rho_a^k \rho_b^k} \underline{\nabla}_a w_{ab} \underline{dr}_b \quad (3.14)$$

$$- \frac{1}{\gamma_a} \int_{\partial\Omega} \frac{\rho_a^{2k} f_b + \rho_b^{2k} f_a}{\rho_a^k \rho_b^k} \underline{n}_b w_{ab} \underline{dr}_b,$$

$$\mathbf{Div}_a^{\gamma,c,k}(\underline{B}) = \frac{1}{\gamma_a \rho_a^{2k}} \int_{\Omega} \rho_a^k \rho_b^k (\underline{B}_b - \underline{B}_a) \cdot \underline{\nabla}_a w_{ab} \underline{dr}_b \quad (3.15)$$

$$- \frac{1}{\gamma_a \rho_a^{2k}} \int_{\partial\Omega} \rho_a^k \rho_b^k (\underline{B}_b - \underline{B}_a) \cdot \underline{n}_b w_{ab} \underline{dr}_b,$$

where the superscript  $\gamma$  indicates the renormalization. Apart from the additional density terms in the denominator of the **Grad** operator, these formulae are the continuous analog to Eqs. (2.125) and (2.129) for  $k = 1$ . In Appendix A using the gradient and divergence given by Eqs. (3.14) and (3.15) the left-hand side of the skew-adjoint operator definition, Eq. (3.7), can be shown to reduce to

$$SA \xrightarrow{(h \rightarrow 0)} - \int_{\partial\Omega} f_a \underline{B}_a \cdot \underline{n}_a dr_a. \quad (3.16)$$

This is equivalent to Eq. (3.7) showing the skew-adjoint property for SPH continuous operators with boundary terms in case of the correct imposition of the boundary conditions in the limit  $h \rightarrow 0$ . Note that it is essential for this result that the operators are renormalized with  $\gamma$ . Furthermore, the process of taking the limit is only required due to the violation of the Kronecker delta property by the SPH interpolation.

The derivation shown in Appendix A could have been made significantly shorter, if we were only interested in continuous operators. However, the reason for explicitly going through this derivation was to show the steps necessary to prove the same in the case of discrete operators. It would thus be necessary to have a discrete version of the Stokes' theorem. Additionally, the Kronecker delta property is required, but that is violated even by the continuous SPH interpolation. The difficulty for a discrete Stokes' theorem is due to the fact that  $\underline{\nabla}\gamma$  is calculated analytically along the wall (see Section 2.3.2.1), whereas the volumetric integral over  $\underline{\nabla}w$  is approximated via a discrete sum.

As a consequence, discrete SPH operators with boundary terms as presented here are not exactly skew-adjoint contrary to continuous SPH operators. Inside the fluid, however, ( $\gamma = 1$ , no boundary terms) the skew-adjoint property is fulfilled in the discrete case as it is equivalent to the standard differential operators (**Div**<sup>s,c,k</sup>, **Grad**<sup>s,c,k</sup>) given by Eqs. (3.12) and (3.13).

Finally, the discretized forms of Eqs. (3.14) and (3.15) are given by

$$\mathbf{Grad}_a^{\gamma,k}(f) = \frac{1}{\gamma_a} \sum_{b \in \mathcal{P}} V_b \frac{\rho_a^{2k} f_b + \rho_b^{2k} f_a}{\rho_a^k \rho_b^k} \underline{\nabla}_a w_{ab} - \frac{1}{\gamma_a} \sum_{s \in \mathcal{S}} \frac{\rho_a^{2k} f_s + \rho_s^{2k} f_a}{\rho_a^k \rho_s^k} \underline{\nabla} \gamma_{as} \quad (3.17)$$

$$\begin{aligned} \mathbf{Div}_a^{\gamma,k}(\underline{B}) &= \frac{1}{\gamma_a \rho_a^{2k}} \sum_{b \in \mathcal{P}} V_b \rho_a^k \rho_b^k (\underline{B}_b - \underline{B}_a) \cdot \underline{\nabla}_a w_{ab} - \\ &\quad \frac{1}{\gamma_a \rho_a^{2k}} \sum_{s \in \mathcal{S}} \rho_a^k \rho_s^k (\underline{B}_s - \underline{B}_a) \cdot \underline{\nabla} \gamma_{as}. \end{aligned} \quad (3.18)$$

Note that these operators are a generalization from the ones derived by Ferrand *et al.* given by Eqs. (2.125) and (2.129) (where  $k = 1$ ). In the following  $k = 0$  is used unless otherwise noted. According to the authors' experience this choice has, at best, a marginal influence on the results.

### 3.1.2 A numerical experiment

As the above theoretical investigation indicates the SPH discrete operators for the semi-analytical boundary conditions are not skew-adjoint, and thus do not conserve total energy. Hence, a periodic flow between two infinite plates (at  $y = 0$  and  $y = h$ ) is used to address this issue from a numerical perspective. Equations (2.124) and (2.6) are solved with the pressure calculated via the equation of state (2.11) and the particles are moved according to  $dr_a/dt = \underline{v}_a$ . The viscosity is set to zero and the following velocity profile is used as the initial condition

$$v_x = 0, v_y = \frac{c_0}{10} \sin(4\pi y),$$

where  $c_0$  is the numerical speed of sound and  $y \in [0, 1]$ . The quantity of interest is the energy  $E$  which is defined by

$$E(t) = \sum_{n=1}^t (\langle \mathbf{Grad}^\gamma(p), \underline{v} \rangle + \langle p, \mathbf{Div}^\gamma(\underline{v}) \rangle)^n, \quad (3.19)$$

where the subscript  $n$  indicates the current time-step. The value of  $E$  is equal to the time integral of the left hand side of Eq. (3.7) and it is zero if the operators under investigation are skew-adjoint.

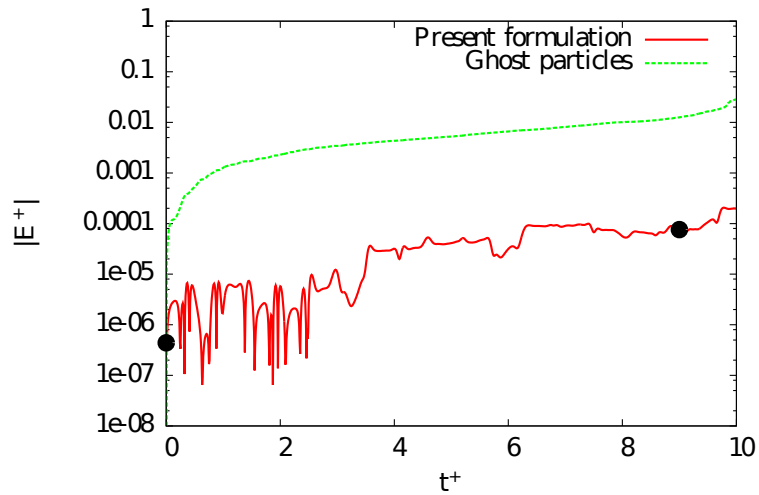


Figure 3.1: Non-dimensional energy budget over time  $t^+ = tc_0/h$  for ghost particles and present approach. Black dots correspond to time time instants in Figure 3.2.

In Figure 3.1 the non-dimensionalized value  $E^+ = E/(\rho_0 c_0^2 h^2)$  can be seen plotted over time for the present boundary condition as well as the ghost particle approach (Libersky *et al.* (1993)) using Eqs. (3.12) and (3.13) for the differential operators. The present boundary conditions feature a kernel renormalization factor, whereas the ghost

particle approach implements solid boundaries by mirroring particles on a wall. Two important features of this plot shall be highlighted. The first is that the value  $E$  is never zero, indicating that the operators are indeed not analytically skew-adjoint in cases where boundaries are present. Compared to the ghost particle formulation the energy introduced to the flow is lower with the present boundary conditions.

It shall be noted that this simulation was also run with the formulation by Kulasegaram *et al.* (2004) which resembles the present approach but, in contrast to the present method, is analytically skew-adjoint. However, as Ferrand *et al.* (2012) already pointed out, the operators by Kulasegaram lack a term in the gradient and thus do not represent the physics accurately. The simulation was also conducted with the formulation by Monaghan and Kajtar (2009) but the results were completely non-physical.

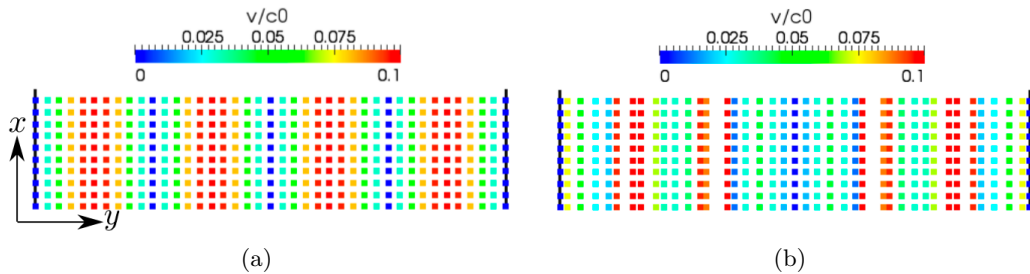


Figure 3.2: Values of  $v^+$  at different times (Figure 3.2(a):  $t^+ = 0$ , Figure 3.2(b):  $t^+ = 9.0$ )

The second observation is that the flow starts exhibiting non-physical fluctuations after some time. In Figure 3.2 the flow can be seen at  $t^+ = t c_0/h = 0$  and  $t^+ = 9.0$  (corresponding to the times indicated by black circles in Figure 3.1) where the non-dimensionalized values of  $v$  are plotted at each particle. It was already remarked in the previous section that the deficiency has to originate from the boundaries, as inside the fluid the operators are skew-adjoint.

At present it is not possible to recover the skew-adjoint property. Due to the collocated nature of SPH spurious numerical noise will alter the solution which can potentially introduce energy into the system. In the following section a diffusion term for numerical noise will be presented that will ameliorates this issue.

### 3.2 A volume diffusion term for numerical turbulence

It is well known that collocated methods, such as SPH, are prone to spurious oscillations in the solution which can lead to undesired behaviour as shown by Basa *et al.* (2009). For this reason many SPH methods incorporate some sort of artificial viscosity in order to dampen these residuals. One of the earliest techniques is the artificial viscosity term

by Monaghan (1992). In the following section this problem is tackled by assuming that the numerical noise causes a laminar flow to become turbulent. If the numerical noise is assumed to be isotropic and time-independent the laminar flow can be recovered by using an averaging operation such as commonly used in the Reynolds averaged Navier-Stokes context (see *e.g.* Pope (2001)). It should be emphasized that the approach in the following, although stemming from a physical background, is purely numerical.

### 3.2.1 Basic idea

In the context of turbulent flows the continuity equation in the Reynolds averaged context is given by

$$\frac{d\langle\rho\rangle}{dt} = -\langle\rho\rangle\underline{\nabla}\cdot\langle\underline{v}\rangle - \underline{\nabla}\cdot(\langle\rho'\underline{v}'\rangle), \quad (3.20)$$

where the primes refer to turbulent fluctuations and the angle brackets the Reynolds averaging (see Chapter 5.1.2). Moreover, the the Lagrangian derivative is in principle the ensemble averaged one. In laminar flows, as considered here, the fluctuating quantities are supposed to be zero. Still Eq. (3.20) can be applied to numerical fluctuations in an attempt to stabilize them. The Reynolds averaging approach is generally valid only for incompressible flows, however, as the density variations in the present weakly-compressible approach are relatively small it is applied in the present setting. The gradient-diffusion hypothesis states that

$$\langle\rho'\underline{v}'\rangle = -K\underline{\nabla}\langle\rho\rangle, \quad (3.21)$$

where  $K$  is the turbulent diffusivity. Inserting this into the averaged continuity equation yields

$$\frac{d\langle\rho\rangle}{dt} = -\langle\rho\rangle\underline{\nabla}\cdot\langle\underline{v}\rangle + \underline{\nabla}\cdot(K\underline{\nabla}\langle\rho\rangle). \quad (3.22)$$

As no fluctuating quantities remain the angle brackets are dropped in the following. Expressing Eq. (3.22) in terms of SPH operators the following is obtained

$$\frac{d\rho_a}{dt} = -\rho_a\mathbf{Div}_a^\gamma(\underline{v}) + \mathbf{Lap}_a^\gamma(K, \rho), \quad (3.23)$$

where  $\mathbf{Lap}^\gamma$  is an SPH discrete operator, here applied to  $\rho$  with a diffusion coefficient  $K$ . If the model by Morris *et al.* (1997) is used for the discretization of the  $\mathbf{Lap}^\gamma$  operator as in Eq. (2.135), without boundary terms, then the full discretization reads

$$\frac{d\rho_a}{dt} = \rho_a \sum_{b \in \mathcal{P}} V_b \left( \underline{v}_{ab} + (K_a + K_b) \rho_{ab} \frac{\underline{r}_{ab}}{r_{ab}^2} \right) \cdot \underline{\nabla}_a w_{ab}, \quad (3.24)$$

where  $\rho_{ab} = \rho_a - \rho_b$ . It is common to write the diffusivity term as  $K = \nu_T/\sigma_T$ , where  $\nu_T$  is the turbulent viscosity and  $\sigma_T$  is the turbulent Prandtl number. Continuing the analogy with physically-based turbulence, one may use the mixing length model to estimate  $\nu_T$  (see *e.g.* Pope (2001)), leading to

$$K \sim \frac{1}{\sigma_T} L_m^2 \frac{U}{L}, \quad (3.25)$$

where  $U$  and  $L$  are characteristic velocity and length scales, respectively, and  $L_m$  is the mixing length. Defining the numerical Mach number as  $M = U/c_0$ , where again  $c_0$  is the numerical speed of sound, yields

$$K \sim \frac{M}{\sigma_T} L_m^2 \frac{c_0}{L}. \quad (3.26)$$

Typically,  $\sigma_T \approx 1$ ,  $L_m = L/10$  and in weakly compressible SPH  $M = 1/10$  (Monaghan (2005)), which yields

$$K \sim \frac{L}{\Delta r} \frac{c_0 \Delta r}{10^3}, \quad (3.27)$$

where  $\Delta r$  is the initial particle spacing. Depending on the resolution,  $K$  can thus be given as

$$K = \frac{c_0 \Delta r}{\xi}, \quad (3.28)$$

where  $\xi \approx 10^3 \Delta r/L$  typically has the range of values of  $\mathcal{O}(10) - \mathcal{O}(100)$  depending on the ratio of  $\Delta r/L$  used to resolve the length scale  $L$ .

Ferrari *et al.* (2009) proposed a diffusion term which is remarkably similar to the one above (Eqs. (3.24) and (3.28)). It is based on the theory of Riemann solvers which were first introduced to SPH by Vila (1999). Ferrari *et al.* (2009) use an approximate Riemann solver to obtain the following continuity equation

$$\frac{d\rho_a}{dt} = \sum_{b \in \mathcal{P}} V_b \left( \rho_b \underline{v}_{ab} + c_{a,b} \frac{r_{ab}}{r_{ab}} \rho_{ab} \right) \cdot \nabla_a w_{ab}, \quad (3.29)$$

where

$$c_{a,b} = \max(c_a, c_b), \quad (3.30)$$

and

$$c_a = c_0 \sqrt{\left( \frac{\rho_a}{\rho_0} \right)^{\zeta-1}}, \quad (3.31)$$

with  $\rho_0$  being the reference density and  $\zeta$  the exponent of the equation of state (2.11). Comparing Eqs. (3.24) and (3.29) it can be deduced that our model is equivalent to

that of Ferrari *et al.* (2009) if

$$r_{ab}c_{a,b} = K_a + K_b. \quad (3.32)$$

Now a closer examination of  $c_a$ , given by (3.31), Eq. (2.11) shows that

$$c_a = c_0 \left( \frac{\rho_a}{\rho_0} \right)^{\frac{\zeta-1}{2}} = \sqrt{\left. \frac{\partial p}{\partial \rho} \right|_a}, \quad (3.33)$$

so  $c_a$  is the speed of sound of particle  $a$ . Thus  $K$  has the dimension  $m^2/s$  as expected for the turbulent diffusivity term.

Comparing Eqs. (3.32) and (3.28) shows that the correction as proposed by Ferrari *et al.* (2009) applies a significantly higher viscosity term than considering the simple mixing length model. This fact can be of importance when it comes to the use of this correction in the context of turbulent flows, where SPH is used increasingly (*e.g.* Ting *et al.* (2006)). The turbulent viscosity introduced due to the volume diffusion term by Ferrari *et al.* (2009) can dissipate more than just the numerical noise and thus have an influence on the energy spectrum of the flow.

Finally, note that in the Reynolds averaged context the Navier-Stokes equations would also need to be averaged. This was neglected in the above as the aim was to find a different interpretation for the volume diffusion term by Ferrari *et al.* (2009) which only acts on the continuity equation.

### 3.2.2 Semi-analytical wall boundary framework

After this interpretation the question arises of how this additional numerical diffusion term can be included in the wall boundary formulation as described above. To do so, the flux of the quantity  $K\nabla\rho$  has to be investigated in the normal direction of the wall. As the boundary condition on the density implies  $\partial\rho/\partial n = 0$  for flows without external forces, this flux is zero as well. Thus, using the Laplacian of Ferrand *et al.* (2012, 2010) and the divergence given by Eq. (3.18) the continuity equation with volume diffusion term reads

$$\frac{d\rho_a}{dt} = \frac{\rho_a}{\gamma_a} \sum_{b \in \mathcal{P}} V_b \left( v_{ab} + \frac{c_{a,b}}{\xi \rho_a} \rho_{ab} \frac{r_{ab}}{r_{ab}} \right) \cdot \nabla_a w_{ab} - \frac{\rho_a}{\gamma_a} \sum_{s \in \mathcal{S}} v_{as} \cdot \nabla \gamma_{as}. \quad (3.34)$$

As can be seen from the above, the volumetric term also contains vertex particles. In turn however, their density is determined from the boundary condition. As this volume diffusion term can be seen as transferring volume from one particle to the next it is important that this term is anti-symmetric, *i.e.* the volume taken from a particle  $a$  due to the influence of particle  $b$  needs to be added to particle  $b$  as a result of the influence

of particle  $a$ . This principle is thus violated if vertex particles are taken into account in the volumetric sum. In two-dimensional simulations this change has negligible impact on the flow.

### 3.3 Imposing a volume flux in periodic viscous flows

Related to the issue of solid boundaries are open boundary conditions. In the following the focus lies on periodic boundaries which itself do not pose an issue with SPH. However, in order to drive such a periodic flow with a fixed volume flux and thus variable force only one formula exists, which shows relatively large errors as shown in the following.

Imposing movement in the standard Poiseuille flow is normally achieved with a fixed driving force. This is however only possible if the value of the latter was known *a priori*, since the expected velocity profile is known. It is more common to drive a flow with a certain volume flux  $Q$ . In the following it is described how to impose a variable driving force based on the expected volume flux.

The volume flux  $Q$  is defined as

$$Q = \int_A \underline{v} \cdot d\underline{A} = \int_A \underline{v} \cdot \underline{n} dA, \quad (3.35)$$

where  $A$  is the cross-section area of the flow,  $\underline{n}$  its normal and  $\underline{v}$  the velocity. To obtain this value in the SPH framework an average over all particles in a slice of the domain is taken, *i.e.*

$$Q_{SPH} = \frac{1}{\Delta r_A} \sum_{b \in \mathcal{P}_A} V_b \underline{v}_b \cdot \underline{n}_A, \quad (3.36)$$

where  $\Delta r_A$  is the width of the slice and the set  $\mathcal{P}_A$  contains the particles in the slice. Herein,  $\Delta r_A$  is twice the particle spacing  $\Delta r$ . This can also be written as

$$Q_{SPH} = A \tilde{v}, \quad (3.37)$$

where  $\tilde{v}$  is the cross-averaged velocity.

In Violeau (2012) this average velocity is used to calculate the force via

$$F^{ext,n} = \frac{v - 2\tilde{v}^{n-1} + \tilde{v}^{n-2}}{2\Delta t}, \quad (3.38)$$

where  $n$  is the  $n$ -th time-step,  $F$  is the force in direction of the normal and  $v = Q/A$  the desired velocity. This formula originates from the finite volume community (Rollet-Miet (1998)). As can be seen in Figure 3.3 this value does not converge to the analytical (expected) one. The reason for this deficiency comes from the fact that

internal forces are not considered in the above formulation and so the external force is always underestimated. The equilibrium that should be reached is defined by

$$F^{ext} + F^{int} = 0, \quad (3.39)$$

where  $F^{ext}$  and  $F^{int}$  are the external and internal force respectively (the latter includes pressure and viscous forces). If the system is not in equilibrium the following holds

$$F^{ext,n} + F^{int,n} = \frac{\tilde{v}^n - \tilde{v}^{n-1}}{\Delta t^n}. \quad (3.40)$$

Ideally the velocity reached at time  $n$  is equal to the desired velocity  $v = Q/A$ . So

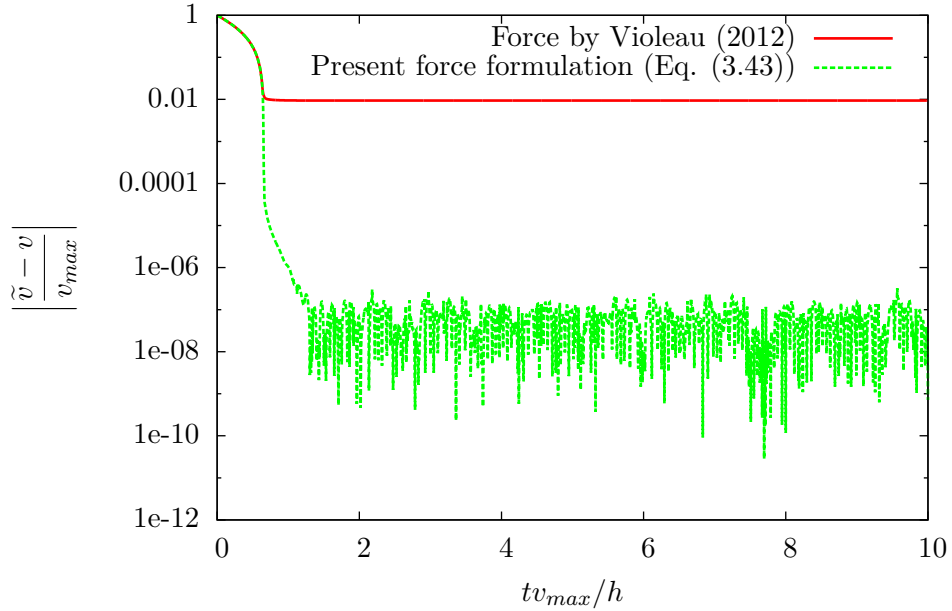


Figure 3.3: Comparison of the error in the bulk velocity of the Poiseuille flow.

rewriting the above yields

$$F^{ext,n} = \frac{v - \tilde{v}^{n-1}}{\Delta t^n} - F^{int,n}. \quad (3.41)$$

Clearly  $F^{int,n}$  is not available but it can be assumed to vary only a little between two consecutive time-steps, *i.e.*  $F^{int,n} \approx F^{int,n-1}$ . The latter value can then be calculated using Eq. (3.40) to give

$$F^{ext,n} \approx \frac{v - \tilde{v}^{n-1}}{\Delta t^n} - \frac{\tilde{v}^{n-1} - \tilde{v}^{n-2}}{\Delta t^{n-1}} + F^{ext,n-1}. \quad (3.42)$$

Finally rearranging the above yields the following new formula for calculating the external force:

$$F^{ext,n} = \frac{v - 2\tilde{v}^{n-1} + \tilde{v}^{n-2}}{\Delta t} + F^{ext,n-1}, \quad (3.43)$$

where it is assumed that the time-step  $\Delta t$  is constant. The first term on the right-hand side of Eq. (3.43) is twice that of Eq. (3.38). Thus (3.38) amounts to considering that  $F^{ext}$  is independent of time, which is a crude approximation.

In Figure 3.3 the two different means of imposing a driving force based on a volume flux are compared in the Poiseuille flow case. To do so the relative error in the bulk velocity is plotted over time. In Figure 3.3 it can be seen that with this new formulation the external force converges much more closely to the theoretical value. In the case of the Poiseuille flow it is not necessary to impose a volume flux but instead the analytical force can be used. However, in cases where the analytical value of the internal (viscous) force is not known *a priori* the above formulation provides the means to impose a volume flux which converges to the desired value.

As it can be seen from Figure 3.3 the present approach reduced the error by about five orders of magnitude. The error obtained with the original formulation is close to 1% which is not negligible.

### 3.4 Generalization of wall boundary conditions

After this analysis of the unified semi-analytical wall boundary conditions and the reinterpretation of the volume diffusion term the focus in the following two sections shifts towards novel developments which expand the boundary model.

#### 3.4.1 Theory

As mentioned in Section 2.3.2.5, to satisfy von Neumann boundary conditions Ferrand *et al.* (2012) showed a first-order approximation approach (see Eqs. (2.136) and (2.137)). In the following this approach shall be generalized to arbitrary orders of accuracy and to Robin boundary conditions, which include Neumann boundary conditions as particular case. Ryan *et al.* (2010) implemented Robin boundary conditions for SPH with the use of an additional source term in the governing equation. In this section a different approach is shown that enables Robin boundary conditions to be imposed directly.

Such an arbitrary Robin boundary condition for a scalar field  $f$  is given by

$$\left( \mu_1 f + \mu_2 \frac{\partial f}{\partial n} \right) \Big|_{\partial\Omega} = \mu_3, \quad (3.44)$$

for an arbitrary scalar field  $f$  with given  $\mu_1, \mu_2 \neq 0, \mu_3$ . To impose Neumann boundary conditions  $(\mu_1, \mu_2)$  take the values  $(0, 1)$ . The above can be rewritten as

$$\frac{\partial f}{\partial n} = \frac{\mu_3 - \mu_1 f}{\mu_2}. \quad (3.45)$$

The key idea is to use a weighted linear least squares approximation of the desired field

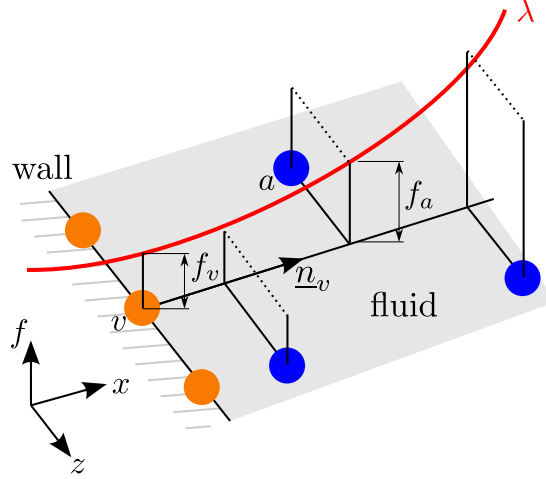


Figure 3.4: Illustration of the arbitrary order Robin boundary conditions for SPH. Blue particles denote fluid particles and particle  $v$  in orange is a vertex particle under consideration.

in the direction of the normal  $\underline{n}_v$  of a vertex particle  $v$ , which is defined as the average over the two adjacent segment normals. This implies that the problem is considered locally as one dimensional projected onto the normal  $\underline{n}_v$  of the vertex particle  $v$ . The procedure presented in detail in the following is illustrated in Figure 3.4.

Let  $m$  be the desired order of approximation and define a polynomial  $\lambda$  as

$$\lambda(x) = \sum_{i=2}^m \beta_i x^i + \frac{\mu_3 - \mu_1 \beta_1}{\mu_2} x + \beta_1, \quad (3.46)$$

$x$  being the normal distance to the wall.

We set  $\beta_1 = f|_{\partial\Omega}$ , *i.e.*  $\beta_1$  is the value of  $f$  prescribed at the wall. The polynomial can also be written as

$$\lambda(x) = \sum_{i=2}^m \beta_i x^i + \frac{\mu_3}{\mu_2} x + \beta_1 \left(1 - \frac{\mu_1}{\mu_2} x\right). \quad (3.47)$$

This represents an approximation of  $f$  in the direction of the normal  $\underline{n}_v$  with  $f_v = \lambda(0)$ . For a fluid particle  $a \in \mathcal{F}$  and  $x_a = \underline{r}_{av} \cdot \underline{n}_v$  the value of  $\lambda_a$  is thus given as  $\lambda(\underline{r}_{av} \cdot \underline{n}_v)$

when no external forces are present. Let  $\underline{\underline{X}} \in \mathbb{M}(|\mathcal{F}|, m)$  be a matrix defined as

$$\underline{\underline{X}}_{aj} = \begin{cases} 1 - \frac{\mu_1}{\mu_2}(\underline{r}_{av} \cdot \underline{n}_v) & \text{if } j = 1, \\ (\underline{r}_{av} \cdot \underline{n}_v)^j & \text{if } j > 1, \end{cases} \quad (3.48)$$

where  $j$  is the second index of the matrix  $\underline{\underline{X}}$ ,  $|\mathcal{F}|$  is the number of fluid particles and defining  $\underline{y} \in \mathbb{R}^{|\mathcal{F}|}$  as

$$y_a = f_a - \frac{\mu_3}{\mu_2}(\underline{r}_{av} \cdot \underline{n}_v). \quad (3.49)$$

The goal is to minimize  $f_a - \lambda_a$ . Hence, we are looking for a solution of the over-constrained system of linear equations

$$\underline{\underline{X}} \cdot \underline{\beta} = \underline{y}, \quad (3.50)$$

where  $\underline{\beta}$  is the vector of components  $\beta_i$  and the dot represents a single contraction, in this case the matrix multiplication. A common approach to this type of over-constrained problem is to use the least squares method which can be solved via

$$\underline{\underline{X}}^T \cdot \underline{\underline{X}} \cdot \underline{\beta} = \underline{\underline{X}}^T \cdot \underline{y}. \quad (3.51)$$

In order to put more weight on particles closer to the vertex particle, the SPH kernel is used to construct a weighted least squares interpolation. To include this into the above let  $\delta_{ab}$  be the Kronecker delta and  $\underline{\underline{\Lambda}} \in \mathbb{M}(|\mathcal{F}|)$ , a square matrix, be defined with elements given by

$$\underline{\underline{\Lambda}}_{ab} = \delta_{ab} V_a w_{ba}, \quad (3.52)$$

(there is no summation over indices here). Then the weighted least squares interpolation can be found by solving

$$\underline{\underline{X}}^T \cdot \underline{\underline{\Lambda}} \cdot \underline{\underline{X}} \cdot \underline{\beta} = \underline{\underline{X}}^T \cdot \underline{\underline{\Lambda}} \cdot \underline{y}. \quad (3.53)$$

Due to the fact that the problem is one dimensional the matrix on the left-hand side is of size  $m \times m$  and can be inverted easily. Of interest is  $\lambda(0)$  which is  $\beta_1$ . Thus finally

$$f_v = \lambda(0) = \beta_1 = ((\underline{\underline{X}}^T \cdot \underline{\underline{\Lambda}} \cdot \underline{\underline{X}})^{-1} \cdot \underline{\underline{X}}^T \cdot \underline{\underline{\Lambda}} \cdot \underline{y})_1, \quad (3.54)$$

where the subscript 1 on the right hand side refers to the first component of the vector in brackets.

If  $m = 1$  the above reduces to the equation shown in Eq. (2.136) thus showing that this indeed is a generalization to arbitrary order. Note, the matrix that needs to be inverted  $(\underline{\underline{X}}^T \cdot \underline{\underline{\Lambda}} \cdot \underline{\underline{X}})$  is contained in  $\mathbb{M}(m)$  and thus to obtain second-order boundary conditions the inversion of a  $2 \times 2$  matrix is required in two dimensions.

Finally, two things should be noted. Firstly, the matrix is non-degenerate if at least  $m$  fluid particles are in the neighbourhood of  $v$  and that they have different values of  $(\mathbf{r}_{av} \cdot \mathbf{n}_v)$ . Secondly, the formulation as presented above is independent of the method used to describe the walls, so it could also be used *e.g.* for the SPH ghost particle approach by Colagrossi and Landrini (2003).

In comparison to the present method where the boundary condition is directly imposed, Ryan *et al.* (2010) add an extra term to the governing equations. The present work is an extension of Ferrand *et al.* (2012) such that it is now possible to specify Robin boundary conditions and not only Neumann ones. Moreover, these can be imposed in an arbitrary order.

### 3.4.2 The wave equation as an example

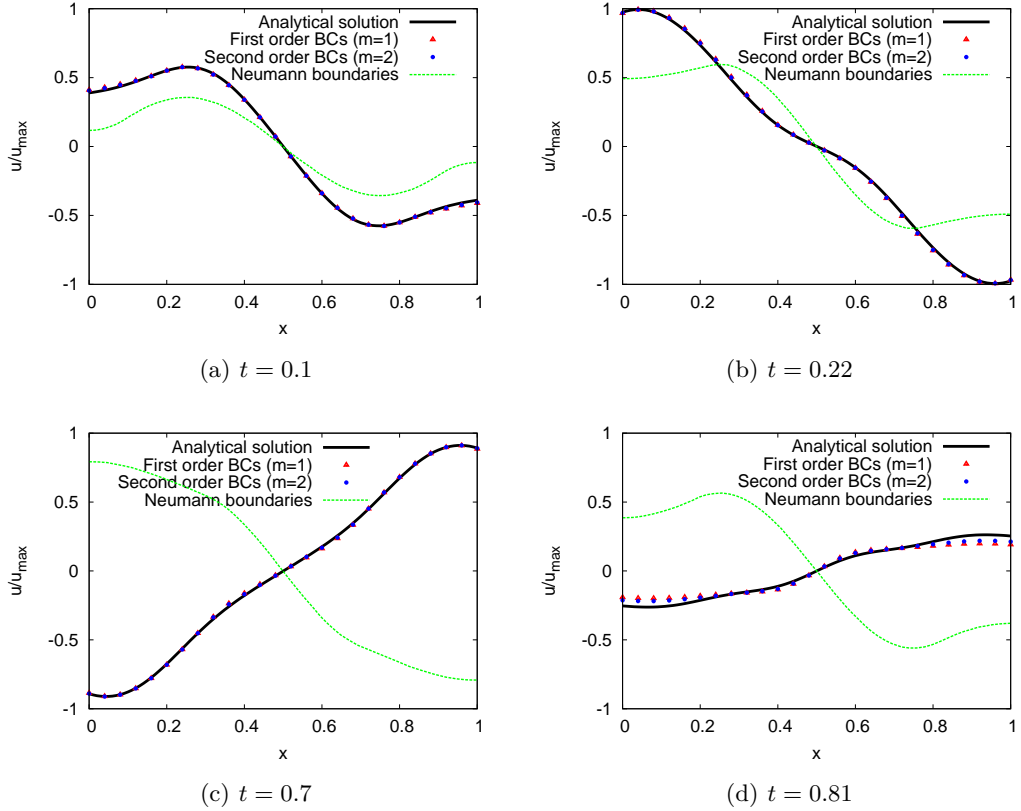


Figure 3.5: Wave equation (3.55) with Robin boundary conditions Eq. (3.56) at four different time-steps. Analytical solution given by Eq. (3.58). For the SPH solution, the matrix size in Eq. (3.54) is given by first ( $m = 1$ ) or second ( $m = 2$ ) order according to Eq. (3.46)

In this section it is shown that the above formulation works whereby Robin boundary conditions can be enforced. For this purpose, a wave equation is considered in one dimension:

$$\frac{\partial^2 u}{\partial t^2} = \frac{\partial^2 u}{\partial x^2}, \quad (3.55)$$

with boundary conditions

$$\frac{\partial u}{\partial n}(\{0, 1\}, t) = u(\{0, 1\}, t), \quad (3.56)$$

and initial conditions

$$u(x, 0) = 0 \quad \text{and} \quad \frac{\partial u}{\partial t}(x, 0) = \sin(2\pi x). \quad (3.57)$$

The domain  $[0, 1]$  is discretized with an initial particle distance  $\Delta r = 0.01$  and the particles are fixed. The second-order spatial differential operator is again discretized by using the Laplacian as given in Eq. (2.135). The temporal derivative is discretized by a second-order finite difference scheme. The analytical solution given by Haberman (2004) of this problem as a function of the dimensionless variables  $x$  and  $t$  is given by

$$u_{ana}(x, t) = \sum_{i=1}^{\infty} \alpha_i \sin(\kappa_i t) [\sin(\kappa_i x) + \kappa_i \cos(\kappa_i x)], \quad (3.58)$$

where  $\kappa_i$  is given as the  $i$ -th root of

$$\tan(\kappa_i) = \frac{2\kappa_i}{\kappa_i^2 - 1}, \quad (3.59)$$

and the  $\alpha_i$  are uniquely determined by the initial condition.

First, a qualitative view on the solution is given in Figure 3.5 at times  $t = \{0.1, 0.22, 0.7, 0.82\}$ . It can be seen that the main features of the field  $u$  are reproduced by the SPH solution and that, due to the new boundary condition formulation, the Robin boundary conditions are correctly imposed as we observed a distinct difference in the solution when using Neumann boundary conditions, *i.e.*  $\mu_1 = 0$ . In order to illustrate this the analytical solution for the Neumann boundary case was superimposed in Figure 3.5. The snapshots in Figure 3.5(a) and 3.5(d) are plotted at instants where the error on the boundary is maximal. Compared to these snapshots, the error between the SPH solution and the analytical solution is smaller throughout the domain at intermediate times (Figure 3.5(b) and 3.5(c)).

There is a notable difference in the SPH solution depending on whether the boundary conditions are of first or second order, *i.e.* whether  $m = 1$  or  $m = 2$  in Eq. (3.46). To quantify this more precisely consider Figure 3.6 where the error at the boundary

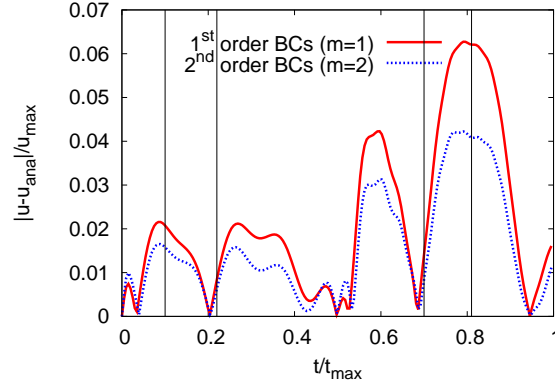


Figure 3.6: Wave equation with Robin boundary conditions: Relative error of the SPH solution over time at the boundary.

is plotted over time. It can be observed that the error is sensitive to the order of the boundary condition and that it can be reduced by up to 30% by choosing a second-order approximation. The vertical bars in Figure 3.6 show the instants that were shown in Figure 3.5.

## 3.5 Still water with a free-surface

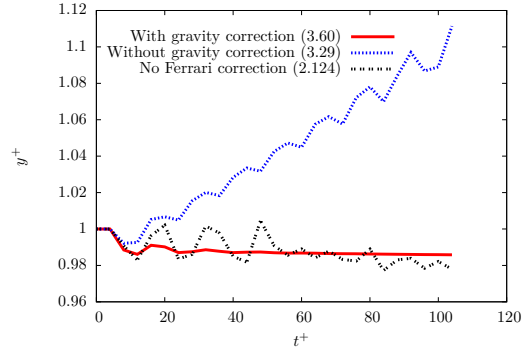
In the following, two of the above presented improvements are reviewed in the context of still water free-surface evolution. The first section below focuses on the volume diffusion term and the second on the arbitrary order boundary conditions.

### 3.5.1 Modification of the volume diffusion term

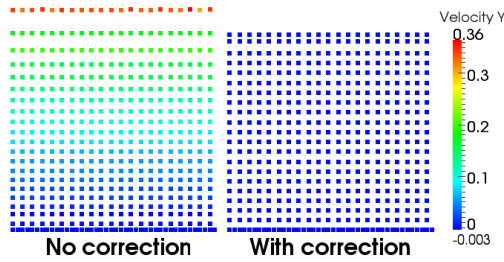
Using the volume diffusion term presented in Section 3.2 in a simulation of still water shows that the term as shown above does not have a zero contribution towards the density equation. This is caused by the fact that the boundary terms in Eq. (3.34) do not vanish when gravity is present. However, there are no segments on the free-surface and the problem can thus not be resolved by adding a boundary term.

In order to compensate for this deficiency the correction can be modified so that it reads

$$\frac{d\rho_a}{dt} = \frac{\rho_a}{\gamma_a} \sum_{b \in \mathcal{P}} V_b \left( \underline{v}_{ab} + \frac{c_{ab}}{\rho_a} \rho_{ab} \frac{\underline{r}_{ab}}{r_{ab}} \right) \cdot \nabla_a w_{ab} - \frac{\rho_a}{\gamma_a} \sum_{s \in \mathcal{S}} \underline{v}_{as} \cdot \nabla \gamma_{as}, \quad (3.60)$$



(a) Free-surface position over time



(b) Flow without and with free-surface correction

Figure 3.7: Position of free-surface in infinite open channel at rest.

in place of Eq. (3.34) where the density difference  $\rho_{ab}$  was replaced by the modified density difference  $\varrho_{ab}$  which is given by

$$\varrho_{ab} = \rho_a - \rho_b - \frac{g\rho_0}{c_0^2}(y_b - y_a). \quad (3.61)$$

where  $g$  is the gravitational constant and  $y$  the vertical elevation. This is a linear approximation of the difference between the non-hydrostatic densities of two particles. The external force in the formula above is gravity, but adaptation to other forces is straightforward.

In Section 3.1 it was remarked that the volume diffusion term should be anti-symmetric with respect to particles  $a$  and  $b$  in order to avoid that the global volume is changed. Clearly Eq. (3.61) obeys this principle. A similar correction was simultaneously proposed by Antuono *et al.* (2012).

To illustrate the difference between using the traditional  $\rho_{ab} = \rho_a - \rho_b$  and  $\varrho_{ab}$  consider Figure 3.7, which shows the non-dimensionalized position of the free-surface of an open channel-flow at rest where the initial density is set to  $\rho_0$ . In the plot the time was renormalized by  $h_{swl}/c_0$ , where  $h_{swl} = 1$  is the still water-level and  $c_0 = 10$  the

numerical speed of sound. It can be seen that without the above modification the free-surface detaches due to a transfer of volume from the denser lower part to the upper part of the fluid. The modification proposed above clearly avoids this issue keeping the free-surface elevation almost constant as expected. The decrease is due to the initial condition and the weak compressibility of the fluid.

### 3.5.2 Modification of the boundary interpolation

In this section the generalized boundary conditions presented in Section 3.4 are investigated in the presence of gravity. This means that the function  $f$  is equal to the pressure for which the classical Neumann boundary condition ( $\partial p / \partial n = \rho \underline{g} \cdot \underline{n}$ ) are applied.

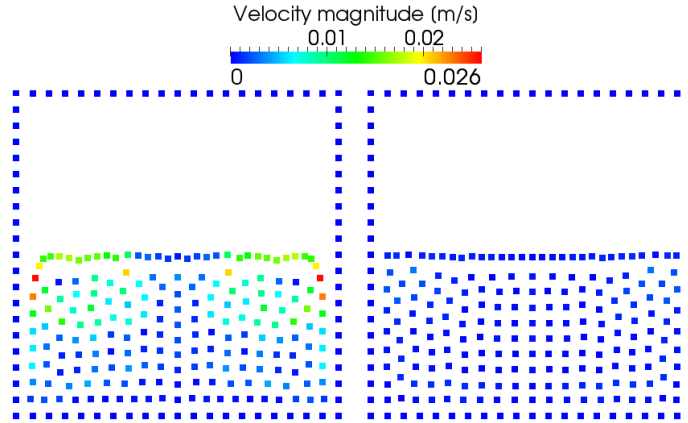


Figure 3.8: Still water in a closed tank (left: without correction (3.62), right: with correction (3.63)).

The approach presented in Section 3.4 produces unsatisfactory results at the intersection of free-surface and a wall as tangential variations are not neglected. The constraint above (Eq. (3.49)) reads

$$\lambda_a \approx y_a = p_a. \quad (3.62)$$

In order to neglect tangential variations for external forces such as gravity, the proper constraint is given by

$$\lambda_a \approx y_a = p_a - \rho_a [\underline{r}_{av} - (\underline{r}_{av} \cdot \underline{n}_v) \underline{n}_v] \cdot \underline{g}. \quad (3.63)$$

In Figure 3.8 the difference between Eqs. (3.62) and (3.63) is shown. The resolution is chosen to be relatively low in order to highlight the impact of the proposed correction. The picture on the left hand side shows particle movement which is an order of magnitude larger than the one on the right hand side which demonstrates the corrected approximation. Similar to the velocity field, the pressure prediction is improved

as well by lowering the magnitude of pressure waves originating from this corner. To explain the formula presented above consider the setup in Figure 3.8 with a perfect hydrostatic pressure distribution. Now we look at a vertex particle on a vertical wall which is located next to the free-surface. When constructing the polynomial  $\lambda$  (Eq. (3.46)) as given in Section 3.4 the fluid particles considered for the approximation all have a pressure greater than or equal to zero. This causes the pressure of the vertex particle to be greater than zero, although its theoretical value is zero. This in turn causes a repulsive force that can be seen on the left hand side of Figure 3.8. If, on the other hand, the hydrostatic part is subtracted from the fluid particles as in Eq. (3.63) then all fluid particles used for the approximation of  $\lambda$  have zero pressure and thus the vertex particle has the correct pressure.

### 3.6 Dam-break with wedge

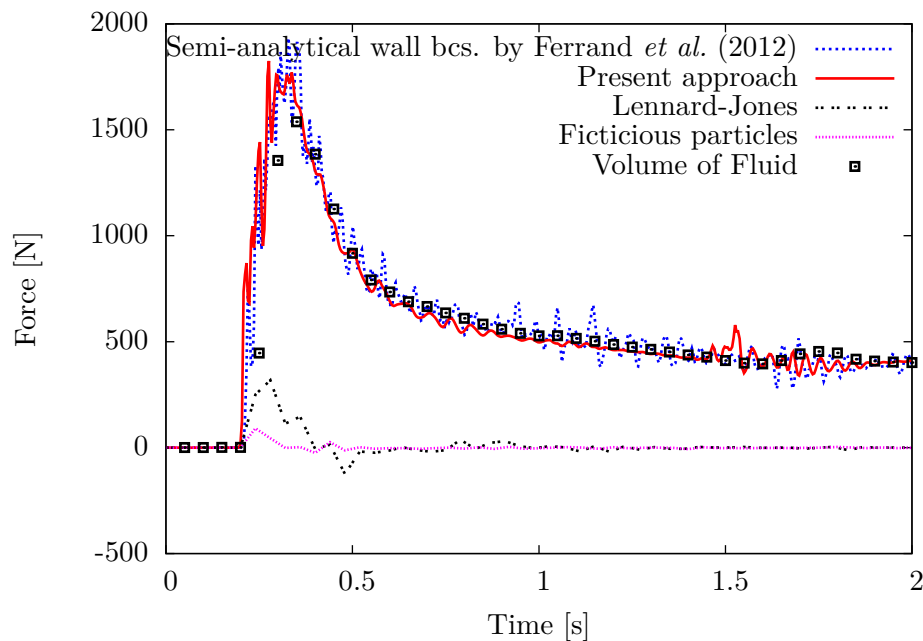


Figure 3.9: Schematic dam-break on a wedge: Comparison of forces on left wedge wall.

After having analyzed and extended the present wall boundary conditions a final simulation shall be performed. This uses most of the theoretical results presented above in a more complex free-surface flow.

A schematic dam-break over a wedge is simulated in 2-D with the same geometry as used by Ferrand *et al.* (2012). The initial water column is 1 m high and 0.5 m long and

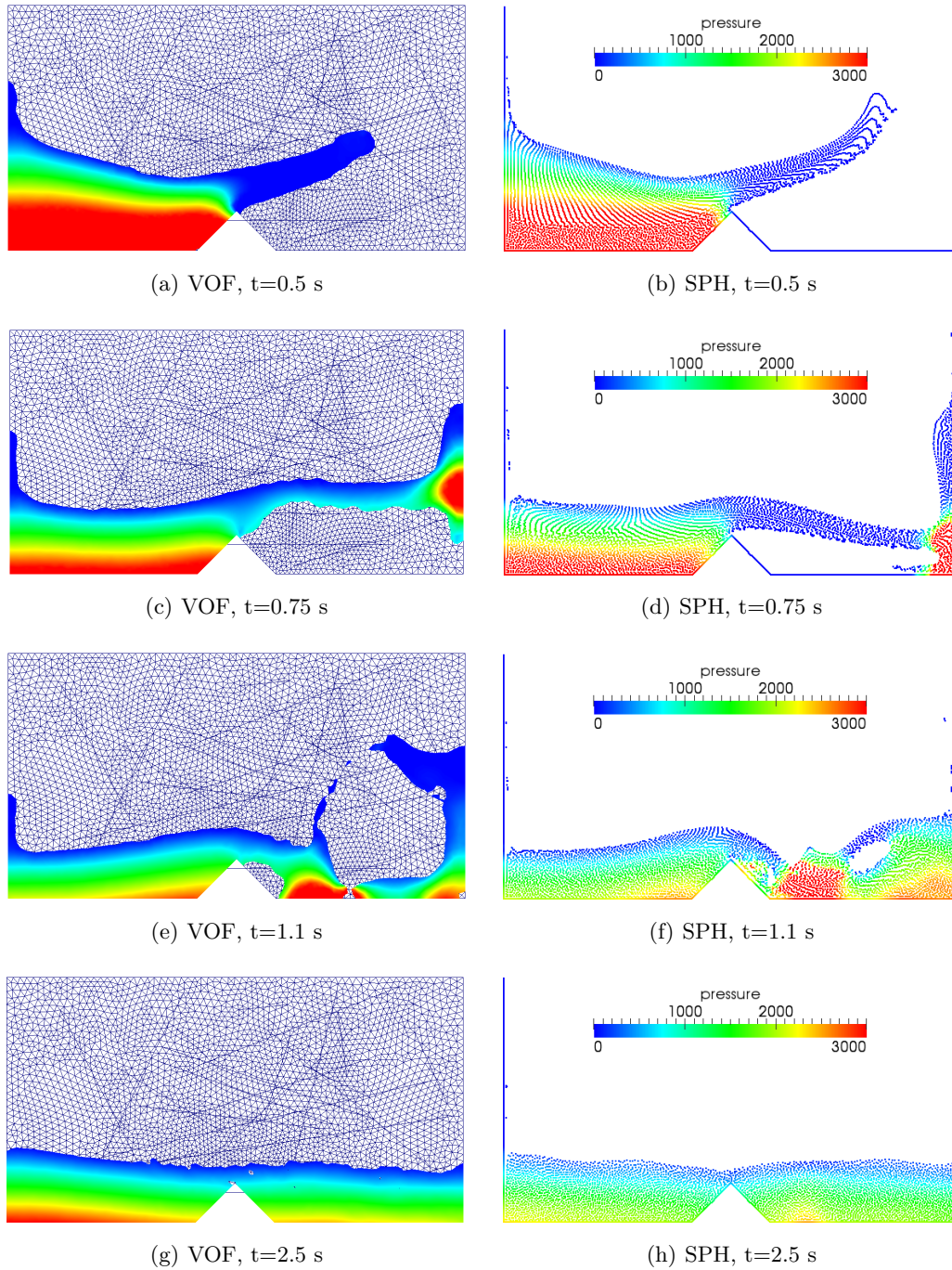


Figure 3.10: Comparison between VOF and SPH.

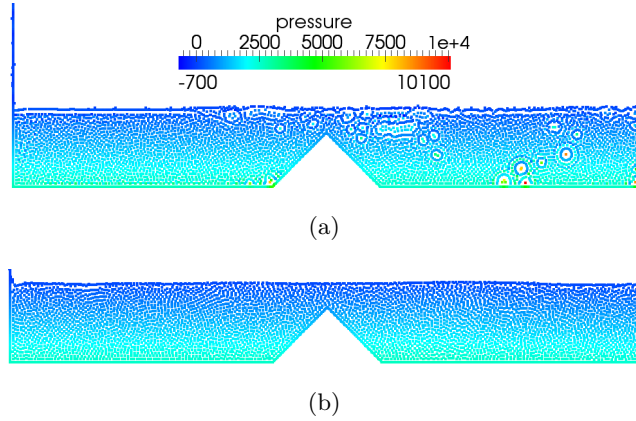


Figure 3.11: Steady flow on a wedge: Without (Figure 3.11(a)) and with (Figure 3.11(b)) the volume diffusion term (3.64) to avoid particle repulsion.

the dynamic viscosity is set to  $\nu = 0.01 \text{ m}^2/\text{s}$  resulting in a Reynolds number of approximately 140 based on the maximum velocity. The box has a length of 2.2 m where the wedge begins after 0.85 m with a side-length of 0.25 m. The force is calculated as the integral of the pressure along the left wedge wall. A Volume-of-Fluid (VOF) simulation is taken as reference solution (OpenFoam, Weller *et al.* (2012)). It should be noted that the latter is a multiphase simulation and thus some discrepancies are to be expected when compared to the SPH single-phase simulation as illustrated in Figure 3.10. As shown, the traditional boundary conditions using fictitious particles (Dalrymple and Knio (2001)) or the Lennard-Jones potential (Monaghan (1994)) fail in predicting the force. The fictitious particle approach is well known to repulse particles too much as already noted by, *e.g.* Hughes and Graham (2010), whereas the Lennard-Jones boundary conditions apply a force that is based on a physical principle that normally holds only at a molecular level. Due to these issues the limitations of these two approaches can be explained. Comparing the approach by Ferrand *et al.* (2012) with the present one, it can be seen that the volume diffusion term successfully reduces the numerical noise, while still showing closer agreement with VOF in Figure 3.9.

Finally, Figure 3.11(a) shows the steady state solution of the dam break with the time-independent continuity equation (Eq. (2.118)) without the heuristic free-surface correction. Particles that were initially on the free surface have retained their larger volumes producing the strange bubbles and unphysical pressures. Following the developments in Section 3.2.1 the integrated-in-time volume diffusion term was added, so that the continuity equation now reads

$$\gamma_a^n \rho_a^n = \gamma_a^{n-1} \rho_a^{n-1} + \sum_{b \in \mathcal{P}} m_b (w_{ab}^n - w_{ab}^{n-1}) + \Delta t \sum_{b \in \mathcal{F}} m_b c_{ab} \frac{r_{ab}}{r_{ab}} \frac{\rho_{ab}}{\rho_b} \nabla_a w_{ab}, \quad (3.64)$$

where the superscripts refer to the time iteration. Note that again the gravitationally corrected volume diffusion term (Eq. (3.61)) is used through  $\varrho_{ab}$ . The continuity equation above is equivalent to using  $\mathbf{Div}^{\gamma,k}$  (Eq. (3.18)) with  $k = 1$  so for consistency  $\mathbf{Grad}^{\gamma,1}$  (Eq. (3.17)) has to be used for the discretization of the pressure gradient.

From Figure 3.11(b) it can thus be concluded that the heuristic free-surface correction is no longer required (contrary to Ferrand *et al.* (2012)) as the volume diffusion term successfully redistributes the higher volume of particles initially on the free surface once they become entrained in the fluid body.

### 3.7 Preliminary conclusion

This chapter has investigated SPH boundary conditions for wall-bounded, potentially turbulent, flows within a semi-analytical framework. Three distinct but equally important areas have been investigated.

The semi-analytical wall boundary conditions for SPH introduced by Ferrand *et al.* (2012) have been further developed where the skew-adjoint property of discrete operators was examined both theoretically and numerically. It was shown that the skew-adjoint property does not hold in the discrete case leading to errors in the conservation of energy and demonstrated for two-dimensional channel flows. As shown by Morinishi *et al.* (1998) for non-uniform grids, exact conservation is not required if errors are small and remain bounded. A detailed error analysis of the conservation of different boundary conditions would be of interest for further research.

Another general issue with SPH is instability within the method that manifests itself as numerical noise. As shown in this chapter the noise can be explained by analogy with a Reynolds-averaged continuity equation which is shown to be equivalent to the density diffusion introduced by Ferrari *et al.* (2009) which used an approximate Riemann solver. This interpretation justifies the addition of a constant that depends on the relative resolution. As the volume diffusion term introduces artificial viscosity this constant prevents excessive damping which would be problematic for Direct Numerical Simulation or Large Eddy Simulation.

With the aim of simulating turbulent flows in periodic geometries, a novel formulation was presented to prescribe a variable driving force with an imposed volume flux which improves the predicted flow rate by 5 orders of magnitude. Additionally, the Neumann boundary conditions by Ferrand *et al.* (2012) were generalized to arbitrary orders of interpolation and Robin-type boundary conditions. The formulation was shown to impose Robin boundary conditions correctly thereby extending their potential application. Finally, two modifications to the boundary conditions as well as the volume diffusion term were presented in order to deal with free-surface flows correctly, reducing unphysical velocities at the surface by at least an order of magnitude for still water.

The new numerical scheme was demonstrated for a dam-break flow over a wedge showing the capabilities of the present improved model compared to a well-known VOF code. This simulation was also used to highlight the fact that the volume diffusion term can correct the free surface when using the time-independent continuity equation, as proposed by Ferrand *et al.* (2012)

## Chapter 4

# Extension to three dimensions

In order to extend the formulation based on Section 2.3.2 to 3-D two major issues need to be resolved. At first the mass of the vertex particles also need to be calculated. This depends on the spatial resolution as well as local geometric properties. Secondly, the calculation of the gradient of  $\gamma$  needs to be investigated. In 2-D it was possible to obtain an analytical formula for this vector and in the following an analytical formula for the three-dimensional case is presented.

### 4.1 Calculating the mass in 3-D

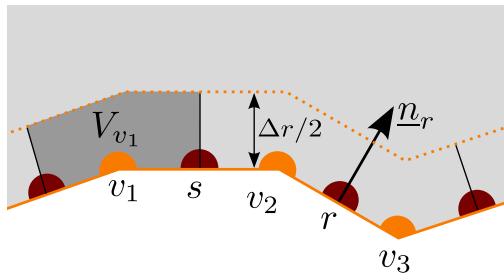


Figure 4.1: Partition of the boundary extended in wall-normal direction.

The goal of this section is to demonstrate how the mass of vertex particles is computed in a pre-processing step. In order to do so the volume of a vertex particle needs to be computed. The main idea in the following is that a partition of the boundary shall be created. The volume is then created by expanding this partition in wall-normal direction by  $\Delta r/2$ . Thus, each vertex particle obtains a volume that when combined yields a partition of the boundary with a certain thickness as illustrated in a two-dimensional example in Figure 4.1.

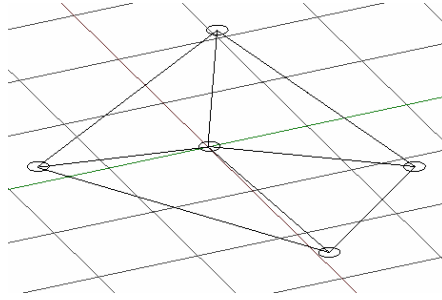


Figure 4.2: Initial view of coplanar faces surrounding a vertex.

In order to demonstrate how the calculation of the vertex particle mass works, Figures 4.2 to 4.7 are presented. The algorithm loops through all vertex particles and only requires the connected vertices and faces for one specific vertex particle. The integration of  $\int_v \rho dV$  is achieved by means of a Cartesian grid centred around the vertex particle. Its typical edge length is  $2\Delta r$  and the grid size is  $\Delta r/N$  with  $N \approx 100$ . Initially all the grid points are initialized with value 0, indicating that they are not being used for integration. In the following, points are either added or deleted which corresponds to setting the value to 1 or 0 respectively. The calculation is described in four steps.

**Step 1:** For each (associated) face two cubes with side length  $\Delta r$  are added. They are orientated according to one edge of the face and the normal of the face. The origin coincides with the vertex particle for which the volume is calculated. This is illustrated in Figure 4.3.

**Step 2:** In the next step the points outside the geometry are removed. In order to do so the average normal of all faces is calculated, in this case it is equal to  $(0, 0, -1)$ . Then, as shown in Figure 4.4, an infinite tetrahedron is created which is spanned by this average normal and the two edges associated to one face.

**Step 3:** Now the edges are one by one used to calculate the Voronoi tessellation which means that planes are placed at the midpoint between two vertices. All the points outside the created convex hull are removed as shown in Figure 4.5.

**Step 4:** The final step consists in removing all points which are outside the local group of faces that is associated to each vertex. In order to do this the plane spanned by the edge opposite of the vertex and the edge normal is calculated. All points outside are once again discarded as can be seen in Figure 4.6. The edge normal is the average of the normals of the two adjacent faces.

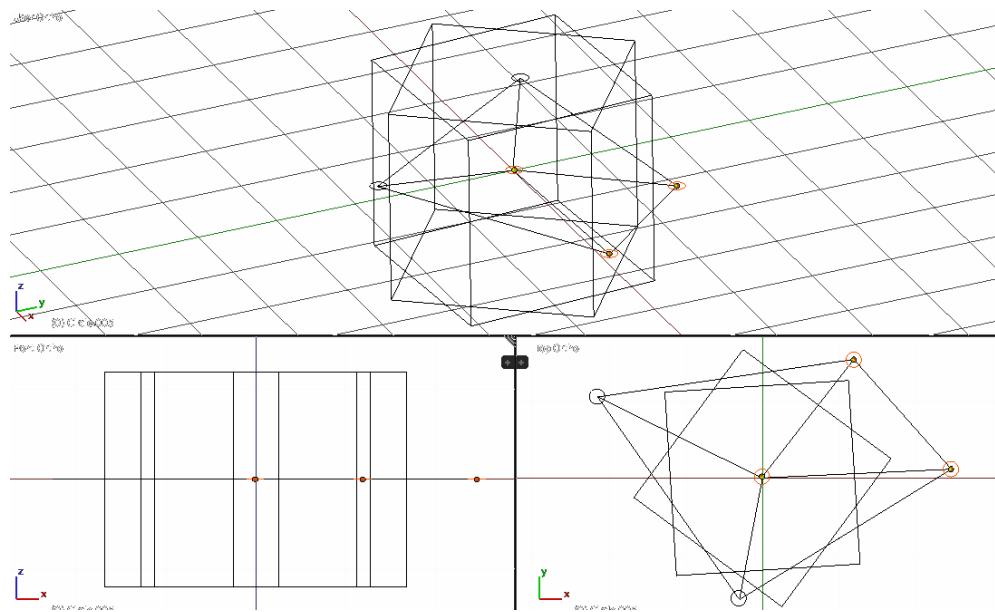


Figure 4.3: Creating two cubes according to the highlighted face.

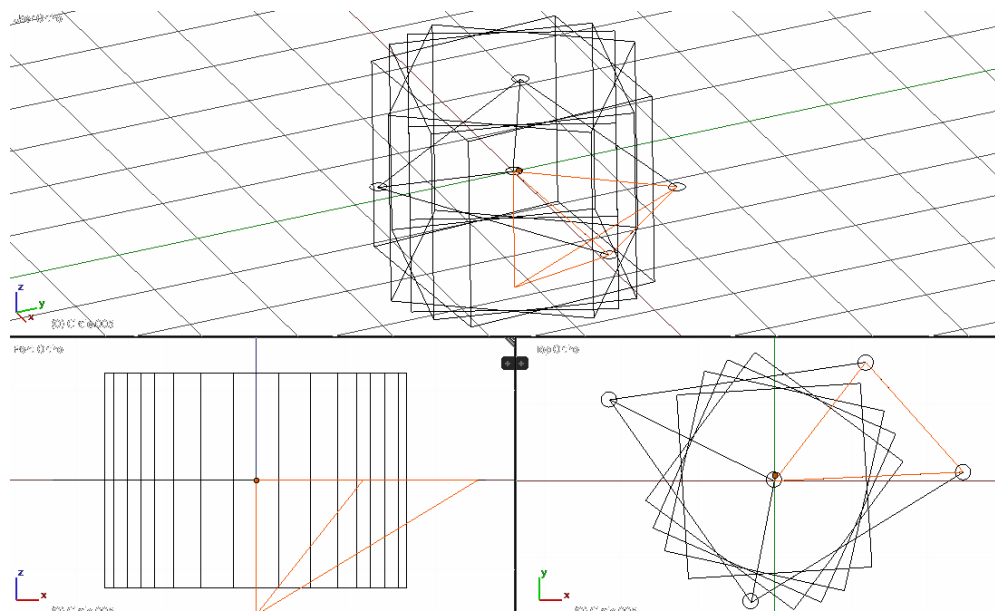


Figure 4.4: Use of tetrahedron (orange) to delete parts outside of geometry.

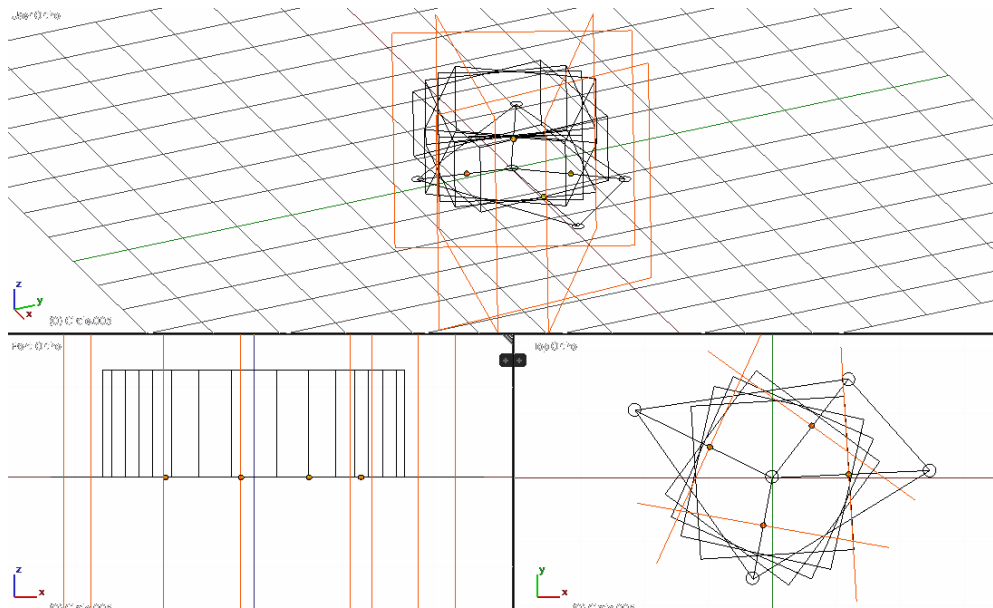


Figure 4.5: Voronoi tessellation.

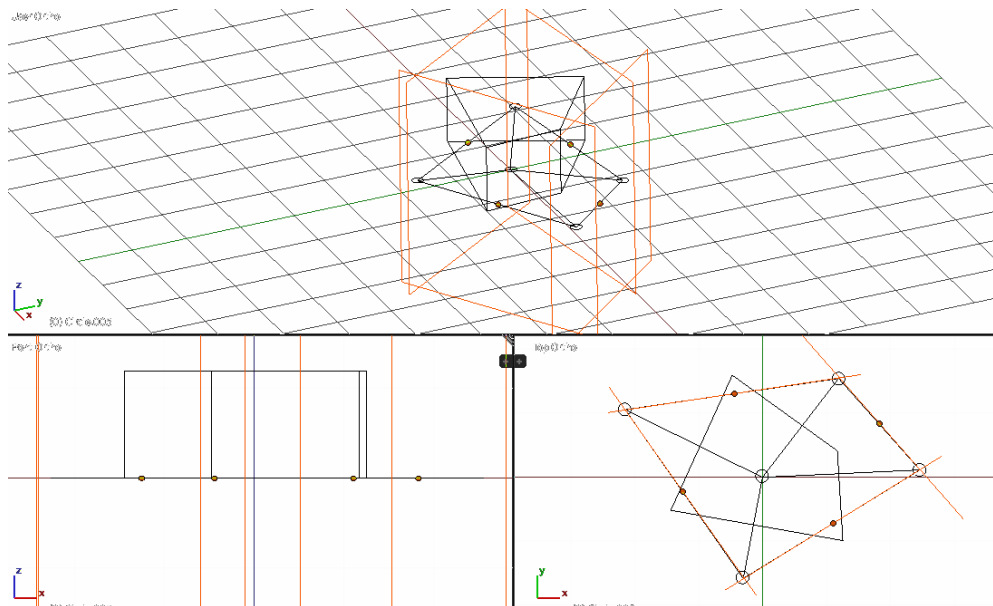


Figure 4.6: Cutting off at face boundaries.

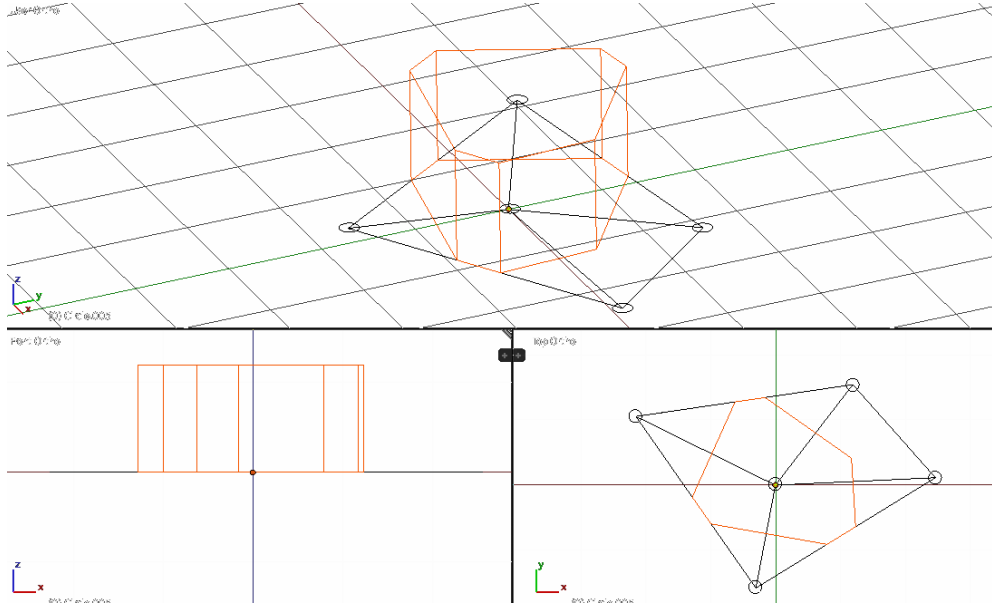


Figure 4.7: Final vertex particle volume.

The final volume is shown in Figure 4.7, its value is determined by numerical integration of the above mentioned Cartesian grid. To summarize the above, the algorithm provides a seamless cover of the boundaries with height of  $\Delta r/2$ . This cover is split into non-intersecting portions which represent the volumes of the vertex particles. The approach shown above is rather complicated, considering it is used within a meshless method. As it is applied only in the pre-processing stage the influence on the computational time is not substantial.

## 4.2 Analytical computation of $\underline{\nabla}\gamma$ in 3-D

In the following the algorithm for the analytical computation of  $\underline{\nabla}\gamma_{as}$  in 3-D is described. The general principle is discussed first before describing the details of the domain decomposition algorithm and the formulae for the special cases. This section is concluded by showing the possibility to optimise the calculation on a plane wall.

Clearly the boundary of a three-dimensional geometry is a two-dimensional manifold. In order to discretize the boundary it is required to generalize the 1-D line segments to a 2-D equivalent. The most basic bounded 2-D element is a triangle. It can be described by 3 vertices which are always coplanar. Thus in the following it is assumed that a boundary segment is given by a triangle and its virtual position, required for the imposition of boundary conditions, is set to be the triangle's barycentre.

Thus,  $\underline{\nabla}\gamma_{as}$ , given by Eq. (2.105), is the integral of the Wendland kernel over a triangle. More precisely it is the integration of a radial polynomial over the intersection

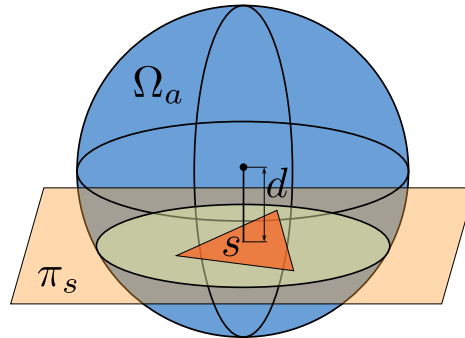


Figure 4.8: Illustration of the general problem.

of a triangle with a sphere as illustrated in Figure 4.8. Clearly this intersection is not necessarily a triangle, further complicating the integration. Due to the inherent singularity of the function  $\underline{r} \mapsto w(\|\underline{r}\|)$  at the origin (only twice continuously differentiable) it is not advisable to use a numerical algorithm. Several numerical approaches were attempted and the only one providing promising results was an adaptive integration which was not viable due to its computational cost. Due to this it was decided to develop an analytical formula, as done in for 2-D by Ferrand *et al.* (2012).

The integration of an arbitrary triangle / sphere intersection is too complicated and thus it was decided to decompose the surface integration domain, denoted by  $s$  in Equation (2.105), into building blocks for which it would be easier to find an analytical solution. This domain decomposition is discussed in detail in the next section. The formulae for the building blocks are shown in Section 4.2.2.

In contrast to the approach by Amicarelli *et al.* (2012), which uses square segments, the triangular decomposition allows more flexibility. Additionally, traditional meshing software can be used in order to create the surface mesh for arbitrary complex geometries.

### 4.2.1 The domain decomposition algorithm

Before the algorithm for the decomposition is given, consider the 8 possible configurations that can result from a triangle / sphere intersection as shown in Figure 4.9. As mentioned above, the integration domain  $s_{as} = \partial s \cap \Omega_a$  consists of an intersection between a triangle and a circle. In the following, one segment  $s$  is investigated with its three associated vertices  $\{v_1, v_2, v_3\}$ . The number  $n_v$  determines how many vertices are inside the integration domain and  $n_e$  is the number of edges intersecting with  $s_{as}$ , the boundary of the integration domain.

A systematic description of the eight possible cases via a decision tree is given below.

- All vertices inside the domain ( $n_v = 3 \Rightarrow n_e = 0$ )  $\Rightarrow$  Case 1

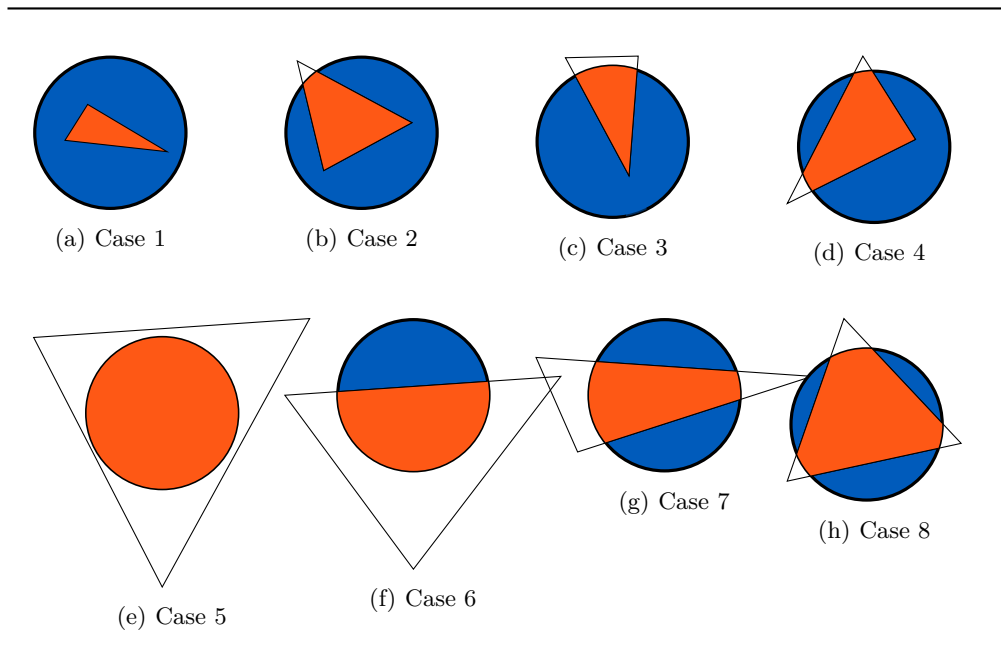


Figure 4.9: The 8 different cases.

- One vertex outside the domain ( $n_v = 2 \Rightarrow n_e = 2$ )  $\Rightarrow$  Case 2
- Two vertices outside the domain ( $n_v = 1$ )
  - Two edges intersecting ( $n_e = 2$ )  $\Rightarrow$  Case 3
  - All edges intersecting ( $n_e = 3$ )  $\Rightarrow$  Case 4
- All vertices outside the domain ( $n_v = 0$ )
  - No edges intersecting ( $n_e = 0$ )  $\Rightarrow$  Case 5
  - One edge intersecting ( $n_e = 1$ )  $\Rightarrow$  Case 6
  - Two edges intersecting ( $n_e = 2$ )  $\Rightarrow$  Case 7
  - All edges intersecting ( $n_e = 3$ )  $\Rightarrow$  Case 8

After identifying the different cases the next step is to decompose the specific domain into the three basic building blocks shown in Figure 4.10. From left to right there is the circular sector, the circular segment and the full circle. In Figure 4.11 the different decomposition algorithms are shown.

In the following Case 1 is explained as an example. The detailed procedure for this can be seen in Figure 4.12. The integration domain is a triangle, completely inside the support. In order to compute the integral, three circular sectors need to be computed. Circular Segment 1 contains the triangle and its center is vertex  $v_1$ . In the next step Circular Segment 2 is subtracted in order to remove the part of Circular Segment 1

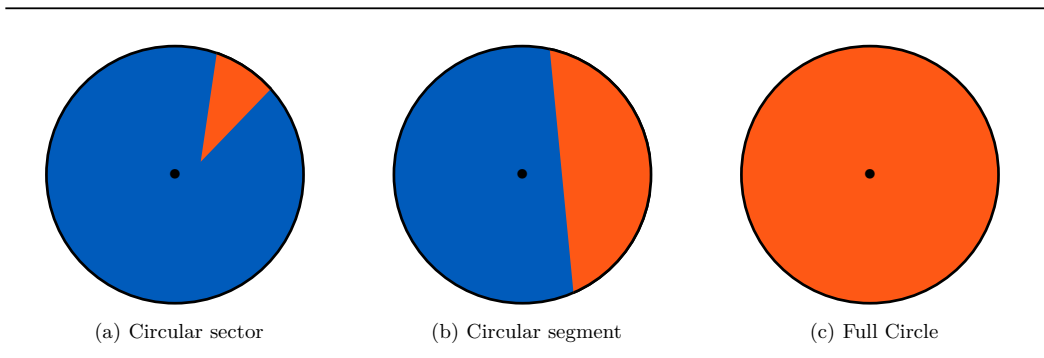


Figure 4.10: The 3 building blocks.

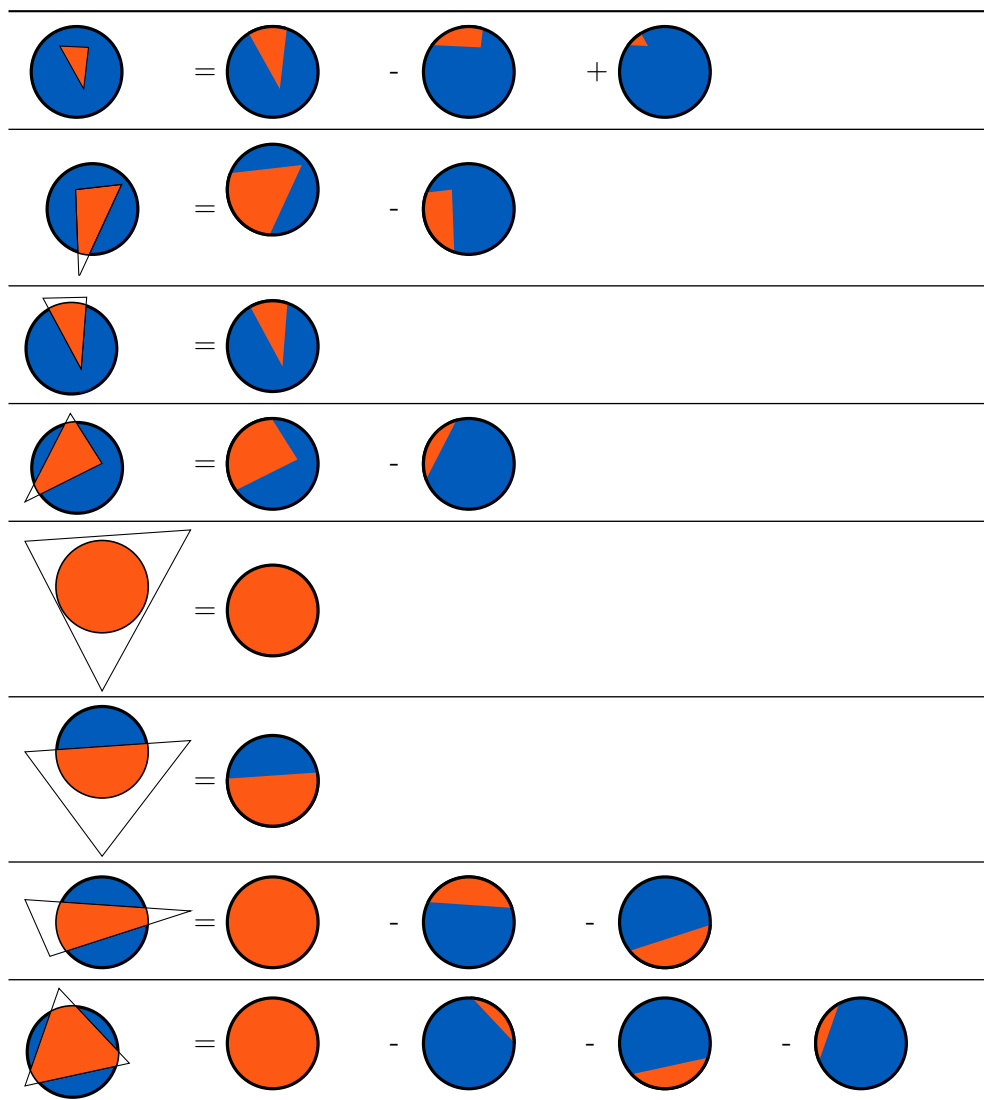


Figure 4.11: Illustration of the domain decompositioning algorithm.

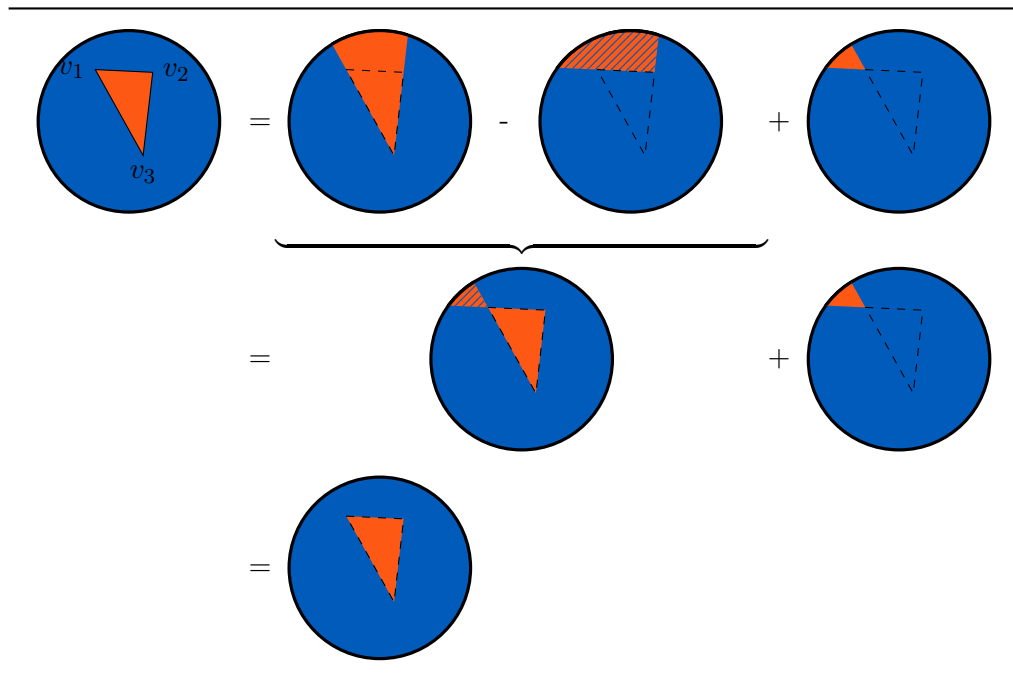


Figure 4.12: Algorithm for Case 1 in detail.

that does not contain the triangle. However, there is Circular Segment 3 that does not overlap with Circular Segment 1 and thus needs to be added in the final step so that the integral really only covers the triangle domain.

### 4.2.2 Analytical formulae for the basic domains

After decomposing the domain in the previous section, the analytical formulae for the integral (Eq. (2.105)) over the three basic domains are given for the Wendland kernel (Eq. (2.63)). Let us first introduce the non-dimensionalised integral  $I$ :

$$I = \int_s w_{ab} dr_b. \tag{4.1}$$

Equation (2.105) then reads:

$$\underline{\nabla} \gamma_{as} = I \underline{n}_s. \tag{4.2}$$

The formulae in the following are specific to the Wendland function given in Eq. (2.63) as it is the one most used in the SPH community. However, the approach can be applied to any radial polynomial by modifying the formulae presented below.

#### 4.2.2.1 Circular sector

The case of a circular sector needs to be simplified to two special circular sectors as illustrated in Figure 4.13(a). One special circular segment can be identified by the

distance  $d$  of the particle to the plane, the distance to the projected center  $r$  and the angle  $\theta$  as shown in Figure 4.13(b). The formula for such a special circular segment is then formally given by

$$I_{sector}(d, r, \theta) = \int_{q=\sqrt{d^2+r^2}}^2 \frac{\alpha_3}{h^3} \omega(q) \left( \theta - \arcsin \left( \frac{r \sin \theta}{\sqrt{q^2 - d^2}} \right) \right) q dq. \quad (4.3)$$

With the help of a standard symbolic mathematics software (Maple) it becomes

$$\begin{aligned} I_{sector}(d, r, \theta) &= \alpha_3 \frac{2}{7} \left( \theta - \arcsin \left( \frac{r \sin \theta}{\sqrt{4-d^2}} \right) \right) \\ &+ \alpha_3 \left[ \Psi_{d,r,\theta}(q) + \Psi_{-d,r,\theta}(q) - r \sin \theta P_{d,r,\theta}(q) \sqrt{q^2 - d^2 - r^2 \sin^2(\theta)} \right. \\ &\quad \left. - r \sin \theta Q_{d,r,\theta} \ln \left( q + \sqrt{q^2 - d^2 - r^2 \sin^2(\theta)} \right) \right]_{q=\sqrt{r^2+d^2}}^{q=2}, \end{aligned} \quad (4.4)$$

where

$$\Psi_{d,r,\theta}(q) = \frac{1}{14} \arctan \left( \frac{r^2 \sin^2 \theta + (d+q)d}{r \sin \theta \sqrt{q^2 - d^2 - r^2 \sin^2(\theta)}} \right) \left( 2 - (2 + 5d + 4d^2) \left( 1 - \frac{d}{2} \right)^5 \right), \quad (4.5)$$

and

$$\begin{aligned} P_{d,r,\theta}(X) &= \frac{1}{2688} \left[ -924d^4 - 1120r^2 \sin^2 \theta - 2800d^2 - 728r^2 \sin^2 \theta d^2 \right. \\ &\quad \left. - 224r^4 \sin^4 \theta + 1344 \right. \\ &\quad \left. + (48d^2 r^2 \sin^2 \theta + 504r^2 \sin^2 \theta + 15r^4 \sin^4 \theta + 57d^4 + 1176d^2)X \right. \\ &\quad \left. + (-252d^2 - 112r^2 \sin^2 \theta - 560)X^2 \right. \\ &\quad \left. + (22d^2 + 10r^2 \sin^2 \theta + 336)X^3 - 84X^4 + 8X^5 \right], \end{aligned} \quad (4.6)$$

and

$$\begin{aligned} Q_{d,r,\theta} &= \frac{1}{2688} [2520d^4 + 105d^6 + (105d^4 + 1680d^2)r^2 \sin^2 \theta \\ &\quad + (504 + 63d^2)r^4 \sin^4 \theta + 15r^6 \sin^6 \theta]. \end{aligned} \quad (4.7)$$

The above formula is valid for  $0 < \theta < \pi/2$ ,  $0 \leq r \leq 2$  and  $0 \leq d \leq 2$ .

#### 4.2.2.2 Circular segment

Let  $r$  denote the minimum distance from the circular segment (Figure 4.10(b)) to  $r_a$  projected to the plane  $\pi_s$  which contains the triangle  $s$  as shown in Figure 4.8. Assume furthermore that the circular segment does not cover this projected point, then the

formula for the integral is given by

$$I_{segment}(d, r) = 2I_{sector}\left(d, r, \frac{\pi}{2}\right). \quad (4.8)$$

Note that many algebraic simplifications and optimizations can be done in  $I_{sector}(d, r, \theta)$  when  $\theta = \frac{\pi}{2}$  (not presented herein).

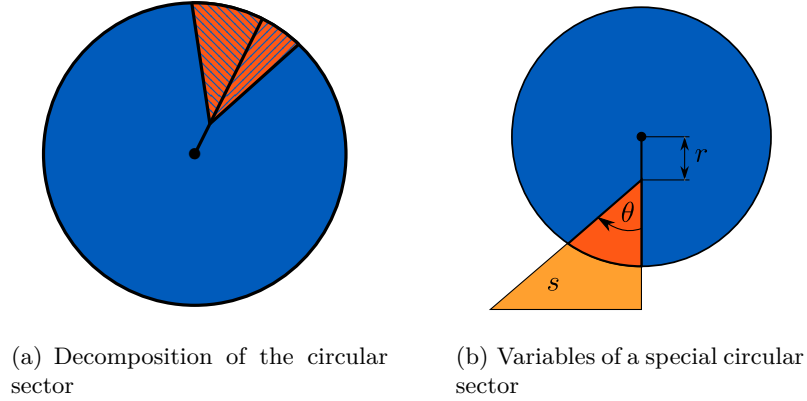


Figure 4.13: The circular sector in detail.

#### 4.2.2.3 Full circle

The integral for the case of a full circle (Figure 4.10(c)) depends only on the distance to the plane  $d$  and can be calculated as

$$I_{full}(d) = 2I_{segment}(d, 0) = \alpha_3 \frac{2}{7} \pi (2 + 5d + 4d^2) \left(1 - \frac{d}{2}\right)^5, \quad (4.9)$$

#### 4.2.3 Optimisation on plane walls

On plane walls the values of  $\gamma_a$  and  $\underline{\nabla}\gamma_a$  can be easily computed in terms of the dimensionless distance  $d$  normal to the wall, normalized by the smoothing length  $h$ . They are given as

$$\gamma_a(d) = 1 - \frac{1}{512} (2 - d)^6 (4 + 6d + 3d^2), \quad (4.10)$$

and

$$\underline{\nabla}\gamma_a(d) = I_{full}(d) \underline{n}. \quad (4.11)$$

This avoids the time-integration of  $\gamma$ , given in Eq. (2.115), for particles only influenced by a plane wall. This reduces the possible time-stepping error and in case a higher order time-stepping scheme is used, lowers the computation time, as  $\underline{\nabla}\gamma_{as}$  must be computed only once.

### 4.3 Simulations

In the following section the algorithm provided above is used to perform three different simulations. The first one is used to compare the proposed algorithm to the analytical value when approaching a plane wall. The second simulation shows a box with a complex floor that is filled with water in order to investigate the spurious velocities. Finally, a dynamic flow is simulated based on the geometry of the second SPHERIC test case.

#### 4.3.1 Particle approaching a plane wall

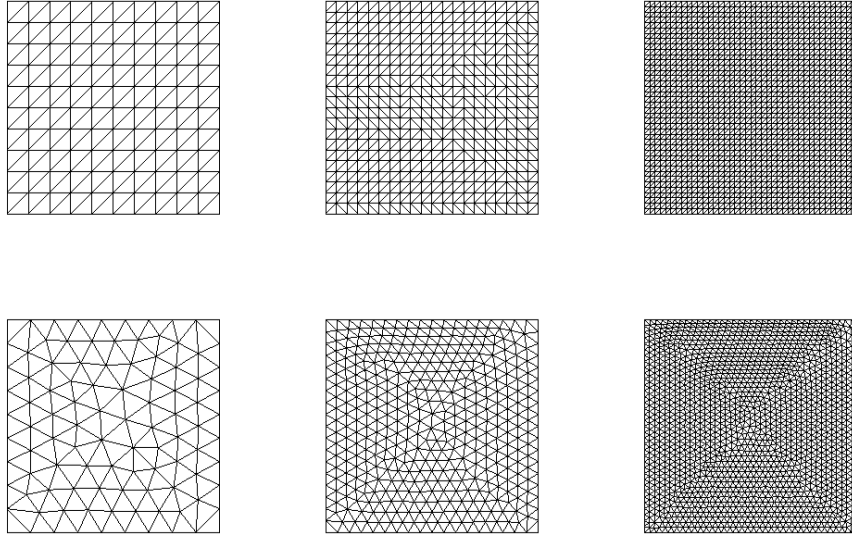
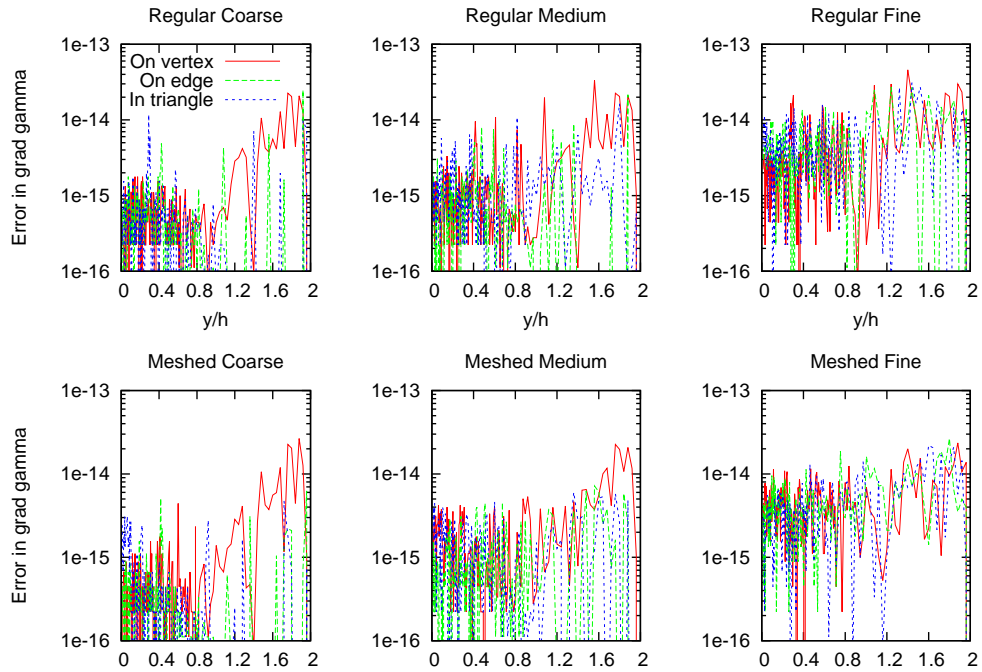


Figure 4.14: Discretizations of the plane walls.

The first simulation consists of three particles approaching six different plane walls. The discretization of these walls is illustrated in Figure 4.14 and as it can be seen there are three planes with a regular discretization and three with a non-regular mesh. For each of those two sets there is one plane where the triangle size is of the order of  $\Delta r$  (particle size), one with double and one with quadruple resolution. Furthermore for each of those six walls there are three particles, initially at  $y = 4\Delta r$  ( $h/\Delta r = 2$ ) which approach the wall with constant speed  $c_0/10$ , where  $c_0$  is the numerical speed of sound in weakly compressible SPH. The difference between these three particles is that one is located above a vertex, one is above an edge and one is located above the interior of a triangle.

The analytical formula for  $\nabla\gamma$  on a plane wall for the Wendland kernel (Eq. (2.63)) is given by Eq. (4.11). Note that the optimization presented in Section 4.2.3 is not used in this simulation. In Figure 4.15 the relative error for the different walls and particle

Figure 4.15: Error of  $\underline{\nabla}\gamma$  for different walls.

positions can be seen. Clearly, the error is as large as machine precision for the used double precision variables and no configuration showed any larger errors, indicating that the formulation adapts perfectly to any given discretization.

### 4.3.2 Still water

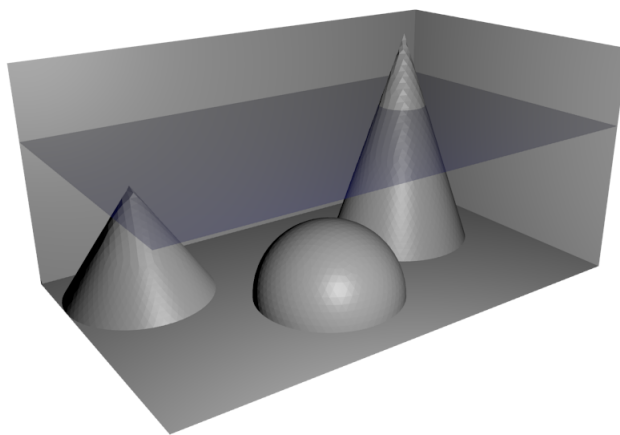


Figure 4.16: Geometry of the still water test case.

After demonstrating the algorithm for a single particle, it must then be tested for complex geometries with a fluid body consisting of a large number of particles in a highly

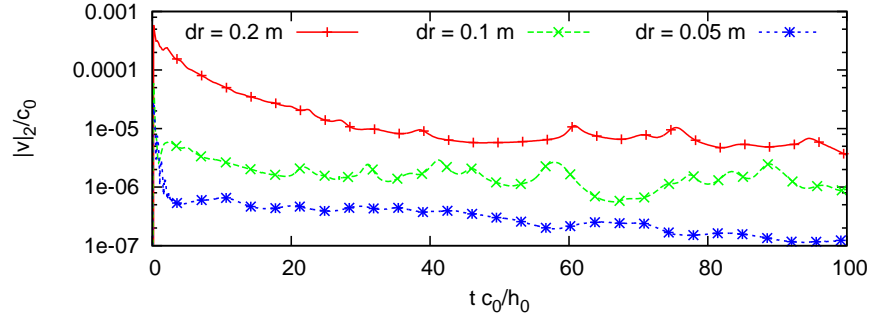
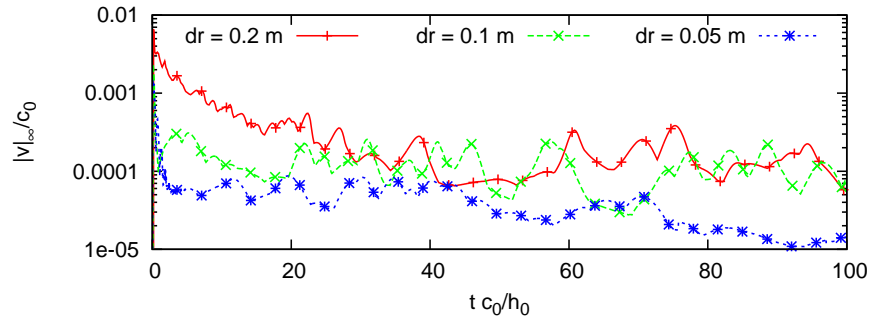
(a)  $L_2$  norm(b)  $L_\infty$  norm

Figure 4.17: Residual velocity.

complex geometry. In the following the box shown in Figure 4.16 is used in order to quantify the decay of velocity in a flow at rest under the influence of gravity. Note that for illustration purposes two side walls were removed to allow viewing the inside of the box. The box is partially filled with water so that there is one submerged half-sphere, one submerged cone and one cone which pierces the surface. The size of the box is  $6.5m \times 3m \times 4m$ , the first cone is centered at  $(1, 0, 3)$  with height  $1.5m$ , whereas the second cone is centered at  $(5, 0, 2.5)$  with height  $3m$  and both have a radius of  $1m$ . Finally, the half-sphere is centered at  $(3, 0, 1.5)$  with radius  $1m$ . Initially all the particles have uniform density (thus uniform pressure) and thus an initial acceleration is expected which should die down quickly. The optimisation presented in Section 4.2.3 is used in all following computations.

The viscosity is set to  $\nu = 0.1m s^{-2}$  and the numerical speed of sound is  $c_0 = 45m s^{-1}$ , which is based on the initial waterdepth of  $h_0 = 2m$ . The Neumann boundary conditions are implemented using the technique described in Section 3.4. In Figure 4.17 the velocity magnitude is presented in both  $L_2$  and  $L_\infty$  norms. The normalized  $L_2$  norm

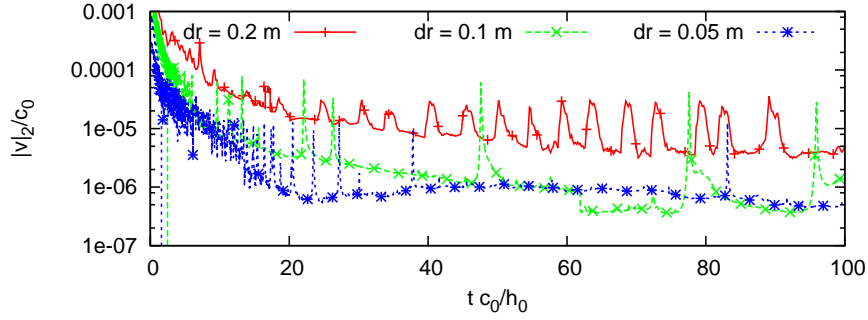


Figure 4.18:  $L_2$  norm using the boundary conditions by Monaghan and Kajtar (2009).

is given as

$$\frac{|v|_2}{c_0} = \sqrt{\frac{1}{|\mathcal{F}|} \sum_{a \in \mathcal{F}} \left( \frac{\|v_a\|_2}{c_0} \right)^2}, \quad (4.12)$$

and the normalized  $L_\infty$  norm is given as

$$\frac{|v|_\infty}{c_0} = \frac{1}{c_0} \max_{a \in \mathcal{F}} (\|v_a\|). \quad (4.13)$$

In order to see whether the formulation provides convergence three different resolutions are compared. After the expected initial damping, the velocity remains more or less constant and convergence can be observed. To compare the present approach to other SPH boundary conditions the same simulations were performed using the boundary conditions by Monaghan and Kajtar (2009). The advantage is that it is possible to reuse the same triangular boundary discretization which allows a direct comparison without the influence of a change in discretization. The  $L_2$  norm errors are shown in Figure 4.18 and are shown to be more oscillatory compared to the ones shown in Figure 4.17(a). Additionally, the error between the two finer resolutions is of the same order showing that at the finest resolution the error is larger when using the boundary conditions by Monaghan and Kajtar (2009). The final pressure distribution for the present boundary conditions can be seen in Figure 4.19.

In Figure 4.20 the present algorithm was compared to a simulation which was conducted using the approximation of Eq. (2.106)

$$\nabla \gamma_{as} = S_s \underline{n}_s w_{as}, \quad (4.14)$$

where  $S_s$  is the surface area of boundary segment  $s$ . In the lower left corner of Figure 4.20(a) a particle can be seen penetrating a wall with a value of  $\gamma_a$  significantly lower than the expected value of  $\gamma_a \approx 0.25$ . At later stages of the simulations further particles penetrate the wall. It shall be noted that due to the modification presented in

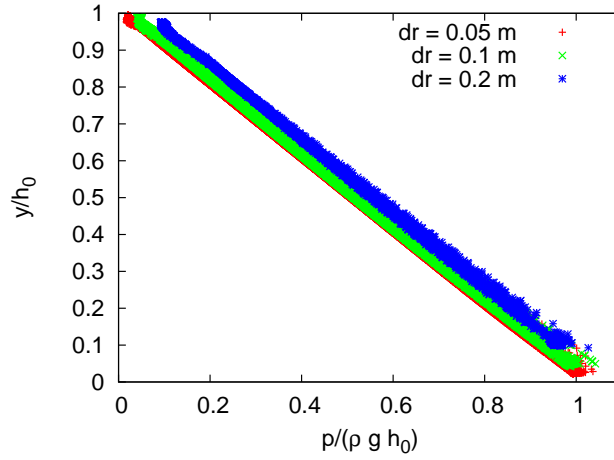


Figure 4.19: Pressure of all particles at the end of the simulation.

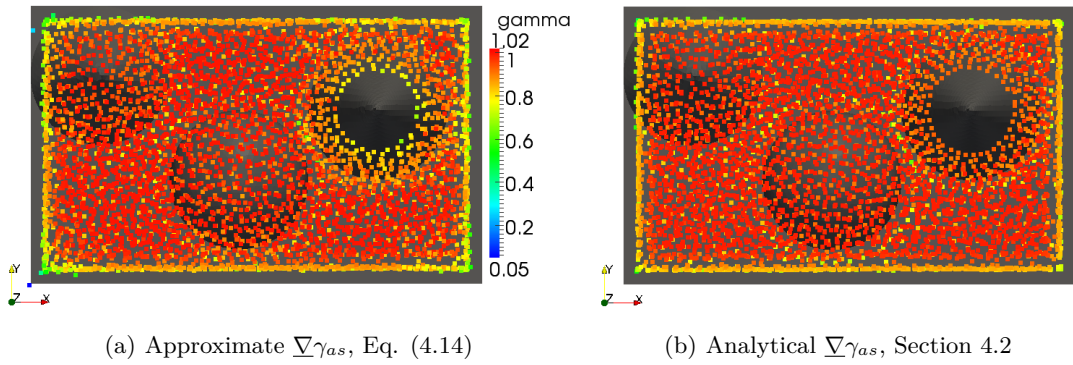


Figure 4.20: Comparison between the approximative and the analytical approach.

Section 4.2.3 the particles along plane walls do not penetrate due to their correct value of  $\gamma_a$ . It can be observed in Figure 4.20(b) that no particles penetrate the walls when the algorithm of Section 4.2 is used. This is due to the value of  $\nabla\gamma_a$  being computed analytically such that the only error in  $\gamma_a$  originates from the time integration which is negligible.

### 4.3.3 Dam-break with obstacle

The final simulation shows a violent free-surface flow in form of a dam break with an obstacle. The geometry used is the same as given in the second SPHERIC validation test (<https://wiki.manchester.ac.uk/spheric/index.php/Test2>). Compared to the proposed viscosity of  $\nu = 10^{-6} m s^{-2}$  a value of  $\nu = 10^{-2} m s^{-2}$  is used to ensure the flow to be laminar since no turbulence models have been implemented in our code

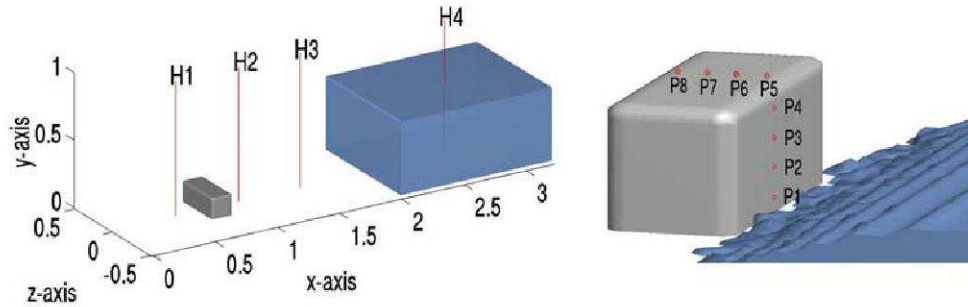


Figure 4.21: Location of probes according to Kleefsman *et al.* (2005).

and thus the results would not be accurate enough with a smaller viscosity. The pressure probes and water depth probes are located at exactly the same position as in the SPHERIC validation test shown in Figure 4.21. In order to compare with a different approach the same simulation was conducted using a Volume-of-Fluid (VOF) code (OpenFoam, Weller *et al.* (2012)). It is expected that this reference solution does not match the solution computed with the SPH method presented above as the former is computed using a multiphase approach. However, before the impact of the fluid onto the obstacle we expect similar results as the air phase has negligible impact on this stage of the flow.

The simulation was run for three different resolutions, the first corresponding to the one of the validation test which is  $\Delta r_0 = 0.55/30m$  and the other two being  $\Delta r = \Delta r_0/\sqrt{2}$  and  $\Delta r = \Delta r_0/2$ . The numerical speed of sound is set to  $c_0 = 40m s^{-1}$  and the modified volume diffusion term presented in Section 3.3 is used.

In Figure 4.23 the result of two different probes measuring the water levels can be observed and Figure 4.22 shows the flow at different stages during the simulation. The effect of particles only sliding slowly down the wall is due to the no-slip boundary conditions. The probe on the left-hand side is located inside the initial cube of water and the decay agrees with the VOF reference solution as expected. It can be seen that there is more fluid being held back by the obstacle as indicated by the difference in levels in Probe H2. This also implies that the wave reflected by the obstacle is only visible in the VOF solution as seen in the plot of Probe H4 after 3.5s. The cause for this difference is most likely to be air entrapped downstream of the obstacle, which causes the water to flow slower over the obstacle thus creating a higher wave upstream.

In Figure 4.24 the result of two pressure probes can be observed. The first probe is located at the front face of the obstacle, whereas the second one is located on top of it. Probe P2 indicates that the pressure peak is not appropriately resolved indicating that either space or time discretization is not fine enough. In comparison with the VOF simulation it is expected that the peak is appearing earlier and higher due to the

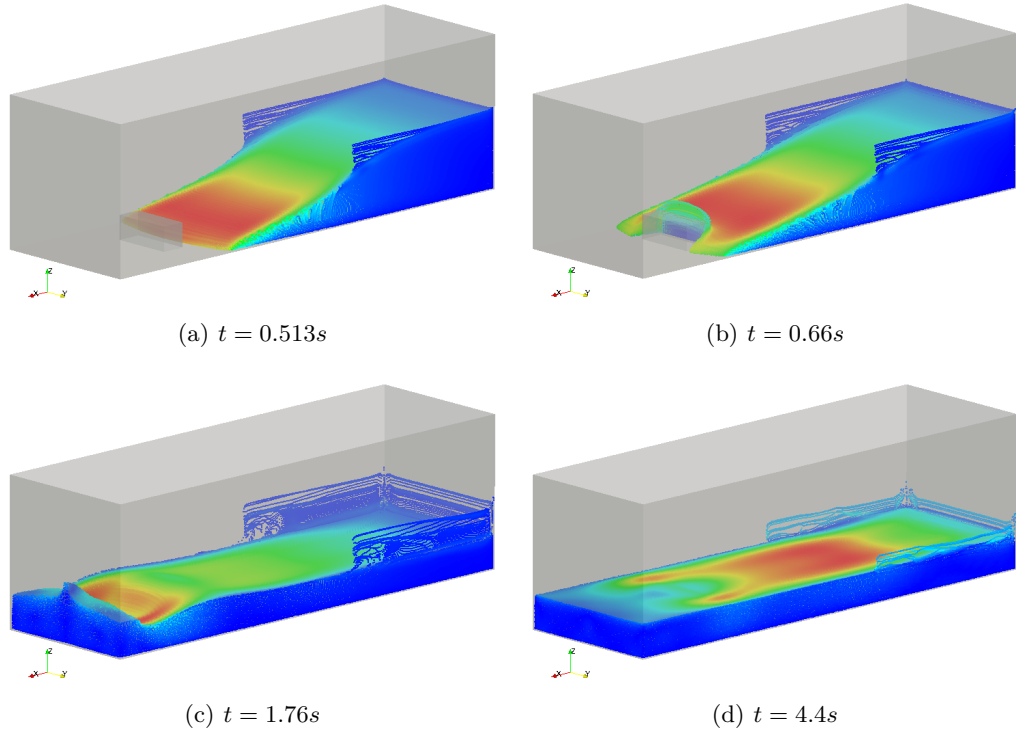


Figure 4.22: Snapshots of the simulation coloured according to velocity magnitude.

absence of air. After the impact event the pressure is slightly lower when compared to the reference simulation which is once again explained by the difference in height of the wave reflected by the obstacle. This can also be observed in the right hand side of Figure 4.24 where the pressure at Probe P5 is shown. Due to the lower water level the pressure is reduced but both reflection events are captured.

In order to investigate whether the differences in the simulations are due to the mono-phase character of SPH or the boundary treatment three additional SPH simulations were performed. The first simulation used exactly the same boundary discretization with the boundary conditions formulation formulated by Monaghan and Kajtar (2009) (M&K BCs) which is based on a repulsive force. The other two simulations were performed using the DualSPHysics package (Crespo *et al.* (2011)) which utilizes the boundary conditions by Dalrymple and Knio (2001) where the two simulations differ only in the resolution. The first, denoted in the figures by *DualSPHysics*, uses the standard  $\Delta r_0$ , whereas the latter, *DualSPHysics*  $\Delta r_0/2$ , uses the double resolution  $\Delta r_0/2$ .

As shown in Figure 4.25 these three simulations are compared to the VOF and coarse SPH simulation which uses the unified semi-analytical boundary conditions using the same probes as in Figure 4.23. It can be observed that M&K BCs show significant

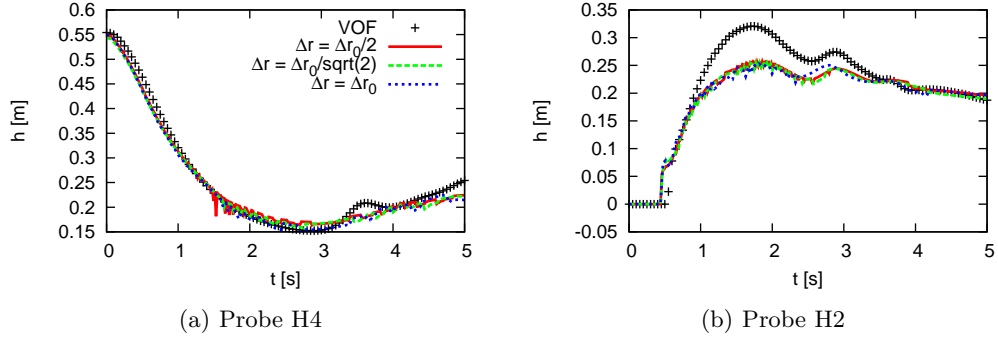


Figure 4.23: Water levels.

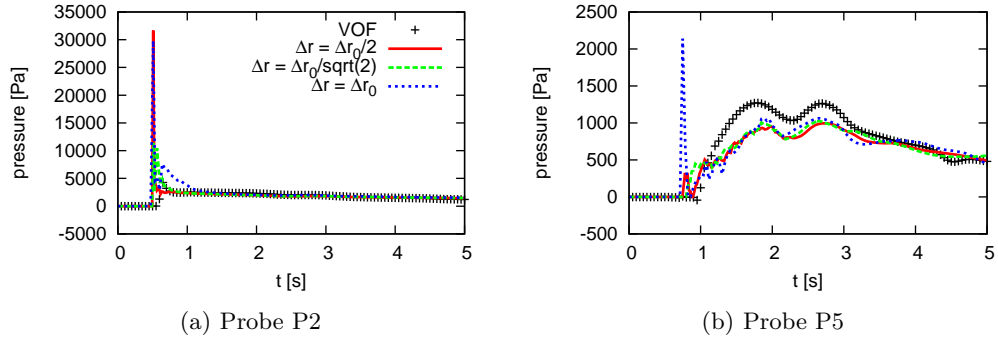


Figure 4.24: Pressure gauges.

deviations from both the VOF and the other SPH solutions. The DualSPHysics simulations on the other hand show a significant difference due to the different resolutions. This was not observed in the simulations shown in Figure 4.23. Probe H2 indicates, particularly during  $t \in [1, 2]$ , that there is a common deviation from all the SPH simulations to the VOF solution.

Figure 4.26 shows the results from the same pressure probes as in Figure 4.24. The M&K BCs exhibit a highly oscillatory behaviour, whereas the DualSPHysics results show a strong dependence based on the resolution. The latter was also shown by Crespo *et al.* (2011) where the same simulation was performed using a lower viscosity.

As the goal of this chapter is to demonstrate the extension of the semi-analytical wall boundary condition to 3-D it shall be mentioned that there were no particles penetrating the walls thanks to the accurate imposition of the boundary terms. If again the approximation shown in Eq. (4.14) is used, the simulation behaves similar to the one presented in the previous section, there are some particles which penetrate the wall. Finally, the computation with the approximative value of  $\underline{\nabla}\gamma_{as}$  requires 0.84s per iteration, whereas the simulation with the analytical value requires 0.97s per iteration. This means that the simulation is about 15% slower, an acceptable value considering

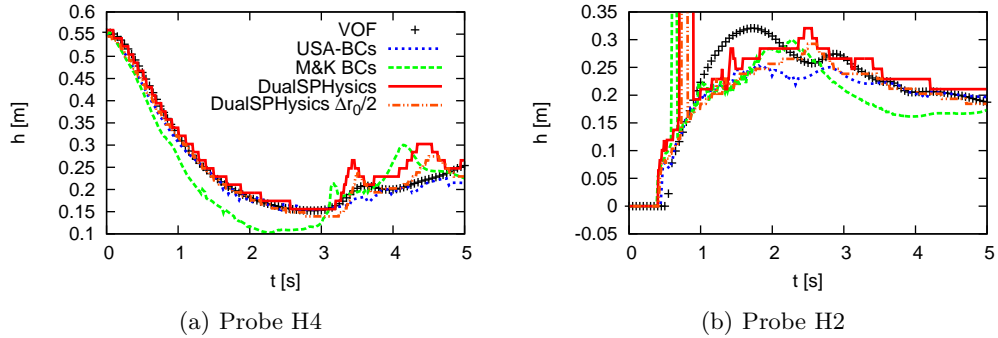


Figure 4.25: Comparison of water levels using different boundary conditions.

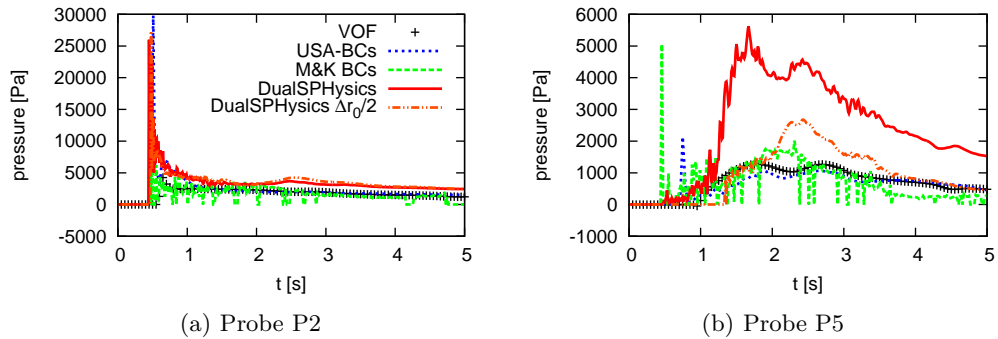


Figure 4.26: Pressure gauges using different boundary conditions.

the improved behaviour of the simulation.

#### 4.4 Preliminary conclusion

The goal of this chapter was to extend the unified semi-analytical boundary conditions of Ferrand *et al.* (2012) to 3-D. In Section 4.1 a method to compute the vertex particle mass in a consistent manner was given, based on geometric principles which is done in a pre-processing step. Moreover, it was necessary to compute the integral of the kernel on a triangle which can possibly be intersected with a sphere. In Section 4.2 an algorithm was presented that achieves the analytical computation of this integral which is based on a domain decomposition as well as analytical formulae for specific integration domains. The domain decomposition is based on the identification of the eight different possible integration domains and their representation based on three geometrical shapes. Using symbolic mathematics software the kernel was integrated on these three shapes, a circular sector, a circular segment and the full circle, thus providing an algorithm to compute all possible shapes analytically.

The formulation has been tested in three different simulations. The first being the computation of  $\underline{\nabla}\gamma$  with individual particles approaching a plane wall which was discretized using different approaches and resolutions. It was shown that the error is as small as machine precision when compared to the analytical solution. The second simulation concerned the simulation of still water in a box featuring a highly complex geometry with two cones and a sphere emerging from the floor. Finally, a laminar version of the second SPHERIC validation test was analysed and compared to a Volume-of-Fluid reference solution. The results were in good agreement despite some expected discrepancies due to the multiphase nature of the VOF simulation. The last two simulations were also conducted using an approximate value of  $\underline{\nabla}\gamma_{as}$  which always resulted in particles penetrating the walls, demonstrating the requirement for a more accurate calculation of this value as presented in this work. Additionally, it was shown that the computation time is only 15% higher when using the analytical algorithm.

## Chapter 5

# The turbulent channel flow

As a prelude to the numerical investigations presented in Chapter 6, the main aim of this chapter is to give a brief survey of closed turbulent channel flow. In Chapter 6 simulations of the channel flow will be shown using both quasi DNS and LES approaches. The survey includes the physical aspects presented in Section 5.1 with an emphasis on the turbulent scales as well as low order statistics. This is followed by the mathematical description of different turbulent structure resolving simulation approaches used for turbulent wall-bounded flows, namely direct numerical simulation (DNS) and large eddy simulation (LES).

### 5.1 Physics of turbulent flow in a channel

#### 5.1.1 Geometrical properties

The geometry of a channel flow is illustrated in Figure 5.1. We assume that the mean flow is oriented in the  $x$  direction between two walls separated by a distance  $\lambda_y = 2\delta$ , where  $\delta$  is the channel half-width. Herein, the channel is periodic in both  $x$  and  $z$  directions. Hence, the main variation in the mean flow is due to the presence of the walls. In experiments a flow-development region can be observed as  $x$  periodicity is impossible to achieve. However, further downstream after a development length of the order of a hundred duct widths, the flow becomes statistically stationary and one-dimensional. Additionally, the mean flow is symmetric with respect to the mid-plane  $y = \delta$ . There are two Reynolds numbers which can be defined on the basis of geometrical properties and velocities. The first is based on the bulk velocity  $\tilde{v}$

$$Re = \frac{2\delta\tilde{v}}{\nu}. \quad (5.1)$$

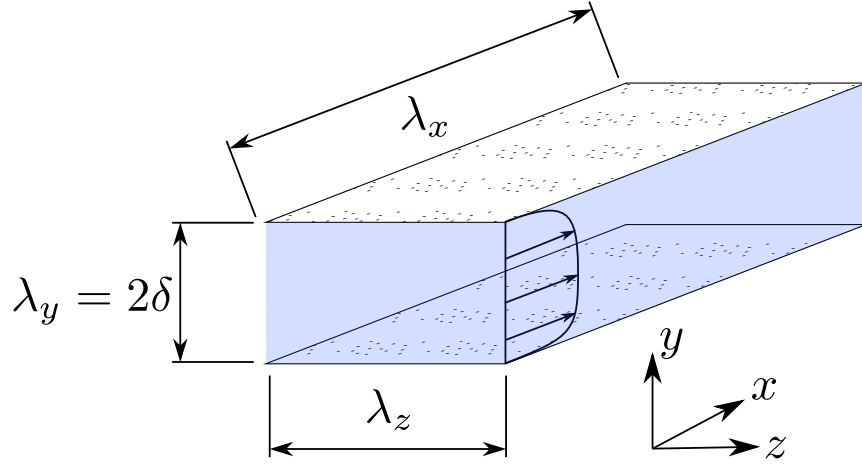


Figure 5.1: Geometry of the channel flow

The other is based on the centerline velocity  $v_0 = v(y)|_{y=0}$  and is defined as

$$Re_0 = \frac{\delta v_0}{\nu}. \quad (5.2)$$

Note particularly that the two Reynolds numbers use two different length scales,  $\delta$  and  $2\delta$ .

In the present section all derivations are made assuming the flow to be incompressible, *i.e.*  $\underline{\nabla} \cdot \underline{v} = 0$ . This significantly simplifies the theoretical analysis to follow. The numerical methods and simulations are still presented in a weakly compressible framework.

### 5.1.2 Reynolds averaged Navier-Stokes

As the flow under consideration is statistically stationary the Navier-Stokes equations can be rewritten to yield information about the mean flow quantities. In order to define mean quantities it is necessary to define the one-point, one-time joint cumulative distribution function as

$$F(\underline{V}, \underline{r}, t) = P\{\underline{v}(\underline{r}, t) < \underline{V}\}, \quad (5.3)$$

where  $P$  is a probability measure. The joint probability density function is given as

$$f(\underline{V}, \underline{r}, t) = \frac{\partial^3 F(\underline{V}, \underline{r}, t)}{\partial V_1 \partial V_2 \partial V_3}. \quad (5.4)$$

The mean can then be defined as

$$\langle \underline{v} \rangle = \int_{-\infty}^{\infty} \int_{-\infty}^{\infty} \int_{-\infty}^{\infty} \underline{V} f(\underline{V}, \underline{r}, t) dV_1 dV_2 dV_3. \quad (5.5)$$

This allows the fluctuating velocities

$$\underline{v}' := \underline{v} - \langle \underline{v} \rangle \quad (5.6)$$

which at the same time yields a decomposition of the velocity. From the fact that

$$\langle \underline{v}' \rangle = 0, \quad (5.7)$$

it can be deduced that

$$\underline{\nabla} \cdot \langle \underline{v} \rangle = 0. \quad (5.8)$$

Moreover, the Navier-Stokes equations can be rewritten to become the Reynolds equations given as

$$\frac{d\langle \underline{v} \rangle}{dt} = -\frac{1}{\rho} \underline{\nabla} \langle p \rangle + \underline{f}_{ext} + \nu \underline{\nabla} \cdot (\underline{\nabla} \otimes \langle \underline{v} \rangle) - \underline{\nabla} \cdot \langle \underline{v}' \otimes \underline{v}' \rangle, \quad (5.9)$$

which is a governing equation for the time-averaged velocity where  $\underline{f}_{ext}$  denotes an external driving force. Comparing the momentum equation for the instantaneous velocity (2.6) to the Reynolds equation it can be observed that the only difference is the last term in Eq. (5.9). The tensor  $\langle \underline{v}' \otimes \underline{v}' \rangle$  is the Reynolds stress tensor which plays a crucial role in describing the behavior of turbulent flows. Without a definition for this term Eq. (5.9) is not closed and unless the Reynolds stress tensor is known or modelled the equations cannot be solved.

### 5.1.3 The balance of forces

From the initial considerations in Section 5.1.1 it can be seen that  $\langle v_z \rangle = 0$  and that  $\langle v_x \rangle$  is independent of  $x$ , *i.e.*  $\partial \langle v_x \rangle / \partial x = 0$ . From this and Eq. (5.8) it can thus be deduced that  $\partial \langle v_y \rangle / \partial y = 0$  and since  $\langle v_y \rangle = 0$  at  $y = 0, 2\delta$  it can be seen that  $\langle v_y \rangle = 0$ . Under steady conditions the Reynolds equation (5.9) in the mean-flow direction reduces to

$$0 = \underline{f}_{ext} + \nu \frac{\partial^2 \langle v_x \rangle}{\partial y^2} - \frac{\partial \langle v'_x v'_y \rangle}{\partial y}, \quad (5.10)$$

where the fact that  $\partial \langle p \rangle / \partial x = 0$  has been used. The total shear stress

$$\tau := \rho \nu \frac{\partial \langle v_x \rangle}{\partial y} - \rho \langle v'_x v'_y \rangle, \quad (5.11)$$

resulting in

$$-\frac{d\tau}{dy} = \rho f_{ext}. \quad (5.12)$$

This formula shows the two forces which are balanced in the statistically stationary state. On the left side is the shear stress in wall-normal direction which is balanced by the external driving force on the right hand side. This also indicates that the shear stress is a linear function and as it is antisymmetric with respect to  $y$  the wall shear stress can be defined as  $\tau_w := \tau(y)|_{y=0} = -\tau(y)|_{y=2\delta}$ , such that

$$\tau(y) = \tau_w \left(1 - \frac{y}{\delta}\right). \quad (5.13)$$

Eq. (5.12) can thus be rewritten to read

$$\frac{\tau_w}{\delta} = \rho f_{ext}. \quad (5.14)$$

As the wall shear stress depends on the velocity the question arises if there is a relationship between the two. Indeed a skin-friction coefficient can be defined based on either the centerline velocity or the bulk-velocity

$$c_f = \frac{2\tau_w}{\rho v_0^2}, \quad (5.15)$$

$$C_f = \frac{2\tau_w}{\rho \tilde{v}^2}. \quad (5.16)$$

Eq. (5.14) allows the imposition of a wall shear stress by using a constant (in time) driving force. On the other hand, using a variable driving force such as the one presented in Section 3.3 allows the control of either  $v_0$  or  $\tilde{v}$ . Under any circumstance the skin-friction coefficient is a result of the simulation or experiment and is thus an important quantity for comparison.

#### 5.1.4 Turbulent scales

In Section 5.1.1 certain scales of the flow have already been defined. However, as indicated by the last paragraph in the previous section the wall shear stress is a quantity that can determine the flow as well. Thus, the question arises if a characteristic velocity can be defined based on  $\tau_w$  and indeed the friction velocity does just that, being given by

$$v_\tau := \sqrt{\frac{\tau_w}{\rho}}. \quad (5.17)$$

The name friction velocity stems from the fact that the turbulence at the wall is negligible as discussed in greater detail in the next section. Thus, viscous forces dominate the near-wall behavior and so the flow close to the wall is essentially laminar. If the

viscous length scale is defined as

$$\delta_\nu = \frac{\nu}{v_\tau}, \quad (5.18)$$

then the local viscous Reynolds number close to the wall can be considered in an identical manner. Hence, it is possible to define a friction Reynolds number as

$$Re_\tau = \frac{v_\tau \delta}{\nu}. \quad (5.19)$$

The question that naturally arises is how the different Reynolds numbers relate to each other. Following from the previous section, using Eq. (5.15), it can be seen that

$$c_f = 2 \left( \frac{Re_\tau}{Re_0} \right)^2. \quad (5.20)$$

Finally, one important consequence from the definition of the viscous length scale is that it can be used to normalise the flow length scales. Such a normalized quantity is denoted by the superscript +, *e.g.*

$$y^+ = \frac{y}{\delta_\nu}. \quad (5.21)$$

From this and Eq. (5.19)  $y^+$  is alternatively given as  $y^+ = Re_\tau \frac{y}{\delta}$ .

### 5.1.5 Mean velocity profiles

At this point it is instructive to examine the different contributions to the total shear stress for a turbulent flow.

Figure 5.2 shows the contributions to the total stress for a flow characterised by  $Re_\tau = 395$  (Moser *et al.* (1999)). Close to the wall it can be observed that the viscous stress dominates compared to the interior where the Reynolds stress is the main contribution. This demonstrates the fact that the mean velocity can be decomposed into two different regimes. Following the discussion from the previous chapters the length scales for these two regimes are readily available. On the one hand there is the viscous scale  $y/\delta_\nu$  and on the other hand  $y/\delta$ . The ansatz given in Pope (2001) concerns the wall-normal derivative of  $\langle v_x \rangle$  which is given as

$$\frac{d\langle v_x \rangle}{dy} = \frac{v_\tau}{y} \Phi \left( \frac{y}{\delta_\nu}, \frac{y}{\delta} \right), \quad (5.22)$$

with a non-dimensional function  $\Phi$ .

As the Reynolds stress converges to zero near the wall Eq. (5.22) can be rewritten to read

$$\frac{d\langle v_x \rangle}{dy} = \frac{v_\tau}{y} \Phi_w \left( \frac{y}{\delta_\nu} \right), \quad (5.23)$$

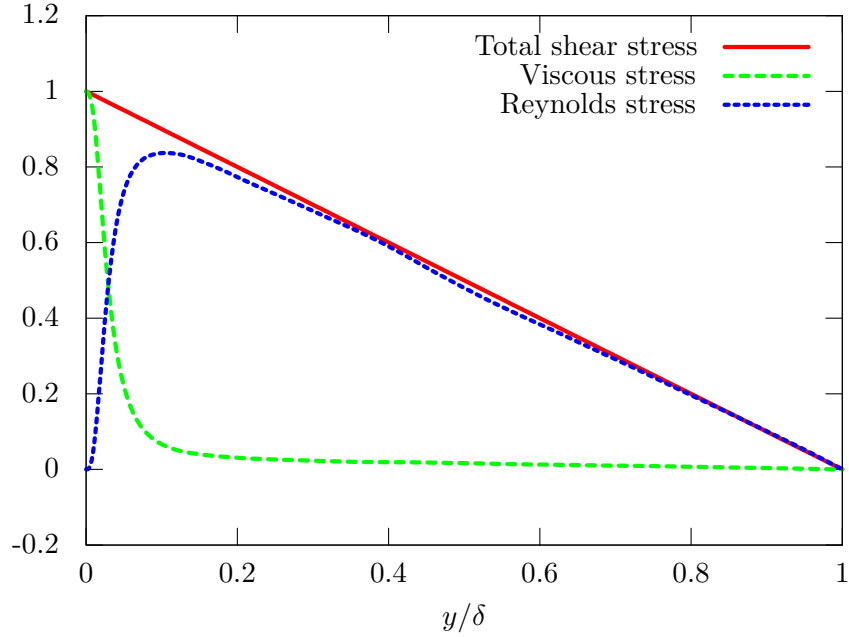


Figure 5.2: Comparison of contributions of viscous and Reynolds stress to the total stress. Data by Moser *et al.* (1999) for a channel flow with  $Re_\tau = 395$ .

for  $y/\delta \ll 1$ . Using a normalized velocity  $v^+$  given as

$$v^+ = \frac{\langle v_x \rangle}{v_\tau}, \quad (5.24)$$

the above equation yields

$$\frac{dv^+}{dy} = \frac{1}{y} \Phi_w(y^+). \quad (5.25)$$

Integrating with respect to  $y$  yields

$$v^+ = f_w(y^+), \quad (5.26)$$

where

$$f_w(y^+) = \int_0^{y^+} \frac{1}{y} \Phi_w(y) dy. \quad (5.27)$$

It is well established that this function  $f_w$  is universal for different types of wall-bounded flows (Pope, 2001, Chapter 7.1.4).

In the following, two regimes of small and large  $y^+$  are investigated separately and formulae for  $f_w$  are shown. Finally, the velocity near the center is discussed.

### 5.1.5.1 Near wall profile

For small  $y^+$  there are two conditions which yield a functional form of  $f_w$ . The no-slip boundary condition implies that  $f_w(0) = 0$ . Close to the wall the shear stress is completely defined by the viscous shear, *i.e.*

$$\tau_w = \rho\nu \frac{d\langle v_x \rangle}{dy}(y) \Big|_{y=0}. \quad (5.28)$$

Together with the definition of  $v^+$  given in Eq. (5.24) this yields

$$\frac{df_w}{dy}(0) = 1, \quad (5.29)$$

and thus

$$v^+ = y^+. \quad (5.30)$$

This relationship holds true for  $y^+ < 5$  which is the viscous sublayer (Pope (2001)).

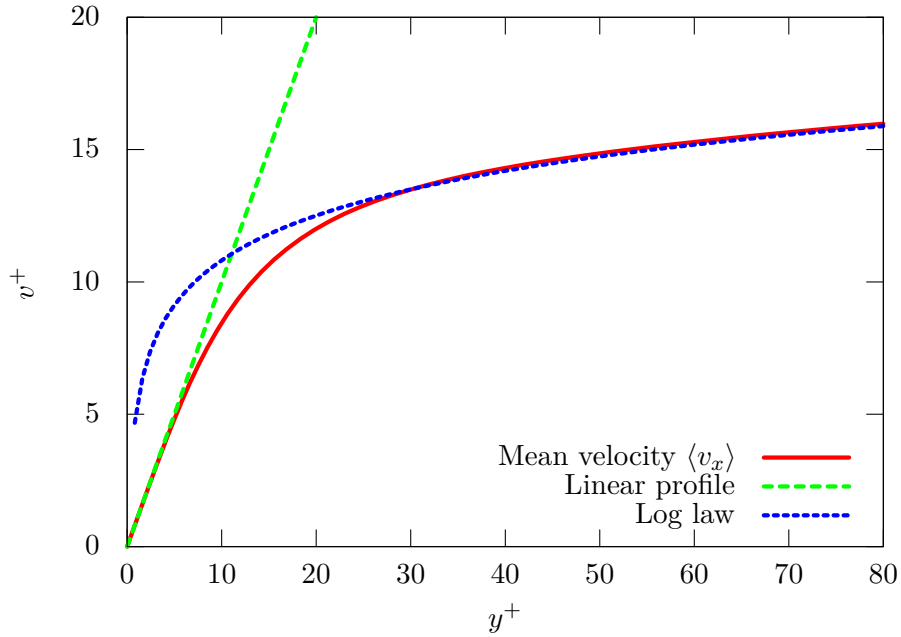


Figure 5.3: Profile of mean-velocity close to the wall including both the linear and the log law. Data by Moser *et al.* (1999) for a channel flow with  $Re_\tau = 395$ .

In Figure 5.3 the linear law can be seen compared to the results of a direct numerical simulation by Moser *et al.* (1999) at  $Re_\tau = 395$ .

### 5.1.5.2 The log law

For larger  $y^+$  the effect of viscosity vanishes as shown in Figure 5.2 and so  $\Phi_w$  is constant. It is common that this is written as

$$\Phi_w = \frac{1}{\kappa}, \quad (5.31)$$

with  $\kappa$  being the von Karman constant. Thus,  $v^+$  is given by

$$v^+ = \frac{1}{\kappa} \ln y^+ + B, \quad (5.32)$$

where again  $B$  is a constant. The values of these two constants are generally given as

$$\kappa = 0.41 \quad \text{and} \quad B = 5.2. \quad (5.33)$$

Figure 5.3 shows the log law which agrees well with the data by Moser *et al.* (1999) for  $y^+ \gg 1$ .

### 5.1.5.3 Velocity near the center

The approximation in Eq. (5.23) breaks down in the center of the channel as  $y/\delta$  is of the order of unity. This is usually referred to as the velocity defect law. In this region it is no longer possible to derive a flow-independent law for this flow regime. As this effect is negligible for channel flows with the Reynolds numbers considered in this thesis this law shall not be discussed any further. The interested reader is referred to Pope (2001).

## 5.2 Numerical approaches for simulating turbulent wall-bounded flows

With the advent of computers and the exponential growth in computing capabilities the numerical simulation of fluid flows has become an important tool in both research and industrial application. There are three main approaches to such a numerical simulation, two of which are dealt with in detail in the following. The third is based on the Reynolds averaged Navier-Stokes equations as presented in Section 5.1.2. The downside of this approach is that it uses statistical averaging, often simplified as Eulerian time-averaging which might not be desirable, for example, when considering time dependent mean flows (*e.g.* large-scale vortex shedding, ramp flow rate, free surface waves)

In the following the requirements for a direct numerical simulation (DNS) is discussed with a particular focus on the application to SPH. This chapter is then concluded by looking at large eddy simulation (LES), a technique in which the large eddies are

resolved and the smaller ones are modelled. Besides showing the standard Smagorinsky and Yoshizawa models, wall functions for non-wall resolved simulations are investigated as well.

### 5.2.1 Direct numerical simulation

From a conceptual point of view direct numerical simulation is the simplest of all approaches as it only requires the simulation of the Navier-Stokes equations. This however implies that all turbulent motion needs to be resolved, leading to extremely high computational demands.

The first direct numerical simulations were performed to investigate the decay of isotropic turbulence using grid-based approaches. This case which is periodic in all directions allows the use of (pseudo-)spectral discretization schemes. The smallest scale present in turbulent flows is the Kolmogorov scale given by

$$\eta := \left( \frac{\nu^3}{\epsilon} \right)^{1/4}, \quad (5.34)$$

where

$$\epsilon := 2\nu \langle \underline{\underline{s}} : \underline{\underline{s}} \rangle, \quad (5.35)$$

represents the dissipation of turbulent kinetic energy and  $\underline{\underline{s}}$  is the rate of strain tensor based on the fluctuating velocities  $\underline{\underline{v}}'$ . An additional time-step constraint due to the CFL condition implies finally that the number of cells times the number of time-steps grows with the cube of the Reynolds number.

To obtain a DNS of wall-bounded flows certain modifications need to be made. In the case of the channel flow this implies that in the  $y$  direction spectral methods can no longer be employed and instead Chebyshev polynomials are used which also provide a orthogonal basis for the function space under consideration. Of particular importance is the near wall behavior and so it is common that schemes are used which allow a variable resolution in the  $y$  direction. As discussed in Section 5.1.4 the typical length scale close to the wall is  $\delta_\nu$  and Pope (2001) recommends a grid spacing smaller than  $\delta_\nu/20$  in order to correctly resolve the dissipative processes.

When using a second-order finite difference scheme for the space discretization then the number of grid points needs to be quadrupled as shown by Ghosal (1996).

#### 5.2.1.1 Quasi DNS

The significant computational demands of a DNS often cannot be met when considering industrial cases where Reynolds numbers tend to be large. A possible circumvention can be achieved by using an underresolved grid while still only solving the Navier-Stokes

equations without any additional model. This enables low order statistics to be obtained such as mean velocity and Reynolds stresses. However, this quasi DNS approach fails to yield correct higher order statistics such as dissipation. An example of such a quasi DNS can be found in the paper by Afgan *et al.* (2013).

### 5.2.2 Large eddy simulation

To lower the computational demand the most common approach is to use some type of modelling. In the introduction of this section the RANS approach was briefly mentioned. Contrary to the time averaging used in RANS methods the large eddy simulation approach uses spatial filtering. Moreover, similar to the unsteady RANS the averaging is of a local nature. The general approach is to define a filtered velocity as given by

$$\bar{v}(\underline{x}, t) = \int_{\Omega} G(\underline{r}, \underline{x}) v(\underline{x} - \underline{r}, t) d\underline{r}, \quad (5.36)$$

where  $G$  is the filter which is required to satisfy

$$\int_{\Omega} G(\underline{r}, \underline{x}) = 1. \quad (5.37)$$

Most LES filters are defined without explicit dependence on  $\underline{x}$  and for computational efficiency they are assumed to be local, *i.e.*  $G(\underline{r}) = 0 \quad \forall \|\underline{r}\| > \Delta_G$ . Looking at Eqs. (2.46) and (2.50) a striking similarity can be observed. Indeed, the SPH method already contains an LES filter as noted by Issa (2004). However, until now the SPH operators were applied directly to the Navier-Stokes equations by assuming the Kronecker delta property  $f_a = \langle f \rangle_a$ . Thus, the effect of averaging was not included, something that is investigated in the context of LES.

Filtering the Navier-Stokes equations yields

$$\frac{\partial \bar{v}}{\partial t} + \nabla \cdot \overline{v \otimes v} = \nu \nabla \cdot (\nabla \otimes \bar{v}) - \frac{1}{\rho} \nabla \bar{p}. \quad (5.38)$$

The residual-stress tensor

$$\underline{\tau}_R := \overline{v \otimes v} - \bar{v} \otimes \bar{v}, \quad (5.39)$$

which is similar to the Reynolds stress tensor  $\langle v' \otimes v' \rangle$  shown in Section 5.1.2. From this it is possible to define the residual kinetic energy as

$$k_r := tr(\underline{\tau}_R)/2, \quad (5.40)$$

where  $tr$  is the trace operator. The anisotropic residual-stress tensor is given by

$$\underline{\tau}_r = \underline{\tau}_R - \frac{2}{3} k_r \underline{I}. \quad (5.41)$$

The filtered Navier-Stokes equations finally read

$$\frac{\partial \underline{v}}{\partial t} = \nu \underline{\nabla} \cdot (\underline{\nabla} \otimes \underline{v}) - \underline{\nabla} \cdot \underline{\underline{\tau}}_r - \frac{1}{\rho} \underline{\nabla} \left( \bar{p} + \frac{2}{3} \rho k_r \right). \quad (5.42)$$

There are two terms in this equation which require closing. The first is the anisotropic residual-stress tensor and the second the residual kinetic energy. Models for the two are presented in the following section.

First however, the continuity equation is investigated. If the equation is filtered similar to the Navier-Stokes equations, then an additional stress term appears. In order to avoid this Favre averaging can be used (Favre (1969)). The idea is to filter all quantities  $(\rho, p, \underline{v})$  with the LES filter but additionally changing the filtered velocity to

$$\tilde{\underline{v}} = \frac{\overline{\rho \underline{v}}}{\bar{\rho}}. \quad (5.43)$$

Favre averaging avoids the appearance of an additional term in the continuity equation which reads

$$\frac{d\bar{\rho}}{dt} = -\bar{\rho} \underline{\nabla} \cdot \tilde{\underline{v}}. \quad (5.44)$$

However, there is an additional term appearing in the momentum equation, which needs closure. This term is neglected in the following due to the weakly compressible nature of the present SPH approach. This is due to the fact that the right and left hand sides of Eq. (5.43) are nearly identical in the weakly compressible setting.

### 5.2.2.1 The Smagorinsky and Yoshizawa models

In order to close the anisotropic residual-stress tensor  $\underline{\underline{\tau}}_r$  the basic Smagorinsky (1963) model is used. It is the equivalent of the mixing-length model in the RANS setting. The first step is to apply the linear eddy-viscosity model which states that the anisotropic residual-stress tensor is aligned with the filtered rate of strain tensor

$$\underline{\underline{\tau}}_r = -2\nu_r \underline{\underline{S}}, \quad (5.45)$$

where  $\nu_r$  is the turbulent eddy viscosity which models the dissipation of the eddies with sizes smaller than the filter width  $\Delta_G$  and  $\underline{\underline{S}}$  is the filtered rate-of-strain tensor. After reducing the unknown tensor to an unknown scalar a model for the latter needs to be found. This comes in the form of the mixing-length model which states that

$$\nu_r = l_S^2 \bar{S}, \quad (5.46)$$

where  $\bar{S} = (2\underline{\underline{S}} : \underline{\underline{S}})^{1/2}$  is the rate of strain and  $l_S$  is the Smagorinsky length scale which is given by

$$l_S = C_S \Delta_G, \quad (5.47)$$

where  $C_S$  is the Smagorinsky coefficient. The value of this coefficient depends on the particular choice of the filter, a common value is  $C_S = 0.17$  which is based on an analysis by Lilly (1967) for the sharp spectral filter (truncation in Fourier space). In Appendix B this analysis is extended to the Wendland kernel showing that  $C_S = 0.158$ . Moreover, the value is flow-dependent and for the particular application of the turbulent channel flow Moin and Kim (1982) used a value of  $C_S = 0.065$ . All simulations with the Smagorinsky model presented below use this value.

In the context of SPH two further issues arise. The first one contains the computation of  $\bar{S}$ . The simplest approach is simply to calculate the derivatives involved and perform the convolution. This requires a certain amount of memory and computation time as nine gradients need to be calculated. Alternatively, a model derived by Violeau and Issa (2007) can be used that was extended by Ferrand (2010) to the present wall-boundary conditions. This model is given by

$$(\nu_r \bar{S}^2)_a = -\frac{1}{2\rho_a \gamma_a} \sum_{b \in \mathcal{P}} V_b (\rho_a \nu_{r,a} + \rho_b \nu_{r,b}) \frac{\bar{v}_{ab}^2}{r_{ab}^2} \mathbf{r}_{ab} \cdot \nabla w_{ab} - \frac{2}{\gamma_a} \sum_{s \in \mathcal{S}} v_{\tau,s}^2 \|\nabla \gamma_{as}\|. \quad (5.48)$$

The second issue concerns the choice of  $\Delta_G$ . According to LES theory the appropriate choice for the Wendland kernel is  $\Delta_G = 2h$ .

After closing the anisotropic residual-stress tensor the remaining unknown is the residual kinetic energy  $k_r$ . Again, a rather simple model by Yoshizawa (1986) is used which was already successfully applied to a three-dimensional SPH-LES by Dalrymple and Rogers (2006). The residual kinetic energy is given by

$$k_r = 2C_Y (\Delta_G \bar{S})^2, \quad (5.49)$$

where  $C_Y$  is the Yoshizawa constant with a value of 0.044. Note that this model is only required in the weakly compressible setting. In the case of an incompressible simulation this residual kinetic energy can be used to define a modified pressure  $P = p + k_r$  and so an explicit model is no longer required.

The LES approach can be considered in two limits with the filter width  $\Delta_G$  tending to zero and infinity respectively. In the first case it is expected that the DNS method is recovered. However, according to Pope (2001) the limiting behavior is dependent on the filter type and no clear conclusion can be drawn in the case of the Smagorinsky model. The more important case on the other hand is the coarse discretisation limit as this might occur if the resolution is not chosen appropriately. In this case the filtered

velocity  $\bar{v}$  tends towards the time-averaged velocity  $\langle v \rangle$ . Or, in the words of Speziale (1998) “the Smagorinsky model goes to a badly calibrated mixing length model in the coarse mesh limit”.

### 5.2.2.2 Wall modelling

The last question that is treated in this section concerns eddies close to a wall. Their size is limited by the distance to the wall and as such the Smagorinsky length scale should decrease. As discussed in Section 5.1.5, near a wall the viscous stresses become increasingly important as an inverse function of distance to the wall. Thus, both the eddy viscosity as well as the residual kinetic energy should converge to zero. In mesh-based methods wall modelling is usually avoided by changing the resolution close to the wall and so effectively changing  $\Delta_G$ . As the present SPH method is not capable of such variable resolution a different approach needs to be found that modifies the Smagorinsky length scale as a function of the distance to the wall. Moin and Kim (1982) propose a van Dries damping function which scales the Smagorinsky length scale according to

$$l_S = C_S \Delta_G (1 - \exp(y^+/A^+)), \quad (5.50)$$

with  $A^+ = 25$ . Additionally, in the viscous term given by Eq. (2.144) the friction velocity can no longer be defined according to the laminar model shown in Eq. (2.146). Alternatively it is possible to use the log law shown in Section 5.1.5 as already applied by Ferrand *et al.* (2012) which reads

$$\frac{\|v\|}{v_\tau} = \frac{1}{\kappa} \ln(y^+) + B, \quad (5.51)$$

where

$$y^+ = \frac{y v_\tau}{\nu}. \quad (5.52)$$

This provides an implicit formula for  $v_\tau$ . To be slightly more flexible, *i.e.* being able to handle particles approaching the wall, Reichard’s law can be used which combines both the log law and the linear law as shown in Sections 5.1.5.1 and 5.1.5.2. The implicit formula for  $v_\tau$  is given by

$$\frac{\|v\|}{v_\tau} = \frac{\ln(1 + \kappa y^+)}{\kappa} + 7.8 \left( 1 - \exp(-y^+/11) - \frac{y^+}{11} \exp(-y^+/3) \right) + 1. \quad (5.53)$$

### 5.2.3 Statistics

In order to qualitatively investigate turbulent flows, both Eulerian as well as Lagrangian statistics can be used. The former type is more readily available in literature due to the fact that they are easily obtainable from mesh-based codes. Conversely, to obtain

Lagrangian statistics mesh-based methods need to use some type of interpolation. As this thesis is based on the Lagrangian SPH method the issue is the opposite one. In order to obtain Eulerian statistics an interpolation is required, whereas Lagrangian statistics can be obtained directly by following the particles. Herein, possible interpolation techniques are shown and the different statistics shown in the following chapter are introduced.

### 5.2.3.1 Eulerian statistics

Two different types of interpolation from Lagrangian particles to a fixed grid are presented in the following. The first is based on a binning technique, *i.e.* the value of a function  $f$  at a grid point  $i$  at position  $\underline{r}_i$  is given by

$$f_i = \frac{1}{|\mathcal{P}_i|} \sum_{a \in \mathcal{P}_i} f_a, \quad (5.54)$$

where  $\mathcal{P}_i$  is the set of all particles around grid point  $i$ , *i.e.*

$$\mathcal{P}_i = \{a \in \mathcal{P} : \|\underline{r}_a - \underline{r}_i\|_1 < \Delta_E\}, \quad (5.55)$$

$\Delta_E$  is the grid-size of the Eulerian grid and  $\|\cdot\|_1$  the one norm. Alternatively to this binning technique, a simple SPH approximation can be used such that

$$f_i = \frac{1}{\sum_{a \in \mathcal{P}} V_a w_{ai}} \sum_{a \in \mathcal{P}} V_a f_a w_{ai}. \quad (5.56)$$

These two techniques are used to investigate several time and space-averaged quantities. Of particular interest are certain RANS quantities such as the average velocity  $\langle \underline{v} \rangle$  and the components of the Reynolds stress tensor  $\underline{v}' \otimes \underline{v}'$ , particularly  $v_x'^2$ ,  $v_y'^2$  and  $v_x'v_y'$ . Furthermore, the two-point spatial autocorrelation function is used as a qualitative measure. The two-point correlation is given as

$$R_{ij}(l) := \langle v_i(\underline{r})v_j(\underline{r} + l\mathbf{e}_j) \rangle, \quad (5.57)$$

and the two-point autocorrelation as

$$\rho_{ij}(l) := R_{ij}(l) / \langle v_i(\underline{r})^2 \rangle. \quad (5.58)$$

As the channel flow is not homogeneous in the  $y$  direction these functions also depend on  $y$ . The significance of the correlation functions are twofold. On the one hand side they determine the correlation between two different points in the flow and on the other hand the Fourier transform of the two-point correlation gives the energy spectrum which

is defined as

$$E_{ij}(\kappa) = \frac{2}{\pi} \int_0^\infty R_{ij}(l) \cos(\kappa l) dl. \quad (5.59)$$

It shall be noted that due to  $R_{ij}$  being even and real functions the same holds true for  $E_{ij}$ .

### 5.2.3.2 Lagrangian statistics

Lagrangian statistics are of interest since since they are difficult to obtain from experimental methods, yet very important for dispersed two phase flow modeling (*e.g.* bubbles, pulverised coal, suspended sediments). Lagrangian statistics from LES or DNS can be used to investigate model constants for certain statistical methods. The statistics used in the following are similar to the ones presented in the paper by Choi *et al.* (2004) which uses an Eulerian DNS to obtain Lagrangian statistics via several interpolation methods.

As in the Eulerian framework correlation functions are of central importance as well as Lagrangian structure functions. They are obtained by following particles which initially are at a certain distance to the wall. The velocity autocorrelation function is defined as

$$\rho_{ii}^L(t) := \frac{\langle v_i(t_0)v_i(t+t_0) \rangle}{\sqrt{v_i^2(t_0)}\sqrt{v_i^2(t+t_0)}}. \quad (5.60)$$

Note that in this section the average  $\langle \cdot \rangle$  denotes an ensemble-average. This also allows the definition of a correlation time scale  $T_{L,i}$  given as

$$T_{L,i} := \int_0^{4T_{E,i}} \rho_{ii}^L(t) dt, \quad (5.61)$$

where  $T_{E,i}$  is an estimated time scale defined such that  $\rho_{ii}^L(T_{E,i}/2) = 1/\sqrt{e}$ . Similar to the velocity autocorrelation function the acceleration autocorrelation can be defined as

$$\rho_{ii}^a(t) := \frac{\langle a_i(t_0)a_i(t+t_0) \rangle}{\sqrt{a_i^2(t_0)}\sqrt{a_i^2(t+t_0)}}, \quad (5.62)$$

where  $a$  is the acceleration of a particle.

In terms of structure functions the ones based on the velocity are given by

$$D_{ii}(t) = \langle (v_i(t+t_0) - v_i(t_0))^2 \rangle, \quad (5.63)$$

$$S_{ii}(t) = \langle (v_i(t+t_0) - v_i(t_0))^3 \rangle, \quad (5.64)$$

$$K_{ii}(t) = \langle (v_i(t+t_0) - v_i(t_0))^4 \rangle, \quad (5.65)$$

which are the deviation, skewness and kurtosis, respectively. The deviation is of importance as there are two Kolmogorov hypotheses which link  $D_{ii}$  to Eulerian quantities via certain constants. Numerical and experimental evidence however indicates that these constants are in fact flow-dependent. As the Kolmogorov theory is only applicable to homogeneous flows it is of interest to study the behavior of this model in non-homogeneous flows such as the turbulent channel flow. The kurtosis  $K_{ii}$  would vanish if the turbulence would follow a Gaussian distribution. It is well known, *e.g.* Frisch (1996), that this is not the case and thus  $K_{ii}$  provides a measure from the deviation of the Gaussian.

Furthermore, the second-order position structure function given as

$$\sigma_i^2(t) = \langle (r_i(t+t_0) - r_i(t_0))^2 \rangle, \quad (5.66)$$

is a measure of flow dispersion.

The final type of Lagrangian statistics is based on probability density functions (PDF), in particular  $P(y; x)$ . To obtain this function particles initially located at  $x = x_0$  are tracked. When they pass certain  $x_i$  a histogram of their  $y$  value is constructed. Note that  $P$  is also a function of the initial  $y$  value of the particles. Averaging over the  $z$  direction is assumed. To investigate more qualitatively these PDFs the first and second moments can be computed as

$$\mu_y = \int y P(y; x) dy, \quad (5.67)$$

$$\sigma_y = \int (y - \mu_y)^2 P(y; x) dy. \quad (5.68)$$

After presenting both the theoretical properties of the closed turbulent channel flow as well as numerical methods suitable to simulate such a flow both a quasi DNS and a LES using SPH are presented in the following chapter.

## Chapter 6

# SPH Simulation of the turbulent channel flow

SPH has been used to simulate turbulent wall-bounded flows for years. However, only a limited number of researchers investigated basic turbulent flows in detail and whether it is possible or not to reproduce their statistical behaviour in SPH. Robinson *et al.* (2008) investigated turbulent flows in 2-D, which are significantly different from three-dimensional turbulent flows (Pope, 2001). Three-dimensional turbulent flow simulations are scarce due to their significant computational demand. Hu and Adams (2012) recently investigated decaying and forced isotropic turbulence in 3-D. However, most engineering applications demand the simulation of turbulent wall-bounded flows. Issa (2004) performed a three-dimensional large eddy simulation (LES) of an open channel flow with Reynolds number  $Re = 538000$ . However, the turbulent intensities did not correspond closely to the experimental values. This issue is discussed in detail in Section 6.2.3. The movement of passive particles in turbulent flows is an issue that arises in certain engineering applications. This is particularly difficult to simulate with Eulerian methods as interpolation routines are required which can significantly influence the result (Choi *et al.*, 2004). A Lagrangian method such as SPH would be ideally suited for the simulation of such flows but to the best of the author's knowledge only Hu and Adams (2012) have investigated Lagrangian statistics of turbulent flows using SPH. As their simulations examined unbounded flows and the investigation of Lagrangian statistics in wall-bounded flows remains an outstanding issue.

In the present chapter the goal is to explore the capabilities of SPH to simulate three-dimensional turbulent wall-bounded flows and reproduce the associated statistics both in Eulerian and Lagrangian frameworks. In order to simulate such flows it is essential that the boundary conditions are properly imposed which was thoroughly investigated in the previous chapters. The main simulations of this chapter show two turbulent

channel flows. The first is a quasi direct numerical simulation on a minimal geometry with a moderate Reynolds number, approximately  $\Re_\tau = 210$ . The second simulation is a large eddy simulation of a flow with  $Re_\tau = 1000$ . Both flows are analysed with respect to their Eulerian and Lagrangian statistics.

## 6.1 Quasi direct numerical simulation

### 6.1.1 Setup

The minimal flow unit is a test case first proposed by Jiménez and Moin (1991) and subsequently used in many other investigations. As the name already suggests it is the smallest computational box to study the flow between two infinite walls that allows turbulence to be self-sustained, *i.e.* exactly one typical turbulent kinetic energy producing turbulent structure, an unsteady streamwise meandering vortex and a low speed streak, is contained in this setup which captures all the flow physics of the viscous sublayer, buffer layer and beginning of the log-law. This makes this minimal channel ideal for our purpose as it reduces computation effort significantly compared to standard size channel flow simulations which would be approximately six times as large, but at the expense of longer time integration to obtain converged statistics.

In the reference paper Jiménez and Moin (1991) simulate three different Reynolds numbers using a spectral Navier-Stokes scheme based on staggered grids. Herein, only the highest Reynolds number of  $Re = 5000$  is reported in order to avoid problems with intermittent relaminarization as observed by both Jiménez and Moin (1991) and in our preliminary attempts (not reported herein). The grid discretization used for their computational box was  $32 \times 129 \times 16$  in the  $x, y, z$  directions. Here, one important disadvantage of SPH is that the discretization is isotropic whereas Jiménez and Moin (1991) used non-homogeneous regular grids in the wall parallel directions with a cell aspect ratio of about 10 in each direction, resulting in savings of a factor 100 as compared to cubic cells. Thus, the particle count depends on the smallest resolution, in this case the  $y$ -resolution, which significantly increases the particle count compared to the node count in the original paper. An additional downside of this case is that, due to the single turbulent structure, convergence takes much longer. Again, SPH with its restrictive time-step thus demands large computation times.

Hence, the question arises whether such an SPH quasi DNS would actually provide any valuable insights. Indeed, there are several points that can be investigated which provide a deeper understanding of SPH and form a basis for future research of turbulent flows. Initially, the interest is to determine whether turbulent Eulerian statistics can be reproduced using SPH. This depends specifically on the dissipation properties of the numerical scheme which have never been investigated in wall-bounded turbulent

Table 6.1: Comparison of the two different minimal channel configurations.

Property	MCF1	MCF2
$\lambda_x$	3.14	2.5
$\lambda_y$	2.0	2.0
$\lambda_z$	1.0	0.6
$\Delta r$	0.015625	0.003333
$ \mathcal{P} $	1.710.912	10.155.014

flows. Additionally, using a quasi DNS means that no model is used, in opposition to LES where it is possible to compensate numerical dissipation by selecting lower than theoretical values for the Smagorinsky eddy viscosity model constant. Moreover it is possible to obtain Lagrangian statistics straight from a Lagrangian method without needing to use any interpolation techniques as used *e.g.* by Choi *et al.* (2004).

In the following two different cases of the minimal channel are simulated, MCF1 and MCF2. They differ in terms of box size, momentum driving force methods and initialization. A comparison of their geometrical details can be seen in Table 6.1. MCF1 is, equivalent to the flow in Jiménez and Moin (1991), driven by a constant volume flux which imposes  $Re = 5000$ , *i.e.* constant mean flow rate. Initially the simulation starts from a parabolic velocity profile with a centerline velocity  $v_0 = 1$  with an overlay of sin functions and random perturbations. The procedure used by Jiménez and Moin (1991) is reproduced whereby a low viscosity is used at the beginning (equivalent to  $Re = 10000$ ) and then it is reduced to the target viscosity as soon as the turbulent structures are sufficiently developed. Contrary to that, MCF2 is driven by a constant force which imposes  $Re_\tau = 210$ , *i.e.* the pressure gradient and consequently the mean friction on the walls is now kept constant whereas the mean flow rate may vary during the simulation depending on how well turbulence is developed. The flow is initialized using a snapshot velocity field from a DNS obtained with a spectral code. The most significant difference between the two flows is the different resolution. MCF1 uses the same resolution as the spectral method of the original paper. However, as SPH does not feature the same order of accuracy and it is not a staggered method it can be expected that the flow is not adequately resolved. The resolution of MCF2 is five times higher than the one of MCF1, which allowed a reasonable resolution while being within the limits of the computational resources that were available.

At variance with the DNS of Jiménez and Moin (1991) which is based on a well established non dissipative spectral method and time integration, the present SPH method is prone to some numerical dissipation, in particular due to the volume diffusion term as

given in Eq. (3.34) which is required, otherwise the turbulent structures are perturbed by pressure fluctuations which, as a result, cause the flow to laminarize. Choosing the constant  $\xi = 1$  as in the paper by Ferrari *et al.* (2009) increases the diffusivity of the SPH scheme, again resulting in the decay of the turbulent fluctuations. Only by choosing  $\xi = 1000 \Delta r/L = 1000 \Delta r/2\delta$  according to mixing-length theory, as described in Section 3.2, ensures that the flow remains turbulent. This supports the interpretation presented in Section 3.2 that the volume diffusion term is responsible for smoothing out numerical “turbulence”. Additionally, choosing the Laplacian based on the discretization by Violeau as given in Eq. (2.100) reduces the diffusivity of the SPH method. This is due to the fact that the  $\nabla \cdot \underline{v}$  term in the stress tensor is not neglected.

Finally, before showing the results, a few details on the computation shall be remarked. Both simulations were run using double precision on IBM BlueGene/Q machines using 2048 MPI-taks, each of which used 16 OpenMP-threads. The simulation was run for approximately 2 million time-steps which corresponds to  $t^+ = 400$ . This long time frame was needed in order to reach converged statistics, which, as already noted by Jiménez and Moin (1991), is needed due to the reduced size of the channel. The flow is over-resolved in the streamwise direction, but this unavoidable because of the nature of the SPH method. A snapshot of the flow can be seen in Figure 6.1.

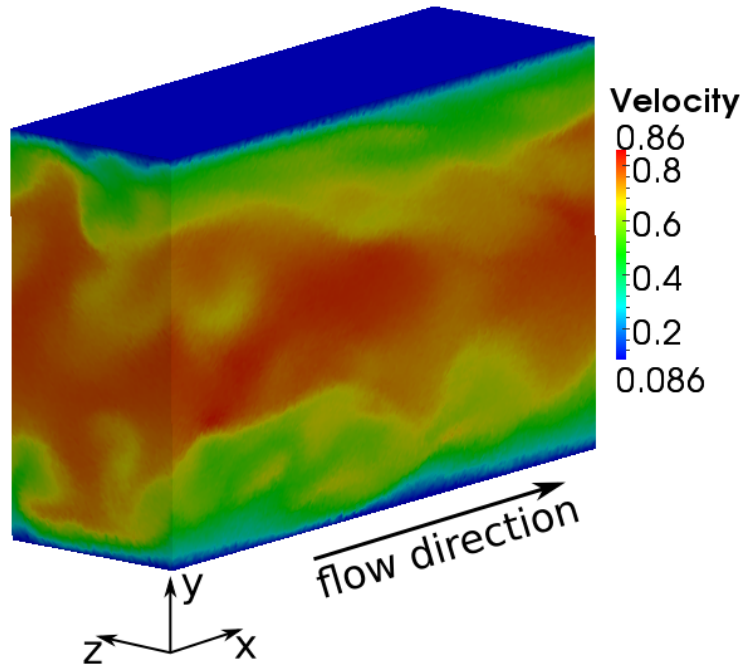
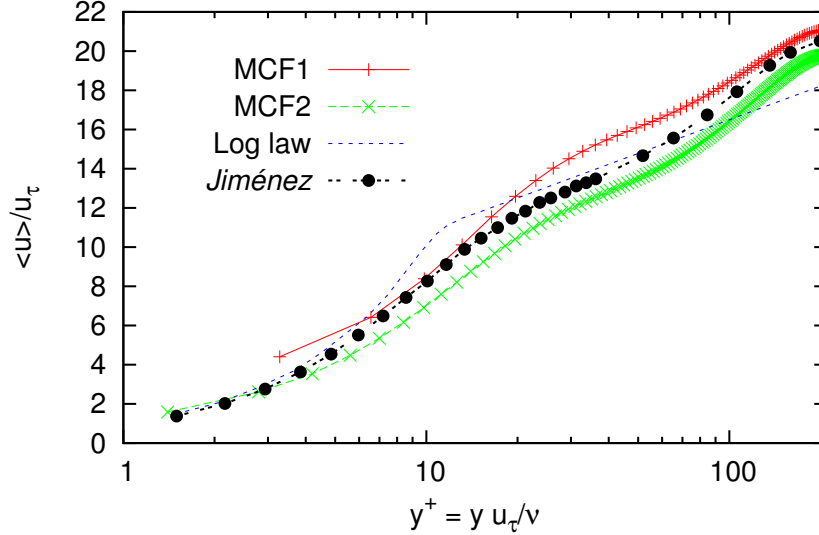


Figure 6.1: Snapshot of the instantaneous velocity of MCF1.

## 6.1.2 Eulerian statistics

Figure 6.2: Minimal channel: average velocity ( $y^+$  in log scale).

The first objective is the comparison of the results with the paper by Jiménez and Moin (1991) and the experimental results by Wei and Willmarth (1989). The respective datasets in the following plots are denoted with *Jimenez* or *J $\mathcal{E}$ M* and *Wei*, respectively. Since all these statistics are based on Eulerian quantities the results from the Lagrangian simulation need to be interpolated onto a grid. There are two different ways of achieving this: either use the SPH interpolation to obtain the value at a grid point or alternatively use a bin sampling technique. In this chapter we choose the latter on a grid with size  $\Delta r$ , the average particle distance. One disadvantage of such a small grid is that there might be none or only one particle inside the bin. To avoid not having values at a certain grid point a simple second order interpolation is used using adjacent grid points. Having only very few particles inside a bin can potentially cause a rather oscillatory output as is shown later. Larger bins would provide smoother statistical results but our objective here is precisely to highlight any defects of the computational method.

In Figure 6.2 the mean longitudinal velocity on the lower half of the channel, normalized by the friction velocity can be seen plotted against the solution by Jiménez and the classical log law (Pope (2001)). MCF2 shows a good agreement with the result by Jiménez. MCF1 on the other hand clearly overestimates the viscous wall region and produces a relatively small log-law region. At this point the value of the friction velocity  $v_\tau$  for MCF1 needs to be mentioned. It is straightforward to compute it from the external force applied to the flow and the resulting value is  $v_\tau/v_0 = 0.38$  which

corresponds to a friction Reynolds number  $Re_\tau = 190$ . Jiménez and Moin report a value of  $Re_\tau \approx 210$  indicating that the friction velocity is underpredicted in the low resolution simulation MCF1.

The results of MCF1 and MCF2 are expressed in dimensionless form using  $v_\tau = 190\nu/(\lambda_y/2)$  and  $v_\tau = 210\nu/(\lambda_y/2)$  respectively. In Figure 6.3 and 6.4 the turbulent intensities  $\sqrt{\langle v_x'^2 \rangle}$  and  $\sqrt{\langle v_y'^2 \rangle}$  can be seen plotted as function of  $y$ . The fluctuations in the streamwise velocity component are in generally good agreement with the benchmark results. Again an issue with the scaling of MCF1 can be observed. The wall normal velocity fluctuations are however rather different in that in the interior of the channel  $v_y'^2$  is overpredicted. A possible explanation for this result are spurious pressure waves which oscillate between the two walls as we have observed even in laminar flow after the breakup of the regular particle distribution. Finally, one should note the kink close to the wall in the MCF1 result at  $y/(\lambda_y/2) = 0.05, 0.95$ . It is possible that this is a numerical “wobble” as the fluid particle alternately passes directly past or in between 2 wall particles and is due to the non affine nature of the kernel function and discretisation, i.e. as a fluid particle moves at constant speed and exactly parallel to the wall it does not experience the same repulsive pressure force and shear stress from the wall particles when it is in an inline position or a staggered position, even if all the wall particles have the same pressure.

In order to investigate the wall behaviour more closely consider Figure 6.5 and 6.6 where the turbulent intensities are plotted over  $y^+ = y v_\tau / \nu$  in log scale. Again for the streamwise fluctuations good agreement can be observed with a slight overprediction

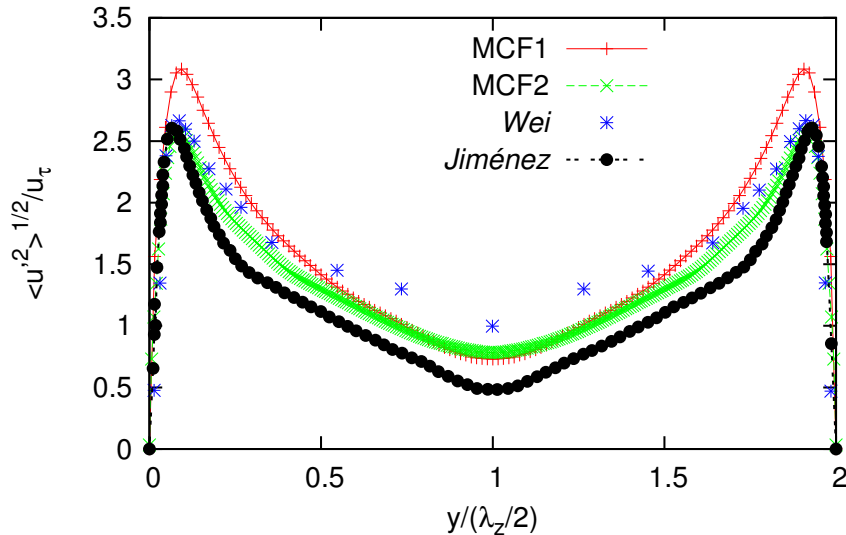


Figure 6.3: Minimal channel:  $\sqrt{\langle v_x'^2 \rangle}$ .

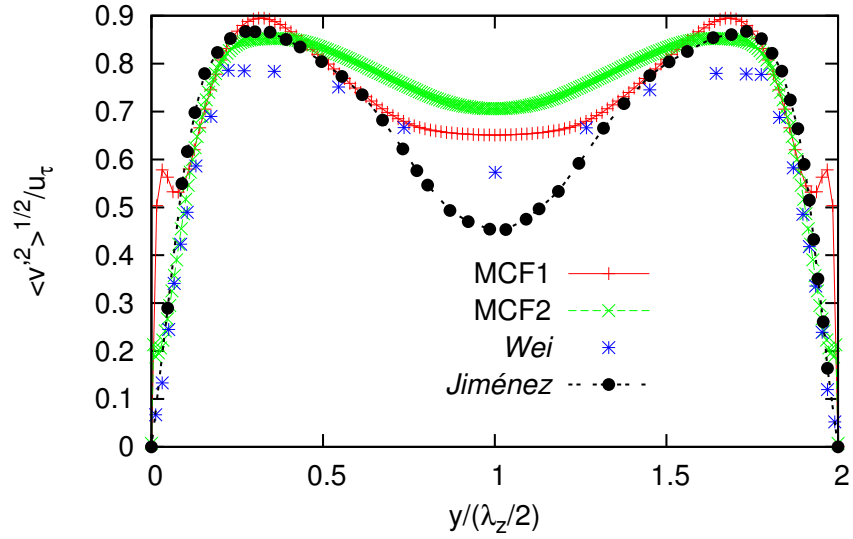


Figure 6.4: Minimal channel:  $\sqrt{v_y'^2}$ .

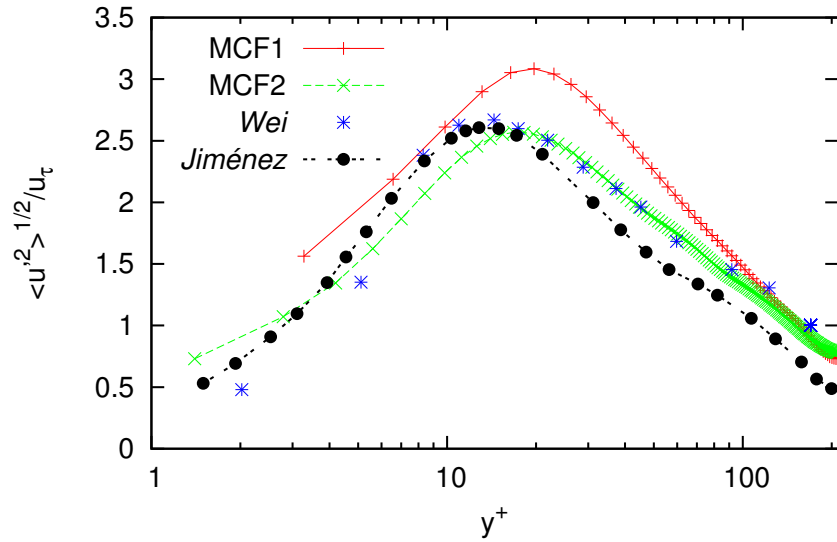
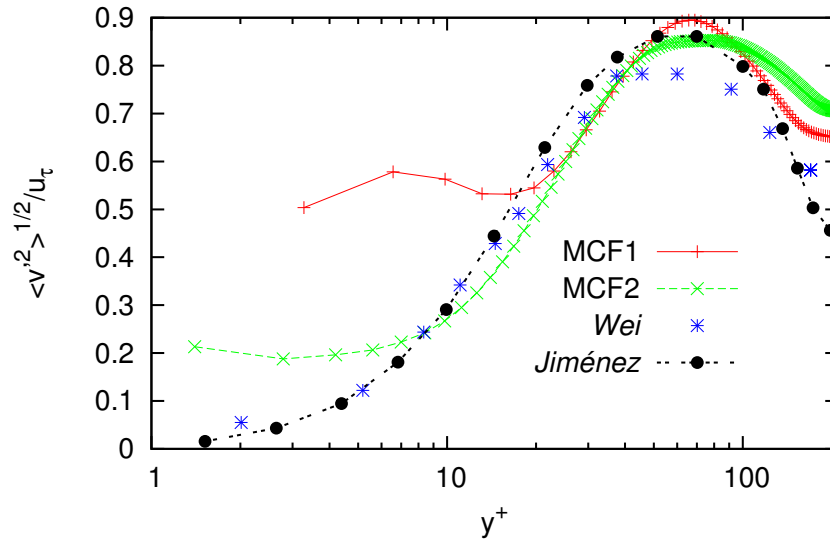
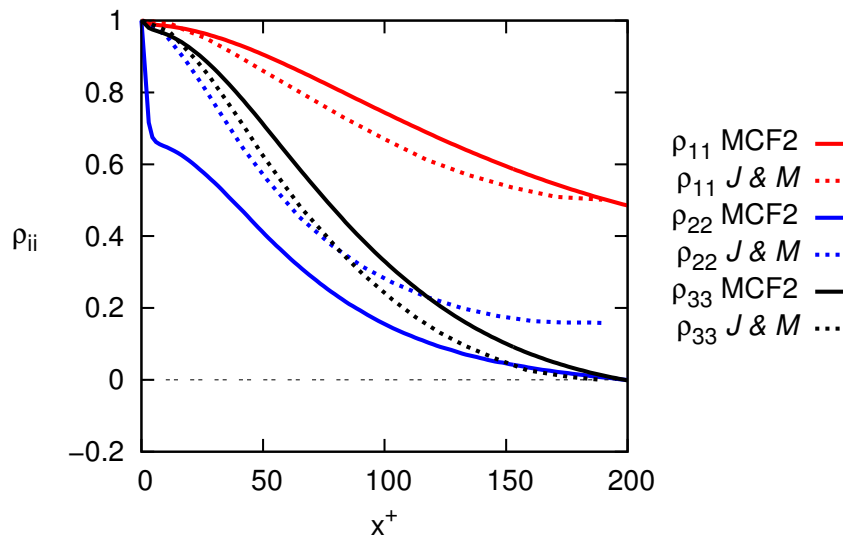


Figure 6.5: Minimal channel:  $\sqrt{v_x'^2}$  on log scale.

close to the wall. This is even more apparent in the wall normal fluctuations which are too high in both SPH simulations even though the effect is significantly smaller in the high resolution simulation. One important question for further research will be to determine whether this is due to the boundary conditions.

In Figure 6.7 the two-point autocorrelation  $\rho_{ij}(l) = \langle v_i(x_j)v_i(x_j + l e_j) \rangle / \langle v_i(x_j)^2 \rangle$ ,


 Figure 6.6: Minimal channel:  $\sqrt{v_y'^2}$  on log scale.

 Figure 6.7: Minimal channel: autocorrelation along the  $x$ -axis.

where the angular brackets denote ensemble averaging, is plotted in streamwise direction and in Figure 6.8 it is plotted in spanwise direction. Both of the plots show only half of the channel. In the streamwise direction a rather good agreement with the reference results of Jiménez and Moin (1991) can be observed for the  $v_x$  and  $v_z$  components. It should be noted that these correlations are at wall distance  $y^+ = 7.5$  and so are in the region where the deviation in the  $\langle v_y'^2 \rangle$  plot was beginning. Thus, it is

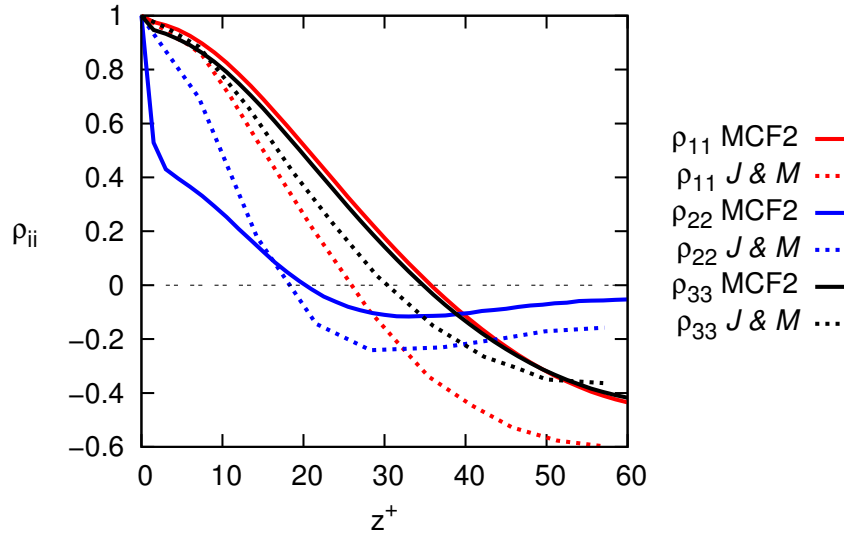


Figure 6.8: Minimal channel: autocorrelation along the  $z$ -axis.

of no surprise that the autocorrelation of the wall normal fluctuation is not very well reproduced. The spike at the origin indicates that there is a high level of fluctuations between two adjacent grid points, *i.e.* the velocity values between two neighbouring points are too weakly correlated, but the general trend at larger separations is correct. In the spanwise direction we observe the same discrepancy in the wall normal correlation. Additionally, the streamwise correlation is overpredicting the negative correlation at half of the channel extent.

### 6.1.3 Lagrangian statistics

Lagrangian statistics can naturally be obtained from SPH and for illustration purpose only some are presented here. As the Lagrangian statistics were unfortunately started late in the simulation only a limited set of data is available, which does not yet provide converged results.

Traditionally, Eulerian codes are used to obtain Lagrangian statistics via interpolation. Clearly, the choice of interpolation scheme influences the result as shown by Choi *et al.* (2004) and so using a native Lagrangian method provides an interesting comparison.

The plots shown in Figure 6.9, 6.10 and 6.11 were obtained from the MCF2 simulation and are compared to the results by Choi *et al.* (2004). Particles initially at three different  $y^+$  levels (30, 100 and 210) were tracked downstream and a probability density function (PDF) of their  $y$  values was computed at  $x/(\lambda_y/2) = 0.5, 1$  and 2. When the last traced particle reached  $x = 2$ , the next iteration for the statistics was started five times later than the duration of the present iteration to avoid statistical dependencies

of the iterations. Due to the late start of statistics gathering the data presented here only contains 16 iterations which is clearly not enough to reach convergence, especially given the presence of only few large scale structures.

The only observation that can be made at this point is that the expected spreading is present and that there is a visible skew towards the center of the channel in the PDF of the plots in Figure 6.9 and 6.10.

#### 6.1.4 Preliminary conclusion

In this section two quasi DNS simulations of a turbulent channel flow with minimum domain size based on the paper by Jiménez and Moin (1991) were shown. The two simulations differ mainly by their resolution where the first could be argued to be underresolved even for a quasi DNS. This is also confirmed by the results based on the Eulerian statistics. Even though the data generally agrees well with the references it can be observed that the wall normal  $v_y'^2$  values are too large. In the middle of the channel this is very likely due to spurious oscillations which exist between the two solid walls. On the other hand it should be noted that the SPH cubic discretization is actually finer in the center of the channel compared to the reference simulation.

Another issue is the excessive level of near-wall fluctuations which can be assumed to derive from the boundary condition and this requires further investigation. Finally the autocorrelations indicated large fluctuations between adjacent grid points. This could be due to the chosen binning method for the interpolation to the grid or more likely due to the SPH method itself which would call for a higher coefficient in the volume

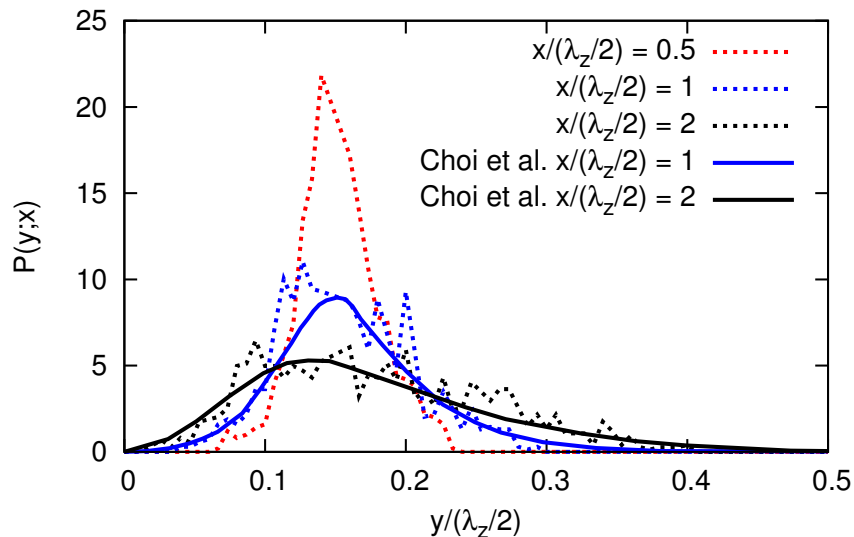


Figure 6.9: Minimal channel: Probability density function at  $y^+ = 30$ .

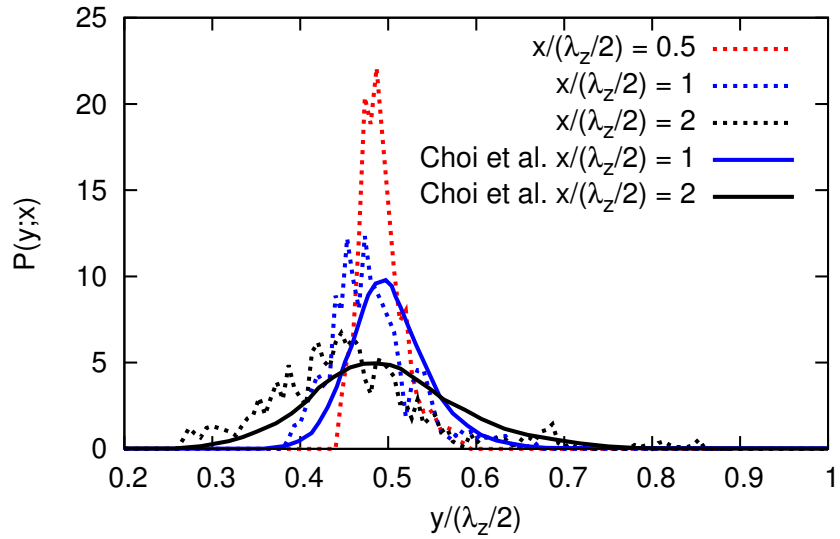


Figure 6.10: Minimal channel: Probability density function at  $y^+ = 100$ .

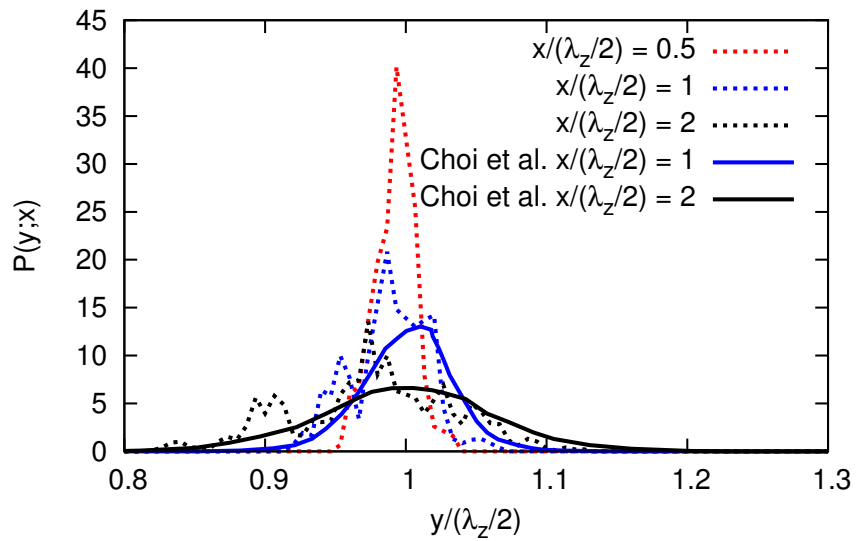


Figure 6.11: Minimal channel: Probability density function at  $y^+ = 210$ .

diffusion term.

Some preliminary Lagrangian statistics were presented to highlight the potential of SPH in this area. Finally, it can be concluded that it is indeed possible to simulate smooth-wall-bounded turbulent flows with SPH. This was proven by the quasi DNS channel flow test case which was really a finer investigation of SPH as pure Navier-Stokes solver highlighting certain numerical issues which could be studied without the influence of any turbulence model. The high computational time could be lowered by

having non-isotropic particles or by moving from quasi DNS to large eddy simulation. The latter is the approach chosen in the following section.

## 6.2 Large eddy simulation

The goal of this section was to run a LES of a turbulent channel flow at  $Re_\tau = 1000$ . In the first part the geometry is described as well as the results from the Eulerian statistics. As it is not possible to achieve the correct behaviour an attempt at explaining the results is shown in the second part based on the Taylor-Green vortex analytical benchmark.

### 6.2.1 The simulation

The simulation consists of a closed turbulent channel flow of size  $2\pi\delta \times 2\delta \times \pi\delta$ , with  $\delta$  being the channel half-width. As this channel is larger than the one used for the quasi DNS there is more than one turbulent structure present near the wall and the velocity between two points which are one channel half-length apart is uncorrelated. The friction Reynolds number is imposed constant at 1000 using a constant driving force. As the Reynolds number is five times larger than in the previous section the viscous length scale is smaller and in general the turbulent structures will exhibit a wider range of scales. All velocities and distances in the following are renormalized using the friction velocity  $v_\tau$  and the channel half-width  $\delta$ , respectively. The results are compared to a DNS performed by Hoyas and Jiménez (2006).

The viscous term used in the simulation is given by Eq. (2.100) and the volume diffusion term is used in combination with the coefficient chosen according to the discussion in Section 3.2. The former reduces the diffusivity in comparison with the term by Morris *et al.* (1997) given in Eq. (2.95) and the latter is required to remove spurious oscillations as in the quasi DNS simulation.

The resolution is chosen such that there are 100 particles in the spanwise direction, *i.e.*  $\Delta r = 0.02\delta$ . The ratio  $h/\Delta r = 1.3$  ensures sufficient accuracy in the numerical integration and implies that the kernel support is inside a sphere of radius  $5.2\Delta r$ . The simulation was run initially for 10 eddy turnover times ( $v_\tau/\delta$ ) after which time averaging was performed for another 10 eddy turnover times.

Compared to mesh-based methods which are used to simulate turbulent flows SPH suffers two important deficiencies. Firstly, the particles are isotropic which implies that the resolution is the same in every direction. Secondly, particle refinement is still an open issue as previously discussed in Section 1.3.2.6. In the case of a channel flow this implies that the flow in the vicinity of the wall cannot be resolved as it would require a fine resolution in the centre of the channel, essentially leading to a quasi DNS simulation as shown previously. Instead wall functions need to be used in order to

impose the correct shear stress near the wall.

In Figure 6.12 it can be seen that the velocity at the wall is well predicted but that inside the channel there is a significant overprediction of the mean streamwise velocity component. As initialization, a snapshot from a mesh-based simulation with hyperviscosity is used, and it seems that there is an issue with the balance of forces. In order to test this hypothesis consider Figure 6.13 where the standard deviation  $\sqrt{\langle v_x'^2 \rangle}$  of the fluctuating streamwise velocity is plotted. While the values near the wall are close to the DNS results by Hoyas and Jiménez (2006), in the center of the flow no decrease is visible. Note that due to the unresolved nature of the present LES the peak at  $y/\delta < 0.1$  is not captured.

In the interior of the channel nearly isotropic turbulence is expected and thus  $\sqrt{\langle v_y'^2 \rangle}$  would need to be nearly equal to its streamwise counterpart. However, compared to that the Reynolds stresses associated with the spanwise and cross-stream velocities are significantly reduced as shown in Figure 6.14. This indicates that the streamwise velocity fluctuations are not correctly converted to spanwise and cross-stream fluctuations. In Figure 6.15 the different components of the fluctuating velocities  $\underline{v}'$  can be seen after  $tv_\tau/\delta = 14$  of a slice in the  $xz$ -plane. The superimposed arrows correspond to the fluctuating velocity vectors.

The mechanism responsible for this transfer of momentum in the center of the channel can be investigated by looking at the Reynolds stress transport equations. They are

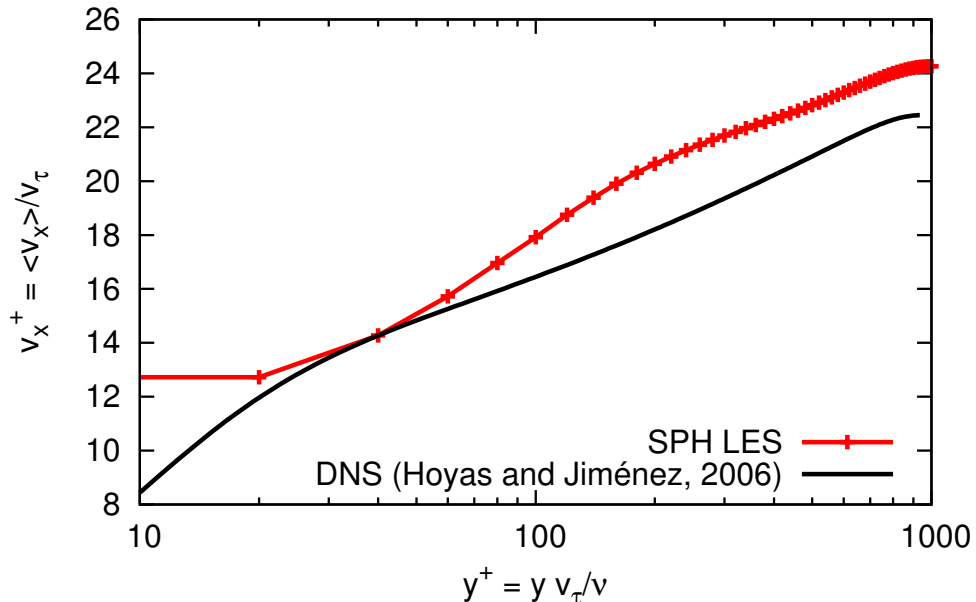


Figure 6.12: Average velocity.

given by

$$\frac{D\langle v'_i v'_j \rangle}{Dt} = -\frac{\partial}{\partial x_k} \langle v'_i v'_j v'_k \rangle + \nu \nabla^2 \langle v'_i v'_j \rangle + P_{ij} + \Pi_{ij} - \epsilon_{ij}, \quad (6.1)$$

where the production tensor

$$P_{ij} = -\langle v'_i v'_k \rangle \frac{\partial \langle v_j \rangle}{\partial x_k} - \langle v'_j v'_k \rangle \frac{\partial \langle v_i \rangle}{\partial x_k}, \quad (6.2)$$

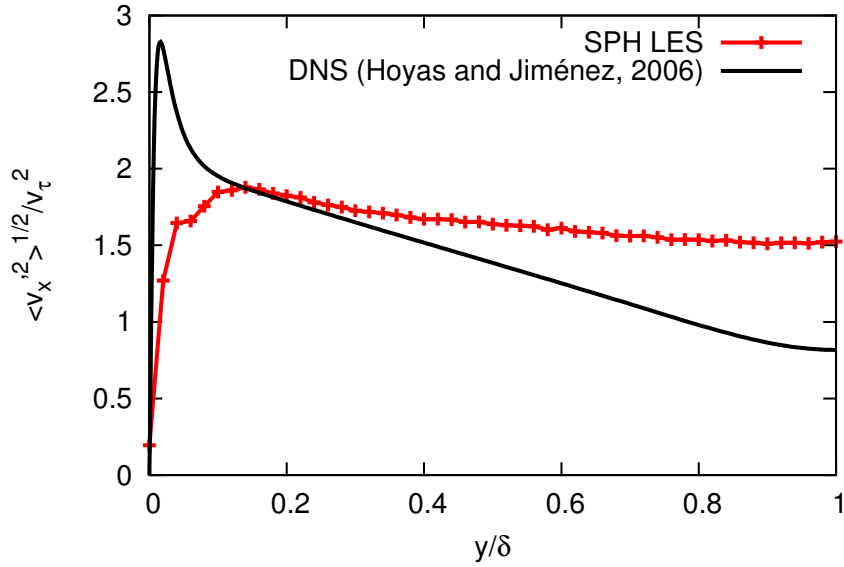


Figure 6.13: Velocity fluctuations in streamwise direction:  $\sqrt{\langle v_x'^2 \rangle}$ .

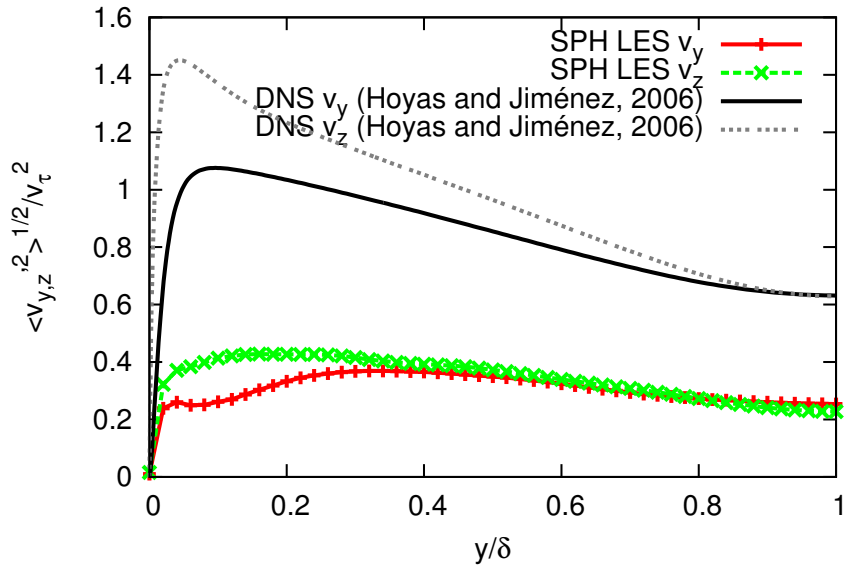


Figure 6.14: Velocity fluctuations in wall normal and cross-stream direction:  $\sqrt{\langle v_{y,z}'^2 \rangle}$ .

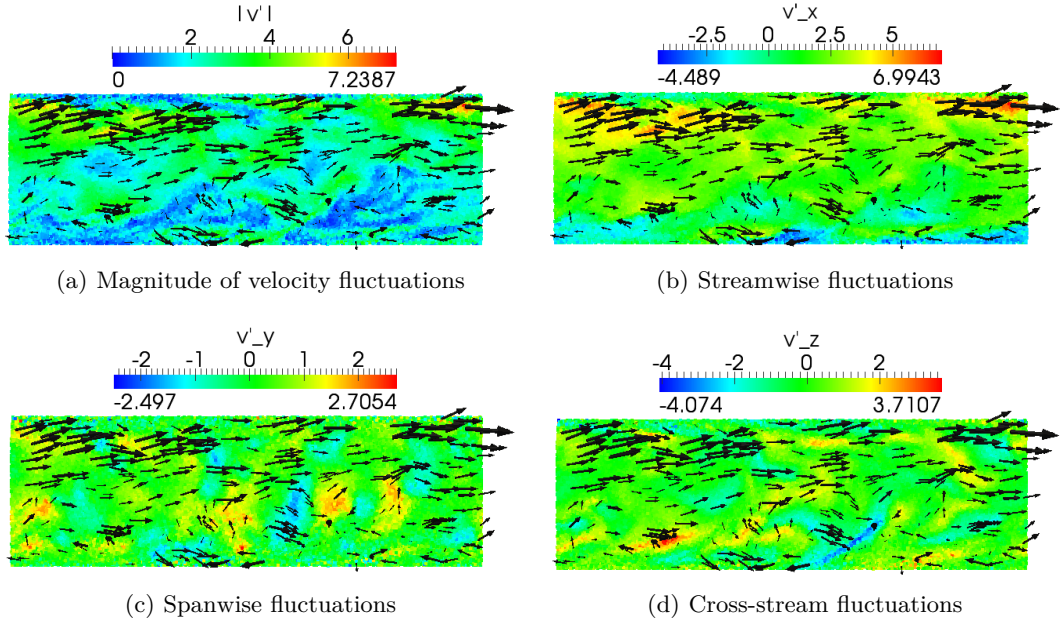


Figure 6.15: Snapshots of velocity magnitude and components from the LES after  $tv_\tau/\delta = 14$ .

the velocity-pressure-gradient tensor

$$\Pi_{ij} = -\frac{1}{\rho} \langle v'_i \frac{\partial p'}{\partial x_j} + v'_j \frac{\partial p'}{\partial x_i} \rangle, \quad (6.3)$$

and the dissipation tensor

$$\epsilon_{ij} = 2\nu \langle \frac{\partial v'_i}{\partial x_k} \frac{\partial v'_j}{\partial x_k} \rangle. \quad (6.4)$$

It was shown by Hoyas and Jiménez (2008) that away from the wall the velocity-pressure-gradient tensor is dominating the gain in the spanwise and cross-stream fluctuations as well as the loss of streamwise fluctuations. The effect of this term is illustrated in Figure 6.16. Two eddies with different streamwise velocities (black arrows) approach each other (Figure 6.16(a)) which causes an increase in pressure in the areas where the two eddies meet as indicated by the red particles in Figure 6.16(b). This results in a pressure gradient which finally alters the momentum of the particles reducing the streamwise velocity on one hand while increasing the spanwise velocity on the other (Figure 6.16(c)).

It can thus be concluded that should the pressure gradient not be calculated accurately enough that a reduced momentum transfer takes place. In order to investigate this issue in greater detail a simpler test case is needed simulating only the basic components of turbulent flows which are eddies. The Taylor-Green vortex provides exactly that and allows a comparison to the analytical solution and is thus considered in the

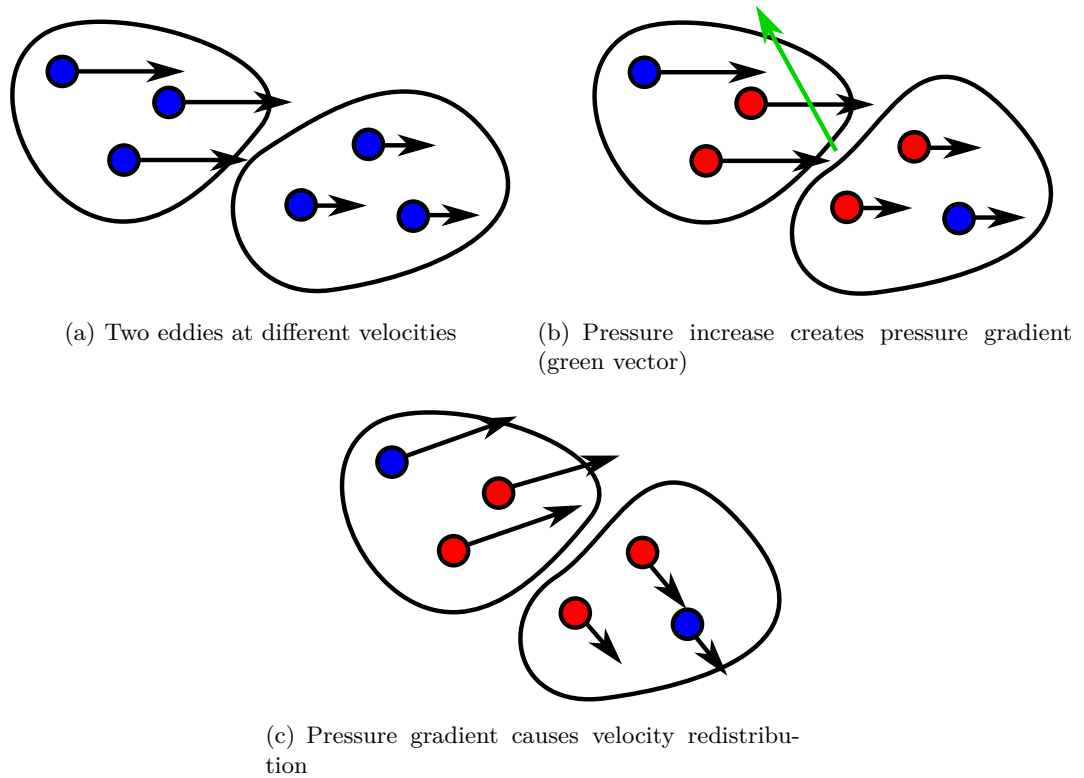


Figure 6.16: Velocity redistribution due to pressure gradient.

following section.

### 6.2.2 Taylor-Green vortices

The Taylor-Green vortex is widely used by the SPH community to study the stability of their respective approach (*e.g.* Xu *et al.* (2009)). Its stagnation points are a particular issue in Lagrangian methods as the integration nodes tend to cluster or coarsen (Xu *et al.*, 2009). From the point of view of turbulence this issue is not of primary importance, instead the focus is on the capability of solving small vortices. In this case small vortices refers to vortices resolved by only very few points.

In Figure 6.17 the analytical solutions of the Taylor-Green vortex can be seen on the domain  $[0, 1]^2$ . Figure 6.17(a) shows the colour map of the velocity magnitude with superimposed arrows showing the velocity vectors, where the analytical solution is given by

$$v_x = \sin(2\pi x) \cos(2\pi y), \quad (6.5)$$

$$v_y = -\cos(2\pi x) \sin(2\pi y). \quad (6.6)$$

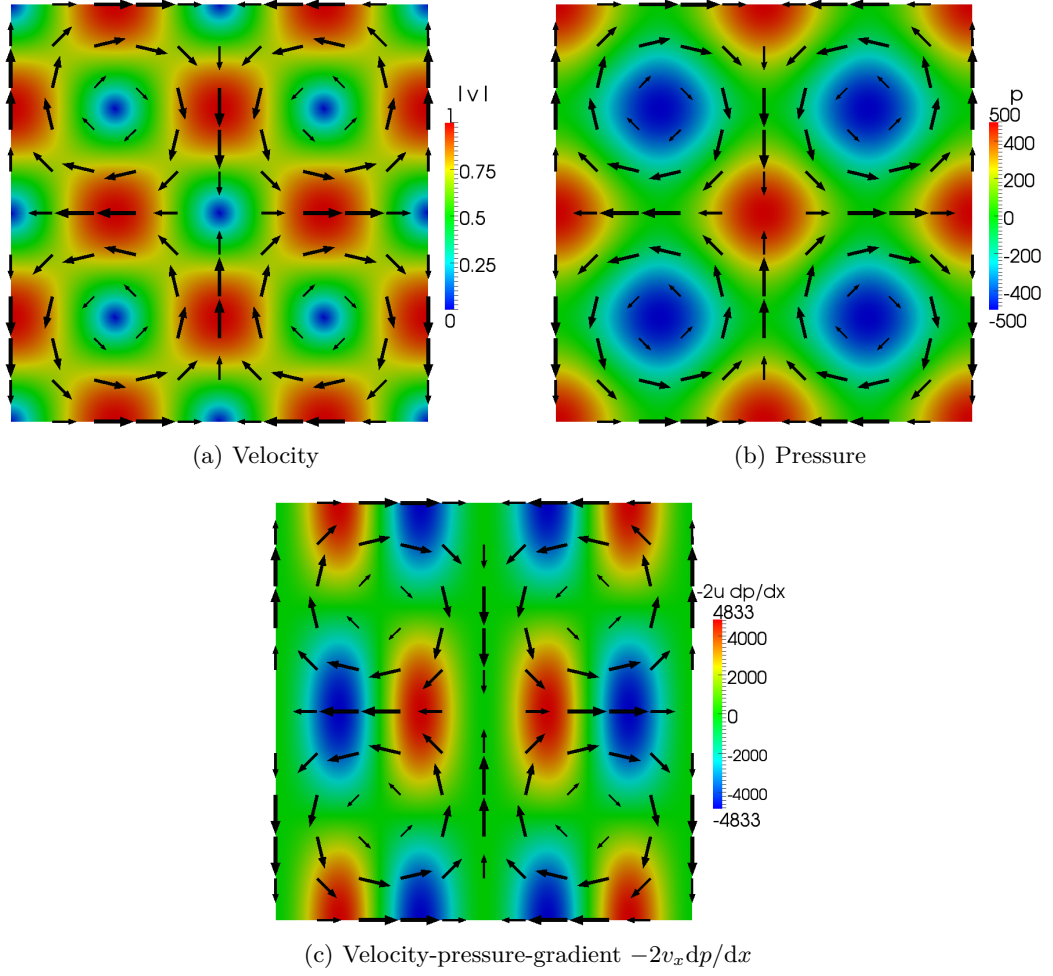


Figure 6.17: Analytical solutions of the Taylor-Green vortex.

The pressure

$$p = \frac{\rho}{4}(\cos(4\pi x) + \cos(4\pi y)), \quad (6.7)$$

is shown in Figure 6.17(b) where the areas of high pressure are shown in red. These areas also coincide with the stagnation points of the solution. Finally, Figure 6.17(c) shows the  $xx$  component of the velocity-pressure-gradient tensor  $\underline{\underline{\Pi}}$  which is given by

$$-2v_x dp/dx = 2\pi\rho(\sin(2\pi x) \sin(4\pi x) \cos(2\pi y)). \quad (6.8)$$

The areas in red and blue indicate acceleration and deceleration of the velocity in  $x$ -direction, respectively. As mentioned above, this is the main mechanism of rotating the velocity vectors, *i.e.* shifting fluctuations from one direction to another.

In the following the pressure gradient is calculated using the SPH method and then the error in  $\Pi_{xx}$  is compared for different resolutions. In Figure 6.18 both the  $L_2$  and

the  $L_\infty$  error can be seen plotted against the number of particles used in each spatial direction to resolve a single vortex, *i.e.*  $1/2/\Delta r$ . As in all previous simulations the ratio between the smoothing length and the particle distance is given by  $h/\Delta r = 1.3$ . If an error of 10% is accepted that implies that the smallest resolved vortices should have a size of at least 18 or 21 particles for acceptable levels of the  $L_2$  and  $L_\infty$  error, respectively. This corresponds to approximately 4 kernel diameters per vortex. The implications of these findings on LES with SPH are discussed in the following.

### 6.2.3 Concluding remarks

In Section 6.2.1 the results of an attempt at performing a LES with SPH was presented. Analyzing the average velocities it could be shown that the agreement with the DNS by Hoyas and Jiménez (2006) is poor. In order to investigate the cause of this failure the Reynolds stresses were analyzed indicating that the momentum transfer from stream-wise to spanwise and cross-stream directions was not working properly. Based on a combination of a heuristic analysis as well as the Reynolds stress transport equations the most important term for this transfer was identified.

This term was then in turn investigated using the Taylor-Green vortices, showing that vortices should be resolved by around 20 particles in each direction in order to have an error less than 10 percent.

Relating this to the LES that would mean that all vortices with diameter less than  $y^+ = 400$  are not resolved properly. In a moderate Reynolds number flow ( $Re_\tau = 1000$ )

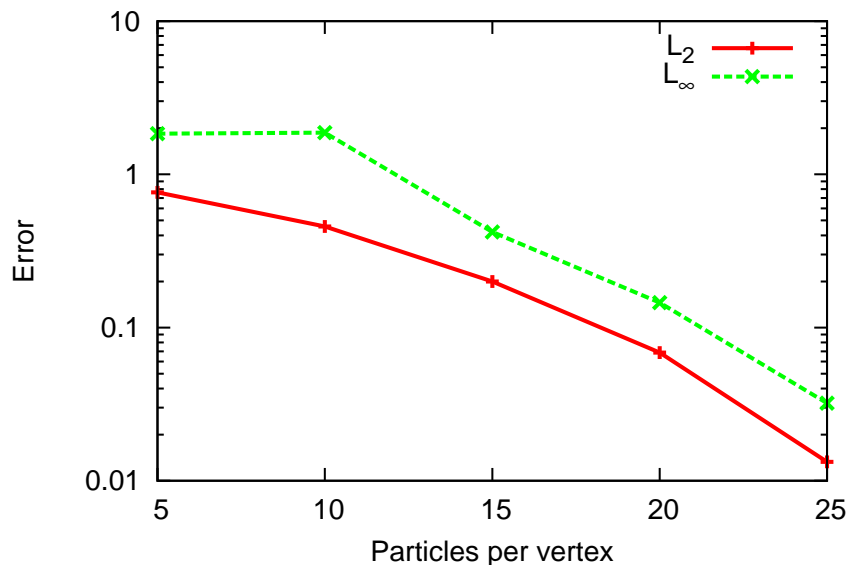


Figure 6.18: Relative error in  $\Pi_{xx}$  for the Taylor-Green vortex.

this clearly implies that the flow is nowhere near resolved enough to capture the relevant physics.

The question arises on how this issue can be solved. The most obvious answer is increasing the resolution. The quasi DNS shown in Section 6.1 shows that an increased resolution predicts the momentum transfer significantly better leading to physically sound simulations. However, seeing as the SPH method itself is already computationally expensive due to the number of neighbours per particle an increased resolution compared to Finite Volume methods, for example, would call for an even higher computational cost.

There is however an important difference between certain FV methods and the present SPH method. It consists in the staggered nature that allows for the physics to be better represented as shown by Harlow and Welch (1965) or Rollet-Miet *et al.* (1999). This allows for coarse LES that combined with wall functions provide reasonable results as demonstrated by De Villiers (2006) who uses as little as 500 cells to simulate a turbulent channel flow at  $Re_\tau = 395$ . It is possible that such a staggered approach would also yield improvements for SPH but as already discussed in Section 1.3.2.5 no suitable method has yet been presented that works in several space dimensions and including boundary conditions.

It was noted that an LES had already been performed by Issa (2004) for an open turbulent channel flow at  $Re = 538000$  with apparently reasonable results in the average velocity profile and boundary conditions that are now known to have significant issues. However, looking at the Reynolds stresses an overprediction of  $v'_x$  could also be seen. This, together with the comparably short averaging time of less than two eddy turnover times would hint at a solution which is not yet converged.

Finally, SPH has been applied to turbulent flows before as discussed in Section 1.5. But these turbulent flows were all isotropic in nature, hence, the redistribution of energy between Reynolds stress components by pressure fluctuations issue presented above has not been observed before. In isotropic turbulence the velocity-pressure-gradient is nil in the Reynolds stress transport equations.

## Chapter 7

# Conclusions

### 7.1 General conclusions

The thesis has presented an investigation into turbulent wall-bounded flow simulations using the Smoothed Particle Hydrodynamics method. The first part of the thesis examined the SPH method itself and the second focused on the simulation of a turbulent channel flow. The unified semi-analytical wall boundary conditions by Ferrand *et al.* (2012) are a novel method to impose solid wall boundaries in SPH and were, at the beginning of this work, only available in two dimensions. This novelty demanded a closer inspection of the properties of this approach. Furthermore, these boundary conditions allow complex geometries and provide means to consistently impose boundary conditions for the pressure and the wall shear stresses which is an important prerequisite for the simulation of turbulent flows. As three-dimensional turbulent flows behave significantly different to two-dimensional flows, it was necessary to extend this boundary condition framework to 3-D.

The results of the first part of this thesis laid the necessary foundation to perform the simulation of a closed turbulent channel flow using two different numerical approaches. Even though SPH is not the preferred numerical method to perform simulations of confined turbulent flows this type of flow was chosen because ample reference data is available. One of the goals of this work is to provide a basis for future simulations of turbulent flows where SPH would be more suitable, such as the simulation of a hydraulic jump. To date, most papers on SPH turbulent simulations considered only isotropic turbulence. Thus, the focus of this work is on the anisotropic channel flow. At first, a quasi DNS was carried out which has the advantage that no turbulence models needed to be used. Finally, a LES was attempted using basic LES models and significant deviations from the expected results could be observed. This was analyzed using both analytical and numerical means, highlighting a significant deficiency of SPH.

In the following the results of this work will be analysed in detail and the thesis is concluded by giving some recommendations for future research.

## 7.2 Detailed conclusions

### 7.2.1 Investigation into wall-boundary conditions for SPH

At the beginning of this thesis a literature review was given in Chapters 1 and 2. Special emphasis was put on developing a SPH method devised by Ferrand *et al.* (2012). This SPH method was analyzed in detail in Chapter 3 showing that the skew-adjoint property in the presence of walls only holds in the limit of  $h \rightarrow 0$ . SPH due to its collocated nature is prone to numerical oscillations a volume diffusion term was introduced via the RANS framework. This term was shown to be similar to a correction proposed by Ferrari *et al.* (2009) with the important difference of a constant that can be determined as a function of the resolution. As part of the investigation into wall boundary conditions a novel formulation for a variable driving force was found which successfully prescribes a constant volume flux. Simulating a Poiseuille flow it could be shown that the novel formulation exhibits an error five orders of magnitude smaller than the original one. Furthermore, it was possible to extend the first-order Neumann boundary conditions by Ferrand *et al.* (2012) to arbitrary-order Robin type conditions. Discretising the wave equation with Robin boundary conditions it could be shown that the boundary conditions were correctly imposed and that increasing the order of the approximation reduces the error in the solution. Both the volume diffusion term and the boundary conditions required external forces to be taken into account which was shown to significantly improve the results by reducing errors at the free-surface. Finally, the formulation was tested using a dam break case and the results were compared to other SPH boundary conditions, showing that the present approach yields superior results.

### 7.2.2 Extension to three dimensions

The aim of Chapter 4 was to extend the wall boundary condition to 3-D. Two issues had to be solved, the first one dealing with the vertex mass computation and the second with the computation of the normalization factor  $\gamma$ . The first issue was solved with a geometrical approach that was implemented in a pre-processing code running on graphic processing units. To determine the normalization factor  $\gamma$  the values of  $\underline{\nabla}\gamma$  need to be computed which requires solving an integral over a particular 2-D domain. Using a domain decomposition algorithm it was possible to divide these 2-D domains into three simple shapes. As the integrand is the kernel it was possible to derive an analytical formula for this integral on these 2-D shapes. The formulation presented in

this chapter was tested using several three-dimensional flows with simple to complex geometries. It could be shown that the formulation is accurate and provides a significant improvement over the use of an approximated computation of  $\nabla\gamma$ . A three-dimensional dam-break was simulated and the results were compared with a Volume-of-Fluid (VOF) simulation and several other SPH boundary conditions. The present method yielded superior results compared to the latter and good agreement to the VOF results was obtained, despite some expected discrepancies due to the multiphase nature of the VOF simulation.

### 7.2.3 Simulations of the turbulent channel flow

The second part of this thesis investigated the application of the SPH method to 3-D turbulent closed channel flows. Their physical properties as well as the numerical methods used to simulate these flows were presented in Chapter 5. In Chapter 6 two different simulations were shown. The first one was a quasi DNS and as such no turbulence models were implemented. This allowed for an evaluation of SPH as a pure Navier-Stokes solver. Two different resolutions were tested and in particular the high resolution simulation showed fairly good agreement with the reference solution by Jiménez and Moin (1991). Only near the wall could some deviations be seen which were most likely originating from the boundary conditions. In the second part of this chapter a Large Eddy Simulation of a turbulent channel flow at  $Re_\tau = 1000$  was attempted. The Eulerian statistics showed a clear deviation from the DNS results by Hoyas and Jiménez (2006). An investigation showed that the spanwise and cross-stream Reynolds stresses were significantly underpredicted. Analysing the budget of these terms it was possible to identify the velocity-pressure-gradient tensor to be the root cause of this issue. Using a Taylor-Green vortex this term was investigated at various resolutions finally showing that a significantly higher resolution would be needed to correctly capture the transfer of momentum in anisotropic turbulence.

## 7.3 Recommendations for future work

Finally, some remarks regarding future work shall be made. With the development of the unified semi-analytical wall boundary conditions it is finally possible to consistently impose solid walls in SPH even in highly complex geometries. However, in the context of turbulent flows, some deficiencies have been highlighted.

- In particular the quasi DNS showed some deviation in spanwise direction which warrant further investigation. These deviations could potentially be overcome by the use of Robin-type boundary conditions which allow the implementation of more flexible relaxation schemes near the boundaries.

- The present SPH formulation is currently being extended to open boundaries and to incompressible SPH. A repetition of the turbulent simulations presented in this work with an incompressible code would be of interest.
- Studying the effect of different kernels and smoothing lengths in the context of anisotropic turbulent flows would be another avenue for future research.
- One further issue related to boundary conditions is variable resolution. Particularly in turbulent flows where the highest resolution is required close to the wall a capability for variable resolution is highly desirable.
- The negative result at the end of this thesis showed that further research is warranted in the area of turbulence, particularly in anisotropic flows. It might be possible to overcome some difficulties by a staggered SPH method but it is unclear whether this will have the same effect as in Finite Volume methods. However, as the momentum transfer issue is not of such importance in (unsteady) RANS simulations this alternative approach is highly interesting in combination with the SPH method.

# Bibliography

- S. Adami, X. Y. Hu, and N. A. Adams. Simulating 3D turbulence with SPH. In *Proceedings of the 8<sup>th</sup> SPHERIC Workshop*, pages 377–382, Trondheim, June 2013.
- I. Afgan, S. Benhamadouche, X. Han, P. Sagaut, and D. Laurence. Flow over a flat plate with uniform inlet and incident coherent gusts. *Journal of Fluid Mechanics*, 720:457–485, 2013. doi: 10.1017/jfm.2013.25.
- A. Amicarelli, G. Agate, and R. Guandalini. Development and validation of a SPH model using discrete surface elements at boundaries. In *Proceedings of the 7<sup>th</sup> International SPHERIC Workshop*, pages 369–374, Prato, 2012.
- M. Antuono, A. Colagrossi, S. Marrone, and D. Molteni. Free-surface flows solved by means of SPH schemes with numerical diffusive terms. *Computer Physics Communications*, 181(3):532–549, March 2010. ISSN 0010-4655. doi: 10.1016/j.cpc.2009.11.002. URL <http://www.sciencedirect.com/science/article/B6TJ5-4XR5N7H-1/2/d02798171f5718d56658d8930b901000>.
- M. Antuono, A. Colagrossi, and S. Marrone. Numerical diffusive terms in weakly-compressible SPH schemes. *Computer Physics Communications*, 183(12):2570–2580, December 2012. ISSN 0010-4655. doi: 10.1016/j.cpc.2012.07.006. URL <http://www.sciencedirect.com/science/article/pii/S0010465512002342>.
- S. E. Arena, J.-F. Gonzalez, and E. Crespe. Characterisation of SPH noise in simulations of protoplanetary discs. *Proceedings of the International Astronomical Union*, 6(Symposium S276):393–394, 2010. doi: 10.1017/S1743921311020485.
- M. Arroyo and M. Ortiz. Local maximum-entropy approximation schemes: a seamless bridge between finite elements and meshfree methods. *International Journal for Numerical Methods in Engineering*, 65:2167 – 2202, 2006.
- S. N. Atluri and T. Zhu. A new meshless local petrov-galerkin (MLPG) approach in. *Computational Mechanics*, 22(2):117–127, August 1998. ISSN 0178-7675, 1432-0924.

- doi: 10.1007/s004660050346. URL <http://link.springer.com/article/10.1007/s004660050346>.
- M. Basa, N. J. Quinlan, and M. Lastiwka. Robustness and accuracy of SPH formulations for viscous flow. *International Journal for Numerical Methods in Fluids*, 60(10):1127–1148, 2009. ISSN 1097-0363. doi: 10.1002/flid.1927. URL <http://dx.doi.org/10.1002/flid.1927>.
- G. K. Batchelor. *An introduction to fluid dynamics*. Cambridge University Press, 2000. ISBN 9780521663960.
- R. C. Batra and G. M. Zhang. Search algorithm, and simulation of elastodynamic crack propagation by modified smoothed particle hydrodynamics (MSPH) method. *Computational Mechanics*, 40(3):531–546, November 2006. ISSN 0178-7675. doi: 10.1007/s00466-006-0124-z. URL <http://www.springerlink.com/content/t623r663526q751g/>.
- T. Belytschko, Y. Y. Lu, and L. Gu. Element-free galerkin methods. *International Journal for Numerical Methods in Engineering*, 37(2):229–256, January 1994. ISSN 1097-0207. doi: 10.1002/nme.1620370205. URL <http://onlinelibrary.wiley.com/doi/10.1002/nme.1620370205/abstract>.
- J. Blackshire and W. Humphreys. 3-dimensional, 3-component velocity measurements using holographic particle image velocimetry(HPIV). In *AIAA, Aerospace Ground Testing Conference, 18 th, Colorado Springs, CO*, 1994.
- S. Borve. Generalized ghost particle method for handling reflecting boundaries. In *Proceedings of the 6th SPHERIC Workshop*, pages 313–320, Hamburg, 2011. ISBN 978-3-89220-658-3.
- H. H. Bui, K. Sako, and R. Fukagawa. Numerical simulation of soil-water interaction using smoothed particle hydrodynamics (SPH) method. *Journal of Terramechanics*, 44(5):339–346, November 2007. ISSN 0022-4898. doi: 16/j.jterra.2007.10.003. URL <http://www.sciencedirect.com/science/article/pii/S0022489807000559>.
- A. Cameron. The origin of the moon and the single impact hypothesis v. *Icarus*, 126(1):126–137, March 1997. ISSN 0019-1035. doi: 06/icar.1996.5642. URL <http://www.sciencedirect.com/science/article/pii/S0019103596956420>.
- T. Capone, A. Panizzo, C. Cecioni, and R. A. Dalrymple. Accuracy and stability of numerical schemes in SPH. In *Proceedings of the 2nd SPHERIC Workshop*, pages 156–164, Madrid, 2007. URL <http://adsabs.harvard.edu/abs/2007sphe.work..156C>.

- S.-H. Cha and A. P. Whitworth. Implementations and tests of godunov-type particle hydrodynamics. *Monthly Notices of the Royal Astronomical Society*, 340(1): 73–90, 2003. ISSN 1365-2966. doi: 10.1046/j.1365-8711.2003.06266.x. URL <http://onlinelibrary.wiley.com/doi/10.1046/j.1365-8711.2003.06266.x/abstract>.
- J.-S. Chen, S. Yoon, and C.-T. Wu. Non-linear version of stabilized conforming nodal integration for galerkin mesh-free methods. *International Journal for Numerical Methods in Engineering*, 53:2587–2615, 2002.
- J.-I. Choi, K. Yeo, and C. Lee. Lagrangian statistics in turbulent channel flow. *Physics of Fluids*, 16:779–793, March 2004. doi: DOI:10.1063/1.1644576. URL <http://adsabs.harvard.edu/abs/2004PhFl...16..779C>.
- P. W. Cleary, J. Ha, and V. Ahuja. High pressure die casting simulation using smoothed particle hydrodynamics. *International Journal of Cast Metals Research*, 12(6):335–356, 2000.
- A. Colagrossi and M. Landrini. Numerical simulation of interfacial flows by smoothed particle hydrodynamics. *Journal of Computational Physics*, 191(2): 448–475, November 2003. ISSN 0021-9991. doi: 10.1016/S0021-9991(03)00324-3. URL <http://www.sciencedirect.com/science/article/B6WHY-49CMJ22-1/2/9d25ed6668fde488a2f4429e97411815>.
- R. Courant, K. Friedrichs, and H. Lewy. Über die partiellen differenzgleichungen der mathematischen physik. *Mathematische Annalen*, 100(1):32–74, December 1928. ISSN 0025-5831, 1432-1807. doi: 10.1007/BF01448839. URL <http://link.springer.com/article/10.1007/BF01448839>.
- A. C. Crespo, J. M. Dominguez, A. Barreiro, M. Gómez-Gesteira, and B. D. Rogers. GPUs, a new tool of acceleration in CFD: efficiency and reliability on smoothed particle hydrodynamics methods. *PLoS ONE*, 6(6):e20685, 2011. doi: 10.1371/journal.pone.0020685. URL <http://dx.doi.org/10.1371/journal.pone.0020685>.
- S. J. Cummins and M. Rudman. An SPH projection method. *Journal of Computational Physics*, 152(2):584–607, July 1999. ISSN 0021-9991. doi: 06/jcph.1999.6246. URL <http://www.sciencedirect.com/science/article/pii/S0021999199962460>.
- C. J. Cyron, M. Arroyo, and M. Ortiz. Second order positive and smooth meshfree approximants selected by maximum entropy. *International Journal for Numerical Methods in Engineering*, 2008.
- R. Dalrymple and B. Rogers. Numerical modeling of water waves with the SPH method. *Coastal Engineering*, 53(2-3):141–147, February 2006. ISSN 0378-3839. doi: 16/j.

- coastaleng.2005.10.004. URL <http://www.sciencedirect.com/science/article/pii/S0378383905001304>.
- R. A. Dalrymple and O. Knio. SPH modelling of water waves. In H. Hanson and M. Larson, editors, *ASCE Conf. Proc.*, volume 260, page 80, Lund, Sweden, June 2001. ASCE. doi: 10.1061/40566(260)80. URL <http://link.aip.org/link/?ASC/260/80/1>.
- R. Das and P. W. Cleary. Application of SPH for modelling heat transfer and residual stress generation in arc welding. *Materials Science Forum*, 654-656:2751–2754, June 2010. ISSN 1662-9752. doi: 10.4028/www.scientific.net/MSF.654-656.2751. URL <http://www.scientific.net/MSF.654-656.2751>.
- M. De Lefte, D. Le Touze, and B. Alessandrini. Normal flux method at the boundary for SPH. In *Proceedings of the 4th SPHERIC Workshop*, pages 150–157, 2009.
- D. De Padova, M. Mossa, S. Sibilla, and E. Torti. Hydraulic jump simulation by SPH. In *Proceedings of the 5th International SPHERIC Workshop*, pages 50–55, Manchester, 2010.
- E. De Villiers. *The Potential of Large Eddy Simulation for the Modeling of Wall Bounded Flows*. PhD, Imperial College, London, 2006. URL <http://powerlab.fsb.hr/ped/kturbo/OpenFOAM/docs/EugeneDeVilliersPhD2006.pdf>.
- C. T. Dyka, P. W. Randles, and R. P. Ingel. Stress points for tension instability in SPH. *International Journal for Numerical Methods in Engineering*, 40(13):2325–2341, July 1997. ISSN 1097-0207. doi: 10.1002/(SICI)1097-0207(19970715)40:13<2325::AID-NME161>3.0.CO;2-8. URL [http://onlinelibrary.wiley.com/doi/10.1002/\(SICI\)1097-0207\(19970715\)40:13<2325::AID-NME161>3.0.CO;2-8/abstract](http://onlinelibrary.wiley.com/doi/10.1002/(SICI)1097-0207(19970715)40:13<2325::AID-NME161>3.0.CO;2-8/abstract).
- J. G. M. Eggels, F. Unger, M. H. Weiss, J. Westerweel, R. J. Adrian, R. Friedrich, and F. T. M. Nieuwstadt. Fully developed turbulent pipe flow: a comparison between direct numerical simulation and experiment. *Journal of Fluid Mechanics*, 268:175–209, 1994. doi: DOI:10.1017/S002211209400131X. URL <http://adsabs.harvard.edu/abs/1994JFM...268..175E>.
- M. Ellero and R. Tanner. SPH simulations of transient viscoelastic flows at low reynolds number. *Journal of Non-Newtonian Fluid Mechanics*, 132(1-3):61–72, December 2005. ISSN 0377-0257. doi: 16/j.jnnfm.2005.08.012. URL <http://www.sciencedirect.com/science/article/pii/S0377025705001990>.

- G. Elsinga, F. Scarano, B. Wieneke, and B. van Oudheusden. Tomographic particle image velocimetry. *Experiments in Fluids*, 41(6):933–947, 2006. ISSN 0723-4864. doi: 10.1007/s00348-006-0212-z. URL <http://www.springerlink.com/content/17008530406263n2/abstract/>.
- P. Espanol and M. Revenga. Smoothed dissipative particle dynamics. *Physical Review E*, 67:26705, February 2003. URL <http://adsabs.harvard.edu/abs/2003PhRvE..67b6705E>.
- R. Fatehi and M. T. Manzari. A consistent and fast weakly compressible smoothed particle hydrodynamics with a new wall boundary condition. *International Journal for Numerical Methods in Fluids*, 2010. ISSN 1097-0363. doi: 10.1002/flid.2586. URL <http://onlinelibrary.wiley.com/doi/10.1002/flid.2586/abstract>.
- R. Fatehi and M. Manzari. Error estimation in smoothed particle hydrodynamics and a new scheme for second derivatives. *Computers & Mathematics with Applications*, 61(2):482–498, January 2011. ISSN 0898-1221. doi: 16/j.camwa.2010.11.028. URL <http://www.sciencedirect.com/science/article/pii/S0898122110009004>.
- A. Favre. Statistical equations of turbulent gases. *Problems of hydrodynamics and continuum mechanics*, page 231–266, 1969.
- M. Ferrand. *Unified semi-analytical wall boundary conditions for inviscid, laminar and turbulent slightly compressible flows in SPARTACUS-2D combined with an improved time integration scheme on the continuity equation*. MPhil thesis, University of Manchester, 2010.
- M. Ferrand, D. Laurence, B. D. Rogers, and D. Violeau. Improved time scheme integration approach for dealing with semi analytical boundary conditions in SPARTACUS2D. In *Proceedings of the 5<sup>th</sup> International SPHERIC Workshop*, pages 98–105, Manchester, June 2010.
- M. Ferrand, D. Laurence, B. D. Rogers, D. Violeau, and C. Kassiotis. Unified semi-analytical wall boundary conditions for inviscid, laminar or turbulent flows in the meshless SPH method. *International Journal for Numerical Methods in Fluids*, 71(4):446–472, 2012. doi: 10.1002/flid.3666. DOI: 10.1002/flid.3666.
- A. Ferrari, M. Dumbser, E. F. Toro, and A. Armanini. A new 3D parallel SPH scheme for free surface flows. *Computers & Fluids*, 38(6):1203–1217, June 2009. ISSN 0045-7930. doi: 10.1016/j.compfluid.2008.11.012.
- T.-P. Fries and H.-G. Matthies. Classification and overview of meshfree methods. Technical Report 3, TU Braunschweig, Braunschweig, 2003.

- U. Frisch. Turbulence. *Turbulence, by Uriel Frisch, pp. 310. ISBN 0521457130. Cambridge, UK: Cambridge University Press, January 1996.*, -1, January 1996. URL <http://adsabs.harvard.edu/abs/1996turb.book.....F>.
- Y. Gasteuil, W. L. Shew, M. Gibert, F. Chillá, B. Castaing, and J.-F. Pinton. Lagrangian temperature, velocity, and local heat flux measurement in rayleigh-bénard convection. *Physical Review Letters*, 99(23):234302, December 2007. doi: 10.1103/PhysRevLett.99.234302. URL <http://link.aps.org/doi/10.1103/PhysRevLett.99.234302>.
- M. Germano, U. Piomelli, P. Moin, and W. H. Cabot. A dynamic subgrid-scale eddy viscosity model. *Physics of Fluids*, 3:1760–1765, July 1991. doi: DOI:10.1063/1.857955. URL <http://adsabs.harvard.edu/abs/1991PhFl....3.1760G>.
- S. Ghosal. An analysis of numerical errors in large-eddy simulations of turbulence. *Journal of Computational Physics*, 125(1):187–206, April 1996. ISSN 0021-9991. doi: 10.1006/jcph.1996.0088. URL <http://www.sciencedirect.com/science/article/pii/S0021999196900881>.
- R. A. Gingold and J. J. Monaghan. Smoothed particle hydrodynamics - theory and application to non-spherical stars. *Monthly Notices of the Royal Astronomical Society*, 181:375–389, November 1977. URL <http://adsabs.harvard.edu/abs/1977MNRAS.181..375G>.
- P. H. Groenenboom and L. Lobovsky. Artificial stress effects on structural dynamics using SPH. In *Proceedings of the 4th SPHERIC Workshop*, pages 302–308, Nantes, May 2009.
- M. Gross. Smoothed particle hydrodynamics modelling of laser cutting. In *ICALEO 2008 Congress Proceeding Proceedings*, pages 637–644, 2008.
- R. Haberman. *Applied Partial Differential Equations: With Fourier Series and Boundary Value Problems*. Pearson Prentice Hall, 2004. ISBN 9780130652430. URL <http://books.google.fr/books?id=alp0QgAACAAJ>.
- F. H. Harlow. Hydrodynamic problems involving large fluid distortions. *J. ACM*, 4(2):137–142, April 1957. ISSN 0004-5411. doi: 10.1145/320868.320871. ACM ID: 320871.
- F. H. Harlow and J. E. Welch. Numerical calculation of time-dependent viscous incompressible flow of fluid with free surface. *Physics of Fluids*, 8(12):2182, 1965. ISSN 00319171. doi: 10.1063/1.1761178. URL <http://scitation.aip.org/content/aip/journal/pof1/8/12/10.1063/1.1761178>.

- D. D. Holm. Fluctuation effects on 3D lagrangian mean and eulerian mean fluid motion. *arXiv:chao-dyn/9903034*, March 1999. doi: 10.1016/S0167-2789(99)00093-7. URL <http://arxiv.org/abs/chao-dyn/9903034>.
- S. Hoyas and J. Jiménez. Reynolds number effects on the reynolds-stress budgets in turbulent channels. *Physics of Fluids*, 20(10):101511, 2008. ISSN 10706631. doi: 10.1063/1.3005862. URL <http://link.aip.org/link/PHFLE6/v20/i10/p101511/s1&Agg=doi>.
- S. Hoyas and J. Jiménez. Scaling of the velocity fluctuations in turbulent channels up to  $re = 2003$ . *Physics of Fluids*, 18(1):011702–011702–4, January 2006. ISSN 10706631. doi: doi:10.1063/1.2162185. URL [http://pof.aip.org/resource/1/phfle6/v18/i1/p011702\\_s1](http://pof.aip.org/resource/1/phfle6/v18/i1/p011702_s1).
- X. Y. Hu and N. A. Adams. A SPH model for incompressible turbulence. *arXiv:1204.5097*, April 2012. URL <http://arxiv.org/abs/1204.5097>.
- X. Hu and N. Adams. An incompressible multi-phase SPH method. *Journal of Computational Physics*, 227(1):264–278, November 2007. ISSN 0021-9991. doi: 10.1016/j.jcp.2007.07.013. URL <http://www.sciencedirect.com/science/article/pii/S0021999107003300>.
- J. P. Hughes and D. I. Graham. Comparison of incompressible and weakly-compressible SPH models for free-surface water flows. *Journal of Hydraulic Research*, 48(sup1): 105–117, 2010. ISSN 0022-1686. doi: 10.1080/00221686.2010.9641251. URL <http://www.tandfonline.com/doi/abs/10.1080/00221686.2010.9641251>.
- S.-I. Inutsuka. Advanced methods in particle hydrodynamics. In S. M. Miyama, K. Tomisaka, and T. Hanawa, editors, *Numerical Astrophysics*, number 240 in Astrophysics and Space Science Library, pages 367–374. Springer Netherlands, January 1999. ISBN 978-94-010-6008-0, 978-94-011-4780-4. URL [http://link.springer.com/chapter/10.1007/978-94-011-4780-4\\_111](http://link.springer.com/chapter/10.1007/978-94-011-4780-4_111).
- S.-i. Inutsuka. Reformulation of smoothed particle hydrodynamics with riemann solver. *Journal of Computational Physics*, 179(1):238–267, June 2002. ISSN 0021-9991. doi: 10.1006/jcph.2002.7053. URL <http://www.sciencedirect.com/science/article/pii/S0021999102970531>.
- R. Issa. *Numerical assessment of the Smoothed Particle Hydrodynamics gridless method for incompressible flows and its extension to turbulent flows*. PhD, University of Manchester, 2004.

- J. Jiménez and P. Moin. The minimal flow unit in near-wall turbulence. *Journal of Fluid Mechanics*, 225:213–240, April 1991. doi: 10.1017/S0022112091002033. URL <http://adsabs.harvard.edu/abs/1991JFM...225..213J>.
- W. Jones and B. Launder. The prediction of laminarization with a two-equation model of turbulence. *International Journal of Heat and Mass Transfer*, 15(2):301–314, February 1972. ISSN 0017-9310. doi: 10.1016/0017-9310(72)90076-2. URL <http://www.sciencedirect.com/science/article/pii/0017931072900762>.
- E. J. Kansa. Multiquadrics—a scattered data approximation scheme with applications to computational fluid dynamics-i. surface approximations and partial derivative estimates. *Computers and Mathematics with Applications*, 19:127–145, 1990.
- C. Kassiotis, M. Ferrand, D. Violeau, B. D. Rogers, P. Stansby, and M. Benoit. Coupling SPH with a 1-d boussinesq-type wave model. In *Proceedings of the 6th SPHERIC Workshop*, pages 241–247, Hamburg, 2011. ISBN 978-3-89220-658-3.
- J. Kim, P. Moin, and R. Moser. Turbulence statistics in fully developed channel flow at low reynolds number. *Journal of Fluid Mechanics*, 177:133–166, 1987. doi: 10.1017/S0022112087000892.
- L. V. King. LVII. on the precision measurement of air velocity by means of the linear hot-wire anemometer. *Philosophical Magazine Series 6*, 29(172):556–577, April 1915. ISSN 1941-5982. doi: 10.1080/14786440408635334. URL <http://www.tandfonline.com/doi/abs/10.1080/14786440408635334>.
- K. Kleefsman, G. Fekken, A. Veldman, B. Iwanowski, and B. Buchner. A volume-of-fluid based simulation method for wave impact problems. *Journal of Computational Physics*, 206(1):363–393, June 2005. ISSN 0021-9991. doi: 10.1016/j.jcp.2004.12.007. URL <http://www.sciencedirect.com/science/article/pii/S0021999104005170>.
- A. N. Kolmogorov. Equations of turbulent motion of an incompressible fluid. *Izvestia Acad. Sci.*, 6:56–58, 1942.
- Y. Krongauz and T. Belytschko. Enforcement of essential boundary conditions in meshless approximations using finite elements. *Computer Methods in Applied Mechanics and Engineering*, 131(1–2):133–145, April 1996. ISSN 0045-7825. doi: 10.1016/0045-7825(95)00954-X. URL <http://www.sciencedirect.com/science/article/pii/004578259500954X>.
- S. Kulasegaram, J. Bonet, R. W. Lewis, and M. Profit. A variational formulation based contact algorithm for rigid boundaries in two-dimensional SPH applications.

- Computational Mechanics*, 33(4):316–325, March 2004. ISSN 0178-7675. doi: 10.1007/s00466-003-0534-0.
- M. Lastiwka, M. Basa, and N. J. Quinlan. Permeable and non-reflecting boundary conditions in SPH. *International Journal for Numerical Methods in Fluids*, 61(7): 709–724, November 2009. ISSN 1097-0363. doi: 10.1002/fld.1971. URL <http://onlinelibrary.wiley.com/doi/10.1002/fld.1971/abstract>.
- E.-S. Lee, C. Moulinec, R. Xu, D. Violeau, D. Laurence, and P. Stansby. Comparisons of weakly compressible and truly incompressible algorithms for the SPH mesh free particle method. *Journal of Computational Physics*, 227:8417–8436, 2008. doi: 10.1016/j.jcp.2008.06.005.
- B. Leimkuhler and S. Reich. *Simulating Hamiltonian Dynamics*. Cambridge University Press, 2004. ISBN 9780521772907.
- Li and Liu. *Meshfree Particle Methods*. Springer, 2004.
- L. D. Libersky, A. G. Petschek, T. C. Carney, J. R. Hipp, and F. A. Allahdadi. High strain lagrangian hydrodynamics: A three-dimensional SPH code for dynamic material response. *Journal of Computational Physics*, 109(1):67–75, November 1993. ISSN 0021-9991. doi: 06/jcph.1993.1199. URL <http://www.sciencedirect.com/science/article/pii/S002199918371199X>.
- D. Lilly. The representation of small scale turbulence in numerical simulation experiments. pages 195–210, 1967.
- S. J. Lind, R. Xu, P. K. Stansby, and B. D. Rogers. A stabilising diffusion-based shifting algorithm for incompressible smoothed particle hydrodynamics. In *Proceedings of the 6th SPHERIC Workshop*, pages 14–20, Hamburg, 2011.
- W. K. Liu, S. Jun, and Y. F. Zhang. Reproducing kernel particle methods. *International Journal for Numerical Methods in Fluids*, 20(8-9):1081–1106, 1995. ISSN 1097-0363. doi: 10.1002/fld.1650200824. URL <http://onlinelibrary.wiley.com/doi/10.1002/fld.1650200824/abstract>.
- L. B. Lucy. A numerical approach to the testing of the fission hypothesis. *The Astronomical Journal*, 82:1013–1024, December 1977. URL <http://adsabs.harvard.edu/abs/1977AJ.....82.1013L>.
- F. Macià, L. M. González, J. L. Cercos-Pita, and A. Souto-Iglesias. A boundary integral SPH formulation consistency and applications to ISPH and WCSPH. *Progress of Theoretical Physics*, 128(3):439–462, September 2012. ISSN 0033-068X, 1347-4081.

- doi: 10.1143/PTP.128.439. URL <http://ptp.oxfordjournals.org/content/128/3/439>.
- O. Mahmood. Conditions aux limites ouvertes dans SPH et applications aux écoulements turbulents. Internship report, EDF R&D, 2011.
- O. Mahmood, C. Kassiotis, D. Violeau, M. Ferrand, and C. Denis. Effect of wall boundary treatment in SPH for modelling turbulent flows with inlet/outlet. In *Proceedings of the 6th SPHERIC Workshop*, pages 333–339, Hamburg, 2011.
- J. Mansour. *SPH and  $\alpha$ -SPH: Applications and Analysis*. PhD thesis, Monash University, October 2007.
- J.-C. Marongiu, F. Leboeuf, and E. Parkinson. Numerical simulation of the flow in a pelton turbine using the meshless method smoothed particle hydrodynamics: a new simple solid boundary treatment. *Proceedings of the Institution of Mechanical Engineers, Part A: Journal of Power and Energy*, 221(6):849–856, January 2007. ISSN 0957-6509. doi: 10.1243/09576509JPE465. URL <http://journals.pepublishing.com/content/e61q371706k87581/>.
- J.-C. Marongiu, F. Leboeuf, J. Caro, and E. Parkinson. Low mach number numerical schemes for the SPH-ALE method. application in free surface flows in pelton turbines. In *Proceedings of the 4th SPHERIC Workshop*, pages 323–330, Nantes, 2009.
- C. A. Micchelli. Interpolation of scattered data: Distance matrices and conditionally positive definite functions. *Constructive Approximation*, 2(1):11–22, 1986. ISSN 0176-4276. URL <http://dx.doi.org/10.1007/BF01893414>. 10.1007/BF01893414.
- P. Moin and J. Kim. Numerical investigation of turbulent channel flow. *Journal of Fluid Mechanics*, 118:341–377, 1982.
- J. J. Monaghan. An introduction to SPH. *Computer Physics Communications*, 48(1):89–96, January 1988. ISSN 0010-4655. doi: 10.1016/0010-4655(88)90026-4. URL <http://www.sciencedirect.com/science/article/B6TJ5-46FXB87-4J/2/6a7e03ab627e024618fb13ad48081026>.
- J. J. Monaghan. Simulating free surface flows with SPH. *Journal of Computational Physics*, 110:399–406, February 1994. URL <http://adsabs.harvard.edu/abs/1994JCoPh.110..399M>.
- J. J. Monaghan. SPH compressible turbulence. *Monthly Notices of the Royal Astronomical Society*, 335(3):843–852, September 2002. ISSN 00358711. doi: 10.1046/j.1365-8711.2002.05678.x. URL <http://onlinelibrary.wiley.com/doi/10.1046/j.1365-8711.2002.05678.x/full>.

- J. J. Monaghan. Smoothed particle hydrodynamics. *Reports on Progress in Physics*, 68(8):1703–1759, August 2005. ISSN 0034-4885. doi: 10.1088/0034-4885/68/8/R01. URL <http://iopscience.iop.org/0034-4885/68/8/R01>.
- J. Monaghan. Smoothed particle hydrodynamics. *Ann. Rev. of Astronomy and Astrophysics*, 30:543–574, 1992.
- J. Monaghan. SPH and riemann solvers. *Journal of Computational Physics*, 136(2): 298–307, September 1997. ISSN 0021-9991. doi: 10.1006/jcph.1997.5732. URL <http://www.sciencedirect.com/science/article/pii/S0021999197957326>.
- J. Monaghan. A turbulence model for smoothed particle hydrodynamics. *European Journal of Mechanics - B/Fluids*, 30(4):360–370, July 2011. ISSN 0997-7546. doi: 10.1016/j.euromechflu.2011.04.002. URL <http://www.sciencedirect.com/science/article/pii/S0997754611000355>.
- J. Monaghan and J. Kajtar. SPH particle boundary forces for arbitrary boundaries. *Computer Physics Communications*, 180(10):1811–1820, October 2009. ISSN 0010-4655. doi: 10.1016/j.cpc.2009.05.008. URL <http://www.sciencedirect.com/science/article/pii/S0010465509001544>.
- Y. Morinishi, T. Lund, O. Vasilyev, and P. Moin. Fully conservative higher order finite difference schemes for incompressible flow. *Journal of Computational Physics*, 143(1):90–124, June 1998. ISSN 0021-9991. doi: 10.1006/jcph.1998.5962. URL <http://www.sciencedirect.com/science/article/pii/S0021999198959629>.
- K. Morishita, T. Ishihara, and Y. Kaneda. Small-scale statistics in direct numerical simulation of turbulent channel flow at high-reynolds number. *Journal of Physics: Conference Series*, 318(2):022016, December 2011. ISSN 1742-6596. doi: 10.1088/1742-6596/318/2/022016. URL <http://iopscience.iop.org/1742-6596/318/2/022016>.
- J. P. Morris. A study of the stability properties of smooth particle hydrodynamics. *Publications of the Astronomical Society of Australia*, 13:97–102, January 1996. URL <http://adsabs.harvard.edu/abs/1996PASA...13...97M>.
- J. P. Morris, P. J. Fox, and Y. Zhu. Modeling low reynolds number incompressible flows using SPH. *Journal of Computational Physics*, 136(1):214–226, September 1997. ISSN 0021-9991. doi: 06/jcph.1997.5776. URL <http://www.sciencedirect.com/science/article/pii/S0021999197957764>.
- R. D. Moser, J. Kim, and N. N. Mansour. Direct numerical simulation of turbulent channel flow up to  $re = 590$ . *Physics of Fluids*, 11(4):943–945, April 1999.

- ISSN 10706631. doi: doi:10.1063/1.869966. URL [http://pof.aip.org/resource/1/phfle6/v11/i4/p943\\_s1?isAuthorized=no](http://pof.aip.org/resource/1/phfle6/v11/i4/p943_s1?isAuthorized=no).
- V. P. Nguyen, T. Rabczuk, S. Bordas, and M. Duflot. Meshless methods: A review and computer implementation aspects. *Mathematics and Computers in Simulation*, 79:763–813, 2008.
- G. Oger, M. Doring, B. Alessandrini, and P. Ferrant. An improved SPH method: Towards higher order convergence. *Journal of Computational Physics*, 225(2):1472–1492, August 2007. ISSN 0021-9991. doi: 10.1016/j.jcp.2007.01.039. URL <http://www.sciencedirect.com/science/article/B6WHY-4N9889C-1/2/f44ff99773571e21f880e0fbe948145a>.
- P. Omidvar. *Wave Loading on Bodies in the Free Surface Using Smoothed Particle Hydrodynamics*. PhD, University of Manchester, Manchester, 2010.
- P. Omidvar, P. K. Stansby, and B. D. Rogers. Wave body interaction in 2D using smoothed particle hydrodynamics (SPH) with variable particle mass. *International Journal for Numerical Methods in Fluids*, 68(6):686–705, 2012. ISSN 1097-0363. doi: 10.1002/flid.2528. URL <http://onlinelibrary.wiley.com/doi/10.1002/flid.2528/abstract>.
- A. N. Parshikov, S. A. Medin, I. I. Loukashenko, and V. A. Milekhin. Improvements in SPH method by means of interparticle contact algorithm and analysis of perforation tests at moderate projectile velocities. *International Journal of Impact Engineering*, 24(8):779–796, September 2000. ISSN 0734-743X. doi: 16/S0734-743X(99)00168-2. URL <http://www.sciencedirect.com/science/article/pii/S0734743X99001682>.
- S. B. Pope. *Turbulent Flows*. Cambridge University Press, 7 edition, 2001. URL <http://stacks.iop.org/0957-0233/12/i=11/a=705>.
- M. Prakash and P. W. Cleary. Three dimensional modelling of lava flow using smoothed particle hydrodynamics. *Applied Mathematical Modelling*, 35(6):3021–3035, June 2011. ISSN 0307-904X. doi: 16/j.apm.2010.12.023. URL <http://www.sciencedirect.com/science/article/pii/S0307904X10005226>.
- L. Prandtl. Bericht über untersuchungen zur ausgebildeten turbulenz. *Z. Angew. Math. Mech*, 5(2):136–139, 1925.
- A. Rafiee, S. J. Cummins, M. Rudman, and K. Thiagarajan. A comparative study on the accuracy of SPH schemes in DNS simulation of 2D wall-bounded decaying turbulence.

- In *Proceedings of the 6th International SPHERIC Workshop*, pages 44–51, Hamburg, 2011.
- P. W. Randles and L. D. Libersky. Smoothed particle hydrodynamics: Some recent improvements and applications. *Computer Methods in Applied Mechanics and Engineering*, 139(1-4):375–408, December 1996. ISSN 0045-7825. doi: 10.1016/S0045-7825(96)01090-0. URL <http://www.sciencedirect.com/science/article/B6V29-41FDG4T-F/2/8220aeb1a97726e157007f98e4215d5a>.
- F. Reif. *Fundamentals of statistical and thermal physics*. McGraw-Hill series in fundamentals of physics. McGraw-Hill, 1965. URL <http://books.google.com/books?id=w5dRAAAAMAAJ>.
- M. Robinson. *Turbulence and Viscous Mixing using Smoothed Particle Hydrodynamics*. PhD, Monash University, July 2009.
- M. Robinson, P. Cleary, and J. Monaghan. Analysis of mixing in a twin cam mixer using smoothed particle hydrodynamics. *AIChE Journal*, 54(8):1987–1998, August 2008. ISSN 00011541. doi: 10.1002/aic.11530. URL <http://onlinelibrary.wiley.com/doi/10.1002/aic.11530/full>.
- B. D. Rogers, R. A. Dalrymple, and P. K. Stansby. Simulation of caisson breakwater movement using 2-d SPH. *Journal of Hydraulic Research*, 48(sup1):135–141, January 2010. ISSN 0022-1686. doi: 10.1080/00221686.2010.9641254. URL <http://www.tandfonline.com/doi/abs/10.1080/00221686.2010.9641254>.
- P. Rollet-Miet. *Simulation des grandes échelles sur maillage non-structure pour géométries complexes*. PhD, Ecole centrale de Lyon, Lyon, 1998.
- P. Rollet-Miet, D. Laurence, and J. Ferziger. LES and RANS of turbulent flow in tube bundles. *International Journal of Heat and Fluid Flow*, 20(3):241–254, June 1999. ISSN 0142-727X. doi: 10.1016/S0142-727X(99)00006-5. URL <http://www.sciencedirect.com/science/article/pii/S0142727X99000065>.
- E. M. Ryan, A. M. Tartakovsky, and C. Amon. A novel method for modeling neumann and robin boundary conditions in smoothed particle hydrodynamics. *Computer Physics Communications*, 181:2008–2023, 2010.
- P. Sagaut. Large eddy simulation for incompressible flows. an introduction. *Measurement Science and Technology*, 12(10):1745–1746, October 2001. ISSN 0957-0233, 1361-6501. doi: 10.1088/0957-0233/12/10/707. URL <http://iopscience.iop.org/0957-0233/12/10/707>.

- P. Sagaut. *Large eddy simulation for incompressible flows*. Springer, 2006.
- U. Schumann. Subgrid scale model for finite difference simulations of turbulent flows in plane channels and annuli. *Journal of Computational Physics*, 18(4):376–404, August 1975. ISSN 0021-9991. doi: 10.1016/0021-9991(75)90093-5. URL <http://www.sciencedirect.com/science/article/pii/0021999175900935>.
- H. F. Schwaiger. An implicit corrected SPH formulation for thermal diffusion with linear free surface boundary conditions. *International Journal for Numerical Methods in Engineering*, 75(6):647–671, August 2008. ISSN 1097-0207. doi: 10.1002/nme.2266. URL <http://onlinelibrary.wiley.com/doi/10.1002/nme.2266/abstract>.
- C. E. Shannon. A mathematical theory of communication. *Bell System Technical Journal*, 27(3):379–423, 1948.
- S. Shao and E. Y. Lo. Incompressible SPH method for simulating newtonian and non-newtonian flows with a free surface. *Advances in Water Resources*, 26(7):787–800, July 2003. ISSN 0309-1708. doi: 10.1016/S0309-1708(03)00030-7. URL <http://www.sciencedirect.com/science/article/pii/S0309170803000307>.
- Y. L. Shi, M. Ellero, and N. A. Adams. SPH implicit turbulence modeling. In *Proceedings of the 6th International SPHERIC Workshop*, pages 52–58, Hamburg, 2011.
- D. J. Shlien and S. Corrsin. A measurement of lagrangian velocity autocorrelation in approximately isotropic turbulence. *Journal of Fluid Mechanics*, 62(02):255–271, 1974. doi: 10.1017/S002211207400067X.
- L. D. G. Sigalotti, H. López, and L. Trujillo. An adaptive SPH method for strong shocks. *Journal of Computational Physics*, 228(16):5888–5907, September 2009. ISSN 0021-9991. doi: 10.1016/j.jcp.2009.04.041. URL <http://www.sciencedirect.com/science/article/pii/S0021999109002423>.
- J. Smagorinsky. General circulation experiments with the primitive equations. *Monthly Weather Review*, 91(3):99–164, March 1963. ISSN 0027-0644, 1520-0493. doi: 10.1175/1520-0493(1963)091<0099:GCEWTP>2.3.CO;2. URL [http://journals.ametsoc.org/doi/abs/10.1175/1520-0493\(1963\)091%3C0099:GCEWTP%3E2.3.CO;2](http://journals.ametsoc.org/doi/abs/10.1175/1520-0493(1963)091%3C0099:GCEWTP%3E2.3.CO;2).
- W. H. Snyder and J. L. Lumley. Some measurements of particle velocity autocorrelation functions in a turbulent flow. *Journal of Fluid Mechanics*, 48:41–71, 1971. doi: DOI: 10.1017/S0022112071001460. URL <http://adsabs.harvard.edu/abs/1971JFM...48...41S>.

- P. Spalart, W. Jou, M. Strelets, and S. Allmaras. Comments of feasibility of LES for wings, and on a hybrid {rans/les} approach. In *International Conference on {DNS/LES}*, Aug. 4-8, 1997, Ruston, Louisiana., 1997.
- C. Speziale. Turbulence modeling for time-dependent RANS and VLES: a review. *AIAA Journal*, 36(2):173–184, February 1998. ISSN 0001-1452, 1533-385X. doi: 10.2514/2.7499. URL <http://arc.aiaa.org/doi/abs/10.2514/2.7499?journalCode=aiaaj>.
- V. Springel. The cosmological simulation code gadget-2. *Monthly Notices of the Royal Astronomical Society*, 364(4):1105–1134, December 2005. ISSN 1365-2966. doi: 10.1111/j.1365-2966.2005.09655.x. URL <http://onlinelibrary.wiley.com/doi/10.1111/j.1365-2966.2005.09655.x/abstract>.
- V. Springel. Simulating the universe with SPH: a mixed blessing. Keynote, Hamburg, June 2011. URL [http://www.tu-harburg.de/t3resources/6th-spheric/keynote\\_springel\\_01.pdf](http://www.tu-harburg.de/t3resources/6th-spheric/keynote_springel_01.pdf).
- V. Springel and L. Hernquist. The history of star formation in a  $\Lambda$  cold dark matter universe. *Monthly Notices of the Royal Astronomical Society*, 339(2):312–334, 2003. ISSN 1365-2966. doi: 10.1046/j.1365-8711.2003.06207.x. URL <http://dx.doi.org/10.1046/j.1365-8711.2003.06207.x>.
- V. Springel, S. D. M. White, A. Jenkins, C. S. Frenk, N. Yoshida, L. Gao, J. Navarro, R. Thacker, D. Croton, J. Helly, J. A. Peacock, S. Cole, P. Thomas, H. Couchman, A. Evrard, J. Colberg, and F. Pearce. Simulations of the formation, evolution and clustering of galaxies and quasars. *Nature*, 435(7042):629–636, June 2005. ISSN 0028-0836. doi: 10.1038/nature03597. URL <http://deepblue.lib.umich.edu/handle/2027.42/60629>.
- C. Struck. Simulations of collisions between two gas-rich galaxy disks with heating and cooling. *The Astrophysical Journal Supplement Series*, 113(2):269–309, December 1997. ISSN 0067-0049. doi: 10.1086/313055. URL <http://iopscience.iop.org/0067-0049/113/2/269>.
- N. Sukumar. Where do we stand on meshfree approximation schemes?, 2009. URL <http://dilbert.engr.ucdavis.edu/suku/blog/meshfreeblog.html>.
- N. Sukumar, J. Dolbow, A. Devan, J. Yvonne, F. Chinesta, D. Ryckelynck, P. Lorong, I. Alfaro, M. A. Martínez, E. Cueto, and M. Doblaré. Meshless methods and partition of unity finite elements. *International Journal of Forming Processes*, 8:409–427, 2005.
- J. Swegle. SPH in tension. Technical report, Sandia National Laboratories, 1992.

- P. Tait. Report on some of the physical properties of fresh water and sea water. *Rept. Sci. Results Voy., H.M.S. Challenger, Phys. Chem.*, 2:1–76, 1888.
- T. S. Ting, M. Prakash, P. W. Cleary, and M. C. Thompson. Simulation of high reynolds number flow over a backward facing step using SPH. In A. Stacey, B. Blyth, J. Shepherd, and A. J. Roberts, editors, *Proceedings of the 7th Biennial Engineering Mathematics and Applications Conference, EMAC-2005*, volume 47 of ANZIAM J., page C292–C309, October 2006.
- E. F. Toro. *Riemann solvers and numerical methods for fluid dynamics: A practical introduction*. Springer, 2nd edition, August 1999.
- F. Toschi and E. Bodenschatz. Lagrangian properties of particles in turbulence. *Annual Review of Fluid Mechanics*, 41:375–404, January 2009. doi: DOI:10.1146/annurev.fluid.010908.165210. URL <http://adsabs.harvard.edu/abs/2009AnRFM..41..375T>.
- C. Ulrich, N. Koliha, and T. Rung. SPH modelling of Water/Soil-Flows using a variable-resolution scheme. In *Proceedings of the 6th International SPHERIC Workshop*, pages 101–108, Hamburg, June 2011.
- R. Vacondio, B. D. Rogers, and P. K. Stansby. Smoothed particle hydrodynamics: Approximate zero-consistent 2-D boundary conditions and still shallow-water tests. *International Journal for Numerical Methods in Fluids*, 2011. ISSN 1097-0363. doi: 10.1002/flid.2559. URL <http://onlinelibrary.wiley.com/doi/10.1002/flid.2559/abstract>.
- R. Vacondio, P. Mignosa, B. D. Rogers, and P. K. Stansby. SPH shallow water equation solver for real flooding simulation. In *Proceedings of the 5th International SPHERIC Workshop*, pages 106–113, Manchester, 2010.
- R. Vacondio, B. D. Rogers, P. K. Stansby, P. Mignosa, and J. Feldman. Development of SPH variable resolution using dynamic particle coalescing and splitting. In *Proceedings of the 7th International SPHERIC Workshop*, pages 347–354, Prato, May 2012.
- A. Valizadeh and J. J. Monaghan. Smoothed particle hydrodynamics simulations of turbulence in fixed and rotating boxes in two dimensions with no-slip boundaries. *Physics of Fluids*, 24(3):035107–035107–18, March 2012. ISSN 10706631. doi: doi:10.1063/1.3693136. URL [http://pof.aip.org/resource/1/phf1e6/v24/i3/p035107\\_s1](http://pof.aip.org/resource/1/phf1e6/v24/i3/p035107_s1).
- M. Van Dyke. *An album of fluid motion*. Parabolic Press, Stanford, Calif., 1982. ISBN 0915760037 9780915760039 0915760029 9780915760022.

- C. Vetter, L. Oetting, C. Ulrich, and T. Rung. SPH simulations of pedestrian crowds. In *Proceedings of the 6th SPHERIC Workshop*, pages 261–268, Hamburg, 2011.
- J. P. Vila. On particle weighted methods and smooth particle hydrodynamics. *Mathematical Models and Methods in Applied Sciences*, 9(2):161–209, 1999.
- M. F. Villumsen and T. G. Fauerholdt. Simulation of metal cutting using smooth particle hydrodynamics. pages 17–36, Bamberg, 2008.
- D. Violeau. Dissipative forces for lagrangian models in computational fluid dynamics and application to smoothed-particle hydrodynamics. *Physical Review E*, 80(3):036705, 2009. doi: 10.1103/PhysRevE.80.036705. URL <http://link.aps.org/doi/10.1103/PhysRevE.80.036705>.
- D. Violeau and R. Issa. Numerical modelling of complex turbulent free-surface flows with the SPH method: an overview. *International Journal for Numerical Methods in Fluids*, 53(2):277–304, January 2007. ISSN 02712091. doi: 10.1002/flid.1292. URL <http://onlinelibrary.wiley.com/doi/10.1002/flid.1292/abstract>.
- D. Violeau. One and two-equations turbulent closures for smoothed particle hydrodynamics. In *6th International Conference on Hydroinformatics*, pages 87–94, Singapore, 2004. World Scientific Publishing Company.
- D. Violeau. *Fluid Mechanics and the SPH Method: Theory and Applications*. Oxford University Press, May 2012. ISBN 978-0-19-965552-6. URL <http://ukcatalogue.oup.com/product/academic/earthsciences/hydrology/9780199655526.do>.
- D. Violeau and A. Leroy. On the maximum time step in weakly compressible SPH. *Journal of Computational Physics*, 256:388–415, January 2014. ISSN 0021-9991. doi: 10.1016/j.jcp.2013.09.001. URL <http://www.sciencedirect.com/science/article/pii/S0021999113006050>.
- T. Wei and W. W. Willmarth. Reynolds-number effects on the structure of a turbulent channel flow. *Journal of Fluid Mechanics*, 204:57–95, 1989. doi: 10.1017/S0022112089001667.
- H. Weller, C. Greenshields, and M. Janssens. OpenFOAM, 2012. URL [www.openfoam.org](http://www.openfoam.org). URL: [www.openfoam.org](http://www.openfoam.org).
- H. Wendland. Piecewise polynomial, positive definite and compactly supported radial functions of minimal degree. *Advances in Computational Mathematics*, 4(1):389–396, December 1995. ISSN 1019-7168. doi: 10.1007/BF02123482. URL <http://www.springerlink.com/content/18j8724v5361u767/>.

- J. Westerweel. *Digital particle image velocimetry: theory and application*. PhD, Delft University of Technology, 1993.
- D. C. Wilcox. Reassessment of the scale-determining equation for advanced turbulence models. *AIAA Journal*, 26:1299–1310, November 1988. doi: DOI:10.2514/3.10041. URL <http://adsabs.harvard.edu/abs/1988AIAAJ...26.1299W>.
- R. Xu, P. Stansby, and D. Laurence. Accuracy and stability in incompressible SPH (ISPH) based on the projection method and a new approach. *Journal of Computational Physics*, 228(18):6703–6725, October 2009. ISSN 0021-9991. doi: 10.1016/j.jcp.2009.05.032. URL <http://www.sciencedirect.com/science/article/pii/S0021999109002885>.
- Y. Yeh and H. Z. Cummins. Localized fluid flow measurements with AN he-ne laser spectrometer. *Applied Physics Letters*, 4:176–178, May 1964. doi: DOI:10.1063/1.1753925. URL <http://adsabs.harvard.edu/abs/1964ApPhL...4...176Y>.
- A. Yoshizawa. Statistical theory for compressible turbulent shear flows, with the application to subgrid modeling. *Physics of Fluids*, 29(7):2152–2164, July 1986. ISSN 00319171. doi: doi:10.1063/1.865552. URL [http://pof.aip.org/resource/1/pfldas/v29/i7/p2152\\_s1](http://pof.aip.org/resource/1/pfldas/v29/i7/p2152_s1).

## Appendix A

# Derivation of skew-adjointness

In the following the left hand side of Eq. (3.7) will be analyzed when replacing the nabla operator with the gradient and divergence given by Eqs. (3.14) and (3.15). Initially the part containing the volume integrals of  $SA$  Eq. (3.7) will be investigated.

$$\begin{aligned} SA_v &= \int_{\Omega} \int_{\Omega} \frac{1}{\gamma_a} \left[ \frac{\rho_a^{2k} f_b + \rho_b^{2k} f_a}{\rho_a^k \rho_b^k} \underline{B}_a + f_a \frac{\rho_a^k \rho_b^k}{\rho_a^{2k}} (\underline{B}_b - \underline{B}_a) \right] \cdot \nabla_a w_{ab} dr_b dr_a \quad (\text{A.1}) \\ &= \int_{\Omega} \int_{\Omega} \frac{1}{\gamma_a} \left[ \frac{\rho_a^k}{\rho_b^k} f_b \underline{B}_a + \frac{\rho_b^k}{\rho_a^k} f_a \underline{B}_b \right] \cdot \nabla_a w_{ab} dr_b dr_a \end{aligned}$$

Furthermore, due to the additivity of the integral we can split it up

$$\begin{aligned} SA_v &= \int_{\Omega} \int_{\Omega} \frac{1}{\gamma_a} \frac{\rho_a^k}{\rho_b^k} f_b \underline{B}_a \cdot \nabla_a w_{ab} dr_b dr_a + \int_{\Omega} \int_{\Omega} \frac{1}{\gamma_a} \frac{\rho_b^k}{\rho_a^k} f_a \underline{B}_b \cdot \nabla_a w_{ab} dr_b dr_a \quad (\text{A.2}) \\ &= - \int_{\Omega} \int_{\Omega} \frac{1}{\gamma_a} \frac{\rho_a^k}{\rho_b^k} f_b \underline{B}_a \cdot \nabla_b w_{ab} dr_b dr_a - \int_{\Omega} \int_{\Omega} \frac{1}{\gamma_a} \frac{\rho_b^k}{\rho_a^k} f_a \underline{B}_b \cdot \nabla_b w_{ab} dr_b dr_a. \end{aligned}$$

In the last line the kernel gradient asymmetry  $\nabla_a w_{ab} = -\nabla_b w_{ab}$  was used in both terms. The boundary part of Eq. (3.7) can be reformulated to

$$\begin{aligned} SA_b &= \int_{\Omega} \int_{\partial\Omega} \frac{1}{\gamma_a} \left[ -\frac{\rho_a^{2k} f_b + \rho_b^{2k} f_a}{\rho_a^k \rho_b^k} \underline{B}_a + \frac{\rho_b^k}{\rho_a^k} f_a (\underline{B}_a - \underline{B}_b) \right] \cdot \underline{n}_b w_{ab} dr_b dr_a \quad (\text{A.3}) \\ &= \int_{\Omega} \int_{\partial\Omega} \frac{1}{\gamma_a} \left[ -\frac{\rho_a^k}{\rho_b^k} f_b \underline{B}_a - \frac{\rho_b^k}{\rho_a^k} f_a \underline{B}_b \right] \cdot \underline{n}_b w_{ab} dr_b dr_a \\ &= - \int_{\Omega} \int_{\partial\Omega} \frac{1}{\gamma_a} \frac{\rho_a^k}{\rho_b^k} f_b \underline{B}_a \cdot \underline{n}_b w_{ab} dr_b dr_a - \int_{\Omega} \int_{\partial\Omega} \frac{1}{\gamma_a} \frac{\rho_b^k}{\rho_a^k} f_a \underline{B}_b \cdot \underline{n}_b w_{ab} dr_b dr_a. \end{aligned}$$

Combining the volumic  $SA_v$  and the boundary term  $SA_b$  yields

$$\begin{aligned}
SA &= SA_v + SA_b \tag{A.4} \\
&= - \int_{\Omega} \int_{\Omega} \frac{1}{\gamma_a} \frac{\rho_a^k}{\rho_b^k} f_b \underline{B}_a \cdot \nabla_b w_{ab} dr_b dr_a - \int_{\Omega} \int_{\partial\Omega} \frac{1}{\gamma_a} \frac{\rho_a^k}{\rho_b^k} f_b \underline{B}_a \cdot \underline{n}_b w_{ab} dr_b dr_a \\
&\quad - \int_{\Omega} \int_{\Omega} \frac{1}{\gamma_a} \frac{\rho_b^k}{\rho_a^k} f_a \underline{B}_b \cdot \nabla_b w_{ab} dr_b dr_a - \int_{\Omega} \int_{\partial\Omega} \frac{1}{\gamma_a} \frac{\rho_b^k}{\rho_a^k} f_a \underline{B}_b \cdot \underline{n}_b w_{ab} dr_b dr_a \\
&= - \int_{\Omega} \frac{1}{\gamma_a} \rho_a^k \underline{B}_a \cdot \left[ \int_{\Omega} \frac{f_b}{\rho_b^k} \nabla_b w_{ab} dr_b - \int_{\partial\Omega} \frac{f_b}{\rho_b^k} \underline{n}_b w_{ab} dr_b \right] dr_a \\
&\quad - \int_{\Omega} \frac{1}{\gamma_a} \frac{f_a}{\rho_a^k} \left[ \int_{\Omega} \rho_b^k \underline{B}_b \cdot \nabla_b w_{ab} dr_b - \int_{\partial\Omega} \rho_b^k \underline{B}_b \cdot \underline{n}_b w_{ab} dr_b \right] dr_a \\
&= - \int_{\Omega} \rho_a^k \underline{B}_a \cdot \left[ \frac{1}{\gamma_a} \int_{\Omega} \nabla_b \left( \frac{f_b}{\rho_b^k} \right) w_{ab} dr_b \right] dr_a - \\
&\quad \int_{\Omega} \frac{f_a}{\rho_a^k} \left[ \frac{1}{\gamma_a} \int_{\Omega} \nabla_b \cdot \left( \rho_b^k \underline{B}_b \right) w_{ab} dr_b \right] dr_a,
\end{aligned}$$

where in the last step a reverse integration by parts was used. The terms in square brackets represent SPH approximations which in the limit of  $h \rightarrow 0$  converge to

$$\begin{aligned}
SA &\rightarrow - \int_{\Omega} \rho_a^k \underline{B}_a \cdot \nabla_a \left( \frac{f_a}{\rho_a^k} \right) dr_a - \int_{\Omega} \frac{f_a}{\rho_a^k} \nabla_a \cdot \left( \rho_a^k \underline{B}_a \right) dr_a \tag{A.5} \\
&= - \int_{\Omega} \left[ \rho_a^k \underline{B}_a \cdot \nabla_a \left( \frac{f_a}{\rho_a^k} \right) - \frac{f_a}{\rho_a^k} \nabla_a \cdot \left( \rho_a^k \underline{B}_a \right) \right] dr_a \\
&= - \int_{\Omega} \nabla_a \cdot (f_a \underline{B}_a) dr_a \\
&= - \int_{\partial\Omega} f_a \underline{B}_a \cdot \underline{n}_a dr_a,
\end{aligned}$$

where in the second last line again a reverse integration by parts was used and the final line follows from Stokes' theorem.

## Appendix B

# Derivation of the Smagorinsky constant for the Wendland kernel

In the following the Smagorinsky constant for the Wendland kernel in isotropic turbulence will be computed following the analysis by Lilly (1967). It is assumed that the filter width is in the inertial subrange and that an inertial subrange exists such that the energy-spectrum function is given approximately by

$$E(\kappa) \approx C\epsilon^{2/3}\kappa^{-5/3}, \quad (\text{B.1})$$

with  $C = 1.5$  being the Kolmogorov constant. The mean rate of strain is related to the Energy via

$$\langle \bar{S}^2 \rangle = 2 \int_0^\infty \kappa^2 \bar{E}(\kappa) d\kappa, \quad (\text{B.2})$$

and as shown in Pope (2001) the filtered energy can be related to the unfiltered energy by

$$\bar{E}(\kappa) = \hat{G}(\kappa)^2 E(\kappa), \quad (\text{B.3})$$

where  $\hat{G}$  is the Fourier transform of the filter. In the following  $G$  is assumed to be the Wendland kernel  $W$  given in Section 2.2.2. It is given by

$$\hat{G}(\kappa) = \frac{45}{4h^6\kappa^6} \left( -2 + 2h^2\kappa^2 + 2\cos(2h\kappa) + h\kappa \sin(2h\kappa) \right). \quad (\text{B.4})$$

Using Eqs. (B.2) and (B.3) yields

$$\langle \bar{S}^2 \rangle = 2 \int_0^\infty \kappa^2 \hat{G}(\kappa)^2 E(\kappa) d\kappa, \quad (\text{B.5})$$

and inserting the spectrum of Eq. (B.1) gives the approximation

$$\langle \bar{S}^2 \rangle \approx a_f C \epsilon^{2/3} \Delta_G^{-4/3} \quad (\text{B.6})$$

with

$$a_f := 2 \int_0^\infty (\kappa \Delta_G)^{1/3} \widehat{G}(\kappa)^2 \Delta_G d\kappa. \quad (\text{B.7})$$

The value of  $a_f$  for the Wendland kernel is  $a_f = 7.759$ . The inertial subrange is characterized by the fact that the rate of transfer of energy to the residual motions is balanced by the dissipation. The former is given through the Smagorinsky model as

$$P_r = \nu_r \bar{S}^2, \quad (\text{B.8})$$

the later can be computed inversely from Eq. (B.6). Due to the balance the two are equal and yield

$$C_S = \frac{1}{(Ca_f)^{3/4}} \left( \frac{\langle \bar{S}^3 \rangle}{\langle \bar{S}^2 \rangle^{3/2}} \right)^{-1/2}. \quad (\text{B.9})$$

Using the approximation that  $\langle \bar{S}^3 \rangle \approx \langle \bar{S}^2 \rangle^{3/2}$  results in a value of

$$C_S \approx 0.158. \quad (\text{B.10})$$